Supermassive Black Hole Dynamics and Feedback Across Cosmic Scales

---

Dissertation

zur

Erlangung der naturwissenschaftlichen Doktorwürde
(Dr. sc. nat.)

vorgelegt der

Mathematisch-naturwissenschaftlichen Fakultät

der

Universität Zürich

von

Pawel Biernacki

aus

Polen

Promotionskommission

Prof. Dr. Romain Teyssier (Vorsitz)
Prof. Dr. Lucio Mayer
Prof. Dr. Ben Moore
Prof. Dr. Kevin Schawinski

Zürich, 2018

To my family, as otherwise this would not be possible

Abstract

Supermassive black holes (SMBH) are found in centres of massive galaxies at all epochs. Furthermore, they have been invoked as an important element of the galaxy evolution models. It still remains unclear how the feedback from accretion-powered SMBH, known as Active Galactic Nucleus (AGN), can shape the evolution of its host galaxy. It is believed that AGN reduce or even completely quench star formation and are responsible for ejecting dense gas far out of the galactic disc. Moreover, compelling observational evidence suggests that SMBHs coevolve with their hosts, self-regulating their own growth. With the recent advances in observational techniques of these exotic objects, like the Laser Interferometer Space Antenna or the Event Horizon Telescope, it is a high time to improve our understanding of SMBH-galaxy coevolution.

In this Thesis, I use adaptive mesh refinement hydrodynamical simulations in which I study SMBHs formation, growth, dynamics and feedback in order to understand how they coevolve with their massive, gas-rich, clumpy hosts at the peak of star formation epoch. I examine this connection from two perspectives. Firstly, I focus on the growth of a SMBH and its subsequent dynamical evolution within a supernovae-dominated interstellar medium. In this line of research I propose a new model in which SMBH is embedded within a dense and compact nuclear star cluster. This additional stellar component, supported by observations, locks SMBH in the centre of a galaxy, fostering its subsequent growth. Secondly, I switch the perspective to a galaxy as a whole. I demonstrate how does the AGN feedback impact star formation and argue, that massive molecular outflows seen in observations of high-redshift galaxies can be explained by the cooperation between AGN and supernovae feedbacks. Furthermore, I also show the impact of numerical modelling of hydrodynamics on the AGN feedback efficiency in idealised clusters of galaxies, which are important cosmological testbeds.

Pawel Biernacki
Institute for Computational Science
University of Zurich
Winterthurerstrasse 190
CH-8057 Zürich
Switzerland
biernack@physik.uzh.ch

Contents

List of Figures

1

Introduction

We are an impossibility in an impossible universe.

– Ray Bradbury

1.1. Short story of long galaxy formation and evolution

The Universe is old. About 13.6 millions years old, to be more precise. According to current theories it started with the Big Bang from which space, time and matter came to be. The portrait of the Universe in its infancy, known as Cosmic Microwave Background (CMB) discovered by Penzias & Wilson (1965) and later studied by WMAP and Planck satellites, reveals that the Universe was much hotter and more homogenous than it is now. The tiny fluctuations (of order of ten parts in a million) that are seen in the image of the CMB (see Figure 1.1) were amplified over the time of the evolution of the Universe and led to formation of galaxies. However, the Universe is not built only of the ordinary matter that astronomers observe at night (or from which we are built), but also of mysterious matter and energy components, which, for the lack of knowledge of their nature, we dub 'dark'. Dark matter (DM) and dark energy put together account for about 95% of the content of the Universe. According to the most popular and widely-accepted cosmological model, ΛCDM, dark energy accounts for 70%. Remaining 30% shapes the galaxies that we know. Dark and ordinary matter follow each other thanks to the gravitational force, forming halos in which galaxies are embedded. Such a 'flat' Universe is forever expanding. Initially its expansion rate is slowing down, but thanks to the domination of dark energy over gravity of matter the expansion rate ultimately increases.

But how do galaxies come to be? What we called 'ordinary matter' consists of hydrogen and helium produced in the first seconds of the life of the Universe. This primordial mixture is pulled together by its own gravity as well as that of DM. The gas is heated by shocks during the collapse and if it can efficiently cool, then it starts collapsing further forming dense, self-gravitating (i.e. its own gravitational pull is stronger than that of DM its embedded in) clouds. If the cooling wins over heating, then such Giant Molecular

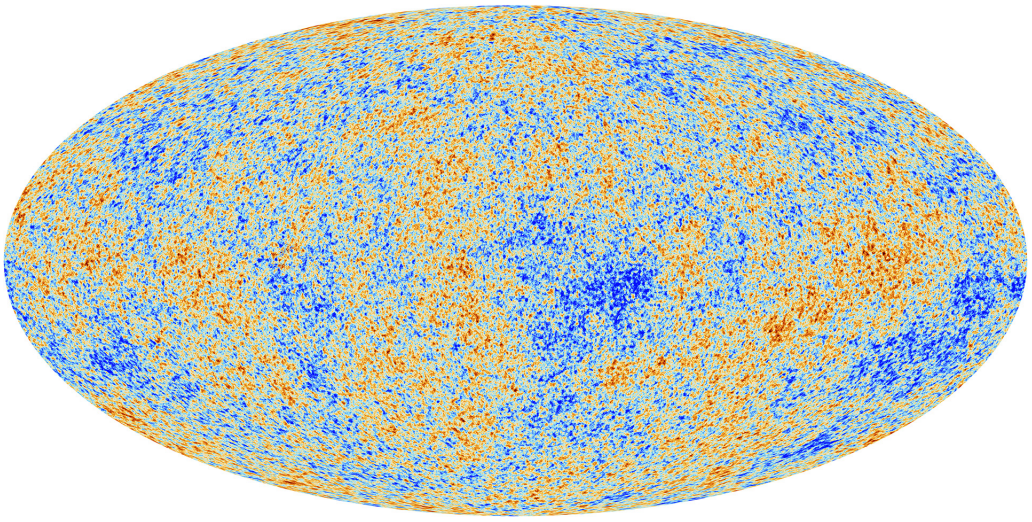

Figure 1.1: Cosmic microwave background as seen by the ESA *Planck* Space Telescope. Imprint of the Universe from when it was 380 thousands years old. *Image credit: ESA and the Planck Collaboration.*

Clouds (GMCs) fragment, collapse further. If these high-density cores reach sufficiently high densities in order to start nuclear fusion we can say that stars were formed! This is naturally a great simplification of the full physical picture, which is still very much an area of active research. What we then typically refer to as a 'galaxy' is a large collection of stars, embedded in its DM halo, forming new stars out of the gas that is constantly being accreted. Some of the oldest examples observed today have formed when the Universe was only 500 Myr old! If we compare the Universe to a human, then first galaxies would start forming at the age of 2-3!

In the ΛCDM model all structures form hierarchically - small DM halos formed first, then either accreted mass violently via mergers or gently via a spherical accretion. This means, that the largest objects observed today, the galaxy clusters, formed now (or, in fact, are still forming!). Galaxy clusters themselves are built of galaxies. These were initially seen as nebulous objects (as in the famous catalogue by Charles Messier compiled at the end of the 18th century) and only in the last hundred years recognised to be residing outside of our own Galaxy, the Milky Way. The discovery of galaxies being 'island universes' (as dubbed by the philosopher Immanuel Kant in the mid-18th century), great collections of stars separated by very large distances from each other came from observations of novae stars in the Messier object M31 (today known as the Andromeda Galaxy; see Curtis, 1917). Almost a decade later Edwin Hubble observed Cepheid variable stars and concluded they cannot be part of the Milky Way Hubble (1929).

Edwin Hubble was also the author of the first galaxy classification based on their appearance (Hubble, 1927). On Figure 1.2 we show the division proposed by Hubble. Galaxies presented on the left are known as elliptical galaxies. The number by their classification describes how close they are to being spherical - 0 for spheres to 7 for elongated ellipsoids. Ellipticals are also known as early-type galaxies, as they formed when the Universe was still young. They are usually characterised by virtually no new star formation and the majority of their stars are old and low-mass. Due to that they are often called 'red and dead' (low-mass stars have yellow-red appearance). It is believed

that supermassive black holes in the heart of each elliptical galaxy prevent the remaining gas from cooling and forming new stars (e.g. Werner et al., 2014). The evolution of elliptical galaxies progresses via repeated mergers with smaller objects, which could explain e.g. a large number of globular clusters in elliptical galaxy halos (Ashman & Zepf, 1992; Elmegreen & Efremov, 1997; Li & Gnedin, 2014). Furthermore, these massive ($\sim 10^{11}$ $M_\odot$) galaxies are often found in the centres of galaxy clusters (e.g. Kravtsov & Borgani, 2012), which are the largest gravitationally bound structures in the Universe, comprised of thousands of galaxies.

The right-hand side of Figure 1.2 shows spiral galaxies, which are sub-divided into barred systems (bottom branch) and bar-free (top branch), as well as compactness of their spiral arms (a for most tightly winded to c for the least). By contrast these are the late-type galaxies, that are usually very blue in their appearance, which is a sign of their young age. In those galaxies new (and blue in appearance) stars are still being formed. Spiral galaxies can be are classically differentiated as having a bar (Sb, like our own Milky Way Galaxy) or not (S), with an additional letter describing tightness of their spiral arms. Furthermore, S0 galaxies are known as lenticular galaxies, which are in the transition between spirals and ellipticals. Centres of spiral galaxies are often occupied by spherically distributed stars which display randomly oriented orbits (called bulges) or coherent orbits (dubbed pseudobulges). The former are believed to be formed by repetitive minor mergers (e.g. Kormendy et al., 2010; Brook et al., 2012). Importantly, spiral galaxies are characterised by much larger gas fractions than galaxies of other types, especially at the peak of galaxy formation (e.g. Madau & Dickinson, 2014) at redshift[1] $z \sim 2$.

Although Hubble morphological classifications illustrates basic differences in galaxy morphology, it does not capture the whole zoo of objects currently observed. Hubble was able to detect only the brightest galaxies in the local Universe and his classification is by no means exhaustive. Two separate classes of objects not mentioned by Hubble are irregular and dwarf galaxies. Irregular galaxies do not have prominent central, spherical distribution of stars (like ellipticals or bulges of some of disc galaxies) nor the clear and coherent spiral arms. Their shape can be explained by gravitational interactions with more massive neighbours, suggesting their overall small masses. Dwarf galaxies are characterised by low luminosity and thus low stellar mass (typically of order of $10^5\,M_\odot$). Some of them can be categorised as irregulars. Two best known examples of dwarf galaxies are Magellanic Clouds which orbit the Milky Way.

It is now widely agreed that all massive galaxies host supermassive black holes (SMBHs) in their centres. In 1963 Schmidt has reported on the discovery of a powerful extragalactic radio source 3C 273, an order of magnitude brighter than brightest galaxies. The first quasi-stellar object (QSO or quasar) was discovered and many more followed soon after. It has been later recognised (e.g. Hoyle & Fowler, 1963; Salpeter, 1964; Zel'dovich, 1964; Lynden-Bell, 1969; Lynden-Bell & Rees, 1971), that this kind of object is a SMBH with the large luminosities due to accretion of gas. The mass of these objects is consistent with the observed energy density in quasar light (a demonstration known as the Sołtan argument). It is argued that galaxies and their SMBHs co-evolve, impacting each others growth. The most recent galaxy evolution models require some sort of feedback from SMBHs in order to reproduce observed stellar properties, as well

[1] Cosmological redshift is a quantity that describes the velocity at which objects recede from an observer due to the expansion of the Universe. If objects are getting closer to the observer, then we talk about blueshift. Typically $z = 1/a_{\rm exp}$, where $a_{\rm exp}$ is the expansion factor and where we have assumed that current expansion factor is 1 (it is equal to zero at the Big Bang).

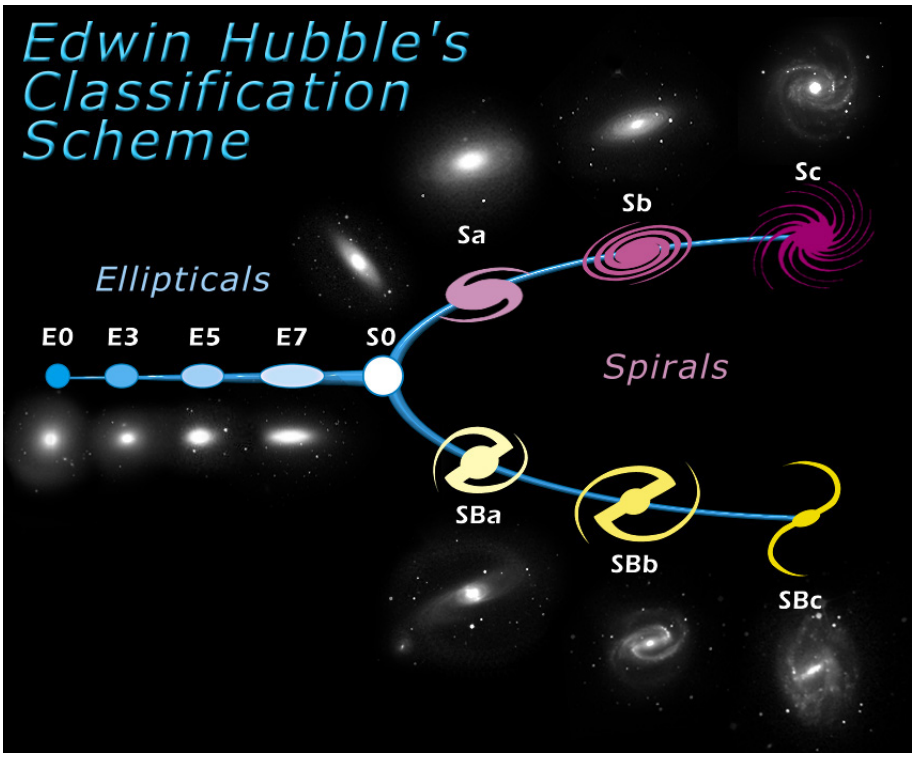

Figure 1.2: Edwin Hubble's classification scheme of galaxies. Left side of the diagram depicts elliptical galaxies, which are also known as early-type galaxies as their progenitors formed at the early times of the evolution of the Universe. Right side of the diagrams shows two branches of spiral (or late-type) galaxies - regular (top) and bar-dominated (bottom). *Image credit: NASA & ESA.*

as the large-scale kinematics of gas. This Thesis will try to tackle some of the remaining issues that these models have.

In the next Chapter I am going to introduce in much greater detail many of the concepts that have been briefly mentioned here.

2

SUPERMASSIVE BLACK HOLE - GALAXY COEVOLUTION

It is not because things are difficult that we do not dare, it is because we do not dare that they are difficult.

– Lucius Annaeus Seneca

2.1. Theory of black holes

The most basic way to describe what a black hole is is to think of a region of spacetime characterised by such strong gravitational pull than nothing, not even light, can escape. According to Einstein's theory of general relativity any mass curves the spacetime, thus a sufficiently compact object can curve it to the degree which would result in the formation of the black hole. The region from which nothing can escape is called the event horizon and is characterised by the Schwarzschild radius (named after Karl Schwarzschild who found a solution of general relativity that describes black holes)

$$R_S = \frac{2GM_{BH}}{c^2}, \tag{2.1}$$

where G is the gravitational constant, M_{BH} is a black hole mass and c is the speed of light in vacuum. This radius can be up to two times smaller if a black hole spin or charge are nonzero. According to the theory of general relativity, the centre of a black hole contains a singularity, i.e. a region of spacetime with infinite curvature and zero volume.

The theory of black holes names three quantities that characterise black holes: mass, spin and charge (the latter not being relevant for astrophysical black holes). The mass of the astrophysical black hole is related to its progenitor. Stellar mass black holes are a final stage of existence of stars more massive than 8 $M_\odot$. The typical mass of such a remnant (known also as collapsar) is between few and several tens of Solar masses.

General relativity does not provide lower nor upper limit for black hole mass. The spin of black hole is related to the angular momentum of material from which a black hole was formed and to a certain degree it regulates how much energy is being released by the black hole. In this Thesis I assume however, that it is not a major effect (but see e.g. King & Pringle, 2006; Sijacki et al., 2009; Fiacconi et al., 2018).

Nothing that falls on a black hole can leave it, which means that black holes can grow by accreting mass from their surroundings. In case of stellar mass black holes the accreted gas comes from a companion star that is being stripped of gas. Larger black holes, with masses of order of 10^5 $M_\odot$ and more (known as supermassive black holes; SMBH) grow via accretion of gas from the interstellar matter (ISM). Due to the angular momentum conservation, the gas accreted circularises around the SMBH before it is being accreted. In the process of losing of the gravitational energy gas produces radiation, which is a physical manifestation of the accretion. The redistribution of the angular momentum within the disc is possible due to turbulence-enhanced viscosity, which is boosted by the presence of turbulent eddies within the disc structure; this model has been widely popularised by a seminal work by Shakura & Sunyaev (1973). In their work they suggest the following relationship between luminosity L and mass accretion rate $\dot{M}$:

$$L = \epsilon_\mathrm{r} \dot{M} c^2, \tag{2.2}$$

where $\epsilon_\mathrm{r} = 0.1$ is the radiative efficiency.

In general, if outward radiation pressure balances the inward gravitational force, we get

$$-\nabla\Phi = \frac{\kappa}{c} F_\mathrm{rad}, \tag{2.3}$$

where $\nabla\Phi = -GM/r^2$ describes the gravitational potential, $F_\mathrm{rad} = L/4\pi r^2$ is the radiation flux, κ is the opacity of material.

Under the assumption of constant opacity ($\kappa = \sigma_\mathrm{T}/m_\mathrm{p}$, where σ_T is Thomson scattering cross-section for the electron and m_p is the mass of a proton) and composition of pure ionised hydrogen the above equation can be integrated at the surface to give the Eddington luminosity

$$L_\mathrm{Edd} = \frac{4\pi G M m_\mathrm{p} c}{\sigma_\mathrm{T}}, \tag{2.4}$$

where M is mass of the object.

The accretion rate of BH is usually normalised to the Eddington rate, which is a reformulation of the Eddington luminosity

$$\dot{M}_\mathrm{Edd} = \frac{4\pi G M m_\mathrm{p}}{\epsilon_\mathrm{r} \sigma_\mathrm{T} c}. \tag{2.5}$$

An important concept that relates to this maximal accretion rate is the so-called Salpeter time during which SMBH doubles its mass

$$t_\mathrm{Salpeter} = \frac{\epsilon_\mathrm{r} \sigma_\mathrm{T} c}{4\pi G m_\mathrm{p}} \approx 45\,\mathrm{Myr}. \tag{2.6}$$

Classically accretion on BH is described with Bondi-Hoyle-Lyttleton (or often Bondi for short) accretion rate (Hoyle & Lyttleton, 1939; Bondi & Hoyle, 1944; Bondi, 1952). In the original formulation this describes a spherical accretion on a compact object (neutron star, black hole) from a uniform and static gas medium. Despite the obvious differences

like the lack of angular momentum treatment or relative velocity between gas and the object, it has been widely applied in numerical simulations of SMBH (starting e.g. with early work by Springel et al., 2005). In it simplest form it can be stated as

$$\dot{M}_{\mathrm{Bondi}} = \frac{4\pi G M_{\mathrm{BH}}^2 \rho}{c_{\mathrm{s}}^3}, \tag{2.7}$$

where ρ and c_{s} are the density and the sound speed of gas, respectively. Certain sophistications to the model where introduced and dropped over the recent years. Springel et al. (2005) introduced a α boost factor which compensated the accretion rate for the lack of resolution, while Booth & Schaye (2009) made it depend on local density.

An alternative, gravitational torque-based, model has been introduced by Hopkins & Quataert (2011) connects large-scale transport of the gas in the galactic disc to the accretion disc around SMBH. This has been parameterised as follows

$$\dot{M}_{\mathrm{visc}} = 3\pi\delta\Sigma\frac{c_{\mathrm{s}}^2}{\Omega}, \tag{2.8}$$

with δ being a dimensionless viscosity parameter, Σ the mean gas surface density and Ω the rotational angular velocity of the gas.

The two prescriptions discussed here represent two families of accretion models - with strong BH mass dependence (former) and with the weak one (latter). They all, however, try to bridge the gap between galaxies and accretion discs, which is a difficult task troubled by complex physical processes, large span of physical and temporal scales and, in case of computer simulations, numerical limitations. For a detailed analysis of effects of various prescriptions I refer curious reader to e.g. Thacker et al. (2014); Negri & Volonteri (2017).

2.2. Observing astrophysical black holes

In the previous section we have learned what (supermassive) black holes should be, but do such extreme objects exist? In this section I am going to review various attempts to observe black holes. The following review tries to follow the observational timeline, but is by no means exhaustive.

2.2.1. Sgr A* and S stars

The Galactic Centre is 8.3 kpc[1] away (Genzel et al., 2010), thus it is possible to resolve individual stars. A young stellar cluster found in the centre of Milky Way consists of more than hundred so-called *S stars*. Two of the stars that have been observed have their orbital periods shorter than 20 years (Meyer et al., 2012), thus their positions are changing significantly within a human lifetime; Figure 2.1 presents a visual summary of twenty orbits of S stars. One of the stars, S2, has an orbital period of 15.8 years and at pericenter it gets as close as 1400 R_{S} to the central object. Thanks to repeated observations by Ghez et al. (2008) and Gillessen et al. (2009), it has been possible to fit their orbits and find constraints for the mass of the object in the centre. Genzel et al. (2010) have shown that the mass of this central object is $\sim 4 \times 10^6$ $\mathrm{M}_\odot$. These measurements

[1]The parsec (pc) is a unit of length equal to the distance to one astronomical unit seen as one arcsecond; 1 pc $\approx 3.086 \times 10^{18}$ cm.

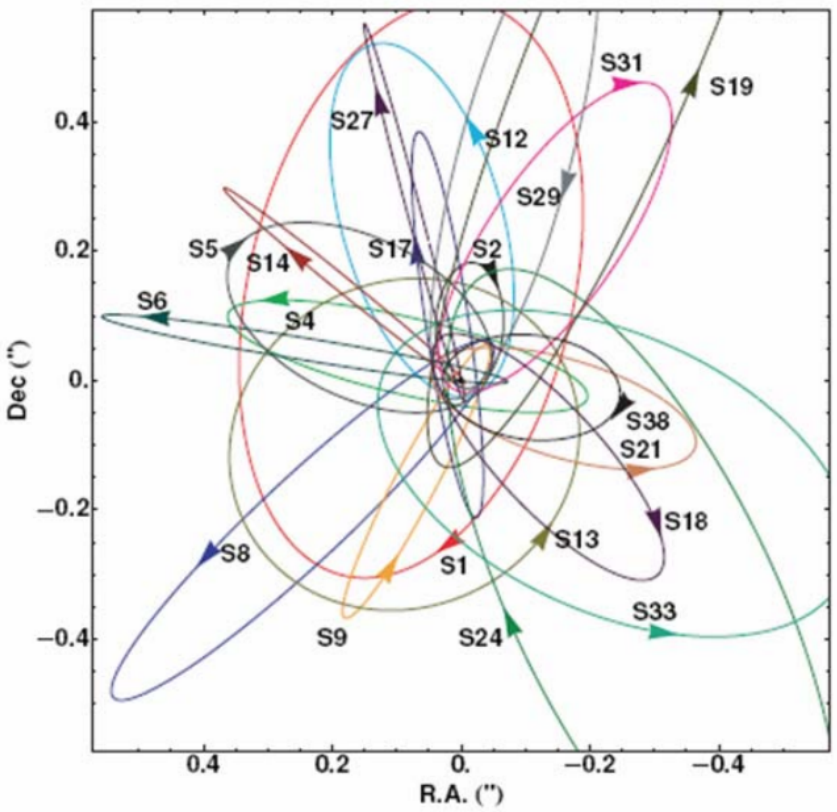

Figure 2.1: Visual summary of twenty orbits of S stars around Sgr A* as reported by Gillessen et al. (2009). Reprinted figure with permission from Genzel R., Eisenhauer F., Gillessen S., Rev. Mod. Phys., 82, 3121, 2010. Copyright 2010 by the American Physical Society.

put strong constrains on the size and thus the density of the central object – it has to be a SMBH, as more exotic explanations have been ruled out.

The origin of the S stars in the vicinity of Sgr A* is still debated. Strong tidal field from SMBH makes the formation *in situ* very unlikely, as it would required accretion of a giant molecular and formation in the resulting gas disc (Bonnell & Rice, 2008). Other scenarios explain the presence of S stars in the Galactic Centre with migration from distances of 0.5 pc and larger (see e.g. Berukoff & Hansen, 2006; Levin, 2007; Gualandris & Merritt, 2009; Fujii et al., 2010, for discussion of specific models).

2.2.2. Gravitational waves and the LIGO discovery

According to the general theory of relativity a merger between any two objects should lead to production of gravitational waves (which can be compared to ripples on the surface of a lake after one drops a stone). The shape and strength of the observed signal depend on masses of objects that undergo a merger. In 2015 the Laser Interferometer Gravitational-Wave Observatory (LIGO) has recorded the first ever merger of two stellar mass black holes – 36 $M_\odot$ and 29 $M_\odot$ (see Figure 2.2 for the measurement of the gravitational wave strain observed during the merger by two LIGO detectors). This has been

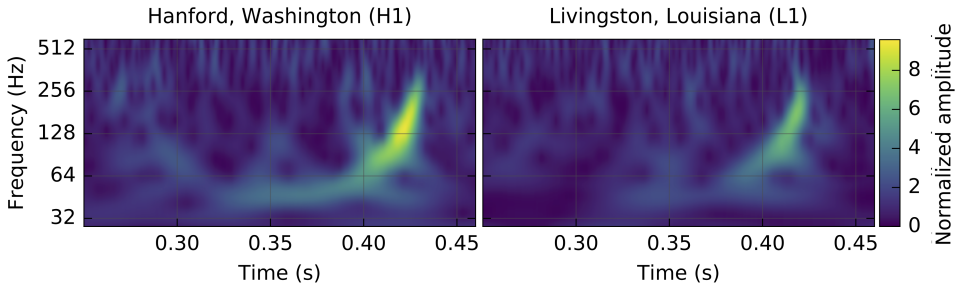

Figure 2.2: The first detected gravitational wave event, GW150914, as seen by two detectors. The two panels show how the gravitational wave strain, i.e. a dimensionless measure of amplitude of gravitational waves, as a function of time (in seconds) and frequency. *Image credit: LIGO Scientific Collaboration, Abbott et al. (2016).*

the first observation of this kind, enabling astronomers to perceive the Universe in a new way. It has been derived that the separation between the two black holes at the moment of merger was 350 km, which is four times their Schwarzschild radius. This in turn meant that these objects had to be extremely compact, which leaves black holes as the only explanation. Future gravitational wave observatories are constructed in order to probe different range of merging black hole masses, which will hopefully provide us with more information also on SMBHs.

2.2.3. Direct imaging

By definition no light escapes from a black hole. How can then one make in image of it? It is indeed an impossible task, but one can make an image of the closest environment of a black hole by imaging its accretion disc. This is the task in front of the Event Horizon Telescope (EHT) Collaboration, which is observing Sgr A* (and other nearby SMBHs) and analysing complex interferometric data collected around the world. The smaller the distances between telescopes, the less data about a black hole is missing, while the larger the telescope separation, the better is the spatial resolution of a final image. Multiple reconstructed images are going to be consistent with sparse data collected by the EHT. The reconstructed set of images is going to be cross-matched with pre-computed models (see Figure 2.3 for an example), which should provide constraints on the models. The observing campaign has finished in April 2017, but at the moment of writing no results have been released by the EHT Collaboration.

2.3. Weighing SMBHs

As it was described in Section 2.1 a black hole has only three properties – mass, spin and charge. In this Section I am going to focus on various ways in which SMBH mass can be measured in nature.

In the case of Sgr A*, measuring the mass of a central object provides information on its nature. More indirect methods have to be applied to search of SMBHs beyond nearby galaxies. An excellent review of the various techniques was written by Kormendy & Ho (2013), thus I will only briefly summarise the most important ones here.

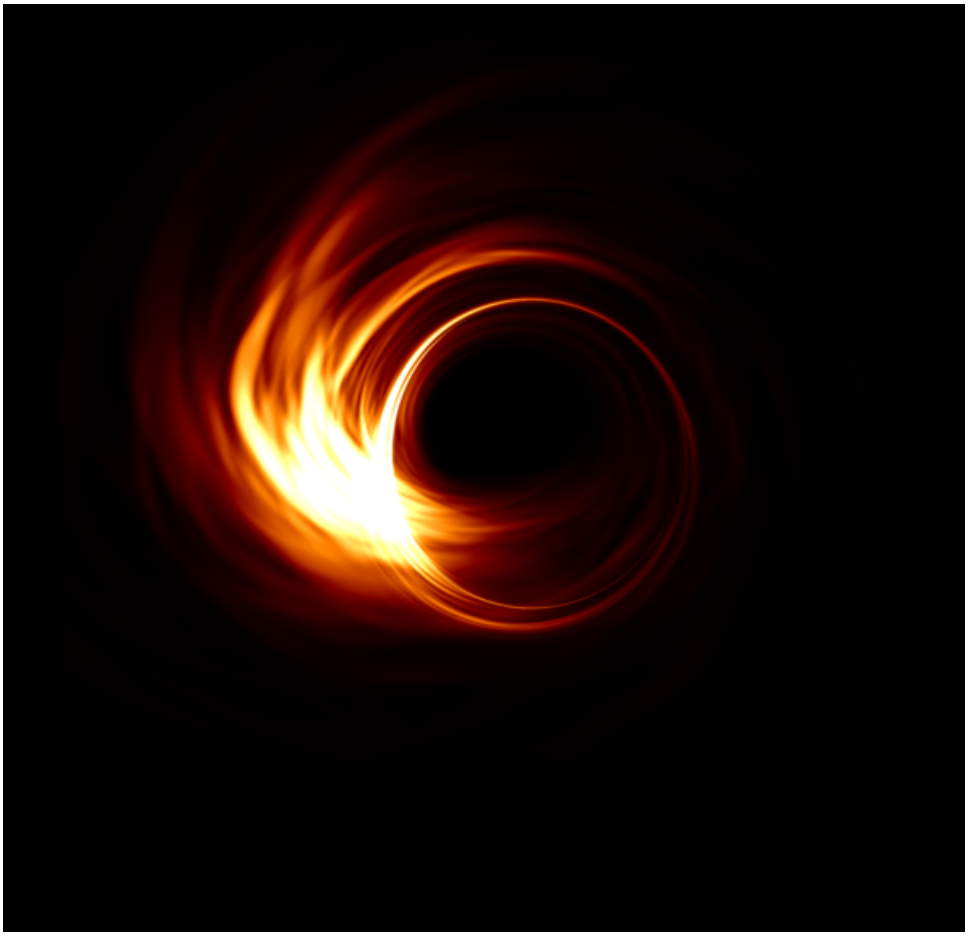

Figure 2.3: Simulated image of the accretion disc around a black hole, seen at angle of 45 deg. The central dark part is the "shadow" of the black hole. *Image credit: Hotaka Shiokawa and the Event Horizon Telescope Collaboration.*

Thanks to high resolution data obtained with the Hubble Space Telescope and ground-based adaptive-optics assisted observations it is possible to study the kinematics of stars in other galaxies. These observations are cross-matched with dynamical models to provide measurements of SMBH masses. By measuring the rotation velocity and velocity dispersions with spectroscopic observations of stellar absorption lines and the density distribution of stars from photometry, it is possible to use the first moment of the collisionless Boltzmann equation[2] to constrain the amount of mass within a studied radius. Most recently this method has be extended by the effects of halo dark matter and the shape of the halo (its triaxality), see e.g. van den Bosch et al. (2008); Gebhardt & Thomas (2009).

The ionised gas dynamics provides results complementary to the previous method, especially that nebular emission lines are easier to measure and interpret. Few assumptions have to be made about the observed gas, namely that it is cold and rotates in the principal plane of the galactic potential. As previously, the observations of velocity and its dispersions have to be compared with analytical models. This method is not free of caveats, however. The gas being modelled can be shocked or impacted by turbulence, radiation or magnetic fields. Furthermore, its apparent distribution can be affected by the obscuration from dust.

Masers are sources of microwave radiation which is emitted with the same physical effect of stimulated spectral light emission as the one occurring in common visible light lasers, hence the name. Megamasers are larger and few orders of magnitude more luminous than any maser source observed in the Galaxy. OH, H_2O, H_2CO and CH are among the molecules responsible for the emissions in known megamasers. In this method Keplerian rotation curves of circumnuclear molecular discs are used to determine the SMBH mass, while typical errors are smaller than for previous methods (Greene et al., 2010; Kuo et al., 2011). Unfortunately, the sample of known megamasers is still small.

The technique known as reverberation mapping (Bahcall et al., 1972; Lyutyi & Cherepashchuk, 1972; Blandford & McKee, 1982) is a particularly useful to study masses of SMBH in galaxies in which the influence radius of the black hole is unresolved. UV and optical observations of the broad emission lines observed originate from the region dominated by SMBH. The size of these regions are not resolvable, but temporal changes in their spectra convey information of the size of the source. This, in conjunction with the velocity width of the gas, provides a mass of BH. As other presented approaches this one is not free of caveats either: there is no consensus as for what constitutes the right velocity width estimator or exact geometry and kinematics of the gas. Impact of these should diminish, as observations and models are becoming better.

2.4. M_{SMBH} versus σ scaling relation

The exact way in which supermassive black holes and galaxies coevolve is still an active field of research. Thanks to measurements of the mass of SMBH it became possible to examine if the evolution of SMBHs in any way correlates with properties of its host. The scaling relation between black hole mass M_{SMBH} and stellar velocity dispersion σ of the host spheroid (either a bulge in spiral galaxies or entire elliptical galaxy, see e.g. Ferrarese & Merritt (2000); Tremaine et al. (2002); Gültekin et al. (2009); McConnell &

[2]The (collisionless) Boltzmann equation provides a statistical description of a thermodynamical system and relates the flow of particles through a 6D phase space element (3D position and 3D velocity).

Ma (2013)) or, earlier, with the spheroid mass (Magorrian et al., 1998; Marconi & Hunt, 2003; McConnell & Ma, 2013).

There is much of a debate whether this scaling relation holds for all black hole masses and for all galaxies displaying spheroid-like features in their morphologies. In the most in-depth recent study, Kormendy & Ho (2013) discuss that this almost linear relation does not hold for what they call *pseudobulges*. The observed relation appears to be flatter than for typical bulges. This is motivated by two different formation scenarios: 1) pseudobulges form due to the secular evolution of disc galaxies, while 2) bulges are a result of galaxy mergers (Brooks & Christensen, 2016). This can be seen on Figure 2.4 reprinted from Kormendy & Ho (2013), where the black hole mass shown on y axis vs. the luminosity of spheroid (panel a), its velocity dispersion (panel b) and its mass (panel c). There is a clear discrepancy between the pseudobulges and the scaling relation. It seems as if the black hole masses in these objects are not massive enough. There is, however, a potential solution to this conundrum, but before discussing it, I must first introduce a one more class of objects.

There is an ongoing debate (e.g. Jahnke & Macciò, 2011) if the observed relation can be explained by the feedback from SMBH (see Section 2.7 below). The slope α of the observed relation seems to lie between 4 and 5. This in turn could potentially explain how feedback from SMBH couples to the environment, i.e. if the momentum ($\alpha = 4$; see e.g. King (2003)) or energy ($\alpha = 5$; see e.g. Silk & Rees (1998)) is conserved.

2.5. Nuclear star clusters

Even a basic review of the process of star formation, a very active field of research, is beyond the scope of this Thesis, but it suffices to say that most of the stars in the Universe form in associations – either as binary (or multiple) stellar systems or as a member of a star cluster. One of a very peculiar classes of star clusters is a nuclear star cluster (NSC).

In the centre of the Milky Way, the SMBH is accompanied by not only by S stars, but also by an NSC. Its mass is comparable to the mass of the SMBH itself (Böker et al., 2002, 2004). NSCs are generally more massive than any of globular clusters, but have similar radii. Their stellar population is dominated by old stars, but very often there is also an imprint of stars younger than 100 Myr (see e.g. Seth et al., 2006; Siegel et al., 2007; Georgiev et al., 2009; Montero-Castano et al., 2009). NSCs are found in majority of galaxies; the *nucleation fraction*, which is the fraction of galaxies hosting NSCs, is around 60-70% (Böker et al., 2002; Georgiev & Böker, 2014). No NSC was found in most massive lenticular and elliptical galaxies (Côté et al., 2006; den Brok et al., 2014). They are the brightest and most compact stellar systems, with typical half-mass radii of 2-5 pc (Böker et al., 2004).

In the previous section I have discussed the problem of the lack of correlation between SMBH masses and pseudobulges. A much better correlation is recovered if one considers $M_{SMBH}+M_{NSC}$ for pseudobulges and late-type galaxies; see Figure 2.5. This strongly suggest that there is not only a coevolution between SMBH and their host galaxies, but that SMBH and NSC coevolve (and form, cf. Subsection 2.6.3) with one another, even if the processes governing their growth are different.

There is no agreement as to how the nuclear star clusters formed. One group of models predicts formation of NSC outside of the core and then later migrates to the centre due to dynamical friction (Tremaine et al., 1975; Andersen et al., 2008; Capuzzo-

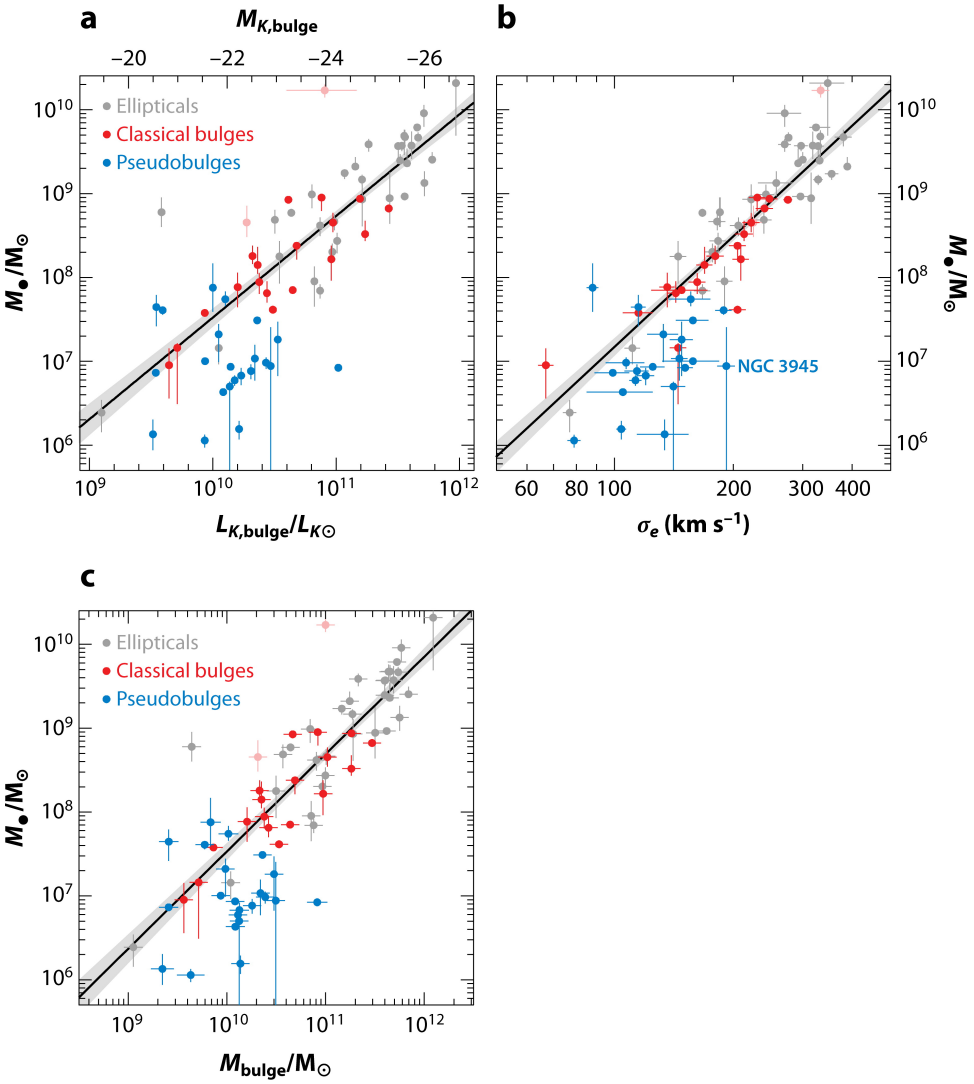

Kormendy J, Ho LC. 2013.
Annu. Rev. Astron. Astrophys. 51:511–653

Figure 2.4: SMBH mass vs. the luminosity of spheroid (panel a), its velocity dispersion (panel b) and its mass (panel c). The scaling relation does not seem to work very well for the pseudobulges. Reprinted with permission from Kormendy & Ho (2013).

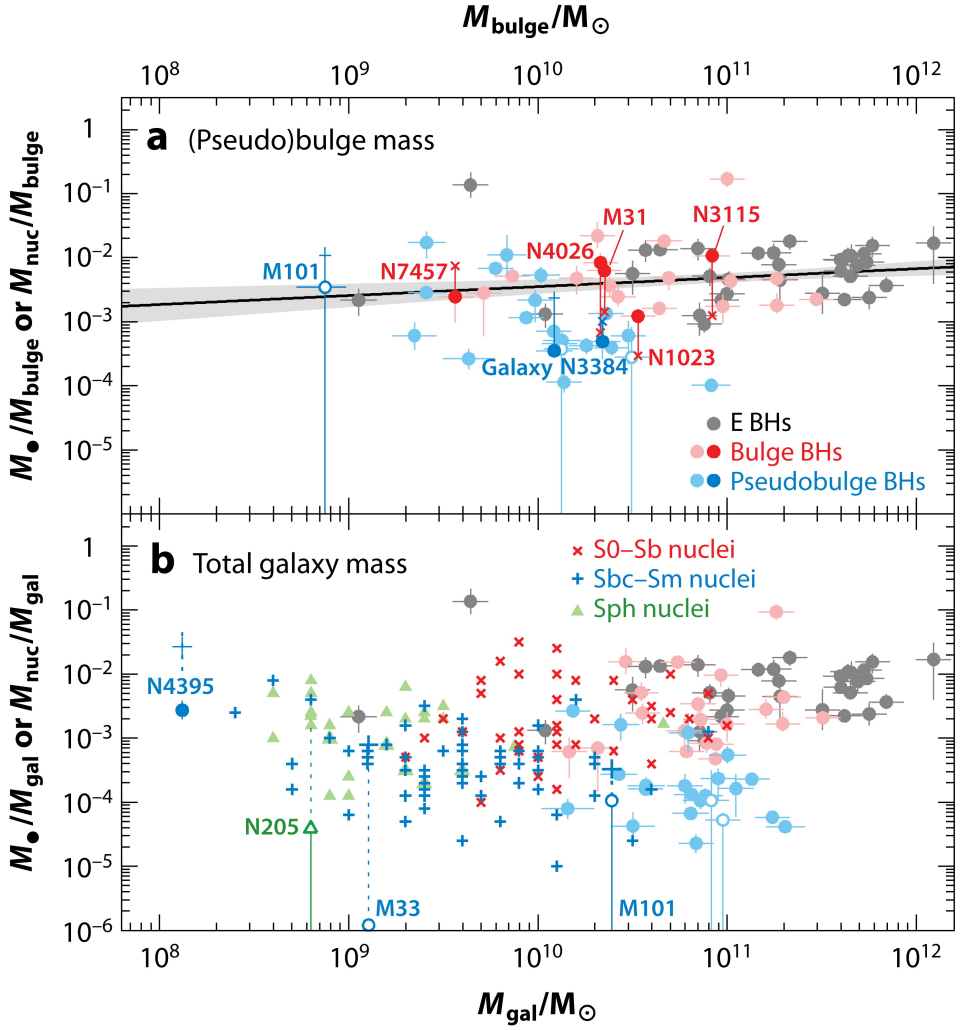

Kormendy J, Ho LC. 2013.
Annu. Rev. Astron. Astrophys. 51:511–653

Figure 2.5: Ratio of central massive object (CMO; the system of SMBH and NSC) to the mass of spheroid component (top panel) or to the total mass of the galaxy (bottom panel) as a function of mass of spheroid (top panel) or total mass of the galaxy (bottom panel). This relations show less scatter than the NSC or SMBH on their own. Reprinted with permission from Kormendy & Ho (2013).

Dolcetta & Miocchi, 2008). In the second scenario a small seed cluster is formed in the centre (in situ formation, Milosavljević (2004)) and is subsequently fed by episodic gas accretion from infalling clouds. Each of this scenarios has its own weaknesses. The latter fails to reproduce the observed scaling relations very well, which is well accounted for in the migratory model (Antonini, 2013; Hartmann et al., 2011), however this was later shown to not be the case (Antonini et al., 2015). In the in situ model it is not clear what process leads to the accumulation of gas in the centre, but magneto-rotational instability or compressive tidal fields have been invoked (Milosavljević, 2004; Emsellem & van de Ven, 2008). It has been recently suggested that NSCs may form via an alternative scenario dubbed 'wet migration' (Guillard et al., 2016). In this model the formation proceeds ex situ, but the resulting proto-NSC is dense enough such that a gas reservoir is not disrupted during the migration to the centre. This can explain both multiple or prolonged star formation episodes and the right scaling relation with the host. Further gas-rich mergers lead to build up to the final mass.

Further theoretical and observational work is required to understand the formation and evolution of NSC. It has to be remembered, that any conclusions drawn are based on a small sample of objects and that the observations of NSCs are difficult and likely biased. However, they might be cradles in which SMBHs form, thus now we shall turn our attention to the formation mechanisms of massive black holes.

2.6. Massive black hole formation scenarios

The formation mechanism behind massive black holes is not yet fully understood. It is not only the question of how, but also when and at what frequency. Here I describe in more detail three possible pathways. Each of the scenarios has some caveats and thus each might be responsible to formation of massive black holes at various redshifts or environments.

2.6.1. Direct collapse

Much attention and effort is given to the seed formation scenario in which a massive black hole ($10^4 - 10^5\,M_\odot$) forms through collapse of dense gas (Haehnelt & Rees, 1993; Umemura et al., 1993; Loeb & Rasio, 1994; Eisenstein & Loeb, 1995; Bromm & Loeb, 2003; Koushiappas et al., 2004). This process has to proceed in massive ($10^6 - 10^7\,M_\odot$), pristine gas clouds, as presence of metals would lead to fragmentation due to enhanced cooling. Another efficient coolant, H_2, needs to be dissociated in such clouds. This can be achieved with the UV radiation coming from nearby star-forming galaxies. These Lyman-Werner photons have typical energies between 11.2 and 13.6 eV (which is a range in which absorption bands of Lyman and Werner lines are found) and excite H_2 molecules, which in turn have 15% of chance of dissociating. Photo-dissociated gas carries some photon energy as kinetic energy, which leads to heating of gas. It has been shown (e.g. Dijkstra et al., 2008), that the chance that a halo has both a right mass to form a massive black hole seed and a rate of UV flux is of order of $\sim 10^{-6}$. Alternatively, fragmentation of halos could be reduced thanks to turbulence that would efficiently mix gas.

Provided that halos do not fragment, they can contract until rotational support stops further collapse. For the halos of interest ($\sim 10^8\,M_\odot$), gas would settle into a disc with radius of about 20 pc. There is thus a need for an additional process taking place, one that could lead to significant angular momentum loss. Few processes have been proposed

and studied. Begelman et al. (2006) looked at angular momentum dissipation via bar instabilities, which efficiently transport the angular momentum outwards via torques, decreasing the disc size. The process repeats at smaller spatial- and shorter timescales, leading to formation of massive object. Lodato & Natarajan (2006); Wise et al. (2008); Regan & Haehnelt (2009) have studied local instabilities in the disc. Due to a non-violent destabilisation of the system, gas collapses instead of fragmenting and establishing star-forming clumps. Supersonic turbulence can lead to removal of up to 90% of system's angular momentum, which results in the formation of a supermassive star (SMS) with mass $10^4 - 10^6$ $M_\odot$.

Once the nuclear reactions in the core of SMS are exhausted, it collapses and forms a ~ 100 $M_\odot$ black holes (Begelman, 2010; Hosokawa et al., 2013). The envelope of SMS will surround the black hole and contract. Due to the angular momentum of the envelope, the gas forms an accretion disc around black hole, linking it to the envelope; this is known as *quasi-star* (Begelman et al., 2006; Begelman et al., 2008; Dotan et al., 2011; Fiacconi & Rossi, 2016). Black hole can grow at the cost of the surrounding envelope, but this process will be regulated by the radiation due to liberation of the potential energy via accretion. The feedback does not disrupt the quasi-star system, but forces the envelope to readjust. The growth of the black hole will proceed as long as the temperature of the envelope is > 4000 K. At this critical temperature the convective envelope releases radiation at a super-Eddington rate, which leads to sudden dispersal of the envelope. As an effect, a seed black hole of $10^4 - 10^5$ $M_\odot$ forms, depending on the details of gas accretion and SMS structure.

2.6.2. Population III remnants

As I have discussed in Chapter 1, initially all gas in the Universe consists of a mixture of hydrogen and helium, without any heavier elements (which astronomers traditionally dub 'metals'). Due to the lack of metals, gas can only cool thanks to hydrogen (either molecular or atomic) (e.g. Tegmark et al., 1997), which leads to formation of minihalos ($M \approx 10^6$ $M_\odot$) at around redshift 20-50. Simulations of such metal-free, molecular clouds hint toward formation of very massive stars with $M < 100$ $M_\odot$ (Bromm et al., 1999; Abel et al., 2000; Gao et al., 2007; Greif et al., 2011; Johnson et al., 2013). This is different than for present-day star formation, in which the metal-line cooling, magnetic fields, stellar radiation from nearby stars etc. can lead to fragmentation of the initially collapsing star.

The fate of such a very massive star depends a lot on its initial mass. A stellar mass remnant is formed, if the stellar mass is between 25 and 140 $M_\odot$, with about 40% of mass forming a remnant (Zhang et al., 2008).

If in turn the star has mass between 140 and 260 $M_\odot$, the central entropy is so high that the neutral, bosonic matter is turn into electron-positron pairs. This process reduces the internal pressure in the stellar core (e.g. Bond et al., 1984), which collapses. As an effect, a runaway nuclear burning occurs, that blows the star apart without leaving a remnant (Kudritzki et al., 2000; Smith, 2014); this explosion is know as a pair-instability supernova.

The situation is once again different in even more massive stars ($M > 260$ $M_\odot$). The physical process that becomes relevant due to very high temperatures and pressures is photodisintegration. This endothermic (for nuclei lighter than iron) process leads to reduction of pressure and temperature in the core of the star (Bond et al., 1984; Woosley

& Weaver, 1986), which in turn causes the core to collapse and form a black hole Fryer et al. (2001); Heger et al. (2003).

Massive black holes formed via this process would naturally reside in the densest density peaks, thus would naturally cluster in cores of massive halos (Madau & Rees, 2001). There is, however, a large uncertainty on the mass function of Population III stars, including question if any of the stars that formed exceeded the threshold mass of $260\,M_\odot$.

2.6.3. Stellar collisions in dense star clusters

In this scenario a massive black hole forms in a dense, compact nuclear star cluster (Schneider et al., 2006; Clark et al., 2008; Devecchi & Volonteri, 2009). Massive black holes would not form primarily out of gas, but through collisions of stars. This scenario has been explored both theoretically and in simulations (Begelman & Rees, 1978; Portegies Zwart et al., 1999; Ebisuzaki et al., 2001; Portegies Zwart et al., 2004; Gürkan et al., 2006; Gaburov et al., 2010). A stellar system will evolve such that it reaches the state of the lowest potential energy. In that process the heaviest stars will sink to the centre of the cluster, while the least massive will move outside, potentially escaping from the cluster. This segregation must follow on timescales shorter than lifetime of massive stars (few Myr). Due to high density of stars and central velocity dispersions in the range of few hundred $\mathrm{km\,s^{-1}}$, stellar collisions will result in mergers, rather than in disruptions. As an outcome, stars with masses $> 100\,M_\odot$ will form, merge and collapse to form black hole seeds with $M_{\mathrm{BH}} \approx 100 - 1000\,M_\odot$.

2.7. SMBH feedback

In Section 2.1 I have briefly discussed how black holes grow due to the accretion. The energy released by infalling gas is radiated away at all wavelengths, shining more brightly than many massive galaxies. This phenomenon has been given a name of active galactic nucleus (AGN) and can be discussed from two different angles – theoretical and observational.

Before diving in the discussion on various way SMBH-related feedback can be seen, we should estimate how much energy can SMBH release during its lifetime and how does this compare to e.g. the binding energy of a galaxy. If the gravitational potential of galaxy is dominated by the bulge (with σ its velocity dispersion), then the binding energy $E_{\mathrm{bulge}} \approx M_{\mathrm{bulge}}\sigma^2$. From the observational evidence, that I reviewed in Section 2.4, we know that $M_{\mathrm{SMBH}} \approx 1.5 \times 10^{-3}\,M_{\mathrm{bulge}}$. Thus, if we use Eq. (2.2) and integrate it in time, then we find that $E_{\mathrm{SMBH}}/E_{\mathrm{bulge}} \approx 1.5 \times 10^{-4}(c/\sigma)^2$. This ratio for typical σ is 50 or larger. Therefore, if all the energy liberated by SMBH in the process of accretion was impacting the galaxy, then it would have been able to significantly shape the gas content of galaxies. It is important to emphasise that the AGN feedback has little to no influence on galactic population of stars.

How does this energy manifests and couple to the environment then? It is thought that there are two distinct modes of operation which relate to the efficiency at which SMBH accretes. The high accretion mode, close to the Eddington limit, manifests itself as a quasar and it is known as the radiative mode (see panel *a* on Figure 2.6). The low accretion mode is observed at lower Eddington rates accompanied by jets (Figure 2.6, panel *b*). While the former mostly impacts cold gas, the latter prevents the hot gas from cooling, thus it is often called maintenance mode. Furthermore, if the light from the AGN

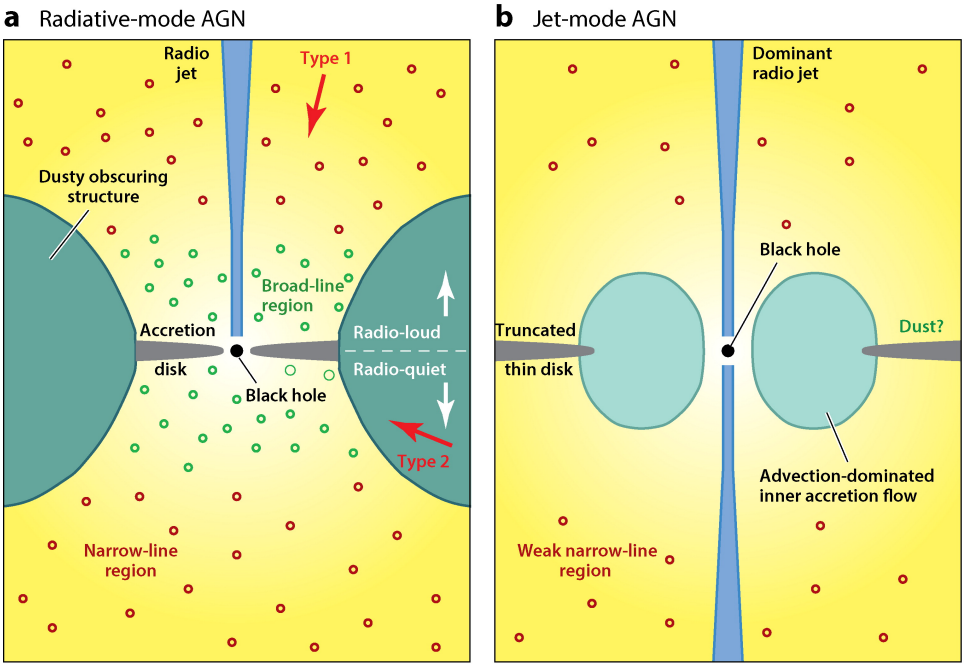

AR Heckman TM, Best PN. 2014.
Annu. Rev. Astron. Astrophys. 52:589–660

Figure 2.6: Simplified cartoon of two types of AGN modes: radiative (panel a) and jet (or maintenance, panel b). Main observational differences arise from the nature of the accretion - via thin accretion disc or advection-dominated accretion flow, respectively. Radiative-mode AGN can display a weak radio jet, which becomes dominant in the maintenance mode. Reprinted with permission from Heckman & Best (2014).

outshines the host galaxy, then it is known as quasi-stellar object (QSO or quasar), while otherwise we call it a Seyfert galaxy.

The peak of star formation in the Universe happens at about $z \sim 2$ (e.g. Madau & Dickinson, 2014). Abundance of gas in galaxies means that this epoch is also relevant for the growth of SMBH due to the availability of the accretion fuel. The same gas reservoir can be used to trigger both star formation and feed SMBH growth. This suggests that these two crucial processes can be connected, impacting one another by their respective feedbacks.

Energy radiated from the accretion disc that reaches close to the R_S (depending on SMBH spin) can couple to the surrounding gas via the radiation pressure on dust. In this scenario radiation would escape perpendicularly to the accretion disc without interrupting the feeding. The radiation gets absorbed by the dust, exchanges part of its momentum and is reemitted at shorter wavelength. The exact coupling efficiency that powers AGN winds in this process is still debated on both observational and theoretical grounds.

The effects of AGN feedback can be seen clearly at scales much larger than the accretion disc. The typical winds can propel thousands of solar masses of gas with velocities of few hundred km/s (Heckman et al., 2000; Veilleux et al., 2005; Strickland & Heckman, 2009; Weiner et al., 2009). The complication of the picture lies in the difficulty in dis-

tinguishing the driving mechanism. It is believed that supernova-driven gas velocities do not exceed 500 km/s. The observations are further complicated if one follows a line of reasoning in which large quantities of gas does not only provide fuel to the SMBH, but also obscures the galactic nucleus. This however was not enough to prevent e.g. Rupke & Veilleux (2011) from finding quasar-driven gas with a velocity of ~ 1000 km/s and an outflow rate of $\sim 420\,M_\odot$. There is no lack of further evidence of outflows in various object classes and at a span of redshifts (from local to the time of the peak of star formation, see e.g. Alexander et al. (2011); Greene et al. (2012)).

A phenomenon that closely, as it seems, connects to the SMBH feeding and feedback is the so-called *AGN downsizing*. In this picture most luminous AGN are observed at higher redshifts. This is contrary to the hierarchical galaxy formation, in which most massive (and thus most luminous) objects form last. Due to the power associated with the AGN feedback, gas can be blown away, which does not only stop the star formation, but also terminates further growth of the SMBH, quenching it.

A less violent picture arises from observations of the most massive objects in the local Universe, namely clusters. It appears that the AGN feedback in these objects is related to low levels of accretion and thus to the radio(jet)-mode. In the bright central galaxies (BCGs), SMBHs are believed to provide enough heat to prevent both the inflowing gas from cooling and subsequent star formation (e.g. Pedlar et al., 1990; Tabor & Binney, 1993; Peterson & Fabian, 2006; McNamara & Nulsen, 2007). The feedback manifests itself in the form of large-scale jets, which inflate radio bubbles. These bubbles rise due to buoyancy and heat up the cluster gas in the process (Churazov et al., 2000, 2001; McNamara et al., 2000), in Figure 2.7 one can see the Perseus cluster as observed by the Chandra X-ray Observatory where multiple bubbles can be seen. Interestingly, the bubbles do not seem to be Rayleigh-Taylor unstable and the Kelvin-Helmholtz timescale for growth of large-scale instabilities is comparable to their rising timescale. It has been suggested that viscosity (Reynolds et al., 2005) or magnetic draping (Lyutikov, 2006) can be responsible for keeping the bubbles from mixing. This is very different from what is typically seen in simulations, a question I return to in Chapter 5.

So far I have discussed signatures of feedback in massive ($M_* = 10^{10} - 10^{11}\,M_\odot$) galaxies at various redshifts and in clusters of galaxies. One could ask: what about dwarf galaxies? Do they not contain SMBHs? Recently, Reines et al. (2013) have shown that only about 0.5% of dwarf galaxies show any signatures of AGN. This means that SMBHs can be hosted by dwarf galaxies, but are not very active in them. Gas in dwarf galaxies is often heavily impacted by SN explosions and thus the SMBH accretion is limited. This lack of AGN activity, on the other hand, could mean that SMBHs are close to their initial mass, which would cast some light on the process of their formation (cf. Section 2.6). Hopefully, as the sample grows we will understand more about SMBHs in dwarf galaxies.

2.8. Numerical techniques and technical numbers

In this Section, I am going to discuss some aspects of the numerical techniques applied throughout this Thesis. I will first describe a few basic terms which are relevant for the theory of galaxy formation and evolution. Then I will briefly review how hydrodynamics can be solved on a grid with adaptive mesh refinement (AMR), and lastly I will focus on the interaction between gas and sink particles, which form a numerical core for this Thesis.

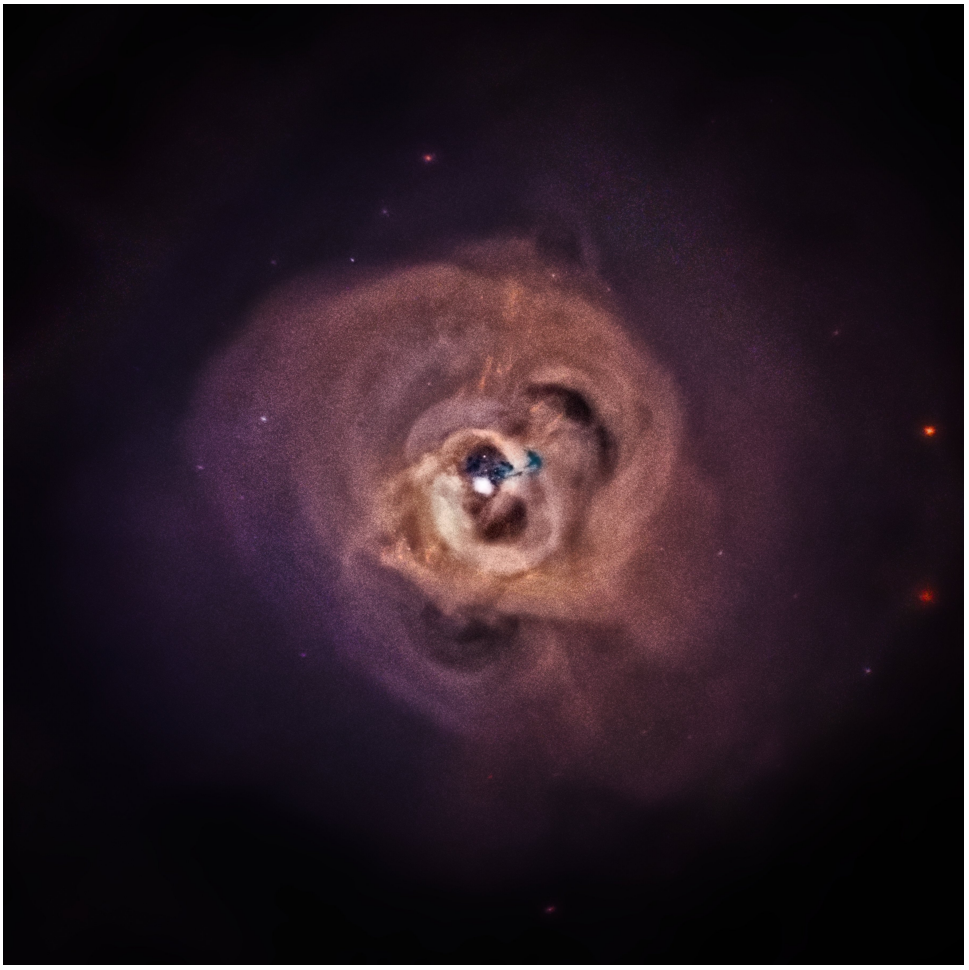

Figure 2.7: Composite image of the Perseus cluster in three different X-ray bands (red to blue is low energy to high energy) from the Chandra X-ray Observatory. Multiple bubbles can be seen as black cavities. Image credit: NASA/CXC/SAO/E.Bulbul, et al..

2.8.1. General concepts

Most variants of the theory of galaxy formation are based on the ΛCDM cosmology, where Λ is a cosmological constant that was first proposed by Einstein and CDM stand for Cold Dark Matter[3]. In order to understand what that means, a few basic theoretical concepts need to be reviewed (this is going to be a very brief introduction, while more in-depth explanation can be found in e.g. Mo et al. (2010); Ryden (2016)).

The Friedmann equations

$$\left(\frac{\dot{a}}{a}\right)^2 = \frac{8\pi G}{3}\left(\rho + \frac{p}{c^2}\right) + \frac{\Lambda c^2}{3} - \frac{Kc^2}{a^2} \tag{2.9}$$

$$\frac{\ddot{a}}{a} = -\frac{4\pi G}{3}\left(\rho + \frac{3p}{c^2}\right) + \frac{\Lambda c^2}{3} \tag{2.10}$$

are a solution to Einstein's field equations, which capture time evolution of a spatially homogeneous and isotropic universe. Here $a(t)$ is the expansion factor of the Universe (assumed to be 0 at the beginning of the Universe and 1 in the present day), G - the gravitational constant, c - the speed of light, ρ and p - the rest-mass density and pressure of the matter fluid, respectively, while K describes the curvature of the universe and Λ is the cosmological constant. Positive $\dot{a}$ would mean that a universe is expanding, while $\ddot{a}$ represents acceleration (if positive) or deceleration (if negative) of the rate of expansion/contraction. All of this tells us that the fate of the Universe depends on its content (ρ and p; representing both matter and radiation), its curvature K, and Λ, associated with dark energy.

Before focusing on the remaining unknowns of ΛCDM, it is handy to define one more quantity, i.e. the critical density $\rho_{\mathrm{crit},0}$. If we assume for the moment that at the present epoch $K = 0$ (the Universe is flat), we can write

$$\rho_{\mathrm{crit},0} = \frac{3H_0^2}{8\pi G}, \tag{2.11}$$

where $H_0 = \dot{a}/a|_{a=1}$ is the present-day expansion rate of the Universe, known as the Hubble constant.

What is cold dark matter (CDM in the acronym above)? The term 'cold' describes the speed with which the hypothetical dark matter particles are moving (just like in thermodynamics - if something is moving fast, then it is hot). 'Dark' refers to the lack of interaction with ordinary, baryonic matter and radiation - the only interaction is via the gravitational force, which is the weakest of the four known elemental forces. There are many candidates for what DM can be, including neutrinos, axions, MACHOs (MAssive Compact Halo Objects) or WIMPs (Weakly Interacting Massive Particles). We are far from a full understanding of the nature of DM, yet it should be noted that the ΛCDM model successfully (but not without caveats) describes how the Universe evolved from the initial, almost homogenous state to the very non-homogenous one observed today, full of galaxies.

According to the theory of structure formation within the ΛCDM model, small objects collapsed first under the force of their own gravity and were merging continuously to form larger and larger structures. If we start with small inhomogeneities (which can arise due

[3]At some point of his career Einstein called it 'the biggest blunder'; it came back around, however, and somewhat modernised, is an important part of the current vanilla cosmology.

to quantum fluctuations), then regions which have a slightly higher density than average will become denser as their gravitational pull will be higher than average. This will lead to an exponential growth in which the density contrast, $\partial\rho/\rho$, increases exponentially. The opposite is true for the regions with density lower than average. The linear approximation of the evolution breaks when $\partial\rho/\rho \sim 1$. This marks a moment when the evolution of the overdensity becomes independent of the cosmic expansion; the overdensity starts to collapse. The fate of the matter in the overdensity depends somewhat on its nature – baryonic matter, while collapsing, will increase its entropy due to shocks and reach the so-called virial temperature $T_{\rm vir}$. Then, if cooling is inefficient, it will relax until it reaches hydrostatic equilibrium. No shocks develop if the matter is collisionless – the dark matter halo will also relax and reach a quasi-equilibrium state; a dark matter halo is born.

As mentioned, a halo can be characterised by its virial temperature. A self-gravitating system, like a dark matter halo, reaches its virial equilibrium if

$$2K + W = 0, \tag{2.12}$$

where K and W are the kinetic and potential energy, respectively. Thus for a uniform cloud of monatomic gas we can write

$$2 \times \frac{3M_{\rm gas}k_{\rm B}T}{2\mu m_{\rm p}} - \frac{3GM_{\rm gas}M_{\rm halo}}{5r_{\rm halo}} = 0, \tag{2.13}$$

where $r_{\rm halo}$ is the halo's radius, $M_{\rm gas}$ and $M_{\rm halo}$ are the masses of gas and halo, respectively; μ is the mean atomic weight, $m_{\rm p}$ is the proton mass, $k_{\rm B}$ and G are Boltzmann and gravitational constants, respectively. Therefore the virial temperature is

$$T_{\rm vir} = \frac{\mu m_{\rm p} GM}{5k_{\rm B}r_{\rm halo}}. \tag{2.14}$$

Another important quantity that describes halos is the virial radius. Here I am going to sketch out only the most important concepts, while the full derivation can be found in e.g. Mo et al. (2010), which this description will loosely follow. The maximum expansion implies total energy $E = -3GM^2/5r_{\rm max}$, since the kinetic energy term vanishes. Then from the virial theorem we know that $W = 2E$, which then means $r_{\rm vir} = r_{\rm max}/2$. The mean overdensity $\Delta_{\rm vir}$ can be estimated from the spherical collapse model to be

$$\Delta_{\rm vir} = 18\pi^2 \approx 178, \tag{2.15}$$

which is true for a universe consisting fully of matter. In spite of that, it became a standard way to describe dark matter halos. A region forms a collapsed and virialized halo if its mean overdensity is 178 (or most commonly 200). Linking this quantity with the critical density allows us to define halo's radius and mass ($M_{\rm vir} = (4/3)\pi\Delta\rho_{\rm c}R_{\rm vir}^3$).

The one remaining piece of the story of DM halos is their density profile (which holds under the assumption of sphericity). A few approximations can be made leading to the singular isothermal sphere (SIS) model where $\rho(r) \propto r^{-2}$. Navarro et al. (1996) have shown by means of high-resolution N-body simulations that the halo profiles differ from those given by approximate solutions. They find that the following formulation describes halos well:

$$\rho(r) = \rho_{\rm crit}\frac{\delta_{\rm char}}{(r/r_{\rm s})(1 + r/r_{\rm s})^2}, \tag{2.16}$$

where r_s is a scale radius and δ_{char} is a characteristic overdensity; this came to be known as the Navarro, Frenk & White (NFW) profile. It can be seen that inside r_s the profile is more shallow than that of SIS, but steeper in the outskirts. It has also been shown that the NFW profile describes well halos of all masses regardless of the exact parameters of ΛCGM cosmology.

δ_{char} can be rewritten

$$\delta_{char} = \frac{\Delta_h}{3} \frac{c^3}{\ln(1+c) - c/(1+c)} \tag{2.17}$$

where $c \equiv r_h/r_s$ is the *concentration parameter* (r_h is the halo radius dependent on a definition of Δ_h).

2.8.2. Hydrodynamics with a mesh

Hydrodynamical evolution of a fluid is a problem that has many commercial applications – from aerodynamics of jet planes to engines of race cars. It can also be used to study plasma in tokamaks, the hydrology of rivers and various astrophysical objects (which is the most relevant for this Thesis). Astrophysical fluids can be roughly split into three categories: *i)* collisionless (e.g. dark matter), *ii)* incompressible (e.g. stellar interiors) and *iii)* compressible (e.g. gas in galaxies). Narrowing the scope again, I will focus on the last one. There are two ways to discretise the gas in order to study its flow, where each has its own pros and cons (where hybrid solutions exist too). In the method known as Smoothed Particle Hydrodynamics (SPH), gas fluid is subdivided into discreet particles, which are followed according to the Lagrangian formulation of hydrodynamics. In grid-based methods it is the domain that is subdivided - discreet cells span the whole computational domain and the fluid flow is regulated according to the Eulerian formulation. It is worth mentioning that a hybrid model has been recently applied to galaxy formation problems. This formulation uses the Eulerian approach to evolve the fluid, but is fully Galilean invariant as SPH implementation; the domain is based on a moving mesh implementation, where the domain is defined by the Voronoi tessellation. Excellent and detailed reviews of the methods can be found in Springel (2010a) and Teyssier (2015), respectively.

The AMR code Ramses (Teyssier, 2002), used throughout this work, belongs to the Eulerian family and in recent years has become a versatile and powerful tool to study a large span of astrophysical problems, from star formation, via galaxy formation and feedback, to cosmology. What distinguishes Ramses from other AMR codes is its grid structure - a 'fully threaded tree' (Khokhlov, 1998) - in which each data element is called an *oct* consisting of $2^{n_{dim}}$ cells (n_{dim} is a number of dimensions considered); other AMR codes rely on patches or blocks (Fryxell et al., 2000; Bryan et al., 2014). All octs are linked forming a tree. Each cell at refinement level l (see Figure 2.8) is linked to its father cell at level $l-1$ and all the neighbours of the father cell. It also has information about its own son cells at level $l+1$. A cell that has no sons is called a *leaf*. Thanks to this approach spatial resolution can follow regions of interests, which can be defined based on properties of gas (density, temperature/pressure, velocity) or physical criteria (like the Jeans mass, which characterises the mass of the gas cloud collapsing under its own gravity).

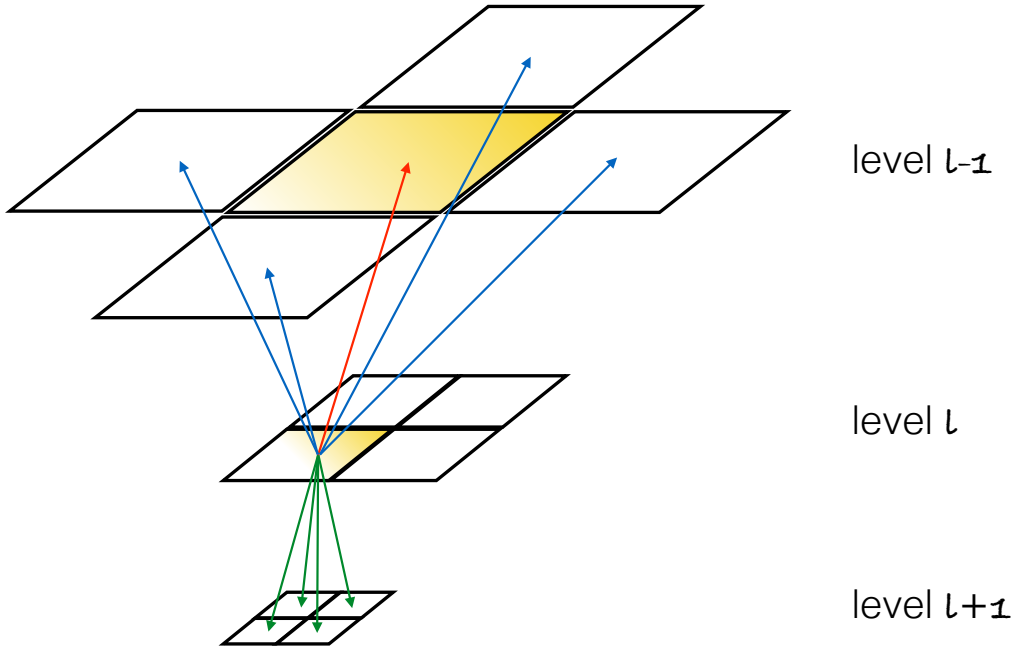

Figure 2.8: Simplified oct tree in Ramses for $n_{\mathrm{dim}} = 2$.

The equations governing hydrodynamics can be written according to the Lagrangian formulation (where problems arise in the treatment of discontinuities) or Eulerian form

$$\begin{aligned} \frac{\partial \rho}{\partial t} + \nabla \cdot (\rho \mathbf{u}) &= 0 \\ \frac{\partial \rho \mathbf{u}}{\partial t} + \nabla \cdot (\rho \mathbf{u} \otimes \mathbf{u} + P \mathbb{1}) &= 0 \\ \frac{\partial E}{\partial t} + \nabla \cdot (E\mathbf{u} + P\mathbf{u}) &= 0, \end{aligned} \tag{2.18}$$

where E is the total energy per unit volume of the fluid

$$E = \rho \left(\frac{\mathbf{u} \cdot \mathbf{u}}{2} + \epsilon \right). \tag{2.19}$$

Here, ϵ is the specific internal energy of the gas, which relates to the pressure by an equation of state of an ideal gas $P = \rho\epsilon(\gamma - 1)$ and γ is the adiabatic index of the gas.

If we define the state vector $\mathbf{U} = (\rho,\ \rho\mathbf{u},\ E)^T$ and corresponding fluxes $\mathbf{F} = (\rho\mathbf{u},\ \rho\mathbf{u} \otimes +P, (E + P)\mathbf{u})^T$, then the Euler equations can be written

$$\frac{\partial \mathbf{U}}{\partial t} + \nabla \cdot \mathbf{F} = 0. \tag{2.20}$$

The Euler equation in this form becomes a conservation law. We are going to apply two modifications to the above. First, we are going to assume that our system is one-dimensional and then we are going to discretise it over cells of length Δx:

$$\frac{\partial \mathbf{U}_i}{\partial t} + \frac{\mathbf{F}_{i+1/2} - \mathbf{F}_{i-1/2}}{\Delta x} = 0, \tag{2.21}$$

where $\mathbf{U}_i$, a cell-centre average quantity, and $\mathbf{F}_{i\pm1/2}$ are the fluxes (in positive x-direction) through the i cell interface (interface values are shifted by 1/2 w.r.t. the cell centre). This formulation naturally leads to conservation of mass, energy and momentum. The temporal evolution of the cell averages can then be formulated as follows

$$\mathbf{U}_i^{n-1} - \mathbf{U}_i^n + \int_{t_n}^{t_n + \Delta t} \frac{\mathbf{F}_{i+1/2} - \mathbf{F}_{i-1/2}}{\Delta x} \mathrm{d}t = 0. \tag{2.22}$$

Ramses uses the Godunov (1959) scheme, in which it is assumed that $\mathbf{U} \equiv \mathbf{U}_i$ is constant throughout the cells. Therefore in order to calculate the fluxes at cell interfaces, the classical Riemann problem has to be solved. The solution can be found if it is assumed that the flux through the interface is constant for a chosen timestep Δt. An excellent review of numerical methods to solve the Riemann problem can be found in Toro (2009), where the description of the HLLC solver used in this Thesis is also given.

The scheme introduced by Godunov can be improved, if the values of states at cell interfaces are not assumed constant, but are instead reconstructed from neighbouring cells. Ramses is using the MUSCL (Monotonic Upstream-centered Scheme for Conservation Laws) method proposed first by van Leer (1979). Such modified states are then used as input for the Riemann solver. There is a caveat to this solution - the self-similarity of the Riemann problem is violated and thus fluxes are no longer constant through the faces. The two most commonly used slope limiters in Ramses are MinMod and MonCen; the choice of the slope limiter is problem-dependent. Full description of this aspect of the Riemann solver can be found in Toro (2009).

The Poisson solver that utilises an iterative Gauss-Seidel relaxation method and the multigrid technique (Guillet & Teyssier, 2011) is used in Ramses to solve for its contribution to hydrodynamics. The contribution from particles is included with the cloud-in-cell (CIC) algorithm, which turns the discreet distribution by projecting it on the grid. Gravity is treated as a source term in the Euler equations

$$\mathbf{F}_{\text{grav}} = -\rho\nabla\phi \tag{2.23}$$

with $\Delta\phi = 4\pi G\rho$. Thus Eqs. 2.18 become

$$\begin{aligned} \frac{\partial\rho}{\partial t} + \nabla\cdot(\rho\mathbf{u}) &= 0 \\ \frac{\partial\rho\mathbf{u}}{\partial t} + \nabla\cdot(\rho\mathbf{u}\otimes\mathbf{u} + P\mathbb{1}) &= \mathbf{F}_{\text{grav}} \\ \frac{\partial E}{\partial t} + \nabla\cdot(E\mathbf{u} + P\mathbf{u}) &= \mathbf{F}_{\text{grav}}\cdot\mathbf{u}. \end{aligned} \tag{2.24}$$

Numerically, the solution can be found with the operator split approach. The five point finite-difference approximation of the gradient is used to calculate final gravitational accelerations.

2.8.3. Sink particle algorithm

Sink particles have been introduced to cope with situations in which the objects of study are collapsed and whose physical size is orders of magnitude smaller than that of the smallest resolution element. Naturally, they were first implemented in SPH codes (Gingold & Monaghan, 1977; Lucy, 1977) with a modern take by Bate et al. (1995) from which most contemporary SPH codes borrow. A more complicated interaction is required between a sink particle and the gas grid, so it was much later that sinks were introduced in grid codes (Krumholz et al., 2004). Ramses was enriched by its own implementation by Dubois et al. (2010) with later improvements by Bleuler & Teyssier (2014), and it has been since used in problems related to star formation and supermassive black holes. Here, I will focus on the most recent enhancements to the sink particle implementation from the point of view of SMBHs.

Currently, SMBHs can be formed with an on-the-fly watershed clump finder Phew (Bleuler et al., 2015). The clump finder can be called with either gas density or particle (dark matter and stars) density fields (the latter is calculated with the CIC technique). The clump finder is going to find peaks, which are later merged into halos based on their relevance. SMBH sink particles will be formed only if the halo does not host another SMBH, if a halo and the central clump have a minimum mass selected by the user and if the average density around the clump centre is larger than the threshold for star formation. These are some basic requirements, which can be easily extended (see e.g. Habouzit et al., 2017, for a model of SMBH seed formation in a high-z Universe).

What practically happens is that the new sink particle is born, receives a minimal mass and its cloud particles are created. The latter can be seen as a lattice of particles filling a sphere with $r_{\text{sink}} = 4\Delta x_{\text{min}}$ (where Δx_{min} is the smallest resolution element) and placed every $0.5\Delta x_{\text{min}}$. The cloud particles allow for easy access to the computational grid at the location of a sink, reducing computational cost and increasing stability of the sink algorithm. They are massless (but see below), and are being destroyed and recreated

every timestep. Subsequently, the target seed mass is 'accreted' from the underlying grid and the desired mass of the sink particle is set.

Before I discuss in more detail how sink particles interact with the grid, it is important to discuss their dynamical evolution first. There are two possibilities for calculating trajectories of sinks in Ramses. A particle-mesh (PM) method (Hockney & Eastwood, 1981) used for dark matter and star particles can be extended to treat sink too. Alternatively, a direct summation of pairwise forces can be executed with the number of operations $n_{\rm sink} \times (n_{\rm sink} + n_{\rm cells})$. While the latter is more precise and deals correctly with collisional dynamics, its computational cost can be excessive. As the PM method can be inaccurate if the local gravitational field is dominated by the sink (Bleuler & Teyssier, 2014), I have opted for a switch between the two methods. Namely, if the mass of a sink particle is larger than a chosen mass, then direct summation is chosen, while otherwise the PM solver is applied. In the former case the sink-sink and sink-gas interactions are calculated with a Plummer softening (Aarseth, 1963)

$$\mathbf{F}(\mathbf{r}) = -\mathbf{r}\frac{GM}{(|\mathbf{r}|^2 + R_{\rm soft}^2)^{3/2}}, \tag{2.25}$$

where $R_{\rm soft}$ is a free parameter, usually set to $2\Delta x_{\rm min}$. If the PM solver is used, then each of the cloud particles receives a partial sink mass and only then the sink mass is deposited on the grid.

The strategy applied to merging sinks will be crucial for the overall SMBH population. If the dynamics of SMBHs are assumed to be captured correctly, then we merge sinks if they are closer than $2\Delta x_{\rm min}$ from each other *and* their relative velocity is low enough, such that they form a bound system

$$\frac{2G(M_{\rm SMBH,1} + M_{\rm SMBH,2})}{|\mathbf{x}_1 - \mathbf{x}_2|} > (\mathbf{v}_1 - \mathbf{v}_2)^2. \tag{2.26}$$

In the equation above $\mathbf{x}_i$ and $\mathbf{v}_i$ are the position and velocity of a sink particle, respectively ($i = \{1, 2\}$). The position and velocity of a resulting sink is shifted according to the centre of mass of the system of two sinks, and masses are summed up. Properties of the merged-in sink particle are zeroed and it is cleaned up from the register at the coarse timestep, while the merging process is executed at every fine step. This major improvement, when compared to older versions of Ramses, was part of my effort as a co-developer of Ramses.

Probably the most important property related to SMBHs in galaxy formation and evolution simulations is their ability to accrete mass and produce feedback. Accretion rate is computed based on the Bondi-Hoyle-Lyttleton prescription (Hoyle & Lyttleton, 1939; Bondi & Hoyle, 1944; Bondi, 1952, see Subsection 3.2.2 for details on the formulation) and limited to the Eddington rate. Gas is subtracted from the grid within $r_{\rm sink}$ in a mass-weighted fashion (which replaced the older, kernel-weighted implementation) and added to the sink. We make sure that the momentum, angular momentum and energy are conserved in this process.

The most important improvement of the code that I have worked on was the introduction of AGN feedback on every fine timestep, instead of every coarse step, as in previous versions. Thanks to that change the AGN feedback became less bursty and was made consistent with other feedback routines (e.g. supernovae) in Ramses. Preloading of the blast has been retained, but is effectively disabled. The accretion energy is directly coupled to the rate measured and deposited in the same $r_{\rm sink}$ sphere in a mass-weighted

fashion. The most recent addition consists of a momentum mode, which provides a kick to the gas in cones that are aligned and counter-aligned with the vector of angular momentum of accreted gas. The feedback mode can be chosen to be constant for the duration of the simulation or modulated by a switch related to the accretion rate. Furthermore, thanks to the radiative transfer extension to Ramses (Rosdahl et al., 2013; Rosdahl & Teyssier, 2015a), I have added a possibility to simulate the AGN feedback with radiation. Photons that are expected to be radiated by an SMBH accretion disc are injected at every fine step according to a prescribed spectrum that can be modified by the user. I discuss the ongoing efforts that explore these most recent improvements in Chapter 6.

2.9. This Thesis

The main purpose of this Thesis is to improve our knowledge on different topics related to the dynamics of supermassive black holes in evolution of high-redshift galaxies and coevolution with nuclear star clusters, as well as the cooperation between AGN feedback and supernova explosions on the outflows. Specifically, I will address the following topics:

- Chapter 3: Dynamical problem

  In order to properly characterise the population of SMBHs, a proper treatment of their growth and mergers is necessary. This, in turn, requires careful consideration of the dynamics. Typically, in cosmological simulations proper treatment of the dynamics of the SMBH is impossible and various tricks are applied in order to keep an SMBH in the centre of a galaxy.

  In this chapter I have shown that in the simulation of a high-redshift, clumpy galaxy the SMBH wanders around the galaxy, unless the SMBH is massive enough to resist perturbations. Therefore, I have proposed a new NSC+SMBH paradigm in which these two massive components co-evolve. This solves the dynamical problem and locks the SMBH in the centre of a galaxy. As a result, an intermediate-mass black hole is hosted by a massive NSC or the SMBH is large enough to survive perturbations; this agrees with observations of nearby galaxies.

- Chapter 4: Stellar feedback regulating growth of SMBH and vice versa

  AGN feedback is often invoked as a mechanism which can quench star formation in galaxies and render them 'red and dead'. Furthermore, it has been recently argued that the early growth of an SMBH is going to be hampered by the stellar feedback blowing the gas away (Dubois et al., 2015; Bower et al., 2017). It has been shown that only when a large enough stellar component (cluster or bulge) is present, the SMBH grows fast enough.

  The model I have presented in the previous chapter naturally produces a large stellar component in the SMBH vicinity. In this chapter I show how this leads to a fast growth of the SMBH, and a subsequent synergy between stellar and AGN feedbacks emerges. The two feedback mechanisms acting in concert lead to the production of dense, molecular outflows that are frequently seen in observations. It seems, however, that this short-lived AGN feedback is unable to fully quench star formation.

- Chapter 5: Blowing AGN bubbles - a numerical comparison

  Clusters of galaxies are often seen as great astrophysical laboratories. These are among the most extreme objects in the Universe - massive bound structures full of X-ray-emitting plasma. AGN feedback in the maintenance mode is invoked in order to reproduce various observational results, but some discrepancies remain. Furthermore, there appear to be some discrepancies where different numerical tools are used.

  In this chapter we explore the differences between hydrodynamical schemes in the study of an idealised galaxy cluster. We compare the impact of injected hot AGN bubbles on gas distribution focusing on differences between numerical implementations. This is an ongoing study in collaboration with Go Ogiya and Oliver Hahn at the Observatory of Côte d'Azur.

- Chapter 6: Outlook: The NSC model and its application to small and large scales

  In this chapter I present future perspectives. First, I introduce preliminary results on SMBH feeding by stellar winds originating from NSC. This study requires a dedicated set of very high-resolution idealised simulations of a galactic nucleus. I also discuss the impact of various numerical models of AGN feedback on SMBH gas accretion.

  This is followed by the discussion of preliminary results of the NSC modelling in large-scale cosmological simulations of galaxy cluster progenitors at $z = 2$ (which is the epoch at which the AGN activity peaks). These objects are of great importance for the formation of present-day galaxy clusters. I will examine what effects AGN have on both the stellar component and the circumgalactic medium.

  Following that, I report on the attempt to try to link recent observations of a $z \approx 3$, starburst galaxy hosting an AGN, which displays massive outflows, with simulations discussed in Chapter 4.

  I end the outlook with the discussion of possible avenues for future research.

3

The dynamics of supermassive black holes in star-forming galaxies

The most exciting phrase to hear in science, the one that heralds new discoveries, is not 'Eureka!' but 'That's funny...'

– Isaac Asimov

In this chapter[1], we introduce a new model for the formation and evolution of supermassive black holes (SMBHs) in the Ramses code using sink particles, improving over previous work the treatment of gas accretion and dynamical evolution. This new model is tested against a suite of high-resolution simulations of an isolated, gas-rich, cooling halo. We study the effect of various feedback models on the SMBH growth and its dynamics within the galaxy. In runs without any feedback, the SMBH is trapped within a massive bulge and is therefore able to grow quickly, but only if the seed mass is chosen larger than the minimum Jeans mass resolved by the simulation. We demonstrate that, in the absence of supernovae (SN) feedback, the maximum SMBH mass is reached when Active Galactic Nucleus (AGN) heating balances gas cooling in the nuclear region. When our efficient SN feedback is included, it completely prevents bulge formation, so that massive gas clumps can perturb the SMBH orbit, and reduce the accretion rate significantly. To overcome this issue, we propose an observationally motivated model for the joint evolution of the SMBH and a parent nuclear star cluster (NSC), which allows the SMBH to remain in the nuclear region, grow fast and resist external perturbations. In this scenario,

[1]The work presented in this chapter has been published in the Monthly Notices of the Royal Astronomical Society, Volume 469, Issue 1 under the title 'On the Dynamics of Supermassive Black Holes in Gas-Rich, Star-Forming Galaxies: the Case for Nuclear Star Cluster Coevolution', following peer-review (**Biernacki**, Teyssier and Bleuler, 2017).

however, SN feedback controls the gas supply and the maximum SMBH mass now depends on the balance between AGN heating and gravity. We conclude that SMBH/NSC co-evolution is crucial for the growth of SMBH in high-z galaxies, the progenitors of massive ellipticals today.

3.1. Introduction

Supermassive Black Holes (SMBH) are found in the central region of massive galaxies at all redshifts, mostly in the form of Active Galactic Nuclei (AGN). There is accumulating evidence that SMBH are tightly linked to the evolution of their host galaxy (Richstone et al., 1998; Ferrarese & Merritt, 2000; Gebhardt et al., 2000; Marconi & Hunt, 2003; Häring & Rix, 2004; Kormendy & Ho, 2013), putting AGN physics at the centre of our understanding of galaxy evolution. The strong correlation of SMBH masses and stellar velocity dispersion, for example, suggests a possible co-evolution of the central SMBH and its host galaxy (Magorrian et al., 1998; Laor, 2001; McLure & Dunlop, 2002; Häring & Rix, 2004). AGN feedback is also often invoked as one of the possible origins of the quenching of star formation in elliptical galaxies (Schawinski et al., 2007; Nandra et al., 2007; Fabian, 2012; Yesuf et al., 2014; Cheung et al., 2016). The formation of the SMBH themselves remains a mystery. Two main scenarios are considered leading to massive enough SMBH: 1) direct collapse of massive clumps of pristine gas (Loeb & Rasio, 1994; Bromm & Loeb, 2003) or 2) mergers of stellar remnants in dense stellar clusters (Quinlan & Shapiro, 1990; Portegies Zwart et al., 1999; Devecchi & Volonteri, 2009), each scenario having clear strengths and weaknesses, as explained in the reviews of Begelman et al. (2006) and Volonteri (2010).

Motivated by these observational hints, theoretical models of SMBH growth and their associated feedback (mostly based on complex numerical simulations) became in recent years more and more sophisticated, with mixed successes when compared against observational data (Springel et al., 2005; Di Matteo et al., 2005; Bower et al., 2006; Croton et al., 2006; Hopkins & Hernquist, 2006; Ciotti et al., 2010; Teyssier et al., 2011; Dubois et al., 2011). AGN feedback in theoretical models of galaxy formation has proven very efficient at regulating the Star Formation Rate (SFR) in massive, red and dead galaxies, but the X-ray properties of the intergalactic gas are very difficult to reproduce. One natural explanation to the difficulties of these models is the formidable range of scales one has to capture, in order to resolve numerically the entire accretion flow from parsec scales towards the last stable orbit (typically 10^{-5} pc). Numerical implementation of SMBH formation, their accretion flows and associated energetic outflows, have to rely on strong approximations, usually referred to as “subgrid models". Note that the same technique is applied to star formation recipes in galaxy formation simulations, making the whole endeavour of simulating galaxies very challenging.

As the resolution of galaxy formation simulations is increasing, from thousands of pc in large-scale cosmological simulations (Dubois et al., 2014; Vogelsberger et al., 2014; Schaye et al., 2015; Dubois et al., 2016), to hundreds of pc in cosmological zoom-in simulations of galaxy formation (e.g. Kim et al., 2011; Anglés-Alcázar et al., 2014; Dubois et al., 2015), ultimately reaching a few pc in isolated discs simulations (Gabor & Bournaud, 2013; Hopkins et al., 2014), these subgrid models need to be tuned and adapted to the increasingly better resolved interstellar medium (ISM) structure, with an increasingly stronger supersonic turbulence.

The goal of this paper is precisely to study such a model of SMBH formation, growth and feedback in highly resolved, turbulent and clumpy galactic discs, typical of high redshift, gas-rich galaxies (Elmegreen et al., 2008a; Dekel et al., 2009; Bournaud et al., 2012). This environment is particularly relevant to SMBH physics, as these clumpy discs are believed to be the progenitors of the giant ellipticals hosting the most massive SMBHs in our present epoch (Kormendy & Ho, 2013; McConnell & Ma, 2013).

Numerical models of SMBH formation and evolution are all based on the so-called "sink particle" technique. The SMBH is represented by a point mass, moving through the fluid and interacting with it through accretion and ejection of mass, energy and momentum. Sink particles were first implemented in simulations of star-forming turbulent molecular clouds (Bate et al., 1995), using a Smoothed Particle Hydrodynamics (SPH) code. Krumholz et al. (2004) was the first one to propose a sink particle implementation for grid-based codes, using Adaptive Mesh Refinement (AMR). The sink particle technique was then adapted to the SMBH formation and evolution, here again first in SPH codes (Springel et al., 2005; Di Matteo et al., 2005) and then later in AMR codes (Dubois et al., 2010; Kim et al., 2011). The key ingredients in our SMBH formation and evolution models are the followings: a) the formation of the SMBH particle and in particular the choice to the initial seed mass (e.g. Begelman et al., 2006; Volonteri, 2010), b) the dynamics of the SMBH particle, with the possible inclusion of a drag force (see the recent work of Tremmel et al., 2015), c) the growth of the SMBH particle mass as a function of time, with two fundamental ingredients being the Bondi-Hoyle-Lyttleton (Hoyle & Lyttleton, 1939; Bondi & Hoyle, 1944; Bondi, 1952) accretion rate, limited to the Eddington accretion rate (for observational constrains see e.g. Kollmeier et al., 2006; Steinhardt & Elvis, 2010), and finally, d) the feedback from the SMBH particle that affects the surrounding gas (Ostriker et al., 2010; Anglés-Alcázar et al., 2013; Choi et al., 2014, 2015; Nayakshin, 2014; Costa et al., 2014), and therefore couples back to all the previous ingredients of the model.

In this work, we present a new implementation of the SMBH formation and evolution model in the Ramses AMR code (Teyssier, 2002), inherited from the earlier work of Dubois et al. (2010) and Teyssier et al. (2011), but significantly improved in many aspects (see Section 3.2). For example, our sink particle formation sites are automatically extracted from the simulation using the recently developed clump finder onboard the Ramses code (Bleuler & Teyssier, 2014). We also improved the dynamical integrator of the sink particle, allowing us to perform detailed dynamical studies. Finally, we added two new ingredients to the model, namely a fully momentum conserving drag force and a model for SMBH and Nuclear Star Cluster (NSC) co-evolution. Our goal is to apply these various ingredients to model simulations featuring a cooling, Milky Way-sized halo (See Section 3.3), leading to the formation of a gas-rich, clumpy and violently turbulent disc, reminiscent of the high-redshift galaxies population detected in deep Hubble Space Telescope images. In Section 3.4, we outline the fact that SMBH dynamics in this turbulent environment is extremely chaotic, leading to the ejection of the SMBH from the central region of the galaxy, unless one considers very specific dynamical models. Realistic stellar and AGN feedback models make the situation even more critical. In Section 3.5, we finally discuss a model where SMBHs are either hosted and protected by a parent NSC, or massive enough to sustain the violent perturbations from their host galaxy. In Section 3.6, we discuss various observational arguments in favour of this new scenario.

3.2. A new model for SMBH formation and evolution

The first generation of SMBH models was developed in the context of cosmological simulations, with resolution around 1 kpc or more (Bellovary et al., 2010; Vogelsberger et al., 2014; Schaye et al., 2015; Dubois et al., 2016) or for relatively smooth galaxy models, using either a pressurised ISM equation of state (Truelove et al., 1997; van de Voort et al., 2011) or a low gas fraction relevant for low-redshift galaxy evolution. The sink particle was not allowed to move away from the galaxy centre, by either forcing it to remain close to the gravitational potential minimum, or by using various drag forces (Springel et al., 2005; Okamoto et al., 2008b; Gabor & Bournaud, 2013). The next generation of SMBH models need to be able to resolve the SMBH dynamics within the galaxy, and more importantly, to follow its evolution within highly turbulent, gas-rich environments typical of galaxy evolution at high redshift. In this section, we present the new-generation SMBH model implemented in the Ramses code. It is heavily based on the old model presented in Dubois et al. (2010) and Teyssier et al. (2011), and capitalises over the new sink particle implementation we have developed within the context of star-forming molecular clouds (Bleuler & Teyssier, 2014).

Although we model SMBHs as collisionless particles, we do not use the Particle Mesh solver designed for the dark matter component. Instead, we place around each sink a spherical uniform distribution of test particles (we call them "cloud particles") of radius $r_{\rm sink} = 4\Delta x_{\rm min}$, where $\Delta x_{\rm min}$ is the size of a cell at the highest refinement level. These cloud particles are evenly spaced within the sphere (with roughly 8 cloud particles per grid cell) and follow the sink particle as a rigid body. These cloud particles are used to probe the gas distribution around the sink and to distribute the accretion and the ejection of mass, momentum and energy. Note that the value for the sink sphere radius can be modified by the user, with recommended values ranging from 1 to $4\Delta x_{\rm min}$.

In the following subsections we give more details on the improvements of our SMBH sink particle implementation.

3.2.1. SMBH formation

The life of the SMBH in our simulations begins with the formation of the sink particle. It is a problem which deserves its own careful consideration, but here we reduce it to the identification of a possible formation site and to the choice of the initial mass $M_{\rm seed}$. The two main scenarios for SMBH formation are 1) direct gas collapse or 2) formation through stellar remnants collisions in a dense stellar system. In both case, SMBH formation is associated to exceptionally dense regions, probably at very high redshift, with properties leading first to the formation of an intermediate mass black hole, which will accrete gas and grow even more into the SMBH regime.

Modelling these processes is clearly out of the scope of this paper, as it would require much higher resolution and the addition of physical ingredients that are absent from our simulations, or that are not even really understood today. We therefore directly create our first and only SMBH when the first dense clump of gas forms. This allows the sink particle to evolve in a dense environment, mimicking the early phase of SMBH growth. For this, we use our built-in clump finder phew (Bleuler et al., 2015) and form the sink particle in the most massive gas clump at a chosen time (see Section 3.3). It is worth emphasising that in this formation scenario seed SMBH is trapped in nuclear gas clump; if the SN feedback is included, then the initial host clump is quickly destroyed.

The value of the initial seed mass is rather arbitrary. A typical value of $M_{\rm seed} = 10^5$ $M_\odot$, is usually adopted in large-scale hydrodynamical simulations (e.g. Booth & Schaye, 2009). Direct collapse scenarios of SMBH formation do predict seed masses of this magnitude (e.g. Begelman et al., 2006). In this paper, we prefer to adopt a more pragmatic approach and consider the seed mass as a free parameter. The Bondi accretion model we describe in the next section is based on the strong assumption that the sink particle gravity field dominates over the gas self-gravity. A minimum seed mass equal to the simulation minimum Jeans mass appears to be the right choice, as our numerical experiments in Section 3.4 indicate.

3.2.2. SMBH accretion

Once the SMBH has formed, it continues to grow in mass via accretion of gas from its surroundings. Spatial and temporal scales related to accretion process are far from being resolved in all simulations focusing on galactic environments. This motivates the need for sub-grid modelling of the accretion process. The most popular approach to compute the accretion rate onto the SMBH particle is to use the Bondi-Hoyle-Lyttleton formulae (later Bondi for short; Hoyle & Lyttleton, 1939; Bondi & Hoyle, 1944; Bondi, 1952):

$$\dot{M}_{\rm Bondi} = 4\pi\rho_\infty r_{\rm Bondi}^2 v_{\rm Bondi}, \tag{3.1}$$

where

$$\rho_\infty = \frac{\bar{\rho}}{\alpha(x_{\rm sink})} \tag{3.2}$$

α is the dimensionless density profile of the Bondi self-similar solution (see e.g. Chapter 6 of Shu, 1992), $\bar{\rho}$ is the average gas density within the sink sphere, and

$$x_{\rm sink} = r_{\rm sink}/r_{\rm Bondi} \tag{3.3}$$

is the dimensionless radius evaluated at the sink sphere radius. This function α, first introduced by Krumholz et al. (2004) in tabulated form, is a crucial ingredient to describe the accretion flow, and is often missing in many sink particle algorithm implementations. The Bondi radius $r_{\rm Bondi}$ and the Bondi velocity $v_{\rm Bondi}$ are defined as follows

$$r_{\rm Bondi} = \frac{GM_{\rm sink}}{v_{\rm Bondi}^2}, \tag{3.4}$$

$$v_{\rm Bondi} = \sqrt{c_{\rm s}^2 + v_{\rm rel}^2}, \tag{3.5}$$

where $c_{\rm s}$ is the local sound speed of the gas and $v_{\rm rel}$ is the relative velocity between the sink velocity $v_{\rm sink}$ and the gas average velocity within the sink sphere $\bar{v}$

$$\mathbf{v}_{\rm rel} = \mathbf{v}_{\rm sink} - \bar{\mathbf{v}} \tag{3.6}$$

One can define the free-fall velocity onto the sink particle as

$$v_{\rm ff,sink} = \sqrt{\frac{GM_{\rm sink}}{r_{\rm sink}}} \tag{3.7}$$

The dimensionless radius can be written as

$$x_{\rm sink} = v^2_{\rm Bondi}/v^2_{\rm ff,sink} \tag{3.8}$$

and obviously indicates whether the accretion flow around the sink is supersonic for $x_{\rm sink} < 1$ or subsonic for $x_{\rm sink} > 1$.

In the strong supersonic regime where $x_{\rm sink} \ll 1$, the dimensionless density profile of the Bondi solution asymptotes to $\alpha(x) \simeq x^{-3/2}$ (without any underlying assumptions for the equation of state of gas). One can re-write the accretion rate in the strong supersonic limit as

$$\dot{M}_{\rm Bondi} \simeq 4\pi\bar{\rho}r^{3/2}_{\rm sink}\sqrt{GM_{\rm sink}} = 3\frac{M_{\rm gas}}{t_{\rm ff,sink}} \tag{3.9}$$

where the sink free-fall time is defined as

$$t_{\rm ff,sink} = \sqrt{\frac{r^3_{\rm sink}}{GM_{\rm sink}}} = \frac{r_{\rm sink}}{v_{\rm ff,sink}} \tag{3.10}$$

and the available gas mass within the sink sphere radius is

$$M_{\rm gas} = \frac{4\pi}{3}\bar{\rho}r^3_{\rm sink} \tag{3.11}$$

One concludes that in the strong supersonic limit, the accretion rate does not depends on the gas properties anymore, but only on the available gas mass and the sink free-fall time. This corresponds to a maximum physically motivated accretion rate onto the sink.

In the strong subsonic limit, where $x_{\rm sink} \gg 1$, one has $\alpha(x) \simeq 1$, and the accretion rate can be written as

$$\dot{M}_{\rm Bondi} \simeq 4\pi\bar{\rho}r^2_{\rm Bondi}v_{\rm Bondi} \tag{3.12}$$

This is this formula that is used in most sink particle implementation, and we would like to stress, as in Krumholz et al. (2004), that this last formulae is only valid in the subsonic regime, where the Bondi radius is much smaller than the sink radius. Manipulating slightly the previous equation, one can rewrite the accretion rate formulae as

$$\dot{M}_{\rm Bondi} \simeq 3\frac{M_{\rm gas}}{t_{\rm ff,sink}}\frac{1}{x^{3/2}_{\rm sink}} \tag{3.13}$$

This shows explicitly that the subsonic accretion rate is much smaller than the supersonic one. The transition between the two regimes will of course depend on $v_{\rm Bondi}$, $M_{\rm sink}$ and the adopted resolution ($R_{\rm sink}$). Assuming for example that $v_{\rm sink} = c_{\rm s} = 10\,{\rm km/s}$ and $R_{\rm sink} = 100\,{\rm pc}$, then accretion will become supersonic if $M_{\rm sink} \gtrsim 4.6 \times 10^6\ {\rm M}_\odot$ and increases to $M_{\rm sink} \gtrsim 2.3 \times 10^8\ {\rm M}_\odot$ for $c_{\rm s} = 100\,{\rm km/s}$. We would like to emphasise that in the cold accretion regime $R_{\rm Bondi}$ is always resolved provided that seed mass is chosen accordingly to the resolution (see Subsection 3.4.1).

Then it can be also seen that if the simulation time step is controlled by the sink Courant condition

$$\Delta t \leqslant \frac{t_{\rm ff,sink}}{3} \tag{3.14}$$

one cannot remove more than the available gas mass within the sink sphere in one time step.

It has been proposed by Springel et al. (2005) and Booth & Schaye (2009) to boost the previous accretion rate formula, to account for unresolved density and temperature fluctuations at scales lower than the cell size. In this paper, we follow the same idea, allowing the sound speed of the gas to be reduced, owing to smaller unresolved temperature fluctuations. This boils down to replacing in the previous formulae the sound speed by

$$c_s \rightarrow c_s/\beta_{\rm boost}(\bar{\rho}) \tag{3.15}$$

where the boost factor is defined as

$$\beta_{\rm boost}(\rho) = \max[(\rho/\rho_*)^{2/3}, 1.0], , \tag{3.16}$$

where ρ_* is the critical gas density for star formation (see Eq. (4.1) in the next section).

In case of zero relative velocity, this formula corresponds exactly to the model proposed by Booth and Schaye. We would like to stress that the only effect of this boost is to change the transition from supersonic to subsonic accretion, but the strong supersonic accretion rate will not be modified from its maximally physically allowed value derived above. We would like also to stress that one cannot modified the relative velocity $v_{\rm rel}$ from physical grounds. Sink particles with very high relative velocities are therefore likely to accrete very little mass, as they should. Reducing the relative velocity artificially has been also used in the past to boost the accretion rate, without any physical motivation.

An important ingredient specific to SMBH accretion is the maximal allowed accretion rate onto the black hole, namely the Eddington rate,

$$\dot{M}_{\rm Edd} = \frac{4\pi G M_{\rm sink} m_{\rm p}}{\epsilon_{\rm r}\sigma_{\rm T} c} = \frac{M_{\rm sink}}{t_{\rm S}} \tag{3.17}$$

where $m_{\rm p}$ is the proton mass, $\sigma_{\rm T}$ is the Thomson cross section and $\epsilon_{\rm r}$ is the Shakura & Sunyaev (1973) radiative efficiency for a SMBH accretion; $\epsilon_{\rm r} = 0.1$. These constants are combined into the Salpeter time, as $t_{\rm S} \simeq 45$ Myr. Finally, the accretion rate onto the SMBH is computed using

$$\dot{M}_{\rm acc} = \min(\dot{M}_{\rm Bondi}, \dot{M}_{\rm Edd}). \tag{3.18}$$

We would like to stress that the Eddington rate comes from the following picture: gas is accreted using the Bondi rate towards the SMBH accretion disc, and the accretion energy is converted into accretion luminosity, which in turn will remove the fully ionised gas in the vicinity of the SMBH, if it exceeds the Eddington luminosity. Since our accretion model is applied to very large scales of galactic ISM (say between 10 pc to 1000 pc), we do not resolve the region where radiation pressure will remove the gas and control the accretion onto the SMBH. Eddington limited accretion therefore means that gas is accreted at the Bondi rate, and then decreted at a slightly smaller rate, the net budget being the (small) Eddington rate. This picture is quite different from what is considered usually and will be used later in the paper to introduce an additional gas drag force on the sink particle.

We discuss finally one important technical detail: once we know the sink particle's current accretion rate, we remove gas from the sink sphere by integrating the previous accretion rate over the time step.

$$\Delta M_{\rm gas} = -\dot{M}_{\rm acc}\Delta t \tag{3.19}$$

In order to avoid emptying very low density gas cells in the sink sphere, we remove from each cell (labelled i) the following mass-weighted contribution,

$$\Delta\rho_i = -\rho_i \frac{\Delta M_{\rm acc}}{M_{\rm gas}} \tag{3.20}$$

An important consequence of this strategy is that the centre of mass of the accreted gas within the sink sphere does not coincide with the centre of the sphere $\mathbf{x}_{\rm sink}$.

The Bondi accretion model adopted here is very popular, in both cosmological simulations and star formation communities, because of its great simplicity, which is a strength and a weakness. It completely ignores the role of angular momentum, turbulence and additional physical effects such as the multiphase and magnetised nature of the ISM in the SMBH vicinity. Although one can argue that these effects reduce the actual accretion rate on the SMBH, Negri & Volonteri (2017) have shown that Bondi accretion can both lead to over- and underestimating of the SMBH growth, depending e.g. on resolution. Moreover, Rosas-Guevara et al. (2015) showed recently that modifications to the Bondi formulae implementing the effect of angular momentum have no influence in galaxies larger than $10^{11.5}$ $M_\odot$, like the one we study here (see Section 3.3). In the present work, we are aiming at growing SMBHs as rapidly as possible, in order to help the sink particle remain on stable central orbits, so that the Bondi formula would provide us with an optimistic model, especially when the sink still has a low mass and resides inside cold and dense gas clumps. When the sink mass is larger, and the gas around it becomes hot and diffuse, the role of turbulence, non-radial motion and magnetic fields becomes less important, so that the Bondi approach recovers its general validity.

3.2.3. SMBH dynamics

The next fundamental requirement of our sink particle algorithm is to model properly the dynamics of the SMBH. The sink particle trajectory follows from the dynamical evolution of a point mass particle, subject to the gravitational force of the gas, stars and dark matter particles, and also subject to a drag force due to a tight coupling between the accreted gas and the sink.

Note that the latter has been often invoked in the literature to justify why one could artificially locked the sink particle coordinates to the minimum of the potential well (e.g. Sijacki et al., 2007; Costa et al., 2014), or artificially pushed in the direction of the halo centre (Gabor & Bournaud, 2013). There is no physical motivation for these models. Lower mass SMBH can be expected to get scattered by massive gas clumps (e.g. Gabor & Bournaud, 2013). Other physically motivated models do exist in the literature, that can help preventing the sink particle from wandering around the galaxy. For example, Tremmel et al. (2015) proposed to estimate the amount of dynamical friction that is missing due to poor resolution, which consists in a sub-grid model for a drag force between the sink and the collisionless component. Similar sub-grid model can be constructed for the potentially missing drag force between the sink and the surrounding gas medium (Chandrasekhar, 1943; Ostriker, 1999; Chapon et al., 2013). We will propose here another physically motivated model based on the Eddington limited accretion.

First, the gravitational interaction between the sink and the matter distribution, as well as between the sink and possible other sinks in the computational box, are both treated using a direct summation method of a softened $1/r^2$ Newtonian acceleration. We prefer this new approach than using the Particle Mesh method, as it gives more accurate

trajectories, especially if the SMBH mass dominates the local potential. The softening radius used in the force calculations is set to $2\Delta x_{\rm min}$, as in Bleuler & Teyssier (2014).

When the sink accretes gas from within the sink sphere, it also accretes the corresponding momentum, which translates into an effective drag force between the gas and the sink. When the accretion rate onto the SMBH is Eddington-limited, the situation is however more complicated. As described before, the Eddington limit for the radiation is enforced in the vicinity of the SMBH, where the gas is fully ionised and has reached the SMBH accretion disc. We consider in this paper that the gas accretion rate towards the SMBH accretion disc is set by the Bondi formula, and corresponds to the large scale flow, while the gas accretion rate onto the SMBH is set by the Eddington limit. The difference between the two rates, Bondi minus Eddington, corresponds to gas being decreted from the accretion disc region and redistributed on large scale, in our case within the sink sphere.

$$\dot{M}_{\rm dec} = \dot{M}_{\rm Bondi} - \dot{M}_{\rm acc} \tag{3.21}$$

This process of accretion and ejection will lead to an additional exchange of momentum between the gas and the sink, hence an additional drag force.

We model this additional drag force by requiring that the centre of mass of the joint gas + sink system remain fixed during the accretion, and that its total momentum is conserved. If we note the gas centre of mass within the sink sphere as $\mathbf{x}_{\rm gas}$, this translates into a shift in the sink coordinates given by

$$\begin{aligned} M_{\rm gas}\frac{{\rm d}\boldsymbol{x}_{\mathbf{gas}}}{{\rm d}t} &= \dot{M}_{\rm dec}\boldsymbol{x}_{\mathbf{sink}} - \dot{M}_{\rm Bondi}\boldsymbol{x}_{\mathbf{gas}}, \\ M_{\rm sink}\frac{{\rm d}\boldsymbol{x}_{\mathbf{sink}}}{{\rm d}t} &= \dot{M}_{\rm Bondi}\boldsymbol{x}_{\mathbf{gas}} - \dot{M}_{\rm dec}\boldsymbol{x}_{\mathbf{sink}}, \end{aligned} \tag{3.22}$$

and a similar momentum transfer between the sink and the gas (in other words a drag force) given by:

$$\begin{aligned} M_{\rm gas}\frac{{\rm d}\boldsymbol{v}_{\mathbf{gas}}}{{\rm d}t} &= \dot{M}_{\rm dec}\boldsymbol{v}_{\mathbf{sink}} - \dot{M}_{\rm Bondi}\boldsymbol{v}_{\mathbf{gas}}, \\ M_{\rm sink}\frac{{\rm d}\boldsymbol{v}_{\mathbf{sink}}}{{\rm d}t} &= \dot{M}_{\rm Bondi}\boldsymbol{v}_{\mathbf{gas}} - \dot{M}_{\rm dec}\boldsymbol{v}_{\mathbf{sink}}, \end{aligned} \tag{3.23}$$

These equations are solved for each time step, and are used to modify the sink position and velocity, but also the gas density, momentum and total energy within the sink sphere. More details on the numerical implementation are given in the Appendix. Note that in case of zero decreted mass (pure unlimited Bondi accretion), the momentum transfer only comes from the accreted gas mass onto the sink, as it should. In the opposite case, when the accretion rate is strongly Eddington limited, the mass decretion rate is maximal and almost equal to the Bondi rate. This results in a strong drag force between the sink and the gas.

3.2.4. SMBH feedback

In this paper, we only consider a model for which thermal energy is injected within the sink sphere, using for the SMBH luminosity the following formula

$$L_{\rm AGN} = \epsilon_{\rm c}\dot{M}_{\rm acc}\epsilon_{\rm r}c^2, \tag{3.24}$$

where $\epsilon_r = 0.1$ is the accretion disc radiative efficiency and ϵ_c is a free parameter representing the coupling efficiency between the blast wave energy at small scale and the resulting thermal energy deposited at large scale. Based on previous work using the Ramses code (Teyssier et al., 2011; Dubois et al., 2012), we fixed its value to $\epsilon_c = 0.15$, which is quite typical of the corresponding literature, with values ranging from 0.05 (Springel et al., 2005; Wurster & Thacker, 2013) to 0.15 (Booth & Schaye, 2009; Gabor & Bournaud, 2013).

An important improvement compared to the previous Ramses implementation is that we deposit now thermal energy at every *fine* timestep (i.e. the timestep of the maximum level of refinement ℓ_{max}), and not only at main coarse time steps as before. We also do not consider a minimum injection temperature, as in Booth & Schaye (2009) or Teyssier et al. (2011). Moreover, the thermal energy is distributed in every gas cell within the sink sphere proportionally to the gas density. This mass-weighted deposition scheme prevents the apparition of unrealistically large gas temperature, as opposed to the volume-weighted deposition scheme.

These important changes now allow us to model the competition between heating and cooling within the sink sphere. Indeed, one can write an energy equation for the average gas specific internal energy within the sink sphere as

$$\rho \frac{\mathrm{d}\epsilon}{\mathrm{d}t} = \frac{L_{AGN}}{V_{sink}} - n^2 \Lambda(T) \tag{3.25}$$

where the specific internal energy is related to the temperature and the sound speed by

$$\epsilon \simeq \frac{k_B T}{\mu m_H} \simeq c_s^2(t) \tag{3.26}$$

and V_{sink} is the volume of sink accretion zone, n is the gas density in units of H/cc, and Λ is a temperature-dependent cooling rate per number density.

We want now to distinguish two regimes of accretion on the sink. First, we have the cold accretion regime, for which cooling dominates over heating. The Bondi accretion rate is so high that we consider the accretion to be Eddington limited,

$$\dot{M}_{acc} = \frac{M_{sink}}{t_S}. \tag{3.27}$$

We consider for the cooling function only Bremsstrahlung so that

$$\Lambda(T) = \Lambda_0 T^{1/2} \tag{3.28}$$

where $\Lambda_0 \simeq 1.2 \times 10^{-27}$ erg s^{-1} cm^3 K$^{-0.5}$. This is a good approximation for high temperature and low metallicity gas. We conclude immediately that, for a given average gas density within the sink sphere, cooling will always win over heating, and the sink will remain in the cold accretion regime, unless the SMBH mass becomes large enough, so that

$$M_{sink} > n_H^2 \Lambda_0 T^{1/2} \frac{t_S}{\epsilon_c \epsilon_r c^2} V_{sink}. \tag{3.29}$$

Because the sink is now massive enough, heating dominates over cooling, and the sink sphere enters the second phase, namely the hot accretion regime. For this, we now assume that the gas temperature is always large enough that the accretion rate is equal

to the Bondi rate. We also consider the SMBH to be at rest in the centre of the galaxy. We then obtain for the accretion rate

$$\dot{M}_{\rm acc} \simeq 4\pi\rho\frac{(GM_{\rm sink})^2}{c_s^3(t)} \tag{3.30}$$

We can now solve the energy equation, ignoring the cooling term, and obtain the time evolution of the sound speed within the sink sphere

$$c_s(t) = \left[\frac{15}{2}\epsilon_c\epsilon_r c^2\left(\frac{GM_{\rm sink}}{r_{\rm sink}}\right)^2\frac{t}{r_{\rm sink}}\right]^{1/5} \tag{3.31}$$

Obviously, the temperature in the sink region will not grow indefinitely. As soon as it reaches a high enough value, the gas in the vicinity of the SMBH will expand and cool adiabatically. We consider that we have reached the maximum temperature after one sound crossing time of the sink sphere, namely $t_{\rm cross}(t) = r_{\rm sink}/c_s(t) = t$. Combining this with the previous equation gives us the maximum possible sound speed in the hot accretion phase

$$c_{s,\rm max} = \left[\frac{15}{2}\epsilon_c\epsilon_r c^2\left(\frac{GM_{\rm sink}}{r_{\rm sink}}\right)^2\right]^{1/6} \tag{3.32}$$

It can be compared to the galaxy escape velocity to assess the possibility for the SMBH to unbind the gas from the nuclear region (see below).

Besides various constants that we set to our fiducial values ($\epsilon_c = 0.15$ and $\epsilon_r = 0.1$), we see that the only variables entering theses various formulae are the SMBH mass, $M_{\rm sink}$, the sink sphere radius $r_{\rm sink}$, and finally the average gas density within the sink sphere $n_{\rm H}$. Inserting typical values for our present simulation, we can compute first the critical SMBH mass beyond which heating dominates over cooling, so that the sink sphere can exit the cold accretion regime and actually heats the gas around the SMBH

$$M^{\rm cool}_{\rm sink,crit} \simeq 8\times10^4\ M_\odot\ \left(\frac{n_{\rm H}}{100\ {\rm H/cc}}\right)^2\left(\frac{r_{\rm sink}}{100\ {\rm pc}}\right)^3, \tag{3.33}$$

where we assumed the gas temperature to be fixed at 10^6 K in the cooling function. If this is the case, then the temperature within the sink sphere will steadily increase according to Eq. (3.32) and reach the maximum sound speed

$$c_{\rm s,max} \simeq 750\ {\rm km/s}\ \left(\frac{M_{\rm sink}}{10^8\ M_\odot}\right)^{1/3}\left(\frac{r_{\rm sink}}{100\ {\rm pc}}\right)^{-1/3} \tag{3.34}$$

This last equation can be used to define another critical mass, $M^{\rm esc}_{\rm sink,crit}$, corresponding to $c_{\rm s,max} = v_{\rm esc}$, the escape velocity from the centre of the halo, so that AGN heating would result in the unbinding of the hot gas in the vicinity of the SMBH. We find

$$M^{\rm esc}_{\rm sink,crit} = 10^8\,{\rm M}_\odot\left(\frac{v_{\rm esc}}{750\ {\rm km/s}}\right)^3\left(\frac{r_{\rm sink}}{100\ {\rm pc}}\right) \tag{3.35}$$

In summary, if enough gas makes it into the sink sphere, the density will be high and cooling will dominate, maintaining the gas temperature to relatively low values and the accretion rate to the Eddington limit. If, on the other hand, the gas density within the

sink sphere is too low, or if the sink mass is too large, we enter the hot, adiabatic regime for which the gas temperature is quickly rising to its maximum value. Unfortunately, as we will see in the Results section, all these quantities depend sensitively on the adopted resolution. A better spatial resolution, resulting in a smaller sink radius, can reduce the critical SMBH mass, but can also increase it by allowing for larger gas densities. Better spatial resolution can also increase the gas temperature in the hot accretion regime significantly.

On the other hand, we could also apply the same formalism to the ISM in the vicinity of the SMBH, using the fundamental properties of a realistic multiphase gas rather than the relatively artificial properties of our finite resolution simulations. For example, one can relate the gas density in the cooling critical mass formula to the average density of typical gas clouds that are bombarding the SMBH in the nuclear region, and one can argue that the feedback energy should be deposited within a fixed radius, invoking other physical processes to set this energy deposition scale. In what follows, we will only apply our simple analytical arguments to interpret our numerical results, and defer a more general and realistic description of the ISM around the SMBH to future work.

3.3. Numerical setup

We use the AMR code Ramses (Teyssier, 2002) and its second-order, unsplit Godunov scheme to solve the Euler equations. The evolution of dark matter and stars is performed with the Adaptive Particle-Mesh solver with cloud-in-cell interpolation. The dynamical evolution of the sink particle is performed the direct gravitational acceleration (see Subsection 3.2.3).

Our initial conditions feature an isolated, gas-rich, slowly rotating (spin parameter of 0.04) dark matter halo of 2×10^{12} $M_\odot$ sampled using one million dark matter particles. The halo has a truncated NFW (Navarro et al., 1997) profile with a concentration parameter $c = 10$ and with the circular velocity $V_{200} = 160\,\mathrm{km\,s^{-1}}$, which results in the radius $R_{200} = 230\,\mathrm{kpc}$, while the halo is truncated at 514 kpc. Initially, the gaseous halo is in hydrostatic equilibrium and has the universal gas fraction of $f_{\mathrm{gas}} = 15\%$. The initialisation follows the setup of Teyssier et al. (2013). Our fiducial run has a spatial resolution of $\Delta x_{\mathrm{min}} = 78\,\mathrm{pc}$.

Using an isolated cooling halo is dictated by a compromise between realistic but expensive cosmological simulations and idealised but highly resolved isolated disc simulations. Since we are using a realistic initial angular momentum profile inspired from the average angular momentum distribution from N body simulation (Bullock et al., 2001), gas will be continuously accreted from the halo into the disc, with the right amount of angular momentum, giving us the possibility to feed the nuclear region, and possibly the central SMBH.

We use the Sutherland & Dopita (1993) model for radiative cooling of gas for H, He and metal lines for gas hotter than 10^4 K and from metal fine-structure cooling processes at lower temperatures. We advect the metallicity in the form of a passive scalar and we choose the initial metallicity to be $Z_{\mathrm{ini}} = 0.05\ Z_\odot$. A pressure floor is introduced at high density and low temperature, to prevent the uncontrolled fragmentation of gas beyond the spatial resolution, possibly leading to the formation of numerical singularities (especially because we are using a low star formation efficiency). The temperature corresponding to

the pressure floor is set to

$$T_{\rm floor} = T_* \left(\frac{n_{\rm H}}{n_*} \right)^{\Gamma-1} \tag{3.36}$$

with a critical gas number density $n_* = 9\,{\rm cm}^{-3}$, a critical temperature $T_* = 2 \times 10^3\,{\rm K}$, and $\Gamma = 2$. This results in the minimum Jeans length

$$\lambda_{\rm J} = c_{\rm s}\sqrt{\frac{\pi}{G\rho}} = \sqrt{\frac{\Gamma \pi k_{\rm B} T_*}{m_{\rm H}^2 G n_*}} \simeq 332\,{\rm pc} \simeq 4\,\Delta x_{\rm min} \tag{3.37}$$

and in the minimum Jeans mass

$$M_{\rm J} = \frac{4\pi}{3} n_* m_{\rm H} \left(\frac{\lambda_{\rm J}}{2} \right)^3 \simeq 4 \times 10^6 M_\odot \tag{3.38}$$

The mesh refinement strategy we have adopted for all our simulations is a quasi-Lagrangian approach, where cells are refined once their mass exceed $8 \times m_{\rm res}$, where our mass resolution is set to $m_{\rm res} \simeq 1.5 \times 10^5 M_\odot$, so that our minimum Jeans mass is always sampled by at least 32 resolution elements. In all simulations, star formation is modelled with a Schmidt law with a rather low efficiency $\epsilon_* = 0.01$ coming from observations of local molecular clouds (Krumholz & Tan, 2007). Collisionless star particles of fixed mass 1.3×10^5 $M_\odot$ are spawned stochastically with a Poisson distribution if the gas density in the cell is larger than $n_* m_{\rm H}$ (Rasera & Teyssier, 2006). Feedback from supernovae, if considered, is modelled with a non-thermal energy injection with efficiency of 10% (i.e. 10% of stellar population explodes, each SN with energy of 10^{51} erg) and yield of 10% (1 $M_\odot$ of metals for each 10 $M_\odot$ of ejected material). The non-thermal energy dissipation timescale is set to 10 Myr. We boost the efficiency of our supernovae feedback recipe by grouping stochastically multiple star particles into one single star cluster of mass 10^8 $M_\odot$.

As it was already mentioned in Section 3.2.1, we allow only one sink to form in our galaxy. While star formation and stellar feedback are both modelled since the very beginning, we only form the sink particle at around 200 Myr after the start of the simulation. This time roughly corresponds to the stage in the disc evolution in which massive gas clumps are present and the environment of SMBH is well established in terms of gas and stars. This should promote most stable growth conditions for the newly seeded sink. We use the PHEW clump finder (Bleuler et al., 2015) to identify the most massive gas clump of a mass of order of 10^8 $M_\odot$ as the formation site for the SMBH, and let the sink evolve from there. Initial velocity of the sink corresponds to that of gas out of which it was formed. Mass, momentum and angular momentum are conserved during the formation process. All fiducial parameters of our SMBH model are listed in Table 3.1.

3.4. Results

We now present our simulation results, including each important process one by one, in order to compare them, and gauge their relative importance. These processes are listed in Table 3.2. For each feedback process, we use the parameters described in the previous section. We however consider the SMBH seed mass as a free parameter, and we explore values ranging from 10^5 to 10^9 $M_\odot$, as listed in Table 3.2.

Table 3.1: Summary of fiducial parameters related to SMBH sink particles in Ramses simulations.

Parameter	Fiducial value	Description
$M_{\rm seed}$	10^6 $M_\odot$	Sink seed mass
$M_{\rm clump}$	10^8 $M_\odot$	Mass of the clump in which we seed the sink
Direct solver	yes	The direct N-body solver used to evolve the trajectory of a sink
Drag	yes	Gas drag force from accretion
$\alpha_{\rm boost}$	Eq. (3.16)	Boost factor for the Bondi velocity

3.4.1. Accretion-limited growth

Our first suite of simulations has been performed without any feedback processes and with only one sink particle seeded in the first, massive enough, nuclear gas clump, growing via Eddington-limited Bondi accretion. Because of the relatively low angular momentum in our cooling halo, mimicking what we expect from cosmological simulations, these simulations without feedback lead to the formation of a gas-rich, clumpy and bulge-dominated galaxy (see also Teyssier et al., 2013; Dubois et al., 2016) that resembles many observed high-z galaxies, in particular the so-called "blue nuggets" (see e.g. Damjanov et al., 2009).

The trajectory and the mass growth of the SMBH are shown in Figure 3.1. For all our adopted seed masses, the SMBH remains well within the nuclear region (defined here as the central kiloparsec), in which they were born. Interestingly, the lowest seed mass 10^5 $M_\odot$ shows a very different behaviour than the other, larger seed masses. Its growth is very slow, for almost 1 Gyr, and only when it reaches 10^6 $M_\odot$ does it have a high enough accretion rate and grows exponentially. The other seed masses start growing exponentially immediately after their creation, which means that they are massive enough to have a sustained, larger than Eddington, Bondi accretion rate.

We argue that the critical mass for the sink particle to accrete fast enough is the minimum Jeans mass associated to our adopted mesh resolution. Indeed, assuming that $v_{\rm rel} = 0$, we can re-write the parameter that controls whether Bondi accretion is subsonic or supersonic (see Eq. 3.8) as

$$x_{\rm sink} = \frac{c_s^2 \lambda_{\rm J}}{G M_{\rm sink}} \simeq \frac{M_{\rm J}}{M_{\rm sink}} \tag{3.39}$$

where we used the fact that $r_{\rm sink} = 4\Delta x_{\rm min} = \lambda_{\rm J}$. For our fiducial resolution, the Jeans mass $M_{\rm J}$ is 4×10^6 $M_\odot$. For the lowest seed mass, which is below the Jeans mass, accretion follows the Bondi rate, and is rather low, because the accretion is subsonic. Note that in this regime, because the accretion rate is low, the dynamical coupling between the sink and the gas is weak, making the sink very sensitive to external perturbations. One can see in Figure 3.1 that the trajectory of the sink particle is quite perturbed, with visible oscillations around the centre of the galaxy. These oscillations increase the relative velocity between the gas and the sink, further contributing to the low accretion rate. Once the sink mass grows beyond 10^6 $M_\odot$, about 800 Myr after the start of the simulation for the small seed mass or immediately after creation for the other seed masses, the Bondi

Table 3.2: Summary of simulation runs and parameters used in this study. Parameters varied with respect to the fiducial run are highlighted in bold print. Columns: (1) subsection in which the simulations are analysed (with exception for fiducial run); (2) maximum allowed refinement level; (3) fraction of SN energy deposited in the gas; (4) drag force modelled (or inclusion of a nuclear star cluster); (5) initial seed mass in $\log_{10}$ $M_\odot$; (6) AGN feedback.

Section (1)	$l_{\rm max}$ (2)	$\epsilon_{\rm SN}$ (3)	drag (4)	$m_{\rm seed}$ (5)	AGN fbk. (6)
3.4.1	14	0.0	yes	**5**	**no**
3.4.1	14	0.0	yes	6	**no**
3.4.1	14	0.0	yes	**7**	**no**
3.4.1	14	0.0	yes	**8**	**no**
3.4.1	14	0.0	yes	**9**	**no**
3.4.2	14	0.0	yes	**5**	yes
3.4.2	14	0.0	yes	6	yes
3.4.2	14	0.0	yes	**7**	yes
3.4.2	14	0.0	yes	**8**	yes
3.4.2	14	0.0	yes	**9**	yes
3.4.3	14	**0.1**	yes	**5**	**no**
3.4.3	14	**0.1**	yes	6	**no**
3.4.3	14	**0.1**	yes	**7**	**no**
3.4.3	14	**0.1**	yes	**8**	**no**
3.4.3	14	**0.1**	yes	**9**	**no**
3.4.4	14	**0.1**	yes	**5**	yes
3.4.4	14	**0.1**	yes	6	yes
3.4.4	14	**0.1**	yes	**7**	yes
3.4.4	14	**0.1**	yes	**8**	yes
3.4.4	14	**0.1**	yes	**9**	yes
3.4.5	14	**0.1**	**NSC**	**5**	yes
3.4.5	14	**0.1**	**NSC**	6	yes
3.4.5	14	**0.1**	**NSC**	**7**	yes
3.4.5	14	**0.1**	**NSC**	**8**	yes
3.4.5	14	**0.1**	**NSC**	**9**	yes
3.4.6	**15**	0.0	yes	6	yes
3.4.6	**15**	**0.1**	yes	6	yes
3.4.6	**15**	**0.1**	**NSC**	6	yes

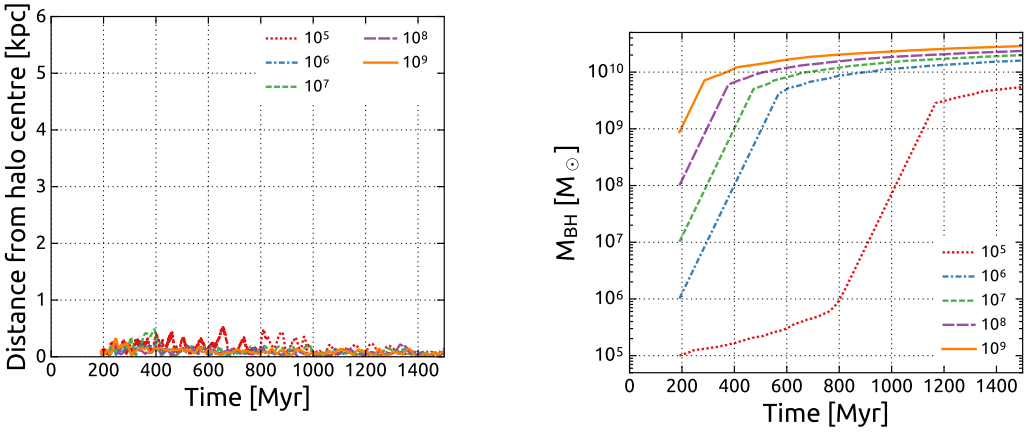

(a) Distance between the sink and the centre of the halo

(b) SMBH mass growth

Figure 3.1: Evolution of distance to the centre of halo and sink mass for the runs without neither SN and AGN feedbacks for five different seed masses: 10^5 $M_\odot$ - red (dotted), 10^6 $M_\odot$ - blue (dash-dotted), 10^7 $M_\odot$ - green (short dashes), 10^8 $M_\odot$ - purple (long dashes), and 10^9 $M_\odot$ - orange (solid). The sink particle occupies position in the centre of the halo and its growth is limited first by Eddington rate and later by angular momentum loss in the gas. Lack of AGN feedback heating leads to worrisomely large SMBH mass.

accretion evolves from subsonic to supersonic. A much more rapid, Eddington-limited exponential growth follows.

After this phase, the SMBH mass seems to saturate, and grows only mildly, mostly because of the slow accretion of fresh gas into the nuclear region. Indeed, since we did not include any feedback processes in this first experiment, the final SMBH mass is regulated by the available gas mass within the nuclear region. This regime, called here accretion-limited growth, was first discussed in Bournaud et al. (2011). The late accretion phase is controlled by angular momentum transfer in the galactic disc, triggered by various instabilities and slowly feeding the SMBH with fresh gas. In this case, the SMBH trajectory remains well within the nuclear region, a dense and massive stellar bulge that provides a very stable environment for the SMBH. As a result, the sink particle never leaves the nuclear region.

3.4.2. AGN feedback-limited growth

We have repeated the same simulations as in the previous section, but this time with AGN feedback. The resulting dynamical and mass evolutions of the SMBH are shown in Figure 3.2a and Figure 3.2b. The only difference with the previous setup is the final mass of the sink, which is now regulated by AGN feedback.

The initial growth of the SMBH in our simulations with AGN feedback is very similar to the runs without feedback. Due to the large amounts of gas in the nuclear region, feedback heating does no affect the gas surrounding the sink, as cooling dominates. As soon as the accretion rate is high enough, heating dominates over cooling and the SMBH quickly reaches its maximum mass, which in our case is around 2×10^8 $M_\odot$.

The maximum, self-regulated mass is related to the heating-cooling balance we have discussed in Subsection 3.2.4 (see Eq. (3.32) and (4.6)). Using the simulation with

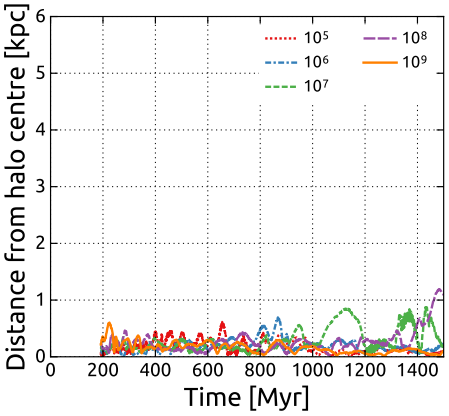

(a) Distance between the sink and the centre of the halo

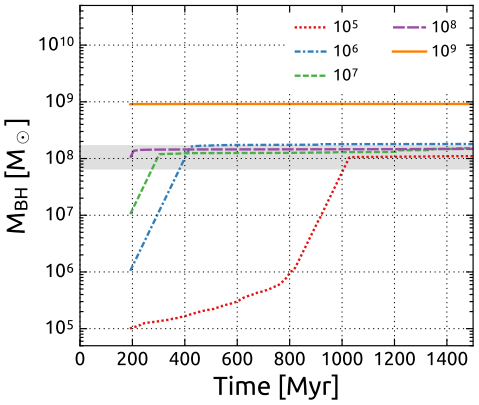

(b) SMBH mass growth

Figure 3.2: Evolution of distance to the centre of halo and sink mass for the runs with AGN feedback only for five different seed masses: 10^5 $M_\odot$ - red (dotted), 10^6 $M_\odot$ - blue (dash-dotted), 10^7 $M_\odot$ - green (short dashes), 10^8 $M_\odot$ - purple (long dashes), and 10^9 $M_\odot$ - orange (solid). Grey band on the right panel shows predicted SMBH mass based on the density in the sink sphere (cf. Eq. (3.33)) - lower envelope corresponds to density of 500 H/cc, while upper to 800 H/cc (see Figure 3.3). The sink particle resides in the centre of the halo travelling with most massive clump and its growth is limited first by Eddington rate and later terminated at self-regulation scale due to its feedback heating.

$M_{\rm seed} = 10^6$ $M_\odot$ as an example, we see that at around 420 Myr, the sink's growth is terminated. Initially, the gas density in the sink sphere is quite large, around ~ 600 H/cm^3, so that clearly cooling dominates the energy budget in the sink sphere. Gradually, as the SMBH mass grows, feedback is able to heat the gas more and more in the sink sphere, until the SMBH mass reaches the critical value for which heating dominates; this can be compared with estimate given by Eq. (3.33), which is plotted as a grey band on Figure 3.2b. Very quickly the gas sound speed within the sink sphere rises, until it exceeds the escape velocity of the halo. When this happens, gas is removed from the nuclear region by a blast wave, which reduces the average gas density down to or even below $\bar{\rho} \simeq 10$ H/cm^3, and makes feedback even more efficient. Feedback is able to maintain the sound speed to a high value ($c_{\rm s} \simeq 400$ km/s), strongly reducing the accretion rate (see Eq. (3.5) and bottom left panel of Figure 3.3).

This is only when feedback processes are able to accelerate gas to the escape velocity that the growth of SMBH is halted (see also Silk & Rees, 1998; Fabian, 1999). This can be seen on Figure 3.3, where we plot various average quantities measured in the sink sphere. The gas density (*top left*) drops by two orders of magnitude as soon as the maximum sound speed significantly exceeds the halo escape velocity ($v_{\rm esc}$, *top right*). The critical SMBH mass $M_{\rm sink,crit}$, for which heating balances cooling, is reached at 420 Myr (*bottom right*), after which the average sound speed quickly exceeds $v_{\rm esc}$, which then marks the end of the cold accretion regime (*bottom left*) and the beginning of the hot mode of accretion. For comparison, we have plotted in Figure 3.3 our simple analytical predictions from Subsection 3.2.4. We can predict quite nicely the onset of efficient heating, when the SMBH mass reaches its critical value, as well as the end of the mass growth, when the

maximum sound speed reaches the escape velocity of the halo.

The case with $M_{\rm seed} = 10^9$ M$_\odot$ is very different than all the other cases. Here, the initial seed mass is already above the maximum, self-regulated mass. AGN feedback immediately blows away the gas from the nuclear region. As a result, the gas in the vicinity of the sink remains very hot and the accretion rate very low.

3.4.3. Supernovae feedback-limited growth

We now remove AGN feedback from the picture, but include instead supernova feedback from dying massive stars. We use the same simulation suite than before, with seed masses from $M_{\rm seed} = 10^5$ M$_\odot$ to $M_{\rm seed} = 10^9$ M$_\odot$. On Figure 3.4, we again plot the time evolution of the distance of the sink particle to the halo centre and of its mass. Here again, we can see two different regimes. Low and intermediate seed masses are quickly removed from the central kiloparsec. There, supernovae feedback is efficient enough to destroy the parent clump, and the sink particles are perturbed by interaction with nearby clumps. As a consequence, the trajectory of the sinks becomes more complicated and eccentric, and the relative velocity between the sink and the gas within the sink sphere grows significantly, reducing the accretion rate and the corresponding drag force accordingly. For seed masses larger than $M_{\rm seed} = 10^8$ M$_\odot$, the sink trajectory appears as much less perturbed and the sink manage to remain within the nuclear region. As a consequence, accretion proceeds much more rapidly and the sink mass can grow up to its accretion-limited value, as in Section 3.4.1.

In order to estimate the mass of the typical clumps that will perturb the trajectory of the SMBH, we use the classical Toomre analysis of gas fragmentation in an idealised razor thin disc (Toomre, 1964). The largest unstable wavelength is the Toomre length

$$\lambda_{\rm T} \simeq \frac{G\Sigma_{\rm gas}}{\kappa^2} \simeq \frac{f_{\rm gas}}{\pi} R_{\rm gal}. \tag{3.40}$$

In this approximate formula G is gravitational constant, $\Sigma_{\rm gas} = M_{\rm gas}/\pi R_{\rm gal}^2$ is the gas surface density, $\kappa \simeq V_{\rm gal}/R_{\rm gal}$ is the epicyclic frequency, $V_{\rm gal} = \sqrt{GM_{\rm tot}/R_{\rm gal}}$ is the galaxy circular velocity and $f_{\rm gas}$ is the gas-to-total mass fraction in the disc. In order for this wavelength to be truly unstable, the Toomre parameter must satisfy

$$Q = \frac{c_{\rm s}\kappa}{\pi G\Sigma_{\rm gas}} < 1. \tag{3.41}$$

where $c_{\rm s}$ can be taken as either the sound speed or the velocity dispersion of the gas. Under such conditions, one can then estimate the mass of the most massive clumps as the Toomre mass $M_{\rm T}$ defined by

$$M_{\rm T} = \Sigma_{\rm gas}\pi \left(\frac{\lambda_{\rm T}}{2}\right)^2 \simeq \frac{M_{\rm tot} f_{\rm gas}^3}{4\pi^2}. \tag{3.42}$$

For a Milky Way-like galaxy, one has $M_{\rm tot} \simeq 10^{11}$ M$_\odot$ in the disc (not to be confused with the total mass in the halo, which is one order of magnitude larger). At low redshift, in galaxies similar to our own Milky Way, one finds $f_{\rm gas} \simeq 0.1$, which results in a typical clump mass of $M_{\rm T} \simeq 2.5 \times 10^6$ M$_\odot$. At high redshift, however, like the cooling halo set-up we are adopting in this paper, the gas fraction is much higher, $f_{\rm gas} \simeq 0.5$, for a similar total mass. This leads to much bigger clumps, with $M_{\rm T} \simeq 3 \times 10^8$ M$_\odot$. This value is typical for

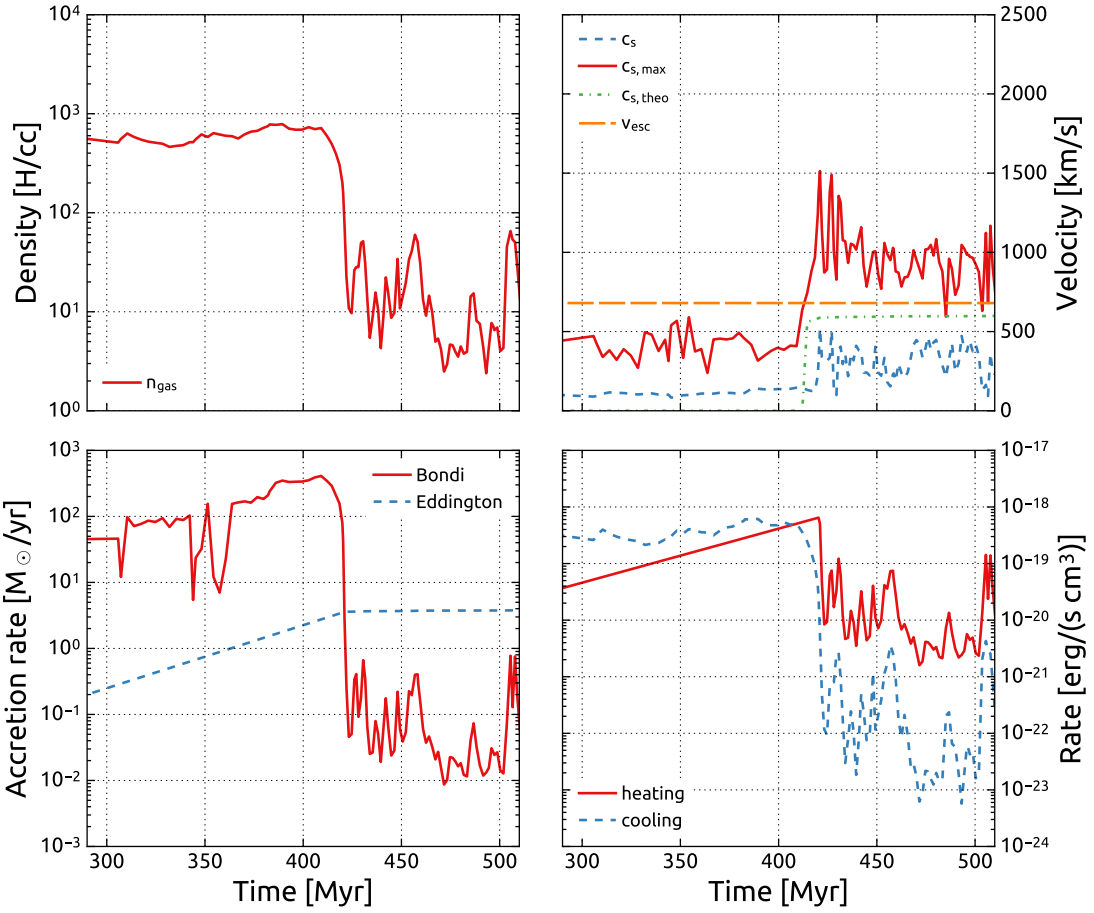

Figure 3.3: Time evolution of 1) average gas density within the sink sphere (*top left*); 2) average, mass-weighted, sound speed (blue, short dashes) and maximum sound speed (red, solid) within the sink sphere (*top right*), we have also represented our simple theoretical model (Eq. 3.32 and 4.6) (green, dot-dashed) compared to the escape velocity from the halo's centre (orange, long dashes); 3) Bondi (red, solid) and Eddington (blue, dashed) accretion rates (*bottom left*) and 4) average heating (red, solid) and cooling (blue, dashed) rates within the sink sphere (*bottom right*) for simulation with AGN feedback only and $M_{seed} = 10^6$ $M_\odot$.

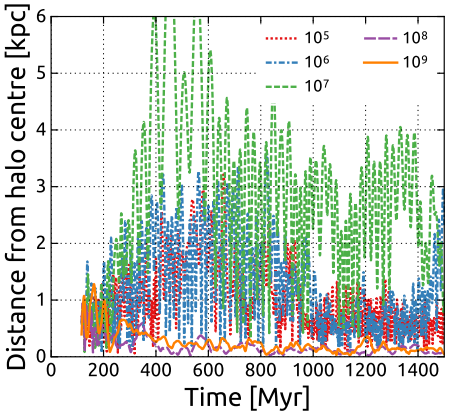

(a) Distance between the sink and the centre of the halo

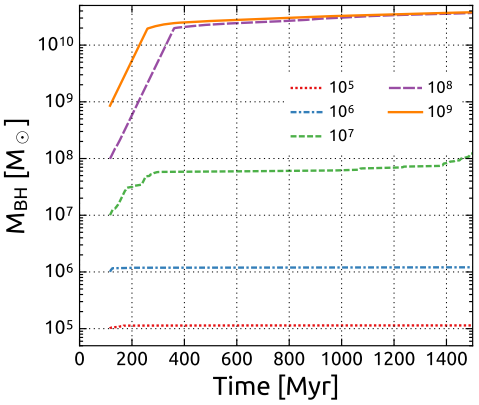

(b) SMBH mass growth

Figure 3.4: Evolution of distance to the centre of halo and sink mass for the runs with SN feedback but *without* AGN feedback for five different seed masses: 10^5 $M_\odot$ - red (dotted), 10^6 $M_\odot$ - blue (dash-dotted), 10^7 $M_\odot$ - green (short dashes), 10^8 $M_\odot$ - purple (long dashes), and 10^9 $M_\odot$ - orange (solid). Grey band on the right panel shows predicted SMBH mass based on the halo escape velocity (cf. Eq. (3.35)).

massive and gas rich galaxies (see. e.g. Genzel et al., 2008, 2011; Guo et al., 2012; Tacconi et al., 2013; Tamburello et al., 2015, for in-depth discussion). We have also attempted measuring masses of gas and stellar clumps in our simulations and found masses of similar order. We have plotted few most massive clumps on Figure 3.10, measuring the mass in the radius of $4\Delta x_{\rm min} \approx 320\,{\rm pc}$. In conclusion, a sink particle with mass $M_{\rm sink} \leqslant M_{\rm T}$ will have its trajectory easily disrupted by clumps in the disc. Larger sink masses, on the other hand, will result in a much more stable orbital evolution (see below).

In order for the sink particle to reach (or remain in) the nuclear region of the galaxy, we need to estimate the dynamical friction timescale as introduced by Chandrasekhar (1943). Although the original formula was derived for a collisionless fluid (dark matter and stars), a very similar formula can be used to compute the dynamical friction on the gas (Ostriker, 1999). For the gas drag, a correction factor must be introduced, compared to the original collisionless case, but only for transonic relative velocities. For a SMBH with a typical orbital velocity of 200 km/s, the drag force is likely to be in the strong supersonic regime, for which no correction is required.

Using Chandrasekhar's formula, we compute the dynamical friction timescale $t_{\rm df}$ (e.g. Eq. 8.12 of Binney & Tremaine, 2008)

$$t_{\rm df} = \frac{1.65}{\ln\Lambda}\frac{R_{\rm orb}^2\sigma}{GM_{\rm BH}} \tag{3.43}$$

where the Coulomb logarithm is given by

$$\ln\Lambda = \ln\left(\frac{R_{\rm gal}V_{\rm orb}^2}{GM_{\rm BH}}\right) \tag{3.44}$$

$R_{\rm orb}$ and $V_{\rm orb}$ are the orbital radius and orbital velocity of the SMBH. Assuming that the velocity dispersion of the collisionless components $\sigma \simeq V_{\rm gal}$, the orbital radius and

velocity of the SMBH to be of the order of the galaxy radius $R_{\rm gal} \simeq 5$ kpc and circular velocity $V_{\rm gal} \simeq 200\,{\rm km\,s^{-1}}$, and finally using $\ln\Lambda \simeq 6.9$ as a typical value for our purposes, we find the dynamical friction timescale to be

$$t_{\rm df} \simeq 2.7\,{\rm Gyr}\frac{10^8\,{\rm M}_\odot}{M_{\rm BH}}. \tag{3.45}$$

Only SMBH with masses greater than 10^9 $\rm M_\odot$ will be able to decay quickly enough to the centre of the galaxy, as they will have an orbital decay rate comparable or faster than their rotation rate. It is interesting to see that the Toomre mass and the critical dynamical friction mass are both comparable to 10^9 $\rm M_\odot$ in high-redshift Milky Way analogues (see also Bournaud et al., 2014).

In a previous section, we have seen that a seed mass lower than $M_{\rm Jeans}$ results in an artificially low, subsonic accretion rate. We see now that a seed mass lower than $M_{\rm T}$ results in the sink particle being scattered out of the nuclear region by large gas clumps. Similarly, a large seed mass with a dynamical friction time scale comparable to (or shorter than) the orbital time $t_{\rm orb} \simeq 200$ Myr will help maintaining the sink particle within the nuclear region.

In summary, large initial seed masses (10^8 and 10^9 $\rm M_\odot$) have a larger accretion rate, as $\dot{M}_{\rm Bondi} \propto M_{\rm BH}^2$, so they can grow fast, at their Eddington-limited rate, and become quickly less sensitive to orbital perturbations. Furthermore, $M_{\rm T}$ is comparable to $M_{\rm seed}$, thus sink particles do not suffer from encounters with larger mass perturbers. Also, its dynamical friction timescale is relatively short, helping the SMBH to remain in the centre.

3.4.4. AGN feedback-limited growth with supernovae feedback

We now combine supernova and AGN feedback, repeating the same numerical experiments. As before, the low and intermediate seed masses $M_{\rm seed} = 10^5$ $\rm M_\odot$, $M_{\rm seed} = 10^6$ $\rm M_\odot$ and $M_{\rm seed} = 10^7$ $\rm M_\odot$ do not really grow, as can be seen in Figure 3.5 for the red (dotted), blue (dash-dotted) and green (short dashes) lines, and as it was already the case for our supernova-only feedback model. The large seed mass, on the other hand, are already too close or even larger than their maximum, self-regulated SMBH mass, as it was already the case for our AGN-only feedback model. So even these large seed masses do not favour a fast growth of the sink particles, which are continuously perturbed by clumps with mass comparable or smaller than the Toomre mass. Moreover, since the sink mass is not growing much beyond 10^9 $\rm M_\odot$, the dynamical friction time scale remains longer or comparable to the orbital time scale and the sink particles keep moving around with eccentric orbits and large pericentre radii (see Figure 3.5 with violet and orange lines; also Figure 3.10, left column).

SN and AGN feedbacks work hand in hand to completely prevent SMBH growth in this gas rich, highly turbulent and clumpy environment. We argue that only SMBH already as massive as 10^{10} $\rm M_\odot$ can survive in the nuclear region of such a galactic environment, because they resist the perturbations from clumps and because they have a short-enough dynamical friction time scale. This conclusion is of course valid only if one considers that our two feedback models are realistic enough, which is of course highly speculative, since they rely on sub-grid physics. These models are nevertheless quite state-of-the-art, and are required to explain the low star formation efficiency (for SN feedback) and to explain star formation quenching in massive galaxies (for AGN feedback).

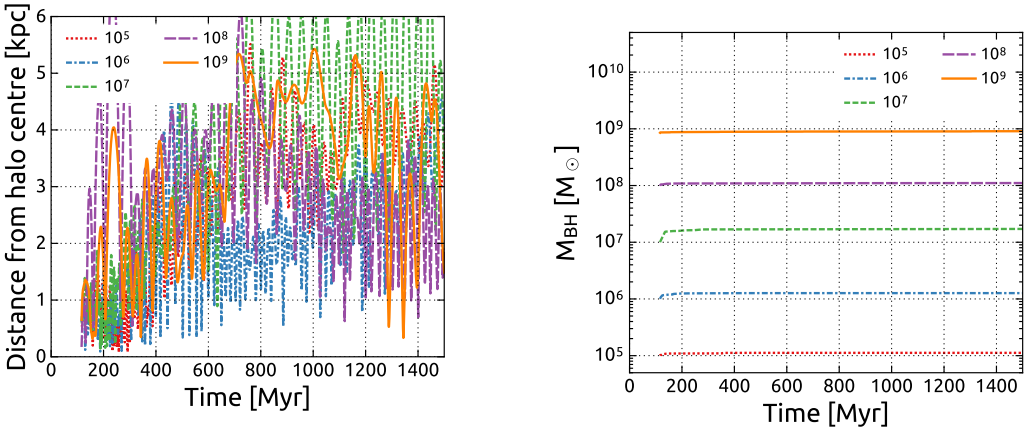

(a) Distance between the sink and the centre of the halo

(b) SMBH mass growth

Figure 3.5: Evolution of distance to the centre of halo and sink mass for the runs with *both* SN and AGN feedbacks for five different seed masses: 10^5 $M_\odot$ - red (dotted), 10^6 $M_\odot$ - blue (dash-dotted), 10^7 $M_\odot$ - green (short dashes), 10^8 $M_\odot$ - purple (long dashes), and 10^9 $M_\odot$ - orange (solid). Grey band on the right panel shows predicted SMBH mass based on the halo escape velocity (cf. Eq. (3.35)).

The fact that SMBH cannot grow at all (except the extremely massive ones) if one combines the two sources of feedback energy is therefore a fundamental problem in the theory of SMBH growth and co-evolution with galaxies. This also explains why many authors have to rely on artificial tricks to maintain the SMBH within the nuclear regions of galaxies, especially when performing high-resolution simulations.

3.4.5. Growth within a Nuclear Star Cluster

One of the key difference between the simulation with supernova-feedback and the simulations without supernova-feedback is the presence of a massive bulge, or in other words, a massive nuclear concentration of stars (see Figure 3.8). Indeed, in the no supernova feedback cases, we do form massive clumps of gas and stars with masses of the order of (or smaller than) the Toomre mass, that appear as bumps in the stellar surface density profile in Figure 3.8. These perturbers do not seem to have an effect on the sink particle in the nuclear region (see Figure 3.1a and Figure 3.2a), even for the small seed masses. The reason lies in the deep potential well provided by the stellar bulge hosting the sink particle. The mass of the bulge appears as large enough to resist the external perturbation and to promote efficient migration towards the centre, using the same arguments as before. It has been argued that the SMBH-bulge co-evolution can be robustly established through observed scaling relations, which is not necessarily the case for the SMBH-galaxy co-evolution (Magorrian et al., 1998; Häring & Rix, 2004; Kormendy & Ho, 2013).

In observed galaxies, we do see massive and isolated SMBH in the nuclear region (like in Andromeda) but also smaller SMBH without a massive bugle to host them (like in the Milky Way). Good candidates for hosting and protecting embedded SMBH in bulge-less galaxies are nuclear star clusters (NSC). NSC are interesting candidates for a co-evolution scenario with SMBH in many aspects. First, one of the plausible SMBH

formation scenarios advocates for the seed to be born within a dense star cluster (e.g. Kochanek et al., 1987; Portegies Zwart et al., 1999; Davies et al., 2011; Stone et al., 2017). Second, NSC are indeed massive enough to survive the perturbations from gas clumps in the host galaxy. Third, NSC are particularly compact (between 1 and 10 pc in size), so they can can trap efficiently their host SMBH within their deep potential well.

The formation of NSC is unfortunately not well understood. In our simulations, the supernova feedback model completely prevent the formation of large and dense star clusters, and our spatial resolution won't allow the survival of parsec-scale objects like NSC anyway. In order to explore this idea, we have implemented a simple subgrid model of a SMBH evolving within a NSC. In our prescription, the sink particle now represents both the NSC and the SMBH. The seed mass is chosen as before for the SMBH, and set to zero for the accompanying star cluster. The Bondi rate is computed using the total sink mass (SMBH plus NSC), and is distributed to each component assuming that the NSC mass grows at a rate 100 times larger than that of SMBH. The Eddington limit is applied only to the SMBH growth rate.

This model is arguably simplistic, and could be improved in many ways, for example by including more star cluster formation physics. Our goal here is to test this idea by analysing the dynamics of the resulting SMBH/NSC co-evolving system. In Figure 3.6a and Figure 3.6b, we show our results for the combined SN and AGN feedback scenario with a NSC and for five different SMBH seed masses, as in the previous sections. The right panel now shows with a thick line the evolution of the NSC mass, while the SMBH mass is shown with thin lines as before. Grey band shows analytical prediction from Eq. (3.35) for $v_{\rm esc} = 680\,{\rm km/s}$ as measured in the centre of the halo. It can be seen that final mass of the SMBH strongly depends on properties of the host halo. Slow and fractional growth after self-regulation should be attributed to loss of angular momentum by the gas in the galactic disc, as seen also in Subsection 3.4.1.

Compared to the similar scenario without NSC, one clearly sees that the sink particle remains now in the central kiloparsec (Figure 3.10, right column), with the exception of the very low seed mass case, which still violates our Jeans mass condition.

For SMBH with initial mass between 10^6 and 10^8 $M_\odot$ initial growth is not Eddington-limited, but appears to be regulated by SN feedback, as they accrete at a sub-Eddington rate (Figure 3.7). The corresponding NSC mass is much larger, close to 10^{10} $M_\odot$, explaining why the combined NSC/SMBH system can survive interactions with clumps and remain in the centre. Interestingly, the final NSC mass seems to depend on the initial SMBH seed mass. We explain this effect by the earlier termination of NSC growth due to AGN feedback. In our scenario, the NSC mass is assembled by fast, SN-regulated Bondi accretion, but is regulated ultimately by AGN feedback. The largest seed mass ($M_{\rm seed} = 10^9$ $M_\odot$) has already reached the self-regulated mass scale and therefore does not grow at all, while its companion NSC can only grow its mass by a factor of 5.

3.4.6. Resolution effects

In order to determine to what extent the evolution of our SMBH mass is sensitive to resolution effects, we have re-run our various simulations with seed mass $M_{\rm seed} = 10^6$ $M_\odot$ and with a better spatial resolution with $\ell_{\rm max} = 15$ and a better mass resolution with $m_{\rm res} \simeq 2 \times 10^4 M_\odot$.

A complication that arises with this exercise is that massive gas clumps will form at different times in the fragmenting discs with different resolutions. To avoid artificial

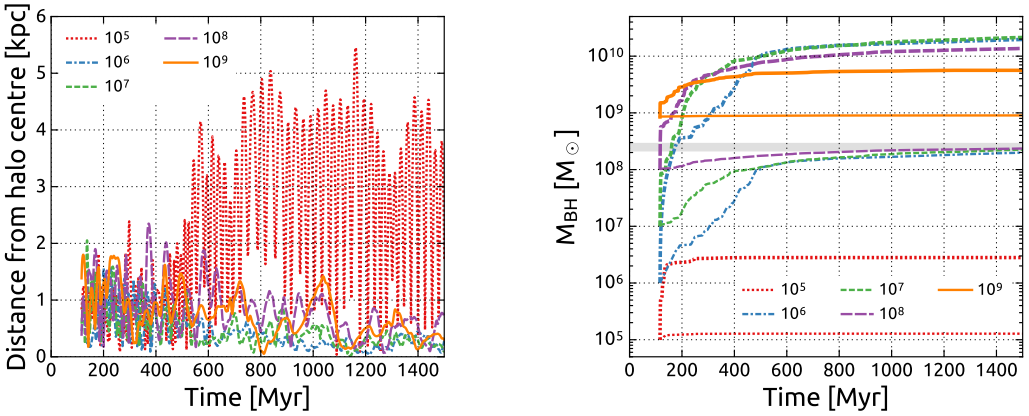

(a) Distance between the sink and the centre of the halo

(b) SMBH (solid) and sink (NSC+SMBH; dashed) mass growth

Figure 3.6: Evolution of distance to the centre of halo and sink mass for the runs with AGN feedback and NSC for five different seed masses: 10^5 $M_\odot$ - red (dotted), 10^6 $M_\odot$ - blue (dash-dotted), 10^7 $M_\odot$ - green (short dashes), 10^8 $M_\odot$ - purple (long dashes), and 10^9 $M_\odot$ - orange (solid). Grey band on the right panel shows predicted SMBH mass based on the halo escape velocity (cf. Eq. (3.35)).

differences due to stochastic effects, we have run the simulations with our highest resolution first, and then introduce the seed sink particle at exactly the same time in the most massive clump of the lowest resolution afterwards.

The AGN-feedback-only case at the different resolutions appears very similar in term of mass growth (basically Eddington-limited) but the final SMBH mass is larger in the high resolution run by a factor of 2. Using Eq. (3.33), we see that the critical SMBH mass for which cooling is balanced by heating, is proportional to the volume of the sink sphere, so that it should be reduced by a factor of 8 in the high resolution run, but is also proportional to the square of the gas density within the sink sphere, which happens to be 4 times larger in the high resolution case with $n_H \simeq 3000$ H/cc than in the low resolution case with $n_H \simeq 750$ H/cc, so that the critical mass should be increased by a factor of 16. Overall, as observed in the high resolution run, the final sink mass is larger by a factor of 2 when compared to the low resolution case. The density in the sink sphere appears to be the critical parameter that controls the final sink mass, because of the delicate balance between heating and cooling. Before the SMBH mass is large enough to overcome the effect of cooling, nothing can prevent the collapse of the cold gas in the nuclear region (we do not include SN feedback yet) and the gas density can grow, up to a maximum value set by the adopted resolution. In conclusion, we argue that in this case (AGN-feedback only) the final, maximum mass is set by the SMBH's ability to overcome cooling with heating, and not its ability to heat the gas at (or above) the escape velocity of the halo.

When we include SN feedback (but without the NSC), the high resolution simulation is identical to the low resolution one, with the sink particle quickly moving out of the nuclear region on eccentric orbits and not growing at all (Figure 3.10, left column, at lower resolution). The high resolution simulation shows SMBH orbits with systematically smaller apocentres, which is consistent with a slightly larger dynamical friction owing

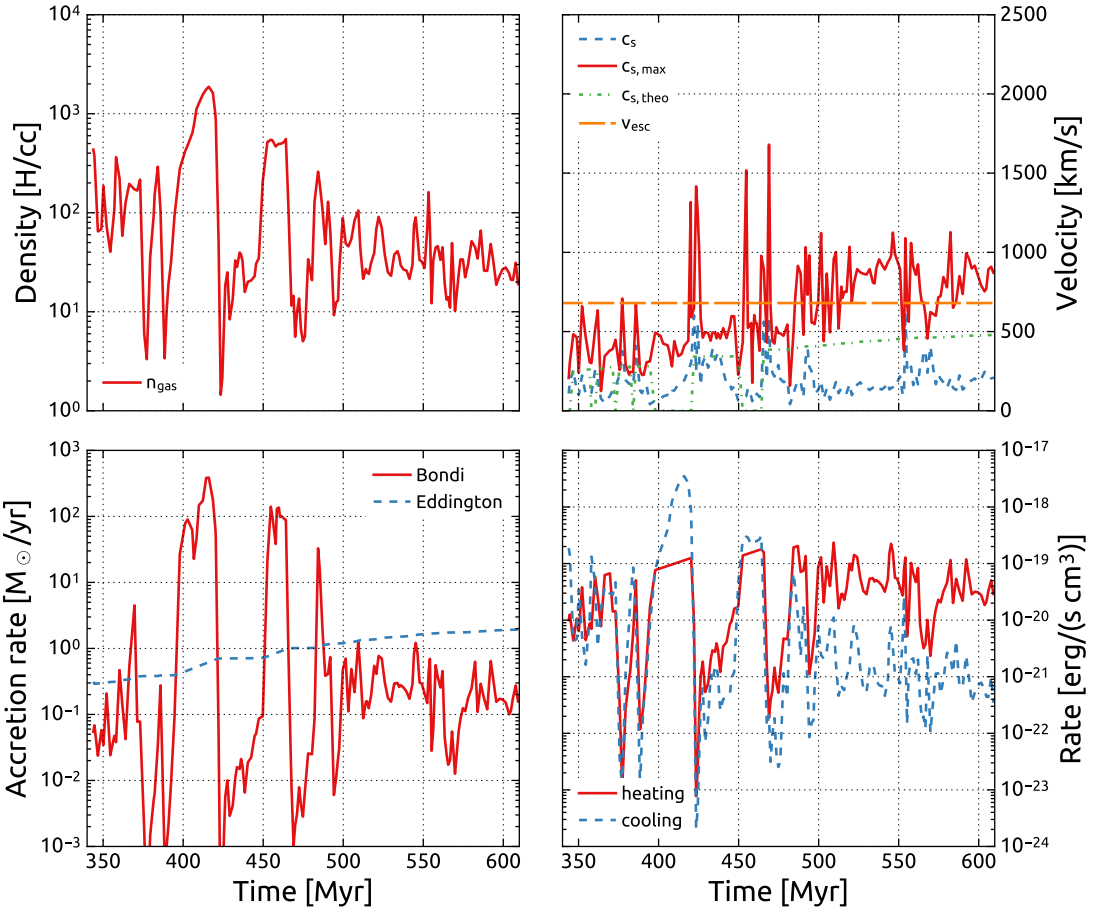

Figure 3.7: Time evolution of 1) average gas density within the sink sphere (*top left*); 2) average, mass-weighted, sound speed (blue, short dashes) and maximum sound speed (red, solid) within the sink sphere (*top right*), we have also represented our simple theoretical model (Eq. 3.32 and 4.6) (green, dot-dashed) compared to the escape velocity from halo's centre (orange, long dashes); 3) Bondi (red, solid) and Eddington (blue, dashed) accretion rates (*bottom left*) and 4) average heating (red, solid) and cooling (blue, dashed) rates within the sink sphere (*bottom right*) for simulation with SN and AGN feedbacks and NSC modelling and $M_{\rm seed} = 10^6$ M$_\odot$.

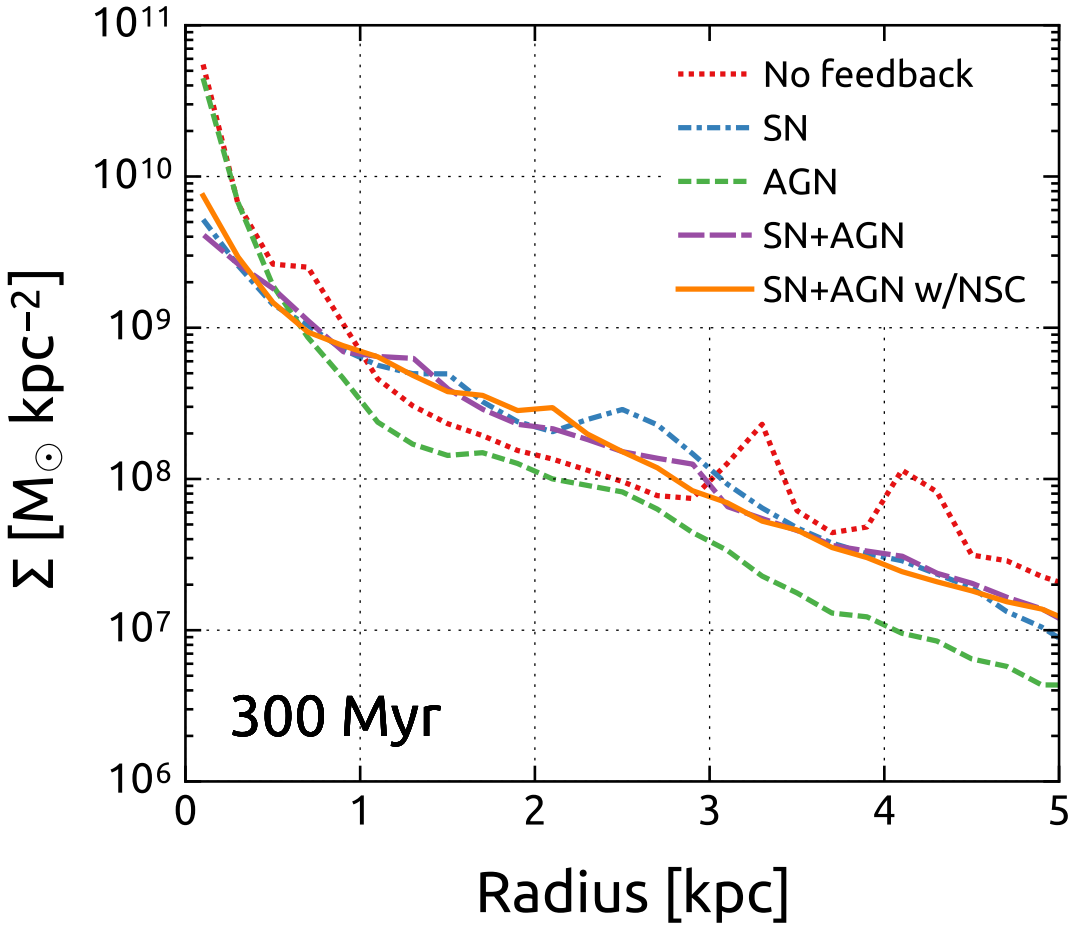

Figure 3.8: Stellar density profile at 300 Myr for five different simulations: no feedback (red), AGN-only (blue), SN-only (green), SN+AGN (purple), and SN+AGN with NSC modelling (orange). All the profiles are centred with a shrinking sphere technique with respect to the total halo mass. Absence of SN feedback leads to creation of steep stellar profile and much more massive stellar bulge than with runs with SN feedback.

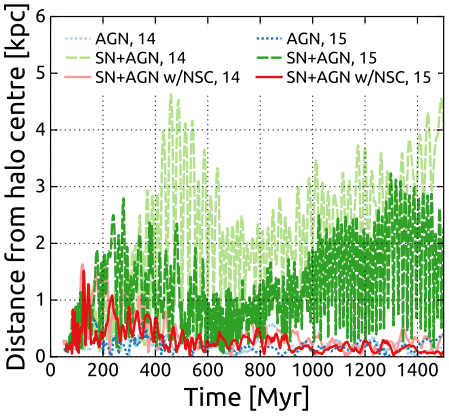

(a) Distance between the sink and the centre of the halo

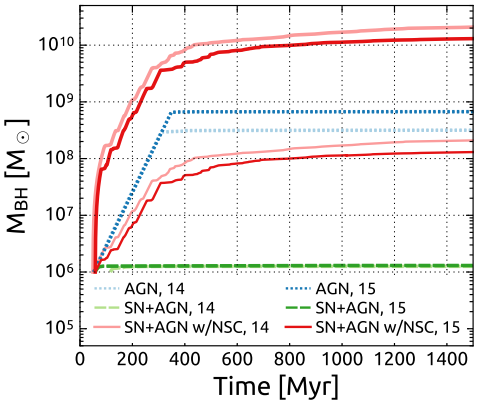

(b) SMBH (thin) and sink (NSC+SMBH; thick) mass growth

Figure 3.9: Distance between halo centre and the SMBH and mass evolution of SMBH for two resolutions (light for $l_{\max} = 14$ and dark for $l_{\max} = 15$) - runs with AGN feedback only (blue, dotted), SN+AGN (green, dashed) and SN+AGN with NSC (red, solid); dashed lines mark SMBH+NSC masses. Accompanying videos can be found at: `https://youtu.be/1ECgXkrGv3U` (AGN), `https://youtu.be/DSeT_5ErJDY` (SN+AGN) and `https://youtu.be/SmMMd040L7s` (SN+AGN w/ NSC).

to the larger Coulomb logarithm due to the higher spatial resolution. Note that in the other two cases (AGN feedback only or NSC) the sink particles always remain in the central kpc (Figure 3.10, right column, at lower resolution), independently on the adopted resolution.

When we finally include our NSC model, with both AGN feedback and SN feedback, the final sink mass appears to depend much less on resolution than the AGN-only case. Because of SN feedback, we have now a succession of intense star forming events, where SN explosions blow the gas out of the sink sphere, hence reducing the gas density and helping AGN heating win over gas cooling, followed by quiescent phases when that gas can fall back again, so that cooling can win over heating, and the SMBH can grow fast (Figure 3.7 for lower resolution run). Overall, the time-averaged density within the sink sphere is controlled (and significantly reduced) by SN feedback. The critical mass set by the balance between cooling and heating is therefore reduced, especially when the gas is completely gone. We can assume we are mostly in the adiabatic regime, and what matters in this regime is the ability of the SMBH to heat the gas at (or above) the escape velocity of the halo. Using Eq. (3.32), we see that the final sink mass should be proportional to the cubic root of the adopted resolution, which is exactly what we observe in Figure 3.9, where the final sink mass in the high resolution run is slightly smaller, but comparable to the final sink mass in the low resolution run.

3.5. Discussion

The evolution of SMBHs has been studied in two different regimes: 1) the merging of binary black holes with sub-AU spatial resolution simulations (Chapon et al., 2013; Fiacconi et al., 2013; Roškar et al., 2015; Souza Lima et al., 2017, to name a few) and 2)

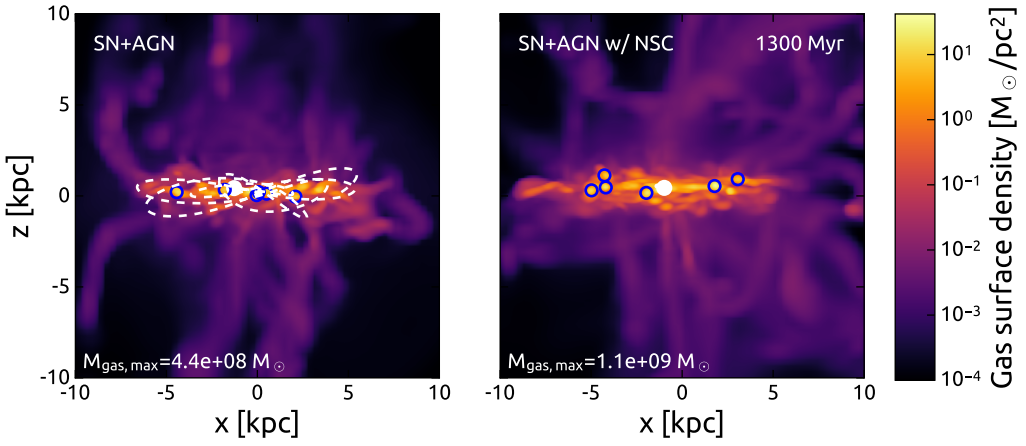

(a) Edge-on volume-weighed projection of gas surface density

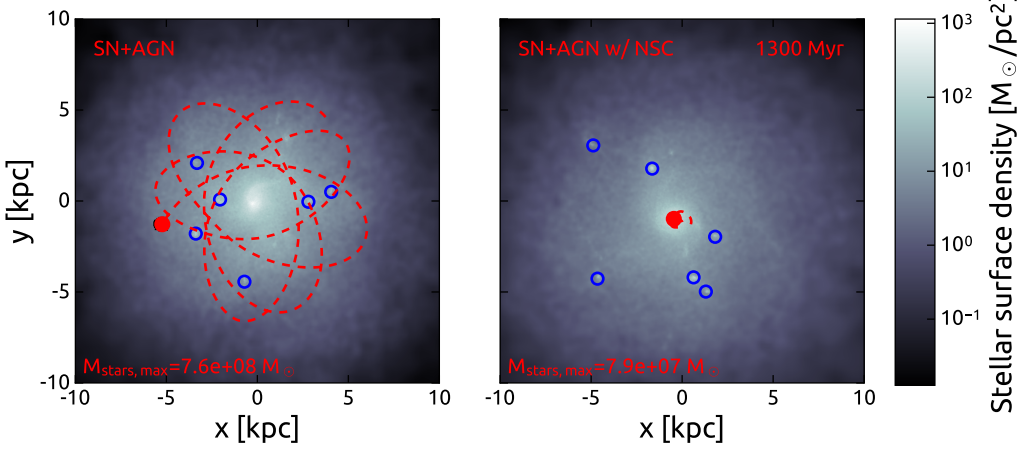

(b) Face-on volume-weighed projection of stellar surface density

Figure 3.10: Volume-weighed projections of gas and stellar surface densities at 1300 Myr for the lower resolution run *without* NSC (left column) and *with* NSC (right column). The position of the sink is marked with a dot, while the dashed line marks past 100 Myr of sink's orbit; $M_{seed} = 10^7$ $M_\odot$ for all runs. Blue circles mark positions of few most massive clumps ($r_{clump} = 320$ pc). (Movies showing dynamical evolution in these two runs can be found at `https://youtu.be/uFcV0u_MFOs` (without NSC) and `https://youtu.be/U0yNnAPTnmA` (with NSC).)

the co-evolution of AGN and their host galaxies in cosmological simulations with spatial resolution of hundreds of parsecs at best (Booth & Schaye, 2009; Kim et al., 2011; Choi et al., 2012; Costa et al., 2014; Dubois et al., 2015; Tremmel et al., 2015). The former is dedicated to the detailed study of the dynamics of binary black holes within a nuclear gas disc at very high spatial resolution, while the latter often discards the dynamical evolution of the SMBHs, as many of the relevant scales are not resolved. In this work, we attempt to bridge the gap between those two different approaches, focusing on the detailed dynamics of the central SMBH while retaining the large scale galactic evolution.

Recent work by Fiacconi et al. (2013); Roškar et al. (2015) and Souza Lima et al. (2017) have showed that binary black holes can be scattered outside of the nuclear disc, if physical processes like SN feedback and gas cooling are present. The former produce outflows, which rarify the medium and thus reduce the effect of dynamical friction, while the latter leads to the formation of gas clumps that can scatter the SMBH out of the disc plane. This is in complete agreement with what we have obtained in this paper on a larger scale and over a longer time scale.

Modelling the precise dynamics of SMBHs in cosmological simulations has not been the priority of galaxy formation simulators in the past decade. There is no consensus on the SMBH formation scenario and on their initial seeding environment. Very often, although AGN feedback is described at length, very little has been said about the possibly complex dynamics of SMBH within their host galaxies (see for example Kim et al., 2011; Choi et al., 2012). Gabor & Bournaud (2013) have reported in their simulations of high-redshift galaxies that the central SMBH is scattered by massive clouds. They decided to add an artificial acceleration towards the centre of mass of the stellar component to maintain the SMBH in the nuclear region (see also Okamoto et al., 2008b). A similar effect has been observed by Bellovary et al. (2010), but they did not correct for it. They obtained many SMBHs with orbits from 10 to 100 kpc from the centre of a halo. They argued that these large, eccentric orbits are physical, as the dynamical friction timescales of the wandering SMBHs are longer than age of the Universe. They also found that low mass seeds grow on average only by 2%.

In Debuhr et al. (2011), the authors used a different methodology by assigning a higher dynamical mass to their SMBH, set to 100 times the black hole mass, justifying it as a way to avoid "Brownian" motion and highly eccentric SMBH orbits. A similar approach was adopted in the simulations of Gabor et al. (2016), but they used a constant dynamical mass of $10^9\,M_\odot$. In Costa et al. (2014), the authors followed the extreme strategy of entirely abandoning the dynamical evolution of the SMBH by keeping it fixed at the centre of the halo. Most recently, Sijacki et al. (2015) and Schaye et al. (2015) opted for repositioning the SMBH to the minimum of the gravitational potential at each time step, following a recipe similar to Springel et al. (2005) and Booth & Schaye (2009). Finally, Tremmel et al. (2015) followed a more physical approach, adding an explicit dynamical friction force to the SMBH acceleration, invoking their limited spatial resolution to correct for the underestimated Coulomb logarithm. All these different authors are trying to address the issue of the dynamics of the SMBH using various strategies, not always physically motivated. In this work, we are attempting to address the same issue, using an additional physically motivated gas drag, or using an observationally motivated solution with the introduction of a companion NSC.

In Sections 3.4.3 and 3.4.5, we have seen that SN feedback can control or prevent the growth of the SMBH, mostly by triggering a complex dynamical evolution of the SMBH.

A similar conclusion has been reached by Dubois et al. (2015), for which SN feedback is responsible for regulating the SMBH growth in high-z halos. In the presence of strong SN feedback, cold gas is removed from the nuclear region. It is only once the bulge mass reaches $10^9 M_\odot$ that the gas flow can stabilise in the centre, so that the SMBH is able to accrete at the Eddington rate. They argue, that this is due a sudden increase of the escape velocity, which exceeds the velocity of SN-powered outflows. A similar argument has been used by Bower et al. (2017). They used a simple analytical model to describe the central SMBH growth in the presence of hot, buoyantly rising, SN-driven outflow, that limit the gas density in the immediate environment of the SMBH. Once the halo mass reaches $10^{12} M_\odot$, the SN bubbles are not buoyant anymore and the gas density can increase, leading to a fast SMBH growth. Both arguments lead to a similar conclusion: in order for the SMBH to grow fast enough, it is required to meet the conditions to form a dense and massive enough central concentration, in the form of a stellar bulge or a dense, gas rich, nuclear region.

In the simulations performed in this paper, we observe a similar effect. The scenarios for which a massive bulge can form, namely without feedback or with only AGN feedback are the only ones leading to a fast growth. Using our efficient SN feedback recipe, we cannot form a large bulge, and our central SMBH does not grow. In our case, however, this is because of its erratic dynamical evolution. We argue in this paper that this is the complex dynamics of the SMBH that can prevent its fast growth, by reducing the Bondi accretion rate due to an increased relative velocity between the sink and the gas. Large, eccentric orbits are unavoidable, due to the combined effects of large mass perturbers and inefficient dynamical friction. In order to stabilise the dynamics of the SMBH in the central kiloparsec, we propose another viable scenario, namely to attach to the SMBH a dense, compact and more massive NSC.

Our NSC hypothesis can be supported by local observations of SMBHs (see e.g. Graham & Spitler (2009) or the excellent review by Kormendy & Ho (2013)). These show that SMBHs coexist with NSCs in the centres of galaxies, regardless of the type of the host (Seth et al., 2008; Graham & Spitler, 2009). This hints towards a scenario in which SMBH coevolves with NSC. The protective environment of NSC is particularly important for the growing SMBH in the presence of massive perturbers in the galaxy. The perturbers can be either giant molecular clouds or stellar clusters. In the sample of Seth et al. (2008) the ratio $M_{\rm SMBH}/M_{\rm NSC}$ is typically between 0.01 and 1, which justifies our simple model for the NSC growth. Graham & Spitler (2009) also lists many galaxies with prominent nuclear component hosting a less massive SMBH.

The nuclear region of the Milky Way (MW) hosts a relatively small SMBH with $M_{\rm SMBH} \simeq 3 \times 10^6$ $M_\odot$, which is comparable to the typical mass of potentially perturbing GMCs, owing to the low gas fraction of the MW. The MW has no massive bulge, but hosts a NSC with mass 3×10^7 $M_\odot$, which can resist external perturbations. The corresponding dynamical friction time scale is quite large, 10 Gyr, but still comparable to the age of the Universe. Similarly, in the Circinus galaxy (Maiolino et al., 1998), a SMBH of mass 1.7×10^6 $M_\odot$ (Gültekin et al., 2009) is believed to sit within a NSC of mass of 10^7 $M_\odot$ and located within the galactic bar, thus being well protected from perturbers.

The Andromeda galaxy, on the other hand, hosts a central SMBH with mass of the order of 10^8 $M_\odot$, which is about two orders of magnitude larger than the typical GMC mass in this galaxy (Blitz et al., 2007; Rosolowsky, 2007). So the Andromeda SMBH can resist alone external perturbations, and benefits from a relatively short, 3 Gyr, dynamical

friction time scale. Interestingly, the NSC in the Andromeda galaxy is four times less massive that its SMBH (Kormendy & Ho, 2013).

More massive galaxies ($M_{\rm halo} \geqslant 10^{12}$ M$_\odot$) are usually bugle-dominated or elliptical galaxies, and typically contain very massive SMBH with no sign of a companion NSC (Graham & Spitler, 2009).

Smaller mass galaxies usually show SMBHs hosted by more massive NSC (Graham & Spitler, 2009). For example, NGC 4395 is a small mass galaxy with $V_{\rm max} \simeq 90$ km/s and total stellar mass within the galactic disc $M_{\rm tot} \simeq 10^9$ M$_\odot$. Mass estimates for dwarf galaxies are challenging, thus value of $M_{\rm tot}$ quoted here for NGC4395 is at most factor of two larger (assuming $f_{\rm gas} = 0.5$), which would support our argument even more. A NSC of mass 1.4×10^6 M$_\odot$ hosts one of the smallest mass SMBH (an Intermediate Mass Black Hole or IMBH) ever detected with $M_{\rm SMBH} = 3.2 \times 10^5$ M$_\odot$ (Seth et al., 2008; Graham & Spitler, 2009; den Brok et al., 2015). These numbers are consistent with our scenario of SMBH and NSC co-evolution. A similar galaxy, POX 52, contains a SMBH with mass also close to with 10^5 M$_\odot$ (Barth et al., 2004; Thornton et al., 2008) and some indications of a companion NSC, although the evidence is not as clear as for the previous case (Thornton et al., 2008).

The situation is somewhat more complicated at higher redshift ($z \simeq 2$), at the peak of star formation, when galaxies are gas rich and fragmented into massive clumps (see e.g. Elmegreen et al., 2008a,b, for discussion on importance of massive gas clumps for bulge and SMBH formation). There is no observational evidence that SMBHs are not hosted by giant NSCs in the early Universe, but see Schawinski et al. (2011) for a peculiar triple AGN galaxy.

Another argument in favour of our scenario is related to possible theories for the formation of NSC and SMBH/IMBH. For the former, our simulations are consistent with the *in situ* formation scenario of Milosavljević (2004), for which NSC form from collapsed gas in the nuclear region. For the latter, we invoke one possible scenario of IMBH formation based on runaway collisions of stars in a dense star cluster (Kochanek et al., 1987; Portegies Zwart et al., 1999; Davies et al., 2011; Stone et al., 2017), the star cluster being in our case the recently formed NSC. If the formation of both NSC and SMBH are related, then this could further support the idea of their subsequent co-evolution. Gnedin et al. (2014) discuss in details this idea of co-formation of NSCs and SMBHs. One serious caveat in this picture is that we do not observe any NSC associated to more massive SMBH in elliptical galaxies. This could be explained by the SMBH becoming massive enough to disperse the stars and evaporate the NSC (e.g. Merritt, 2009).

3.6. Summary and conclusions

In this work, we have presented and tested a new algorithm for SMBH modelling in the Ramses code. This method was designed on top of the previous work of Bleuler et al. (2015) in the context of star formation in molecular clouds. The new, upgraded sink particle algorithm is used here for the first time in the context of SMBH accretion and dynamical evolution, in conjunction with an AGN feedback model. We form SMBH seeds in massive gaseous clumps detected using the new clump finder phew (Bleuler et al., 2015). The SMBH growth is modelled via Eddington-limited Bondi accretion. Its dynamical evolution is treated carefully with a direct N-body integrator and including optionally a drag force due to exchange of momentum with the gas.

We have tested our new model within high-resolution simulations of an isolated, gas-rich cooling halo, whose properties appears very similar to high-z clumpy galaxies. We have explored the effects of our new AGN feedback model on the growth and the orbital evolution of our central SMBH, in conjunction (or in competition) with an efficient model for SN feedback.

In a control simulation without any feedback, we have shown that our sink particle remains trapped within a dense central bulge and accretes gas at the Eddington rate, provided that the seed mass is larger than the minimum Jeans mass set by the mass resolution of our simulation. The final SMBH mass is regulated by gas accretion into the nuclear region, or in other words by starvation of the SMBH.

In the presence of AGN feedback only, we observe also the formation of a massive bulge and the SMBH grows quickly until it reaches a final mass self-regulated by AGN feedback. We have developed a simple analytical model to support our findings and we argue that in absence of SN feedback, the final SMBH mass is equal to a critical mass for which AGN heating balances gas cooling within the vicinity of the SMBH. When this happens, the SMBH can clear out the gas from the nuclear region and stops growing.

In the presence of our efficient SN feedback model, we prevent the galaxy from forming a stellar bulge. As a consequence, the central SMBH is easily perturbed by massive gas clumps and quickly leave the nuclear region on highly eccentric orbits. Due to a large relative velocity between the sink and the gas, its accretion rate drops and the SMBH stops growing. Only models with a high enough seed mass can grow fast enough to sustain external perturbation and maintain the SMBH in the centre.

Finally, using both feedback models together, we have shown that the central SMBH cannot grow at all, because of SN feedback for small seed mass, and because of AGN feedback for large seed mass.

To overcome this apparent dead end in the SMBH evolution in high-z, gas rich galaxies, and inspired by local observation of nuclear regions in nearby galaxies, we propose a new model in which SMBH are seeded and coevolve with a NSC. We have implemented a very simple model for the joint SMBH/NSC system, in which the NSC is allowed to grow fast enough to resist external perturbations and to provide a short dynamical friction time scale, so that the sink particle can accrete mass efficiently and remain within the nuclear region. Interestingly, in this scenario, SN feedback is controlling the gas supply in the vicinity of the SMBH and the balance between gas cooling and AGN heating. As a consequence, using our same analytical model, we show that the final SMBH mass is not determined by the balance between AGN heating and gas cooling anymore, but instead by the balance between AGN heating and gravity, namely by comparing the gas sound speed to the halo escape velocity.

In conclusion, we argue, using dynamical arguments, that the SMBH must remain in the nuclear region of the galaxy in order to grow fast enough. This is possible only if the galaxy can grow a massive bulge or a dense NSC. We have shown that the latter scenario might be plausible, although our NSC formation and growth model could be improved significantly.

4

The combined effect of AGN and supernovae feedback

Wisdom comes from experience. Experience is often a result of lack of wisdom
– Terry Pratchett

In this chapter[1], we study the effects of our new model of SMBH introduced in the previous chapter in massive, gas-rich galaxies with several simulations of different feedback recipes with the hydrodynamics code Ramses. These simulations are compared to a reference simulation without any feedback, in which the cooling halo gas is quickly consumed in a burst of star formation. In the presence of strong supernovae (SN) feedback, we observe the formation of a galactic fountain that regulates star formation over a longer period, but without halting it. If only AGN feedback is considered, as soon as the SMBH reaches a critical mass, strong outflows of hot gas are launched and prevent the cooling halo gas from reaching the disc, thus efficiently halting star formation, leading to the so-called "quenching". If both feedback mechanisms act in tandem, we observe a non-linear coupling, in the sense that the dense gas in the supernovae-powered galactic fountain is propelled by the hot outflow powered by the AGN at much larger radii than without AGN. We argue that these particular outflows are able to unbind dense gas from the galactic halo, thanks to the combined effect of SN and AGN feedback. We speculate that this mechanism occurs at the end of the fast growing phase of SMBH, and is at the origin of the dense molecular outflows observed in many massive high-redshift galaxies.

[1]The work presented in this chapter has been published in the Monthly Notices of the Royal Astronomical Society, Volume 475, Issue 4 under the title 'The combined effect of AGN and supernovae feedback in launching massive molecular outflows in high-redshift galaxies', following peer-review (**Biernacki** and Teyssier, 2018).

4.1. Introduction

A successful model of galaxy formation must reproduce both the observed stellar masses and spatial distributions. Current star formation recipe and their associated feedback mechanisms appear to be able to regulate the stellar content in small mass halos ($M_{\rm halo} < 5 \times 10^{11}\,{\rm M}_{\odot}$), but less so in the most massive galaxies (Shankar et al., 2006; Davé et al., 2011; Moster et al., 2013; Behroozi et al., 2013). Supermassive black holes (SMBHs) are good candidates to quench star formation in early-type galaxies (Nandra et al., 2007; Schawinski et al., 2007; Fabian, 2012; Yesuf et al., 2014; Cheung et al., 2016), as the energy released by active galactic nuclei (AGN) could be large enough to unbind significant amounts of star-forming gas.

SMBHs are ubiquitous elements of galactic environments at all redshifts (see e.g. the review by Cattaneo et al., 2009) – starting with the Milky Way (Schödel et al., 2002; Gillessen et al., 2009), to galaxy groups and clusters (e.g. Magorrian et al., 1998), up to luminous $z > 6$ quasars (Fan et al., 2003). The scaling relations between SMBH mass and its host properties, like the bulge mass or the central velocity dispersion (Ferrarese & Merritt, 2000; Laor, 2001; Häring & Rix, 2004; Tremaine et al., 2002; Gültekin et al., 2009; Kormendy & Ho, 2013), indicate a strong connection between the SMBH and its host, sometimes referred to as "coevolution".

AGN feedback is especially important for groups and clusters of galaxies. Even if some properties of the intragroup medium can be explained by SN feedback alone, a powerful central source is necessary to really quench SF (see e.g. recent work by Liang et al., 2016). Similar effects are seen in most massive clusters of galaxies where presence of AGN feedback is required to match observations (e.g. Puchwein et al., 2008; Teyssier et al., 2011; Martizzi et al., 2013; Le Brun et al., 2014; Planelles et al., 2014; Rasia et al., 2015; Schaye et al., 2015; Hahn et al., 2017).

Efficient SF requires a large reservoir of cold and dense gas. In order to suppress SF in large galaxies, we must reduce this reservoir dramatically. This can happen through two different channels.

First, we can expel this reservoir of dense molecular gas out of the galactic disc. This is what happens in low mass galaxies, where SN feedback leads to the production of a galactic fountain (e.g. Davé et al., 2011) and, in case of dwarf galaxies, to a strong outflow completely removing the gas (see e.g. Dekel & Silk, 1986). In massive haloes, however, the escape velocity is too high for SN feedback to play a significant role (Davé et al., 2011; Zhang & Thompson, 2012), while AGN feedback is believed to take over. However, a single, centrally located source cannot influence SF in the entire galactic disc, like SN feedback does. Indeed, as demonstrated by Roos et al. (2015), the *expulsive* feedback from the AGN has no effect on the instantaneous star formation rate (SFR) or star formation efficiency (SFE) in the galaxy, but could lead to a secular effect by reducing slowly its gas content.

Second, quenching of star formation can be the result of cutting external gas supplies, so that the existing dense gas reservoir is consumed by the local SF and not replenished. In other words, if gas outside the disc gets expelled from the halo or stopped from being accreted, then it cannot contribute to star formation. This *preventive* feedback has been identified in two viable mechanisms for AGN feedback in massive halos: 1) the so-called quasar mode, for which giant outflows halt the global inflow from filamentary accretion, and 2) the so-called radio mode, for which narrow radio-loud jets maintain the halo gas in hydrostatic equilibrium by balancing cooling (Brüggen & Kaiser, 2002; Pizzolato &

Soker, 2005; Sijacki et al., 2007; Ciotti et al., 2010; Gaspari et al., 2013; Choi et al., 2015; Li et al., 2015; Hopkins et al., 2016)

Regarding the physics of outflows, observations reveal a very rich and complex picture. Hot and diffuse outflows have been seen in ultra-luminous infrared galaxies (ULIRGS; Sturm et al., 2011; Veilleux et al., 2013; Spoon et al., 2013), while high-z observations of massive QSOs (e.g. Cicone et al., 2014) display outflows consisting of cold, molecular gas moving with high-velocities. As shown recently by Costa et al. (2015), at $z > 6$ molecular outflows can be explained by hot, AGN-driven gas which cools due to mixing with metal-enriched SN-powered gas and possibly an interaction with cold streams.

Recently, Chapman et al. (submitted) reported a molecular outflow with several 10^{10} $M_\odot$ of gas moving with velocities reaching $1500\,\mathrm{km\,s^{-1}}$ at $z = 2.85$. These extreme outflows pose a severe challenge for galaxy formation models. Because they cannot be driven by stellar winds or SN explosions due to their low energetics, AGN feedback appears as a natural explanation (Anglés-Alcázar et al., 2014; Choi et al., 2015). Indeed, hot, low-density outflows associated with Broad Absorption Lines seen in connection to AGN activity, possibly driven by radiation pressure on dust grains, can reach outflow velocities up to 30'000 km/s (Scoville & Norman, 1995; Thompson et al., 2015), thus providing the necessary kinetic energy to unbind the galactic gas.

Understanding these two very different mechanisms (hot versus cold outflows) and their possible interplay is still a matter of active research. Isolated AGN feedback does not produce gas outflow morphologies as seen in observations, while SN feedback can produce cold, dense outflows, but they remain bound to the disc. Some models have been proposed featuring a competition between these two processes. Dubois et al. (2015) showed that SMBHs cannot grow significantly in the presence of fervent SF and efficient SN feedback, which is the case at the peak of SF around $z = 2 - 3$, and that fast SMBH growth is allowed only when there is a large enough galactic bulge. In Chapter 2, we have also shown that, if the SMBH is hosted by a nuclear star cluster (NSC), it can grow efficiently, creating the conditions for a possible cooperation between AGN feedback in the nuclear region and SN feedback in the extended disc.

In this work, we report on the effects of AGN feedback on regulating SF in the galactic environment and launching strong gas outflows within the halo. We study specifically the case of gas-rich, massive, high-z galaxies, progenitors of the massive ellipticals we see today at the heart of groups and clusters. Our setup, due to our rather high numerical resolution, allows us to explore the interplay between the SMBH and the interstellar medium (ISM), as well as the effect of AGN feedback on the galactic corona. In Chapter 2, we have presented an improved sink particle implementation for SMBH formation and evolution. This new model is used here to study the effect of the SMBH to the host galaxy and halo. In Section 4.2, we briefly summarise the details of our model and present the numerical setup. In Section 4.3, we discuss the evolution of the SF and its quenching by AGN feedback, demonstrating that it acts as a *preventive* mechanism, while in Section 4.4, we focus on the properties of the gas outflows, focusing on their velocities. Section 4.5 is devoted to the analysis of gas morphologies in our simulations. In Section 4.6 we are discussing our results in the context of current observations of molecular outflows and how they can be applied to large-scale cosmological simulations. We summarise our findings in Section 4.7.

4.2. Numerical setup

The simulations discussed in this paper have been already presented in detail in Chapter 2. We only recall the aspects of our numerical setup that are particularly relevant to this study.

We have run our simulations with the adaptive mesh refinement (AMR) code Ramses (Teyssier, 2002). Gas hydrodynamics is based on solving the Euler equations with a second-order, unspilt Godunov scheme. Stars and dark matter are modelled using collisionless particles, that are evolved with an adaptive Particle-Mesh N-body solver.

Our initial conditions are designed to mimic a typical high redshift galaxy. We start with an isolated, gas-rich, slowly rotating dark matter halo of mass 2×10^{12} $M_\odot$, with a spin parameter of 0.04. We sampled it with one million dark matter particles. The halo profile follows a truncated NFW profile with a concentration parameter $c = 10$. Gas in the halo is initially in hydrostatic equilibrium and follows the same NFW profile. The parameters of our halo are the followings: the circular velocity is $V_{200} = 160\,\mathrm{km\,s^{-1}}$, the viral radius of $R_{200} = 230\,\mathrm{kpc}$, and the halo truncation radius at 514 kpc. This particular Ramses setup was introduced first in Teyssier et al. (2013).

In our simulations, gas cooling for gas hotter than 10^4 K follows the cooling function of Sutherland & Dopita (1993), which accounts for radiative cooling of H, He, as well as a standard mixture of metal. For lower temperatures, we consider only fine-structure metal cooling following the cooling function of Rosen & Bregman (1995). The evolution of metallicity is modelled using a passive scalar, which is advected with the flow. We adopted an initial metallicity $Z_{\mathrm{ini}} = 0.05$ $Z_\odot$, where the solar metallicity was set to a metal mass fraction of $Z_\odot = 0.02$.

In order to minimise numerical problems due to our limited spatial resolution of $\Delta x_{\mathrm{min}} = 78\,\mathrm{pc}$, we use a temperature floor

$$T_{\mathrm{floor}} = T_* \left(\frac{n_{\mathrm{H}}}{n_*} \right)^{\Gamma - 1} \tag{4.1}$$

with a critical gas number density $n_* = 9\,\mathrm{cm^{-3}}$, a critical temperature $T_* = 2 \times 10^3$ K, and $\Gamma = 2$. Our star formation prescription follows the method of (Rasera & Teyssier, 2006), which stochastically spawns stellar particles from a Poisson distribution using a Schmidt law if the gas density in the cell exceeds $n_* = 9\,\mathrm{H/cm^3}$. The efficiency with which stars are formed is set to be $\epsilon_* = 0.01$, based on values measured in local molecular clouds (Krumholz & Tan, 2007). We model supernovae explosions assuming that only 10% of the stellar mass goes supernovae and that a single supernova injects 10^{51} ergs. Furthermore, we assume that each 10 $M_\odot$ of ejecta contains 1 $M_\odot$ of metals. We boost the efficiency of our SN explosions by grouping stars stochastically in clusters of mass 10^8 $M_\odot$. In order to overcome the overcooling problem of supernovae feedback due to our limited resolution, we use a non-thermal energy variable that dissipates over a 10 Myr timescale (see Teyssier et al., 2013, for details).

Supermasive black holes (SMBHs) are modelled with our new sink particle algorithm (Bate et al., 1995; Krumholz et al., 2004; Bleuler & Teyssier, 2014; Biernacki et al., 2017). We allow for only one sink to form in our simulations. The sink formation site is identified on the fly with the clump finder phew (Bleuler et al., 2015) as the first massive enough gas clump. This is usually, but not always, at the centre of the galaxy. The adopted initial SMBH mass (the seed mass) is a free parameter in our simulations and spans the range

10^5 $M_\odot$ to $10^8\,M_\odot$. SMBH accretes according to the Bondi-Hoyle-Lyttleton (Hoyle & Lyttleton, 1939; Bondi & Hoyle, 1944; Bondi, 1952, or Bondi for short) accretion

$$\dot{M}_{\rm Bondi} = \frac{4\pi\rho_\infty G^2 M_{\rm SMBH}^2}{\left(c_{\rm s}^2/\beta_{\rm boost} + v_{\rm rel}^2\right)^{3/2}} \tag{4.2}$$

where G is the gravitational constant, ρ_∞ is the density at infinity in the classical Bondi accretion solution (for more details see Krumholz et al., 2004), $M_{\rm sink}$ is the mass of the SMBH. We boost the accretion rate by reducing the average sound speed $c_{\rm s}$ in the sink's vicinity with $\beta_{\rm boost}$ (as in Booth & Schaye, 2009). If we set the relative velocity $v_{\rm rel} = 0$, then we recover exactly the solution originally proposed by Booth & Schaye (2009).

The dynamical evolution of the sink particle is modelled using a direct summation method for the gravity between the sink and the matter. It is more accurate than the Particle Mesh method in case of very massive SMBHs dominating the local gravitational potential. Furthermore, we include an additional drag force due to accretion, which leads to additional momentum exchange between the sink and the surrounding gas. This is performed by requiring that 1) the centre of mass of the sink-gas system remains fixed during the accretion and 2) the total linear momentum is conserved.

In a subset of our simulations, we also include a simple model of coevolution of the SMBH and a host nuclear star cluster (NSC). Here, the sink particle mass is the sum of the two components $M_{\rm sink} = M_{\rm SMBH} + M_{\rm NSC}$ and is the mass used in all the gravity calculations. SMBH grows with the Eddington-limited Bondi rate (Eq. (4.2)), while for the growth of NSC, we used a simple model for which $\dot{M}_{\rm acc,NSC} = 100\dot{M}_{\rm acc,SMBH}$. As shown in Biernacki et al. (2017), this prescription allows us to solve the problem of wandering SMBHs by locking them within a central massive stellar component - either a NSC (as hinted by observations of e.g. Seth et al., 2008) or a bulge (e.g. Silk & Rees, 1998; Magorrian et al., 1998).

Finally, feedback from the AGN is modelled with a simple thermal energy injection in the vicinity of the sink, within the radius of $R_{\rm sink} = 4\Delta x_{\rm min}$ from the sink position, where $\Delta x_{\rm min}$ is the size of the smallest resolution element. The luminosity of the AGN is calculated as

$$L_{\rm AGN} = \epsilon_{\rm c}\dot{M}_{\rm acc}\epsilon_{\rm r}c^2, \tag{4.3}$$

with $\epsilon_{\rm r} = 0.1$ being the accretion disc radiative efficiency (in the so-called quasar mode; Shakura & Sunyaev, 1973) and $\epsilon_{\rm c} = 0.15$ representing the hydrodynamic coupling efficiency, which was calibrated in previous works done with the Ramses code (Teyssier et al., 2011; Dubois et al., 2012; Gabor & Bournaud, 2013). In Table 4.1 we summarise all simulation parameters used in this work, including a reference to the section in which they are first discussed.

4.3. Mass accretion and star formation

In this Section, we discuss the results of our simulations in term of SFR and how it can be impacted by AGN feedback. In Figure 4.1, we show the gas surface density of the disc in an edge-on projection for four of our simulations: no feedback, AGN feedback-only, SN feedback-only, and SN+AGN feedback (from top to bottom) at three different times 300, 750 and 1300 Myr (from left to right). We choose these particular times during different important epochs - the earliest time corresponds to the epoch when SF is at its highest,

Table 4.1: Summary of simulations discussed in this work. Columns: (1) subsection in which the simulations are first analysed; (2) SN feedback modelling (yes/no); (3) SMBH seed mass, if present; (4) final stellar mass of the galaxy (i.e. after 1.5 Gyr).

Section (1)	SN feedback (2)	$m_{\rm seed}$ [$M_\odot$] (3)	M_* [$10^{10}\,M_\odot$] (4)
4.3.1	no	–	8.5
		10^5	8.5
		10^6	5.5
		10^7	4.7
		10^8	4.1
4.3.2	yes	–	7.4
		10^5	7.5
		10^6	4.9
		10^7	4.6
		10^8	3.9

while the SMBH is still growing and did not impact the host galaxy, the intermediate time corresponds to the epoch of AGN outflow launching, while the latest snapshot shows the final state of the galaxy.

4.3.1. Simulations without supernova feedback

In order to quantify the impact of AGN feedback on the star formation history, we always compare to a reference model in which both AGN and SN feedbacks are not modelled – the 'no feedback' simulation (Figure 4.1, first row). It can be seen that the extended initial gaseous halo has settled into a centrifugally supported disc. This large reservoir of gas is slowly consumed by star formation. In Figure 4.2a we plot this reference star formation history with a black dotted line. The peak of star formation happens roughly 300 Myr after the beginning of the simulation and then decays exponentially. This is because fresh gas infall from the outer halo is also slowly decaying; the gas has to be brought to the disc from increasingly larger radii. In Figure 4.3a, we show the mass accretion rate, measured using 1-kpc-thick shells placed at 20 and 50 kpc from the centre of the halo (top and bottom left, respectively; black dotted line). Clearly, the SFR correlates well with the inflow of the gas from the extended halo. At later times, the SFR reaches its lowest value around 30 to 40 $M_\odot$/yr, which is precisely the residual mass accretion rate from the halo we measure at 20 kpc. The characteristic mass accretion profile is related to the shape of the NFW profile we have adopted for our initial conditions. The sharp fall off after 800 Myr (at 50 kpc) is related to the truncation radius of our halo.

The second row of Figure 4.1 presents the side-on gas surface density for one of our simulations with AGN feedback. One can see that the gas distrbution is very similar to the 'no feedback' simulation, with however significantly less gas in the halo. In Figure 4.2a, we plot the SFR for our simulations with AGN feedback, in which we varied the initial seed mass. In Chapter 2, we showed, that the time it takes for the SMBH to reach its self-regulated, final mass is directly related to its seed mass. We see then that quenching of star formation occurs precisely when the SMBH reaches its maximum mass. Initially,

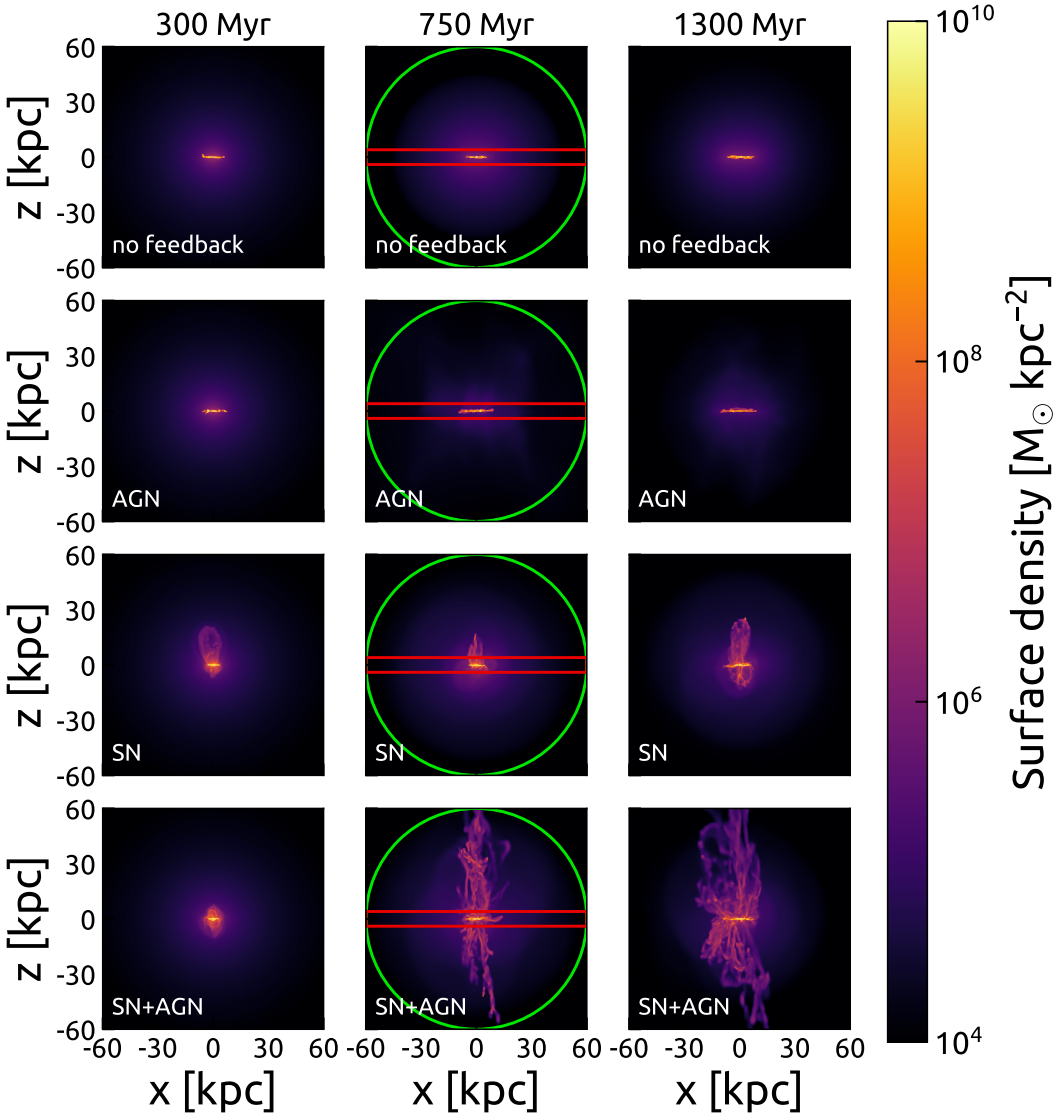

Figure 4.1: Gas surface density for four feedback models (top to bottom: no feedback, AGN, SN, SN+AGN) at three different times (300, 750 and 1300 Myr; left to right). In all cases galaxy is shown edge-on. $M_{\mathrm{seed}} = 10^6$ M$_\odot$ in simulations with AGN feedback modelled. Green circles mark gas selected on Figure 4.5, while the gas from red rectangle has be excluded from the analysis.

the SFR is only slightly reduced due to gas being consumed by the SMBH in its vicinity. Once the SMBH reaches it self-regulated mass – for which it is able to deposit enough energy to overcome cooling – AGN feedback drives powerful outflows. Those halt the infall of fresh gas from the halo, effectively leading to the starvation of the disc - the halo gas is prevented from replenishing it with star-forming gas. This naturally occurs earlier for larger SMBH initial seed masses. As an effect of this quenching, SFR settles in a very inefficient state, around $\sim 10\,M_\odot$/yr, which is a factor of four less compared to simulation without AGN feedback (black dotted line on Figure 4.2a). Traditionally, quenching refers to a state where almost no new stars are formed and the galaxy slowly turns 'red'. This is not what we obtain here, but the total stellar mass is significantly reduced compared to run without AGN (or equivalently with a small seed mass) – see Table 4.1. In the simulation with the smallest seed mass, $10^5\,M_\odot$, the SMBH is unable to grow and do any significant damage to the gas inflow.

A comparison of the various mass accretion rates (Figure 4.3a), measured at 20 and 50 kpc, reveals that AGN feedback does indeed reduce significantly the gas inflow rate, especially immediately after the first outflow is launch. At later times, the inflow rates (especially when measured at 50 kpc) increase again due to transverse flows parallel to the disc plane, bringing in the gas from outer regions. Even at late time, though, re-accreted gas cannot reach the inner disc in large quantities, demonstrating that AGN is able to maintain this quiescent state for a long time. This phenomenon will be discussed in more detail in Section 4.4.

4.3.2. Simulations with supernova feedback – SN+AGN cooperation

A very different picture emerges from simulations with SN feedback. We observe the onset of a galactic fountain. Gas inflow from the halo triggers star formation, which is then regulated by powerful gas outflows launched by SN explosions. These do not only remove gas, but also locally reduce the inflow from the galactic halo. This in turn leads to a reduction of the star formation and a new cycle begins. The resulting SFR is shown in Figure 4.2b as a black dotted line. We see more scatter due to these repeated star bursts. Furthermore, looking at the long term evolution, we see that the peak of the SFH is lower than simulations without SN feedback and more extended.

The global star formation rate has only been slightly reduced. In the simulations without any feedback stellar mass at the end of the runtime is $M_* = 8.5 \times 10^{10}\,M_\odot$, while in the run with SN feedback this is reduced by about 10-15% to $M_* = 7.4 \times 10^{10}\,M_\odot$ (see Table 4.1). This extended, gas-rich galactic fountain (see third row on Figure 4.1), leads to a mere redistribution of gas (and its associated star formation) to larger galactic radii (see the recent work of Sokołowska et al., 2016).

In simulations with efficient SN feedback, gas accretion onto the SMBH (and thus AGN feedback) is regulated by SN feedback; here the final self-regulated mass of the SMBH depends mostly on the halo escape velocity see Chapter 2 for the discusion. Interestingly, the final SFR is largely independent of the SMBH seed mass. The dependence of quenching on SMBH self-regulation we see in the AGN-only runs largely disappears here. The resulting SFR settles at $\sim 20\ M_\odot$/yr, thus being reduced by only a factor of two compared to the SN-only run (but still a factor of two higher than our AGN-only simulations).

The main effect of SN feedback is to inject metals which enhance the cooling of gas. As a consequence, the gas in the SN-driven galactic fountain mix with the halo gas and

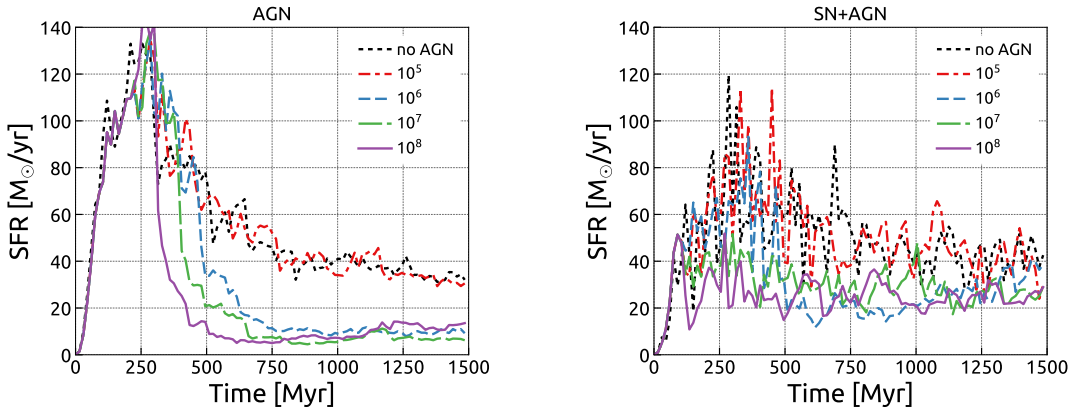

(a) AGN (b) SN+AGN

Figure 4.2: Star formation rate (averaged over period of 15 Myr for clarity) in two sets of simulations - with AGN feedback only (left) and with both SN and AGN feedbacks (right) - for four different seed masses: 10^5 $M_\odot$ - red (dash-dotted), 10^6 $M_\odot$ - blue (short dashes), 10^7 $M_\odot$ - green (long dashes), 10^8 $M_\odot$ - purple (solid). Black dotted lines mark runs without AGN feedback.

increase by a factor of two the mass inflow rate measured close to the disc (Figure 4.3b, top panel), reducing the effect of AGN feedback on reducing the accretion of gas from the outer halo (perhaps with an exception of the most massive seed - bottom panel on Figure 4.3b).

4.4. Outflow properties

In this section, we carefully examine the properties of our AGN-driven outflows, comparing simulations without and with SN feedback. On Figure 4.4 we present a cartoon sketch explaining the various modes of feedback and how they affect the properties of the outflowing gas (see also Figure 4.1). In simulations without SN feedback, the central AGN powers a strong outflow with hot and diffuse gas, while in simulations with SN feedback, the AGN-driven outflow interacts with a clumpy galactic fountain, so that cold and dense clumps are now entrained in the outflow and ejected outside the galactic corona.

4.4.1. Outflow phase space diagram

In order to characterise the physical properties of the gas in the outflow, we restrict ourselves to a sphere of radius 60 kpc (corresponding to the green region in Figure 4.1), excluding a disc of ±4 kpc from the disc plane (corresponding to the red region in Figure 4.1). We compute the mass fraction as a function of density and radial velocity, as well as the mass fraction as a function of density and temperature (which we discuss is more details in Subsection 4.5.1), at 750 Myr (see Figure 4.5). A positive radial velocity v_r corresponds to *outflowing* gas, while a negative value stands for *inflowing* gas.

The simulation with only AGN feedback (left column of Figure 4.5) shows gas velocities up to 1400 km s^{-1}. This velocity cannot be explained by buoyantly rising, AGN-driven bubbles, as the typical gas velocity in such a case would be of the order of the escape

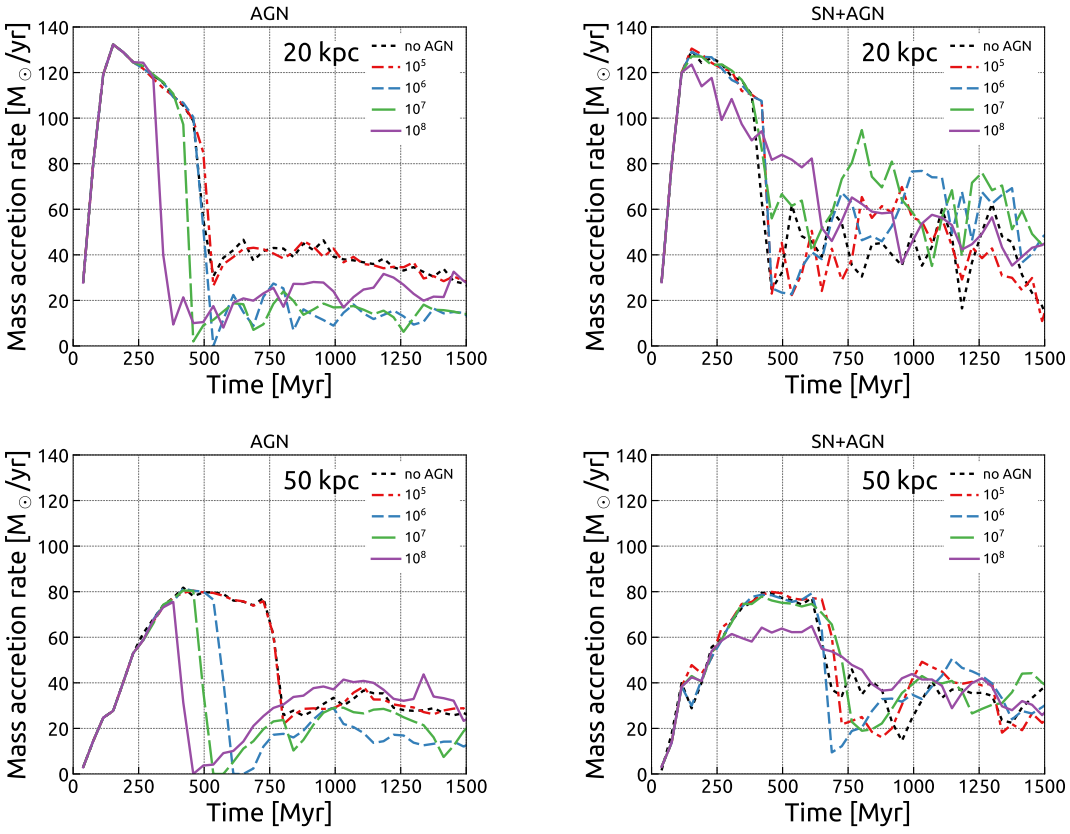

(a) AGN (b) SN+AGN

Figure 4.3: Mass accretion rate in two sets of simulations - with AGN feedback only (left) and with both SN and AGN feedbacks (right) - for four different seed masses: 10^5 $M_\odot$ - red (dash-dotted), 10^6 $M_\odot$ - blue (short dashes), 10^7 $M_\odot$ - green (long dashes), and 10^8 $M_\odot$ - purple (solid); contrasted with runs without AGN feedback (black, dotted)). Left column: AGN only, right column: SN+AGN; top row: outflow measured through shell placed at 20 kpc from halo centre, bottom row: at 50 kpc.

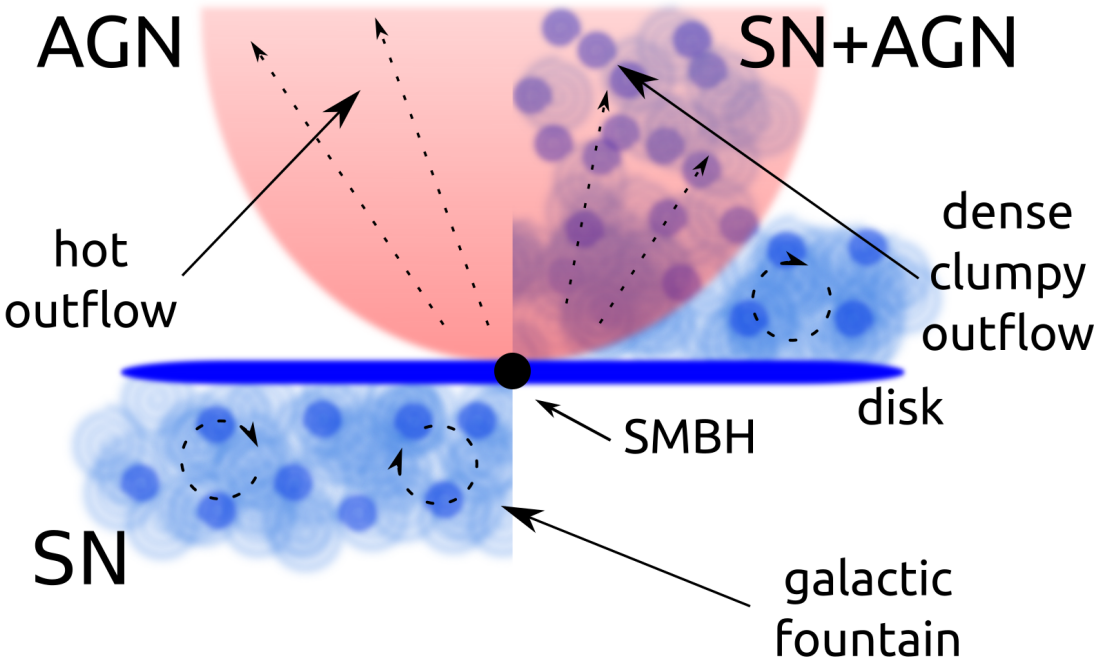

Figure 4.4: Sketch showing different feedback modes and their impact on gas circulation. Top left: in AGN-only SMBH launches hot, diffuse outflow (pink shade); bottom left: in SN-only dense, clumpy gas forms galactic fountain in which gas is being recycled; top right: combination of to previous effects (SN+AGN) leads to dense, fast clumpy outflows which are entrained in hot outflow and escape the disc.

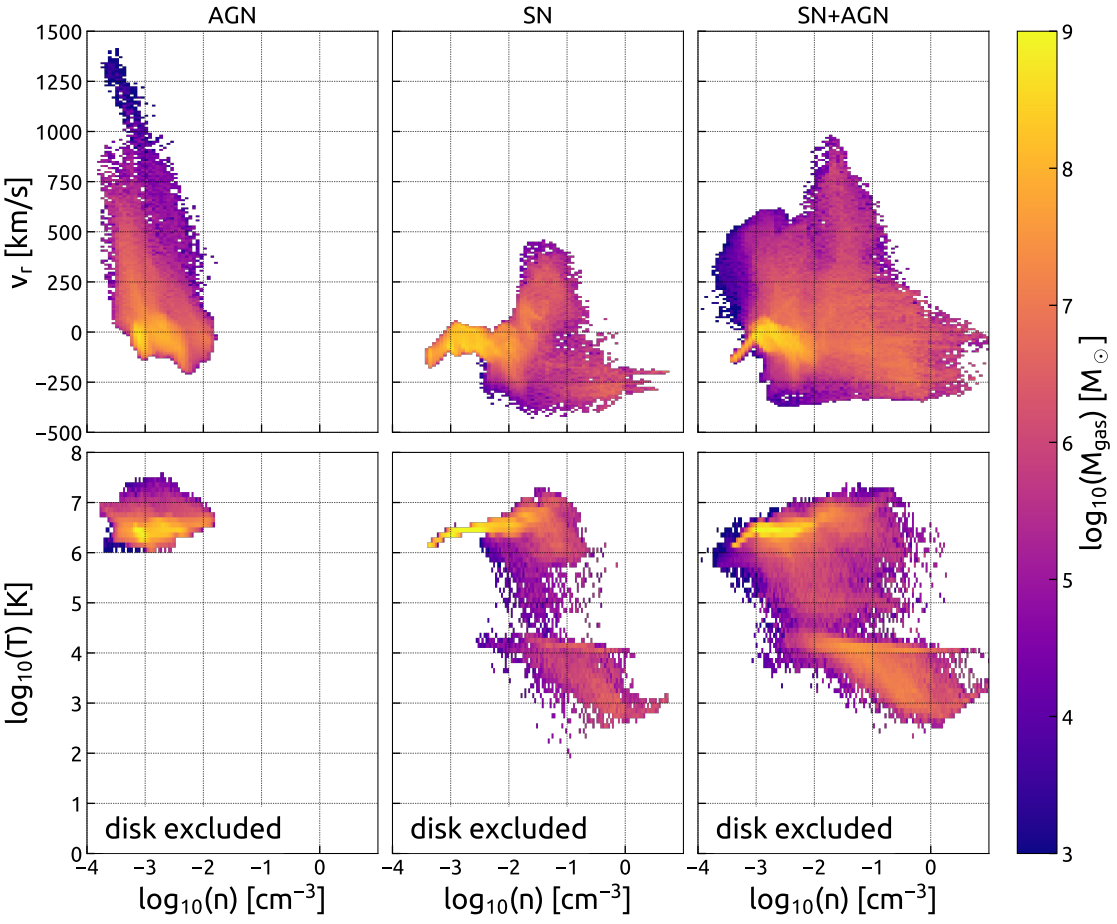

Figure 4.5: Histograms of gas radial velocity with respect to gas density (top row) and gas density-temperature diagrams (bottom row) for three simulations with different feedback modes - AGN-only (left column), SN-only (centre), and SN+AGN (right column). We have selected only gas located at less than 60 kpc from the centre of the halo (green region on Figure 4.1) and excluded central disc of thickness 8 kpc (red rectangle on Figure 4.1). $M_{\rm seed} = 10^6$ $M_\odot$ in simulations with AGN feedback modelled.

velocity (which is here around 700 km s^{-1}). As demonstrated by Costa et al. (2015), the velocity we measure is consistent with an energy-driven wind with negligible cooling losses. This is indeed the case here, due to the lack of metal enrichment since no SN feedback was included in this pure AGN feedback scenario. For similar halo and black hole properties, the analytical model used in Costa et al. (2015) predicts maximum gas velocities in the range 1200–1800 km s^{-1} (see their Figure 6).

The simulation with only SN feedback (middle column of Figure 4.5) features a galactic fountain with velocities up to 400 km s^{-1}, which is less than the halo escape velocity. The simulation with both feedback mechanisms (right column of Figure 4.5) shows outflowing gas with velocities typical of both feedback modes. Most importantly, the high velocity gas is on average one to two orders of magnitude denser than in the AGN only case. Here, the hot, energy-conserving outflow entrains the cold, dense gas of the fountain and accelerates it to much higher velocities.

4.4.2. Outflow mass loading factor

We now study the temporal evolution of the mass outflow rates. We define the mass loading factor as the ratio of the gas *outflow rate* (through a one-kpc-thick shell placed at a given radius from the centre of the halo) to the SFR of the galaxy. We choose 20 and 50 kpc as two representative radii - the former is at the upper edge of the galactic fountain, while the latter corresponds to a significant fraction of R_{200} and captures the large-scale outflow, relevant for the entire halo.

In Figure 4.6a, we plot the mass outflow rate of the simulations without SN feedback. In the reference run (black dotted line) we see no outflowing gas at all, as no feedback mechanism is present. The simulation with $M_{\rm seed} = 10^5$ M$_\odot$ is virtually identical to the 'no AGN' case, since the SMBH did not grow significantly in this case. In the three runs with SMBH seed masses between 10^6 and 10^8 M$_\odot$ we see the same qualitative behaviour: once the SMBH reaches its maximum, self-regulated mass, heating from the AGN overcomes the cooling losses and a strong energy-conserving outflows develops, with a very large mass outflow rate, close to 100 $M_\odot$/yr, but only for a short time. This short-lived outflow is enough to stop the accretion of fresh halo onto the disc (as seen on Figure 4.3a). The mass outflow rate at late time stabilises at the rather low value of 5 $M_\odot$/yr. Comparing the two left panels on Figure 4.6a, we see that the 50 kpc mass outflow rate is higher than the 20 kpc one, which is consistent with an outflow that sweeps the halo gas along its way.

In Figure 4.7a we plot the mass loading factor for our five runs without SN feedback. This quantity is used to estimate if an outflow can efficiently regulate star formation. The evolution of this mass loading factor can be divided in two periods: 1) an early epoch, when the SMBH just reached its maximum, self-regulated mass, for which the mass loading factor is around ~ 5 and 2) a late epoch, when the mass loading factor falls down to ~ 0.5 (~ 1) at 20 kpc (50 kpc).

The mass outflow rate measured in the simulation with only SN feedback is plotted as a black dotted curve on Figure 4.6b. It rarely exceeds 5 M$_\odot$/yr at 20 kpc from the centre, and is almost zero at 50 kpc. If AGN feedback is enabled, a strong and sustained outflow is produced, with a mass outflow rate around 20 M$_\odot$/yr up to 50 kpc. It is worth noticing that in this case the mass outflow rate at late time is a factor of 5 larger than in the AGN-only simulations.

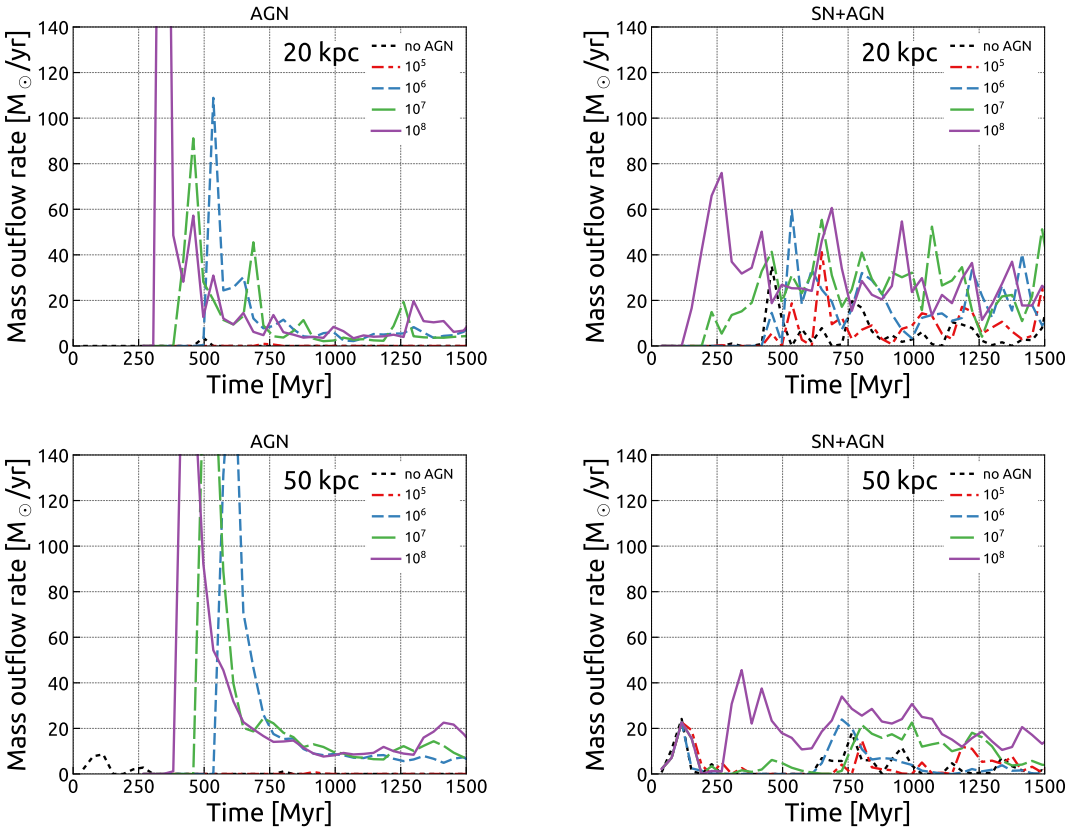

(a) AGN (b) SN+AGN

Figure 4.6: Outflow mass in two sets of simulations - with AGN feedback only (left) and with both SN and AGN feedbacks (right) - for four different seed masses: $10^5\,M_\odot$ - red (dash-dotted), $10^6\,M_\odot$ - blue (short dashes), $10^7\,M_\odot$ - green (long dashes), and $10^8\,M_\odot$ - purple (solid); contrasted with runs without AGN feedback (black, dotted)). Left column: AGN only, right column: SN+AGN with NSC; top row: outflow measured through shell placed at 20 kpc from halo centre, bottom row: at 50 kpc.

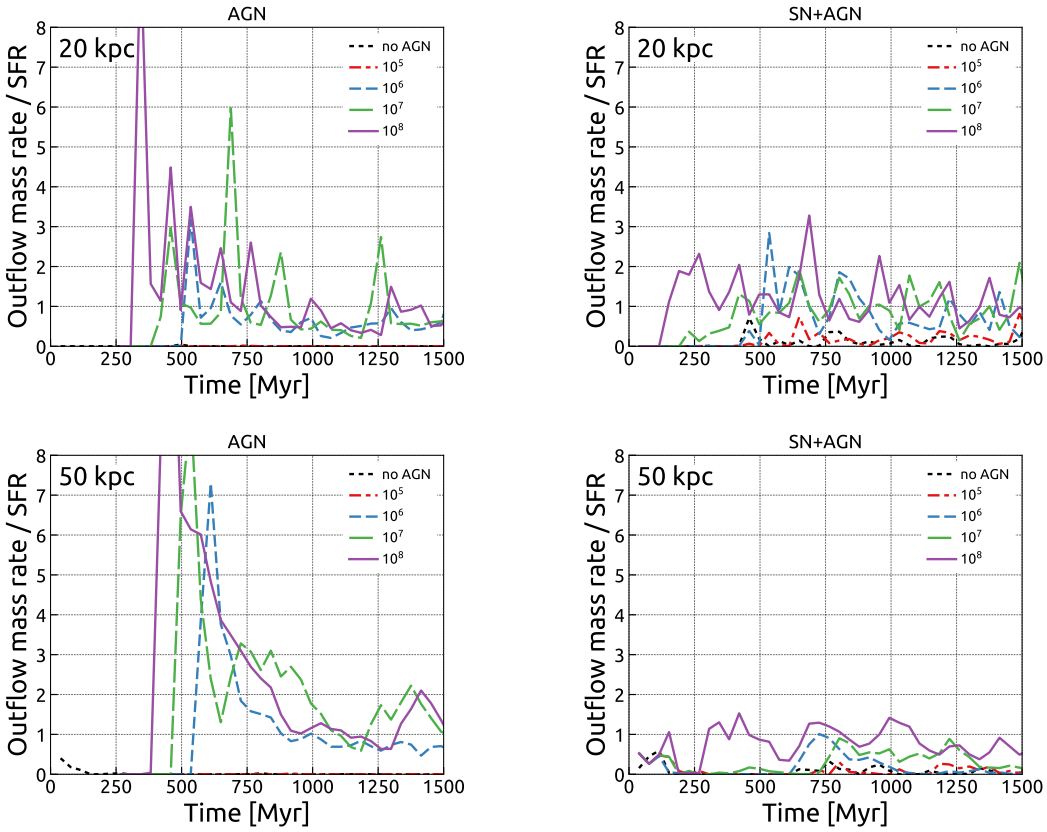

(a) AGN (b) SN+AGN

Figure 4.7: Mass loading parameter (outflow mass rate per star formation rate) in two sets of simulations - with AGN feedback only (left) and with both SN and AGN feedbacks (right) - for four different seed masses: $10^5\,M_\odot$ - red (dash-dotted), $10^6\,M_\odot$ - blue (short dashes), $10^7\,M_\odot$ - green (long dashes), and $10^8\,M_\odot$ - purple (solid); contrasted with runs without AGN feedback (black, dotted)). Left column: AGN only, right column: SN+AGN; top row: outflow measured through shell placed at 20 kpc from halo centre, bottom row: at 50 kpc.

Förster Schreiber et al. (2014) find in their sample of massive galaxies at $z \sim 2$ ($\log(M_*/M_\odot) \geqslant 11$, comparable to our runs) clear signatures of AGN-driven outflows with $\dot{M}_{\rm out}/{\rm SFR} \approx 3$, but ranging from 0.5 to 15, well within the range of the values produced by our simulations. We will compare our results to observations in greater detail in Section 4.6. One effect that becomes apparent from a careful inspection of Figure 4.6 is the dependence of the outflowing mass to the initial seed mass. This weak effect is related to the synchronisation between the peak of the SF and the epoch when the SMBH reaches its maximum, self-regulated mass. It appears that the closer these events are to each other, the stronger is the outflow. This is due to the synchronisation of a strong SMBH accretion (due to the large reservoir of gas available) and a strong galactic fountain (in case SN feedback is present).

Observationally, it is possible to characterise the outflows by comparing the amount of gas entrained in the outflow to the mass of the gas in a disc. In Figure 4.8 we plot

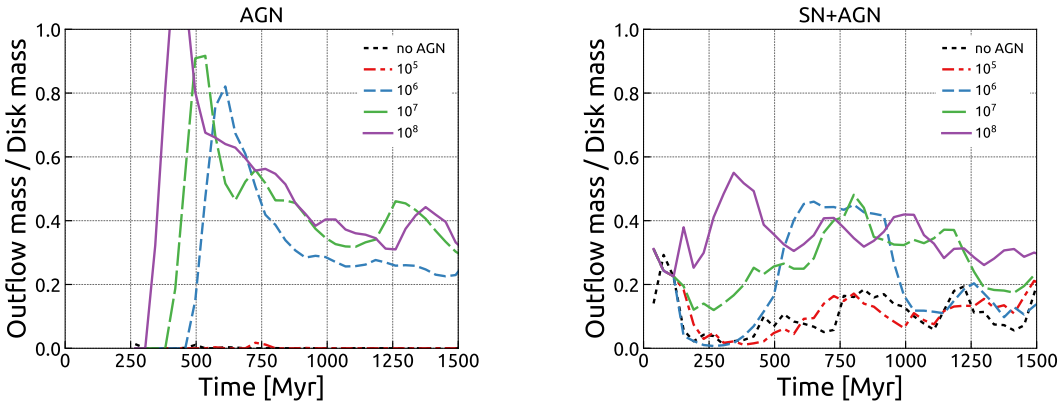

(a) AGN (b) SN+AGN

Figure 4.8: Time evolution of ratio between outflowing gas mass (green region in Figure 4.1, but excluding red) and gas mass in the disc (±4 kpc from disc plane, red box in Figure 4.1) - for four different seed masses: $10^5\,M_\odot$ - red (dash-dotted), $10^6\,M_\odot$ - blue (short dashes), $10^7\,M_\odot$ - green (long dashes), and $10^8\,M_\odot$ - purple (solid); contrasted with runs without AGN feedback (black, dotted)). Left column: AGN only, right column: SN+AGN.

the ratio between the mass of all of the outflowing gas (selected as shown in Figure 4.1, i.e. out to 60 kpc from the centre but excluding the galactic disc) and the mass of the gas contained in the disc (±4 kpc from the disc plane; the red region in Figure 4.1). This ratio reaches one when the outflow is the strongest (at early time) and falls down to 40% at late time. In simulations with both feedback modes, AGN feedback is able to more than double the amount of gas entrained in the outflow, compared to the mass in the galactic fountain in the SN-only simulation. A larger SMBH seed leads to a more massive outflows , and earlier, an effect that we have already seen in Figure 4.7b.

4.5. Outflow morphology

In this Section we focus on the morphology of gas in our simulations at three different times that are fairly representative for different stages of the evolution. On Figure 4.1 we have shown mass-weighted surface density projections for four different simulations (no feedback, AGN, SN and SN+AGN; top to bottom) at three different times (300, 750 and 1300 Myr; left to right). In the 'no feedback' simulation there are no visible outflows and most of the gas is quickly consumed in star formation. In simulations with only AGN feedback there are no dense outflows, but halo gas is removed by a hot outflow, as discussed in Section 4.4. SN feedback on its own is able to produce gas that is violently evolving as a galactic fountain, propelled by continuous SN explosions in the galactic disc. The morphology seen in the simulation with the cooperation between SN and AGN feedbacks is very different. Initially it resembles that of runs with SN only, as the SMBH requires time to grow to its self-regulation mass. Later on, AGN feedback launches dense and cold gas from the fountain to large radii.

4.5.1. Temperature density diagram

In Subsection 4.4.1 we have discussed how the mass fraction changes as a function of density and radial velocity, while here we want to focus on the mass fraction as a function of density and temperature (see Figure 4.5). The gas in the simulation with only AGN feedback is very diffuse and never cools below 10^6 K. This is in strong contrast with the temperatures found in the runs with SN feedback, where the outflow gas can cool to temperatures as low as few hundred Kelvin. This significant difference is explained if we recall that our simulations start with $Z_{\rm ini} = 0.05\,Z_\odot = 0.001$ and that the only source of metal enrichment of the gas is via SN explosions. This leads to a lack of metals and associated cooling in the AGN-only simulation.

In the simulation with SN feedback a galactic fountain develops. The gas that is returning to the disc is cooler and denser (>1 H/cc) than the outflowing gas, as revealed by the location of the densest gas on the phase space diagram.

If both feedback modes are included, we see very similar properties between the SN and the SN+AGN runs. In the latter, however, more *dense* gas is entrained in the outflow (cf. Figure 4.8b), that cools efficiently due to the higher metal enrichment. AGN feedback does not only accelerate the fountain gas, but also pushes it to larger radii, giving it more time to cool.

4.5.2. Radial profiles

In Figure 4.9 we show the radial profiles of the average density (top row) and the average mass flow rate (bottom row) of the inflowing gas for three times representative for the halo evolution. All the gas is plotted with thin lines, while the dense gas, defined as $n_{\rm gas} > 0.01$ H/cc with thick lines. We use this threshold as it corresponds to self-shielded, neutral or possibly molecular gas (see below). Initially (left column), the profiles are typical for an accretion flow from the extended halo, especially for the AGN run (plotted with green dashed line) which is not impacted by mixing from SN feedback. In runs with only AGN feedback we see that after the SMBH reaches its maximum self-regulated mass (middle and right panels), the gas has a significantly lower average density compared to runs where SN feedback is included. This means that the halo gas has been swept more efficiently in the AGN run than in the others.

Interestingly, thanks to the effect of the combined feedback mechanisms (red lines), more dense gas is able to reach 50 kpc (middle column) and beyond (right column). Part of the outflow loses kinetic energy and starts falling back, thus also increasing the inflow rate. This is also reflected in the bottom row, where we plot average mass flow rate of the gas. As we discussed in Section 4.3, star formation is largely quenched, as AGN feedback *prevents* gas from falling back onto the disc. This is in contrast with the SN+AGN run, in which an order of magnitude more gas is infalling onto the disc. We stress again the difference in metal enrichment between the runs - in simulations with SN feedback thanks to metal injection we observe more cooling and thus more dense gas. As a consequence, in the SN+AGN simulation, cooling boosts gas re-accretion and attenuate the effect of AGN feedback. This explains why the SFR is not quenched as efficiently as in the AGN only case, as the mass inflow rate is an order of magnitude lower at all radii in the AGN only case compared to the other two runs.

Turning our attention to the outflowing gas (Figure 4.10, top row) we once again find lower density gas in the AGN-only simulation and higher density gas in the SN-only

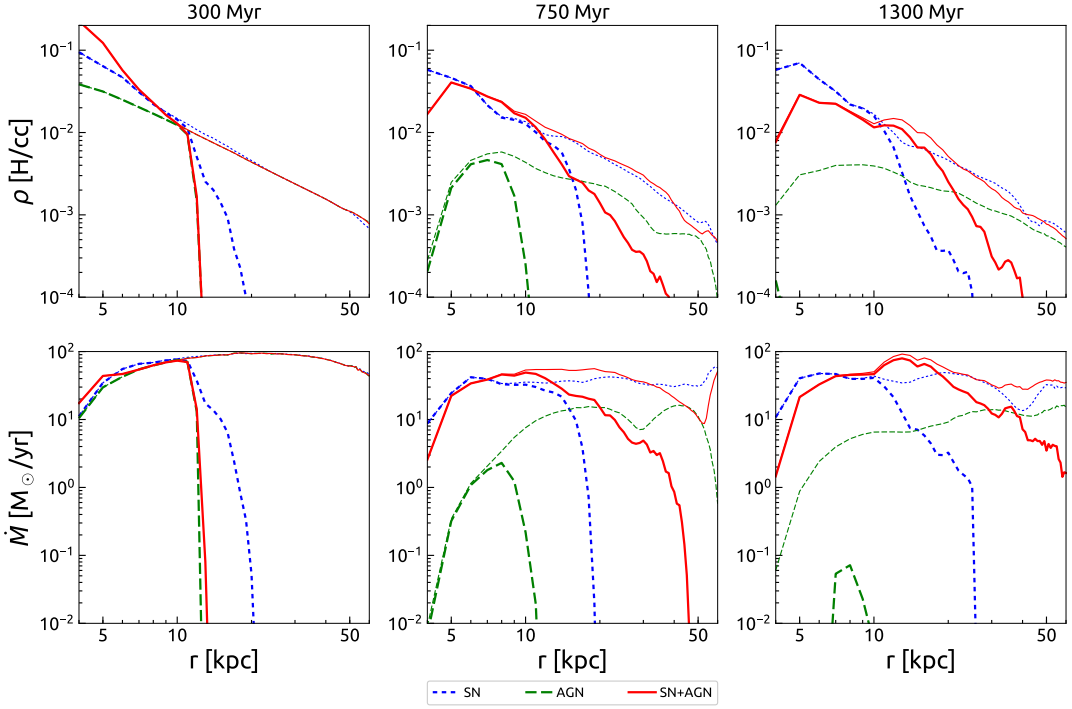

Figure 4.9: Radial profiles of average density and average mass flow of *inflowing gas* in a subset of simulations at three times: 300, 750 and 1300 Myr (blue, dotted - SN feedback only; green, dashed - AGN feedback only; red, solid - SN+AGN). Thin lines mark all gas, while thick lines mark dense gas (> 0.01 H/cc). In all panels we consider only gas in the region outlined on Figure 4.1. $M_{\mathrm{seed}} = 10^6\ \mathrm{M}_\odot$ in simulations with AGN feedback modelled.

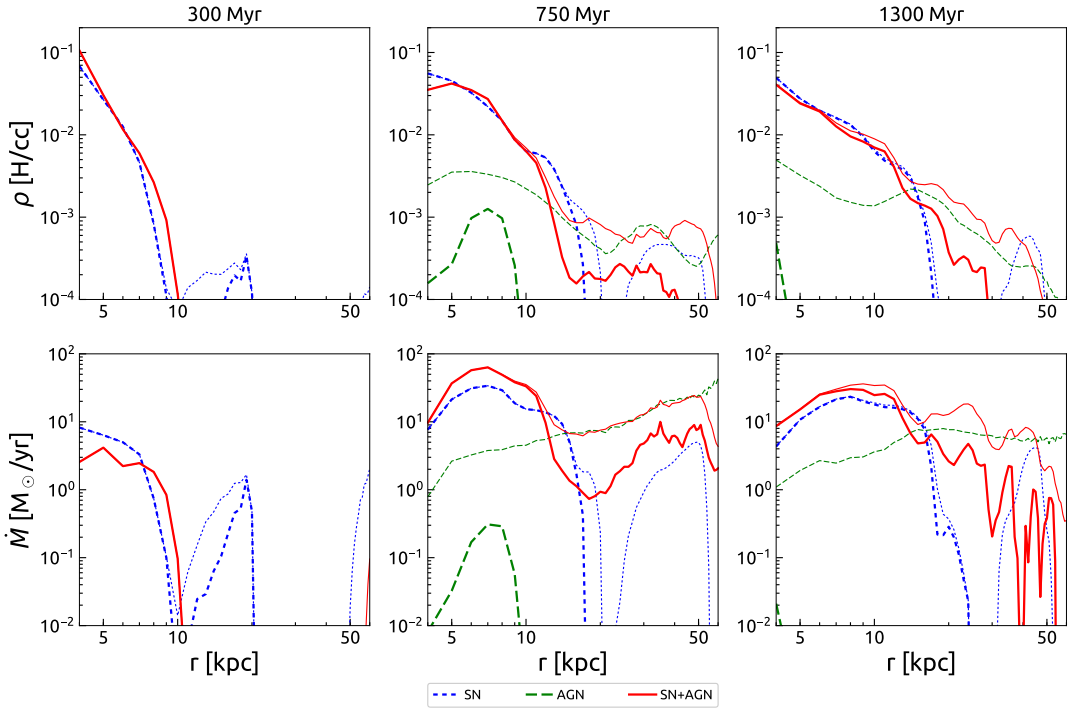

Figure 4.10: Radial profiles of average density and average mass flow of *outflowing gas* in a subset of simulations at three times: 300, 750 and 1300 Myr (blue, dotted - SN feedback only; green, dashed - AGN feedback only; red, solid - SN+AGN). Thin lines mark all gas, while thick lines mark dense gas (> 0.01 H/cc). In all panels we consider only gas in the region outlined on Figure 4.1. $M_{\rm seed} = 10^6$ M$_\odot$ in simulations with AGN feedback modelled.

run in the galactic corona (up to 20 kpc from the centre). The absence of any outflowing gas at 300 Myr in the AGN-only run is explained by the fact that the SMBH has not reached its maximum self-regulated mass yet. At later times, as seen in the bottom row of Figure 4.10, very large quantities of dense gas are being expelled by combined AGN and SN feedbacks – with $\dot{M}$ between 1 and 10M$_\odot$/yr, the latter value being larger than the inflow rate. At 750 Myr we clearly see that the mass outflow rate is rising with increasing radius, as it entrains more and more gas. In the case of the simulation with combined feedback mechanisms, the outflow is loaded with dense gas up to 50 kpc from the disc, as revealed by the thick line.

Another way to describe the gas distribution in our simulations is via cumulative mass profiles, which we show on Figure 4.11. At 750 Myr there is overall less gas at all radii in the simulation with AGN feedback only (green dashed line) compared to the other two runs. This means that more gas was removed and thus SF has been quenched more efficiently in the AGN-only case. If we now focus on the amount of the outflowing gas at > 30 kpc from the disc, we find that combined SN+AGN feedback is able to carry larger amounts of gas than each individual feedback mechanism on its own. Furthermore, limiting our analysis to only the dense outflowing gas (right column) we can make three important observations: 1) in simulations with only AGN feedback there is no dense gas, 2) the profile of SN feedback (blue dotted line) has no dense gas present beyond ~ 15 kpc,

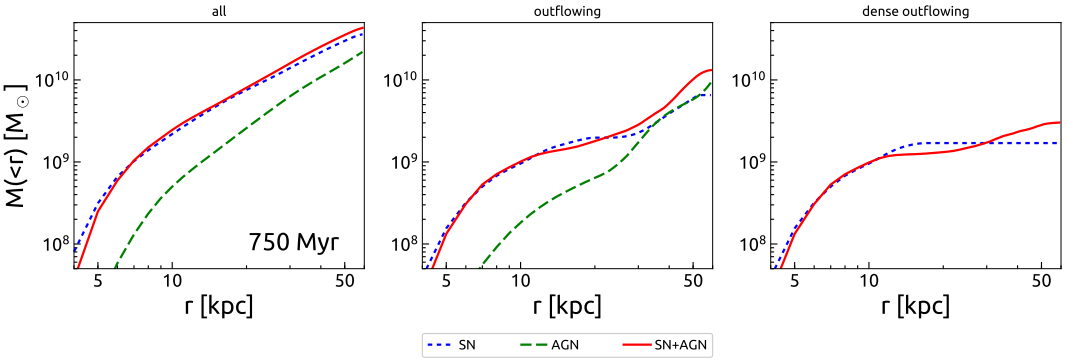

Figure 4.11: Cumulative mass profile in a subset of our simulations at 750 Myr. Left panel: all gas, middle panel: only outflowing gas, right panel: only dense, outflowing gas. Blue, dotted - SN feedback only; green, dashed - AGN feedback only; red, solid - SN+AGN. In all panels we consider only gas in the region outlined on Figure 4.1. $M_{\rm seed} = 10^6$ M$_\odot$ in simulations with AGN feedback modelled.

while 3) we have twice more dense gas overall (up to 50 kpc) in the SN+AGN simulation.

On Figure 4.12 we show mass-weighted histograms of the line-of-sight velocity $v_{\rm los}$ at a given galactic radius $r_{\rm cyl}$ (averaged in rings). In the AGN-only run the fastest moving gas is seen in the very centre; here gas is diffuse and hot. The fountain launched by the SN feedback shows lower velocities with a weaker radial dependency. The combination of the two feedback mechanisms is also centrally peaked in the same fashion as the AGN-only simulation, but this time it contains more dense and cold gas. It appears that our simulations seem to be in agreement with the radial dependency in observed galaxies in Genzel et al. (2014), and with the simulations of star forming discs in Gabor & Bournaud (2014).

4.5.3. Evolution of baryonic mass

The long-term secular processes can lead to slow depletion of the gas from the halo. In order to investigate if these processes take place in our simulations, we have measured the baryonic mass (stars, gas and a black hole) in four of our runs (no feedback, SN-only, AGN-only with $M_{\rm seed} = 10^6$ M$_\odot$, and SN+AGN with $M_{\rm seed} = 10^6$ M$_\odot$) within 100 kpc from the centre of the halo ($\sim 0.5R_{\rm vir}$); see Figure 4.13. The baryonic mass in the no feedback run steadily increases with time and is always the highest among the four runs (reaching 1.6×10^{11} M$_\odot$ at 1500 Myr). The baryonic content in the SN feedback run is reduced compared to the no feedback run (1.55×10^{11} M$_\odot$), suggesting that part of the halo gas can be removed by the long-term SN feedback. In the AGN-only run, in which we have initially the same evolution as in the SN-only case. Once the SMBH reaches its self-regulation mass, the AGN feedback is able to regulate the inflow via preventive feedback (to 1.06×10^{11} M$_\odot$ at 1300 Myr). By 1500 Myr some of the rate increases a bit, which suggests a traverse flow along the disc plane develops. In the SN+AGN run the baryonic mass increases with time, but at a rate few percent lower than that of SN-only run (1.52×10^{11} M$_\odot$ at 1500 Myr), suggesting that the AGN feedback is less efficient than in AGN-only run, but still reducing the baryonic mass within $\sim 0.5R_{\rm vir}$.

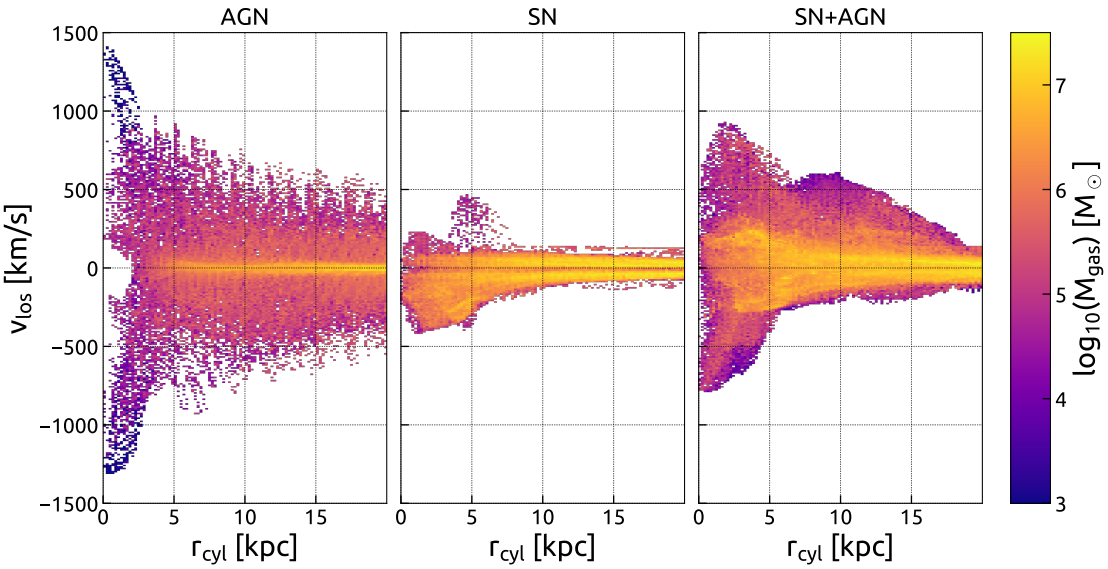

Figure 4.12: Histograms of gas line-of-sight velocity when looking at the disc face on with respect to galactic radius $r_{\rm cyl}$for three simulations with different feedback modes - AGN-only (left column), SN-only (centre), and SN+AGN (right column). We have selected only gas located at less than 60 kpc from the centre of the halo (green region on Figure 4.1) and excluded central disc of thickness 8 kpc (red rectangle on Figure 4.1). $M_{\rm seed} = 10^6$ M$_\odot$ in simulations with AGN feedback modelled.

4.6. Discussion

4.6.1. Molecular gas formation

In order to compare our simulation results to observed molecular outflows at high-redshift, we would need to form molecular hydrogen self-consistently, which is far beyond the scope of this paper, and for which one would require much better spatial resolution. As a consequence, we rely on a rather loose definition of "dense gas", adopting a density threshold $n_{\rm H} > 0.01$ H/cc. We would like to stress here that this value is often associated with the *self-shielding* density for neutral hydrogen (Schaye, 2004; Aubert & Teyssier, 2010; Rahmati et al., 2013). Gas denser than this threshold will not be photo-heated and therefore can cool to arbitrary low temperature and ultimately form star. In order to strengthen our argument, we demonstrate now that this dense gas is indeed able to cool to low temperature, and is therefore a good candidate for molecular gas.

In this paragraph, we will compare the cooling time of the dense gas in the outflow to the dynamical time in the halo. The latter can be estimated as usual as

$$t_{\rm dyn} = \sqrt{\frac{R_{200}^3}{GM_{200}}}, \tag{4.4}$$

where R_{200} is a virial radius, G is gravitational constant and M_{200} virial mass of the halo. Using the particular values in Section 4.2, we find that $t_{\rm dyn} \approx 1.1$ Gyr. The cooling time can be estimated as

$$t_{\rm cool} = \frac{\epsilon}{\dot{Q}} = \frac{3/2 n k_{\rm B} T}{n^2 \Lambda(T)}, \tag{4.5}$$

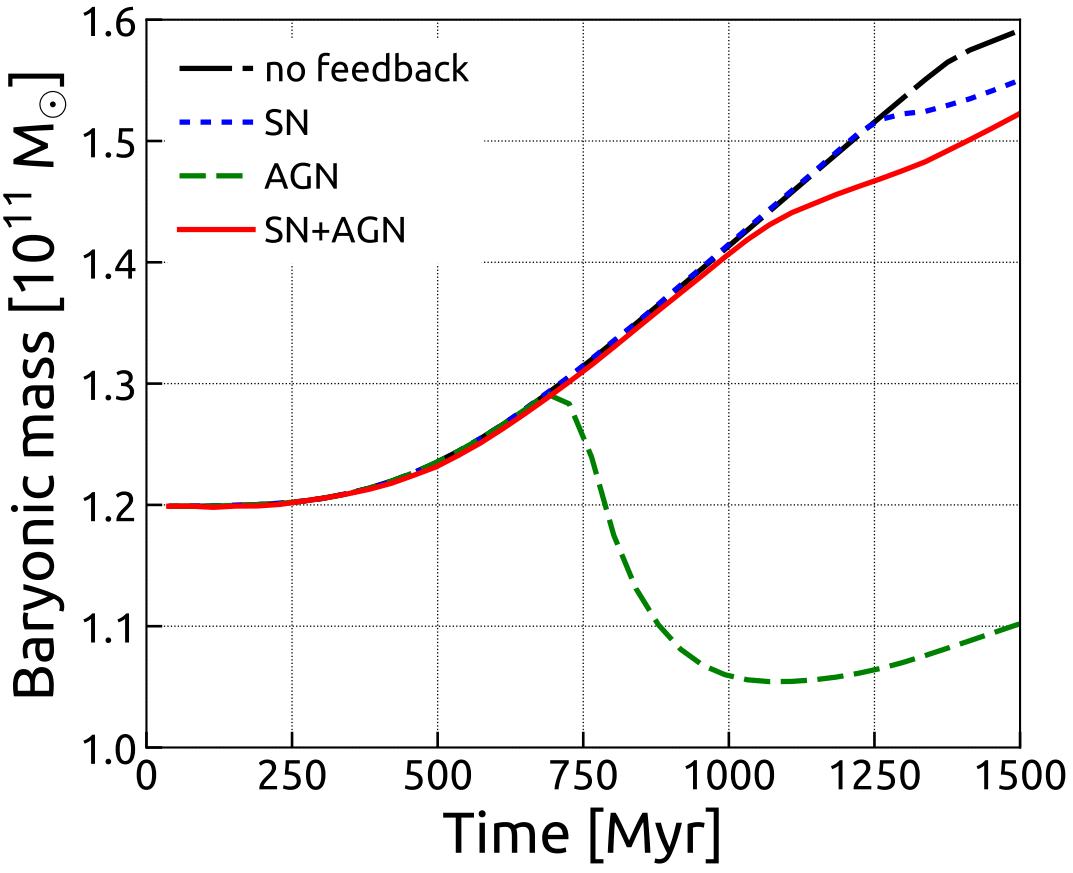

Figure 4.13: Evolution of mass of baryons in simulation without feedback (black, long dashes), SN-only (blue, dotted), AGN-only (green, short dashes) and SN+AGN (red, solid). We have selected all the gas, stars in inner 100 kpc of the halo and the black hole (if simulated).

where ϵ is the internal energy of the gas, $\dot{Q}$ is the cooling rate, k_B the Boltzmann constant, n the gas number density and $\Lambda(T)$ the cooling function at temperature T.

To compute the cooling time, we select all the gas from the regions marked on Figure 4.1 that is outflowing and with a density greater than 0.01 H/cc. We then compute the emission-weighted average density and temperature which turn out to be respectively 0.15 H/cc and 2×10^6 K. Substituting these values in Eq. (4.5) and using $\Lambda \simeq 2.3\times10^{-23}$ erg cm^3 s^{-1}, which is the value of the cooling function at the average outflow temperature and metallicity (we find $Z \simeq 0.1\,Z_\odot$), we obtain $t_{cool} \approx 3.8$ Myr, which is three orders of magnitude shorter than the halo dynamical time.

One could argue that computing the dynamical time for the entire halo is not adequate, as we want to form molecular gas already in the galactic corona. If we define the corona crossing time as $t_{cross} = R_{corona}/v_g$, where we choose the size of the corona as $R_{corona} \simeq 50$ kpc and the maximum outflow velocity as $v_g \simeq 1000$ km/s (see Figure 4.5), we get $t_{cross} \simeq 50$ Myr, still comfortably higher than the cooling time.

This means that our dense outflowing gas will have enough time to turn molecular before traversing a significant fraction of the corona, not to mention the halo as a whole. To confirm our estimate, we analysed the temperature distribution within the outflow and found $\sim 10^9\,M_\odot$ of gas colder than $< 10^4$ K and $\sim 10^8\,M_\odot$ of gas colder than $< 10^3$ K. However, we would like to re-emphasise that we do not model explicitly molecular and radiation physics, thus this cold gas can only be interpreted as a tracer for the true molecular gas.

4.6.2. Comparison to observations

There is an increasing body of observational evidence of SMBH activity in galaxies at all redshifts. In the local Universe, AGNs are observed with fast, hot outflows ionising large quantities of gas in Seyfert 2 galaxies (e.g. Greene et al., 2011; Harrison et al., 2014; McElroy et al., 2015). Powerful jets are also observed to produce large spherical cavities in galaxy clusters (see e.g. reviews by McNamara & Nulsen (2007); Fabian (2012); Heckman & Best (2014)).

Observations at high redshifts ($z \approx 1-3$) reveal massive molecular outflows in galaxies at the peak of star formation history, that also host bright quasars. For example, the observations of $z = 2.3$ ultra-luminous infrared galaxy by George et al. (2014) find molecular outflow reaching velocities of 700 km s^{-1}, somewhat lower than the estimated escape velocity of that object. Even more extreme outflow was recently observed by Feruglio et al. (2017) who have found a quasar with the outflow velocity of ~ 1340 km s^{-1}. In a very recent study, Chapman et al. (submitted) found a more extreme example of AGN-driven molecular outflows from the quasar HS1549+19 at $z = 2.84$. They report observations of molecular gas with $v_{out} \sim 1500$ km s^{-1}. The stellar mass of the host galaxy ($\sim 10^{11}\,M_\odot$) is significantly larger than in our case ($5\times10^{10}\,M_\odot$). HS1549+19 also hosts a more massive SMBH with $M_{SMBH} = 4.6\times10^9\,M_\odot$ compared to our case $2\times10^8\,M_\odot$. There are also multiple examples of cold outflowing gas seen at $z > 5$ (e.g. Maiolino et al., 2012; Cicone et al., 2014). Not only cold dense outflows cane be seen in observations of massive galaxies. Genzel et al. (2014) presented a sample of ~ 30 massive galaxies with broad nuclear emission and with a FWHM of > 450 km s^{-1} and reaching ~ 5000 km s^{-1}. These authors argue that stellar feedback can only account for outflows velocities up to ~ 200 km s^{-1}, which in turns mean that also the ionised outflows should be able to escape from the galaxy if they are propelled by AGN.

This observational picture agrees very well with our numerical results, as depicted in Figure 4.5. The typical outflow velocities of the cold and dense gas component are only around $\sim 500\,\mathrm{km\,s^{-1}}$ for the SN-only case, while for the SN+AGN model, they can reach much larger values around $1000\,\mathrm{km\,s^{-1}}$, which is more than 5 times larger than v_{circ}.

In Chapter 2, we have shown that the final mass of the black hole is related to the halo escape velocity and the size of the energy injection region by

$$v_{\mathrm{esc}} \simeq 750\ \mathrm{km/s}\ \left(\frac{M_{\mathrm{sink}}}{10^8\ M_\odot}\right)^{1/3} \left(\frac{R_{\mathrm{sink}}}{100\ \mathrm{pc}}\right)^{-1/3} \tag{4.6}$$

This suggests that, if the energy driving the outflow is deposited in a region similar to our simulations, the outflow velocity can be up to 2.5 times larger than in our simulation, easily reaching the observed value. This means that the escape velocity of HS1549+19 should also be close to $1500\,\mathrm{km\,s^{-1}}$, which is a rather extreme value. Note that Nesvadba et al. (2011) also reported earlier the discovery of two $z \geqslant 3.5$ quasars with large-scale outflows and FWHM velocities up to $5000\,\mathrm{km\,s^{-1}}$.

In Förster Schreiber et al. (2014), a sample of massive $z \sim 2$ galaxies observed with SINFONI has been presented, with stellar masses and mass loading factors similar to our simulations. They have speculated that nuclear outflows driven by AGN feedback is probably a general characteristic of massive galaxies at the peak of their star formation history (i.e. $z \sim 2$). Our simulation clearly confirm this picture and reveal the physical mechanism that powers these massive outflows, namely the combination of efficient SN feedback in conjunction with a powerful AGN. At even higher redshifts than discussed here, evidence of quasar-driven outflows does also exist. Very massive, gas-rich galaxies at $z \approx 5-7$ seem to be excellent hosts for both efficient SMBH-fuelling and efficient SF through dense gas clumps, explaining recent observations (Aalto et al., 2012; Cicone et al., 2014, 2015) with outflows reaching $1400\,\mathrm{km\,s^{-1}}$.

4.6.3. Comparison to previous simulations

Feedback from SMBH has been invoked a long time ago to explain the luminosity function of galaxies at the high mass end (e.g. Silk & Rees, 1998). It has been included since then in both semi-analytical and numerical models of galaxy formation, and acts as the main mechanism leading to the so-called quenching of SF in massive galaxies with $M_{\mathrm{halo}} > 10^{12}\,\mathrm{M}_\odot$ (Di Matteo et al., 2005; Croton et al., 2006; Hopkins & Hernquist, 2006; Somerville et al., 2008; Dubois et al., 2010; Teyssier et al., 2011; Fabian, 2012; Feldmann et al., 2016). It is however still unclear how this process occurs in details.

Results from recent large cosmological simulations (Vogelsberger et al., 2014; Schaye et al., 2015; Dubois et al., 2016) show that AGN feedback is a necessary ingredient of a successful galaxy evolution model. On the other hand, in very high resolution simulations of isolated galactic discs, Gabor & Bournaud (2014) and Roos et al. (2015) have demonstrated that AGN feedback has very little effect on the SF within the disc. The SMBH could in principle release as much as 10^{59} erg of energy ($E_{\mathrm{SMBH}} = 0.1 M_{\mathrm{SMBH}} c^2$), largely exceeding binding energy of the galaxy ($E_{\mathrm{gal}} \approx M_{\mathrm{gas}} \sigma^2$, where σ is the velocity dispersion).

As explained by Gabor & Bournaud (2014) and Roos et al. (2015), this naive expectation turned out to be wrong for mainly two reasons: (1) the energy is deposited in a very small region around the SMBH and (2) this energy quickly escapes the nuclear

region, either buoyantly (if the gas is hot) or ballistically (if the gas is cold), without affecting the disc significantly. A clear result of our simulation suite is that indeed AGN feedback does not affect the SF in the disc via the *ejective* mode, but it does *prevent* gas from inflowing from the corona or from the larger scale halo. This result has been confirmed phenomenologically by recent cosmological simulations (Vogelsberger et al., 2014; Schaye et al., 2015; Dubois et al., 2016). It is therefore crucial to include gas infall from either a cooling halo or a realistic cosmological environment to truly assess the effect of AGN feedback on the SF history of the simulated galaxy.

Another interesting aspect of our simulation is the emergence of a high velocity molecular (or at least dense and cooling) outflow. A recent cosmological simulation by Costa et al. (2015) also obtained such an outflow with dense and cold gas, with velocities reaching $1400\,\mathrm{km\,s^{-1}}$. They argue that these dense outflows emerged through the interaction of dense cold filaments around the galaxy and the hot AGN-driven outflow from the SMBH. Similar results were obtained by Prieto et al. (2017), who showed that the SN-driven galactic fountain could also play a role in their high-z, clumpy galaxies, fed by cold gas-rich filaments. These authors concluded that the origin of the cold gas in their outflows is due to the rarefaction of gas by SN and further push by AGN. In the case of our idealised cooling halo simulations, we can ascertain that the gas propelled by AGN feedback originates from the galactic fountain and is therefore metal-enriched, rather than the pristine gas from cold streams as in simulations of Costa et al. (2015) and possibly in Prieto et al. (2017). We also note that in a very recent cosmological simulations, Pontzen et al. (2017) have also observed AGN feedback launching a low-density and high-velocity outflow sweeping the SN-driven fountain gas.

The SN feedback model used in our simulations is far from being realistic. The physical processes involved in launching of the outflows are modelled phenomenologically with a subgrid model of delayed cooling or not modelled at all (e.g. stellar winds). Naturally, different implementations of SN feedback can lead to drastically different images of a galaxy. We can imagine two opposite results: 1) SN feedback that is too weak to push gas, that would result in a thin gas disc and 2) very strong SN feedback, that would blow all the gas away (e.g. Bournaud et al., 2014; Hopkins et al., 2014). In our setup we have aimed to achieve a qualitative result that produces galactic fountain seen in some of the observations. We caution that our predictions are qualitative, but nevertheless allow us to explore the effects of coupling between SN feedback and AGN feedback.

4.7. Summary

In this work, we have analysed the effect of our new SMBH feedback recipe presented in Chapter 2 on the quenching of star formation and on the launching of gas outflows. Thanks to high-resolution simulations of an isolated, gas-rich cooling halo, we are able to reproduce a realistic galactic environment with gas inflow, while resolving the ISM structure in the disc with a resolution of 100 pc.

The feedback mechanisms included in our simulations have led to the launching of strong outflows with different characteristics. Purely AGN-driven outflows are hot and diffuse, and only sweep up gas in the outer galactic halo. These outflows are launched when the SMBH reaches its maximum, self-regulated mass. These hot outflows are affecting the SF history of the galaxy by preventing fresh gas from being accreted in the disc or ejected gas from falling back to the disc. Without SN metal enrichment, pure

AGN-driven outflows cannot cool and form dense gas that could become molecular.

In simulations with only SN feedback, we observe the formation of a dense galactic fountain, that can be characterised by cold gas with moderate velocities, bound to the galactic disc. In simulations with both feedback models together, a clear synergy was revealed – SN feedback creates a galactic fountain with dense gas clumps and AGN feedback launches a low-density, hot outflow that sweeps the galactic corona, pushing the dense clumps to large distances. The resulting outflows is much more sustained and carries away a larger amount of mass. Metal enrichment from SN feedback promotes more cooling in the corona and, as a consequence, more gas can fall back onto the disc.

The mass loading factor of the simulated outflows are found to be close to unity, as seen in many observations. The analysis of the kinematic properties of the outflows reveals that the AGN is the main source of energy for the dense, molecular outflows. We have shown that these massive outflows can quench star formation in galaxies. This does not proceed via *ejective* feedback, but via *preventive* feedback, cutting the supply of fresh gas into the disc.

One requirement we find is a delicate synchronisation between an active star formation phase, that can trigger the formation of galactic fountain, and a central SMBH reaching its maximum mass, that can trigger the formation of a fast, AGN-driven, hot outflow. We speculate here that the simultaneity of these two conditions – sustained star formation and the SMBH reaching its final mass – can happen immediately after a "wet compaction" event, as described in e.g. Dekel & Burkert (2014). It is sometimes related to the bulge formation epoch (e.g. Dubois et al., 2013).

In summary, we argue that SF can be quenched by AGN through *preventive* feedback. We have also shown that fast and dense outflows can arise when SN and AGN feedbacks act in tandem, and that this happens at a very specific epoch of the galaxy life, when star formation is still active while the SMBH reaches its maximum mass.

5

AGN BUBBLES IN A HOT INTRACLUSTER MEDIUM

He will win who knows when to fight and when not to fight.

– Sun Tzu

In this chapter[1], we study how a rising bubble inflated by AGN feedback in a hot stratified intracluster medijm (ICM) evolves in idealized simulations with four different hydrodynamical schemes: (traditional) smoothed particle hydrodynamics (TSPH), a pressure flavour of SPH (PSPH), a meshless finite mass (MFM) scheme, as well as an Eulerian code with adaptive mesh refinement. In the absence of magnetic fields, the bubble is Kelvin-Helmholtz unstable on short enough time scales to dissolve it fully in the ICM, which is captured by MFM and Ramses simulations, while in the TSPH simulation the bubble survives. When the ICM is turbulent, mixing of the bubble with the ICM is accelerated. This occurs if the numerical scheme can capture the instabilities well. The differences in the evolution of the bubble has a surprisingly small influence on the thermal structure of the ICM. However, in the simulations with MFM and Ramses the bubble disruption leads to turbulent stirring of the ICM which is suppressed in SPH. In the latter the thermal energy remains trapped in the bubble and is transported to large radii. We discuss if the choice of hydrodynamical schemes can lead to systematic differences in the outcomes of cosmological simulations.

[1]The work presented in this chapter is advanced publication draft entitled 'Physical and numerical stability and instability of AGN bubbles in a hot intracluster medium' authored by Ogiya, **Biernacki**, Hahn and Teyssier, which has been presented as an arXiv preprint:1802.02177. In this project we use the two different numerical codes based on different techniques, which is an essential part of this project, rendering the separation of this work into independent pieces impossible. Ogiya prepared the initial conditions, ran Gizmo simulations and contributed to analysis and text writing, Biernacki translated the initial conditions to Ramses, ran simulations with Ramses, wrote the analysis tools and investigated the results, as well as contributed to text writing. Hahn wrote the 1D code used for validation of results, contributed to text writing and supervised the project. Teyssier supervised Ramses runs and contributed to text writing.

5.1. Introduction

The heating mechanisms for the gas in the centre of galaxy clusters is important to explain X-ray observations (McNamara & Nulsen, 2007; Kravtsov & Borgani, 2012; Fabian, 2012, and references therein). The cooling timescale of the gas in the centres of galaxy clusters is much shorter than the Hubble time (Fabian & Nulsen, 1977; Cowie & Binney, 1977; Mathews & Bregman, 1978, and many subsequent works), known as the so-called cooling flow problem. If there is no heating source, intra-cluster medium (ICM) would exhibit a strong cooling flow and thus become highly concentrated in the centre of the cluster. This is in contrast with observations of cluster centres, which show that the ratio of the gas mass to the total enclosed mass can be fairly low, ~ 0.01, compared to the cosmic baryon fraction, ~ 0.16. Furthermore, the temperature of the central gas is high, typically $\gtrsim$ keV $\sim 10^7$ K (e.g. Lea et al., 1973; Evrard, 1997; Pratt et al., 2010; Mantz et al., 2014). These observed properties of the ICM are reviewed by e.g. Fabian (1994) and Fabian (2012, and references therein).

Active Galactic Nuclei (AGN) are promising heating sources to keep the centres of galaxy clusters hot and to prevent gas concentration (McNamara & Nulsen, 2007; Kravtsov & Borgani, 2012, and references therein). If AGN are powerful enough, the jet power of $P_{\rm jet} \gtrsim 10^{42}$ erg/sec (e.g. Cavagnolo et al., 2010; Nemmen et al., 2012; Godfrey & Shabala, 2013), can trigger strong shock waves which compress and heat the ICM (e.g. Sanderson et al., 2005; Sutherland & Bicknell, 2007; Mingo et al., 2012; Gaspari et al., 2011; Wagner et al., 2012; Perucho et al., 2014; Lanz et al., 2015). Even if AGN are less powerful, they may induce bubbles of diffuse hot gas. X-ray observations have detected such AGN bubbles as cavities in the ICM (Fabian et al., 2000; McNamara et al., 2001; Gitti et al., 2006; Dong et al., 2010) and in galaxy groups and galaxies (e.g. Ohto et al., 2003; Forman et al., 2007; Panagoulia et al., 2014).

Observations have also suggested that significant amounts of the thermal energy might be still captured in hot bubbles (e.g. Bîrzan et al., 2004; Dunn et al., 2005; Shurkin et al., 2008; Sanders et al., 2009). Hence, a theoretical investigation of the interaction between the bubble and the surrounding ambient cluster gas would be of great importance to our understanding of the thermodynamics of the ICM. The rising bubble may also play a role in redistributing heavy elements in the ICM. The processes that govern the rising of the bubble and its subsequent mixing with the surrounding ICM are complex and detailed analytical investigations are difficult. Simplified models have provided valuable insights (e.g. Voit et al., 2017, and references therein), and numerical simulations can provide further insight into the complex processes governing gas in cluster cores.

Numerical simulations of the ICM with AGN feedback can be classified into two types - 1) idealised and 2) cosmological. The former aim to understand the physics by means of idealised setups, which provide full control over the cluster environment and processes. For example, early studies showed that energy and matter redistribution by rising bubbles plays a key role in solving the cooling flow problem (e.g. Churazov et al., 2001; Brüggen & Kaiser, 2002). Subsequent simulations with higher resolution and additional physics, including magnetic fields and cosmic rays, demonstrated that the buoyantly rising bubbles redistribute not only energy and mass, but also metals and magnetic fields in the ICM (Reynolds et al., 2005; Sijacki & Springel, 2006; Vernaleo & Reynolds, 2006; Roediger et al., 2007; Dursi & Pfrommer, 2008; Vazza et al., 2010; Guo & Mathews, 2011). An interesting insight obtained by magnetohydrodynamic (MHD) simulations is that magnetic tension suppresses mixing instabilities on the bubble surface and thus

supports bubbles to rise to larger radii (Robinson et al., 2004; Dong & Stone, 2009, see also Biernacki et al., in prep.).

Cosmological simulations provide a more realistic cluster environment and assembly history with turbulence in the ICM driven continuously by both minor and major mergers (e.g. Miniati, 2014). Thanks to recent developments in the modelling of supermassive black holes and AGN feedback in cosmological hydrodynamic simulations (e.g. Di Matteo et al., 2005; Kawata & Gibson, 2005; Sijacki et al., 2007; Okamoto et al., 2008a; Booth & Schaye, 2009; Teyssier et al., 2011; Vogelsberger et al., 2013; Steinborn et al., 2015), they have succeeded in reproducing various observational results (Nagai et al., 2007; McCarthy et al., 2010; Di Matteo et al., 2012; Battaglia et al., 2013; Le Brun et al., 2014; Dolag et al., 2016; Dubois et al., 2016; Barnes et al., 2017a,b; Hahn et al., 2017, and refereces therein).

However, full agreement among them has not been achieved yet. The early discrepancy in predicted cluster entropy profiles between Eulerian and Lagrangian methods in non-radiative simulations (Frenk et al., 1999) has been understood as a severe underproduction of entropy in traditional Smooth Particle Hydrodynamics (SPH) methods (e.g. Wadsley et al., 2008; Mitchell et al., 2009; Power et al., 2014). Modern Lagrangian methods solved these shortcomings, but such discrepancies appear in any case less dramatic when optically thin cooling is added and are overshadowed by differences in subgrid models (e.g. Sembolini et al., 2016). However, some suspicion about fundamental differences might still be in order: for example, the central gas mass fraction in the centres of simulated clusters is typically lower than that observed when grid-based hydrodynamical solvers are used in the simulations (Hahn et al., 2017; Barnes et al., 2017a). On the other hand, simulations that adopt SPH claim to reproduce more realistic gas fractions by carefully tuning the AGN feedback model (Battaglia et al., 2013; Le Brun et al., 2014). Similarly, the distribution of metals in galaxy clusters is reproduced in some SPH simulations (Wiersma et al., 2011; Planelles et al., 2014; Rasia et al., 2015). Schaller et al. (2015) found differences in simulations adopting different flavours of SPH when keeping the feedback models fixed, but the differences are small at galaxy cluster masses.

Such discrepancies motivated us to pose the following questions:

- do different hydrodynamical solvers agree?
- do the simulations lack the resolution to capture important processes?
- are we missing any of other important non-thermal processes?

Physical viscosity and diffusion are typically negligible in most processes of the formation and evolution of galaxy clusters (e.g. Mo et al., 2010). However, neglecting this physics in numerical simulations may lead the code-dependent numerical, i.e. artificial and physically incorrect, effects which can affect the outcomes of the simulations. Thus we need to give careful attention to this point. Agertz et al. (2007) presented the fundamental differences between SPH and grid based methods with a suite of idealised simulations of a cold dense gas cloud moving through a low-density hot medium. Wadsley et al. (2008) tackled the second question using idealized simulations of a buoyantly unstable and rising hot bubble in an ambient medium. They found that the absence of mixing in traditional SPH schemes leads to an underproduction of entropy compared to grid based codes.

Scannapieco & Brüggen (2008) found that unresolved turbulence may play a role in determining the fate of AGN bubbles. They modeled unresolved turbulence as subgrid

physics in their grid-based simulations and found that AGN bubbles can survive for a much longer time than those in pure hydrodynamical simulations (see e.g. Shen et al. 2010 for SPH simulations). While this kind of subgrid modelling is becoming more common (e.g. Close et al., 2013; Schmidt et al., 2014; Iapichino et al., 2017), recent cosmological simulations mentioned above did not take it into account.

In this paper, we update the findings by Agertz et al. (2007) and Wadsley et al. (2008) using state-of-the-art hydrodynamical solvers that are used in more recent major cosmological simulations discussed above. In this paper, we restrict our analysis to ideal hydrodynamics without any subgrid modelling of unresolved turbulence. In order to avoid too much complexity, we employ a well-defined, simple setup of a spherically symmetric ICM with a hot bubble inflated by AGN feedback. This setup is similar to the ones of Wadsley et al. (2008) and Scannapieco & Brüggen (2008), but includes self-gravity of the gas, and for which a naïve analytical expectation can be given. In a next step, we introduce a turbulent velocity field to make the model more realistic. We address also the third question by varying the resolution of the simulations. For the first question, we refer readers to Meece et al. (2017) who compared the commonly-adopted sub-grid models of AGN feedback. Regarding the fourth question, our subsequent project will address one of the possibilities - effects of magnetic fields (Biernacki et al., in prep.).

This paper is organized as follows. In Section 5.2, we describe our simple model of a buoyantly rising bubble inflated by AGN feedback at the centre of a gas sphere of the ICM and also provide the analytical expectation for the fate of the bubble. Section 5.3 gives a brief description for the numerical codes and methods used in this paper. We describe the setup of our numerical experiments and demonstrate the results in Section 5.4. In Section 5.5, we summarize and discuss the results.

5.2. Initial Conditions and Analytic Expectations

In this section, we set the stage for our model of a stratified hydrostatic medium and describe a hot bubble positioned initially near the centre of our idealised cluster. We present also calculations that demonstrate that such bubbles will buoyantly rise, experience ram pressure and undergo interface instabilities that lead to their ultimate demise by mixing with the ambient medium.

5.2.1. The ambient medium

We adopt the analytical model proposed by Komatsu & Seljak (2001, hereafter KS01) as a model for the ambient medium. In the analytical model, a gas sphere is embedded in a dark matter (DM) halo with a Navarro-Frenk-White (NFW Navarro et al., 1997) density profile, and the thermal pressure balances with the gravity of the DM halo with a polytropic equation of state while the self-gravity of the gas is neglected. KS01 adopted empirical prescriptions to give the concentration parameter of the halo, $c = r_{100}/r_s$, where r_s is the scale length of the halo, and the polytropic index, γ, as functions of the virial mass of the DM halo, M_{100}. Here, M_{100} is the mass contained within the virial radius, r_{100}, inside of which, the mean density of the DM halo is 100 times the critical density of the current universe.

Throughout this paper, we adopt a Hubble constant $H_0 = 70.3\,\mathrm{km/s/Mpc}$ (Komatsu et al., 2011) and we assume $M_{100} = 3 \times 10^{14}\,\mathrm{M}_\odot$ and a total gas mass, $M_{\mathrm{gas}} = 4.5 \times 10^{13}\,\mathrm{M}_\odot$. The concentration parameter of the DM halo and effective polytropic exponent

that the analytical model provides are $c = 5.168$ and $\gamma = 1.137$, respectively. The DM halo has a virial radius of $r_{100} = 1.734\,\mathrm{Mpc}$. The dashed line in Figure 5.2 presents the radial profiles of gas density (first row) and temperature (second row) given by this model.

5.2.2. Equation of motion of a bubble

5.2.2.1. Buoyancy

Let us consider a hot underdense bubble embedded in a colder stratified ambient gas sphere in hydrostatic equilibrium. If the bubble is displaced from the centre of the ambient gas sphere, it will rise buoyantly if the Schwarzschild condition for convective stability (Schwarzschild, 1906),

$$\left|\frac{dT}{dr}\right| < \left|\frac{dT}{dr}\right|_{\mathrm{ad}} \tag{5.1}$$

is *not fulfilled*. Here, r and T are the distance from the centre of the gas sphere and the gas temperature, respectively. The subscript "ad" in the second term indicates the respective relation allowing only adiabatic processes. Treating the bubble as a point mass for simplicity, the acceleration due to buoyancy, $\mathbf{a}_{\mathrm{buo}}$, can be written as

$$\mathbf{a}_{\mathrm{buo}}(\mathbf{r}) = \frac{\rho_{\mathrm{amb}}(r) - \rho_{\mathrm{bub}}(r)}{\rho_{\mathrm{bub}}(r)}\mathbf{g}(\mathbf{r}), \tag{5.2}$$

where $\mathbf{r}$ is the position of the bubble relative to the centre, $\mathbf{g}(\mathbf{r})$ the gravitational acceleration at $\mathbf{r}$, and $\rho_{\mathrm{amb}}(r)$ and ρ_{bub} indicate the density of the ambient medium at the radius, $r = |\mathbf{r}|$, and of the bubble, respectively. Note that the first term equates with the gradient of the thermal pressure, $-dp/dr$.

5.2.2.2. Ram Pressure

When the bubble has a non-zero velocity with respect to the ambient medium, it also feels ram pressure. Treating the bubble again as a point mass, the gradient of ram pressure, $\mathbf{a}_{\mathrm{ram}}$, is given as

$$\mathbf{a}_{\mathrm{ram}}(\mathbf{r}, v) = \frac{v^2}{2\rho_{\mathrm{bub}}}\frac{d\rho_{\mathrm{amb}}(r)}{dr}\frac{\mathbf{r}}{r}, \tag{5.3}$$

where v is the relative velocity between the bubble and the ambient medium.

5.2.2.3. Interface instabilities

As the bubble moves through the ambient medium with non-zero v, we expect the bubble boundary to undergo a Kelvin-Helmholtz instability (KHI, cf. e.g. Landau & Lifshitz, 1959) which ultimately will act to dissolve the bubble in the ambient medium. The timescale on which the KHI will act to dissolve the bubble is

$$\tau_{\mathrm{KHI}} \sim \frac{\rho_{\mathrm{amb}} + \rho_{\mathrm{bub}}}{\sqrt{\rho_{\mathrm{amb}}\rho_{\mathrm{bub}}}}\frac{\lambda}{v}, \tag{5.4}$$

where λ is the wavelength of the perturbation on the surface of the bubble. The KHI grows exponentially with time, t, i.e., the amplitude of the KHI, $A_{\mathrm{KHI}} \propto \exp(t/\tau_{\mathrm{KHI}})$.

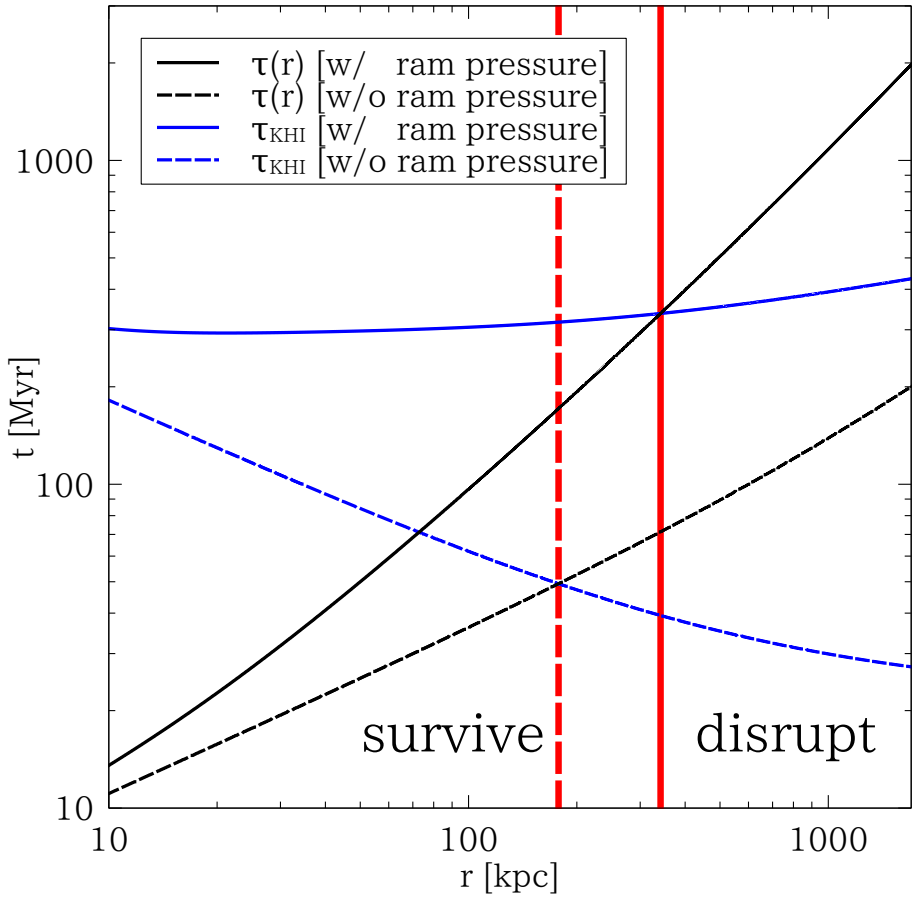

Figure 5.1: Comparison of timescales. Black lines represent the timescale of the bubble to arrive at r, $\tau(r)$. To estimate the KHI timescale, τ_{KHI} (blue), the instantanious relative velocity between the bubble and the ambient medium at r, $v(r)$, and the wavelength, $\lambda = 59.3\,\mathrm{kpc}$ are assumed. For solid (dashed) lines, ram pressure is (is not) taken into account. The bubble is expected to be dissolved at $r \sim 200 - 300\,\mathrm{kpc}$ where $\tau(r) > \tau_{\mathrm{KHI}}$. Red solid and dashed lines indicate the survival radius of the bubble including and not including ram pressure.

5.2.3. Comparison of timescales

Based on our estimates above, the bubble is expected to survive until $\lesssim \tau_{\rm KHI}$ but dissolve after that. Using Eq. (5.2) and Eq. (5.3), we can follow the motion of a bubble and estimate the time for the bubble to arrive at r, $\tau(r)$. To make a hot and less dense bubble, the temperature of gas contained within the innermost sphere of a diameter of 20 kpc is set to be 10^9 K, much hotter than the ambient hydrostatic medium (see Figure 5.2). Assuming that the heated central sphere itself expands adiabatically behind a rapidly propagating shock (see also Figure 5.3) until its pressure balances that of the ambient medium, the diameter of the bubble becomes $\sim$ 60 kpc (with the assumption of adiabatic expansion of the bubble rendering this an upper limit). If the position of the bubble is displaced from the exact centre by some perturbation, it rises buoyantly as long as Eq. (5.1) is not satisfied.

Figure 5.1 compares $\tau(r)$ with $\tau_{\rm KHI}$ and shows that the bubble would be dissolved at $r \gtrsim 200 - 300$ kpc where $\tau(r) > \tau_{\rm KHI}$. We compute the bubble density by assuming that the bubble continues to expand adiabatically and use the instant relative velocity between the bubble and the ambient medium at r, $v(r)$, and the wavelength, $\lambda = 59.3$ kpc to evaluate $\tau_{\rm KHI}$. Since $\tau_{\rm KHI}$ is proportional to the wavelength of the perturbation, this choice of λ would provide the upper limit of the of the KHI-time. Note that we neglect the response of the ambient medium to the motion and expansion of the bubble and assume that its density and temperature stay those of the hydrostatic equilibrium state, for simplicity.

Another fluid instability to possibly play a role is, of course, the Rayleigh-Taylor instability (RTI). Assuming the same wavelength we assumed for Figure 5.1 ($\lambda = 59.3$ kpc) and that the bubble density is much smaller than that of the ambient medium, the timescale of the RTI is $\tau_{\rm RTI} \sim 250$ Myr at $r = 10$ kpc, comparable to $\tau_{\rm KHI}$. As mentioned above, this provides an upper limit for the involved timescales and modes of smaller wavelengths would grow faster. The dependence of the timescale on the wavelength, $\tau_{\rm RTI} \propto \lambda^{0.5}$ and $\tau_{\rm KHI} \propto \lambda$, indicates that the KHI modes of the smaller wavelength grow faster than the corresponding RTI modes since they are comparable at the largest mode. Hence we hereafter consider that the KHI is the main mechanism to dissolve the bubble.

5.2.4. Introducing turbulence

In contrast to our simplistic model above, the ICM is turbulent (e.g. Schuecker et al., 2004; Hitomi Collaboration et al., 2016, and other observational results) and a substantial amount of turbulent energy may be converted into thermal energy to heat the centre of clusters (e.g. Dennis & Chandran, 2005; Zhuravleva et al., 2014; Eckert et al., 2017). In fact, mass estimates of galaxy clusters via the thermal Sunyaev-Zel'dovich effect and assuming hydrostatic equilibrium appear inconsistent with both independent measures of galaxy cluster abundance (cf. Planck Collaboration et al., 2016) and independent mass estimates (Hurier & Angulo, 2018), pointing possibly to a much larger contribution of non-thermal pressure than what is commonly found in simulations (see also e.g. Lau et al., 2009; Nelson et al., 2014).

Here, we introduce turbulence in order to quantify the additional effect it can have on the mixing of rising AGN bubbles in purely hydrostatic simulations, as well as the opposite effect, how the bubble can drive turbulence itself. We adopt a simple model in which we sample an isotropic Gaussian Kolmogorov velocity spectrum (e.g. Landau &

Lifshitz, 1959), for which

$$\left\langle \tilde{\mathbf{v}}(\mathbf{k}) \cdot \tilde{\mathbf{v}}^*(\mathbf{k}') \right\rangle \propto |k|^{-11/3} \delta_D(\mathbf{k} - \mathbf{k}'), \tag{5.5}$$

where a tilde indicates a Fourier transformed field. An arbitrary velocity field can be decomposed into longitudinal (compressible) and transversal (incompressible) modes, with the respective scalar potential ϕ_v and the vector potential $\mathbf{A}_v$, so that

$$\mathbf{v} = \boldsymbol{\nabla}\phi_v + \boldsymbol{\nabla} \times \mathbf{A}_v. \tag{5.6}$$

We assume here that the potentials are being given through multiplication of a random scalar field $G\{0,1\}$ and an independent random vector field $\mathbf{G}\{0,1\}$ (both of which are assumed to be fields of Gaussian white noise with zero mean and unit variance) with the square-root of the spectrum, so that in Fourier space

$$\tilde{\phi}_v(\mathbf{k}) = \alpha\phi_0\, k^{-17/6}\, \tilde{G}\{0,1\}, \quad \tilde{\mathbf{A}}_v(\mathbf{k}) = \beta\phi_0\, k^{-17/6}\, \tilde{\mathbf{G}}\{0,1\}. \tag{5.7}$$

Here, ϕ_0 is a normalisation constant, and the parameters α and β can be used to adjust the relative importance of longitudinal and transversal velocity modes ($\alpha^2 + \beta^2 = 1$ to maintain normalisation and we set $\alpha^2 = \beta^2 = 0.5$). Note that the Kolmogorov spectrum typically holds only between the driving scale and the dissipation scale. In our model, we set the driving scale k_0 by hand and zero all modes with $k < k_0$ where $k_0 = 2\pi/(r_{100}/4)$ in this paper, while we assume that the dissipation scale is unresolved. In practice, we create a random realisation of a velocity field on a mesh of resolution N_v^3, with $N_v = 256$. The finite resolution automatically introduces a small-scale cut off of $2\pi/(r_{100}/128)$, and we assume that the one-point variance on the grid, σ_v^2 can be equated to a non-thermal temperature of T_{nt}. For the simulation codes used in this study, we add the respective velocity by interpolating from the particle/AMR cell positions to the grid on which we made a realisation of the velocity field. Then the corresponding thermal energy of $k_B T_{nt}$, is subtracted from each particle/AMR cell. This keeps the total energy of the system constant down to the level of Poisson noise in the grid and particle distribution.

5.3. Methods

In order to compare theoretical expectations outlined in the previous section with full non-linear calculations, we run idealized hydrodynamical simulations of self-gravitating gas using two independently developed numerical codes. This section gives a brief description of these codes and the methods they adopt to solve the equations of ideal hydrodynamics.

5.3.1. Initial conditions

As a model for the hot cluster gas, we adopt the model of Komatsu & Seljak (2001) that we already described in Subsection 5.2.1. In our numerical experiments, we however make two important modifications compared to this model: First, we include the self-gravity of the gas sphere, which was ignored in the KS01 model. To this end, we rescale the gravitational acceleration of the model to that of only the dark matter by multiplying with a factor of $(1 - M_{gas}/M_{100})$ and calculate the self-gravity of the gas self-consistently. Second, we adopt a polytropic exponent of $\gamma = 5/3$, while KS01 originally adopted the effective polytropic index that they derived as a constraint of the model ($\gamma = 1.137$ for our cluster parameters).

As a model for the bubble inflated by a central AGN, we use a sphere of radius 10 kpc placed close to the centre of the halo and heated to a temperature of 10^9 K. The associated thermal energy, $\sim 3 \times 10^{59}$ erg, is identical in all experiments and roughly consistent with what observations suggest (e.g. Bîrzan et al., 2004).

5.3.2. Lagrangian methods

For all Lagrangian hydrodynamic simulations, we use the Gizmo code (Hopkins, 2015), which includes various Lagrangian methods, among them TSPH, PSPH and MFM, that we use in what follows.

- Traditional SPH (TSPH; e.g. Lucy, 1977; Gingold & Monaghan, 1977; Monaghan, 1992) has been widely used in astrophysics, especially to study structure formation in the universe (for recent reviews e.g. Rosswog, 2009; Springel, 2010a; Monaghan, 2012; Price, 2012, and references therein) because of its great advantages, e.g. Galilean invariance, automatically adopted spatial resolution and exact mass conservation. However, it is also known that TSPH has difficulties to deal with fluid mixing. For example, the artificial tension on the contact surface of multi-phase fluids suppresses the growth of the KHI (e.g. Okamoto et al., 2003; Agertz et al., 2007).

- Subsequent studies have made a lot of efforts to overcome the difficulties (e.g. Ritchie & Thomas, 2001; Inutsuka, 2002; Read et al., 2010; Abel, 2011). One of the modern formulations of SPH, the pressure flavour of SPH (PSPH; Saitoh & Makino, 2013; Hopkins, 2013) resolved them by replacing the volume element estimated from the mass density of an SPH particle (which is a technique used in TSPH) with that estimated from pressure (or energy density) of the particle and handled the fluid mixing instabilities, including the KHI and Rayleigh-Taylor instability.

- Hopkins (2015) recently proposed a new class of particle methods for numerical hydrodynamics, meshless finite mass (MFM) and meshless finite volume (MFV), which have advantages of both SPH and grid-based schemes. These methods adopt a kernel-weighted volume discretization like SPH, but with a high-order matrix gradient estimator. A Riemann solver evaluates fluid (mass, momentum and energy) fluxes between particles, whose effective volume elements are overlapped. The limit of the MFM/MFV method with an infinitely sharply peaked kernel function corresponds to the moving-mesh method with non-regular deformed grids, e.g. the Voronoi tessellation (Springel, 2010b; Duffell & MacFadyen, 2011; Gaburov et al., 2012).

The initial particle distribution which follows the KS01 density profile is drawn by using the rejection sampling scheme and thermal energy is assigned to each particle by interpolating the temperature profile of the KS01 model. To model AGN bubbles in the ICM, we increase the thermal energy of particles contained in the bubble within a radius of 10 kpc to have temperature of 10^9 K. In all runs using Gizmo, we set the smoothing length, h, to the equivalent of what contains 32 neighbour particles and use the cubic spline kernel function. The gravitational softening in computing the gas self-gravity is fixed to be 1 kpc. We employ 67 108 864 particles, unless stated otherwise. The maximum spatial resolution is typically $2h \sim 10$ kpc at the centre and the mass resolution is

$6.7 \times 10^5\,M_\odot$. The self-gravity of the gas is computed using the tree algorithm (Barnes & Hut, 1986) with an opening angle of $\theta = 0.7$ (default setting in GIZMO). The gravity of the DM halo is computed with a fixed analytical potential (see Subsection 5.2.1 and Subsection 5.3.1 for details).

5.3.3. Eulerian methods

For the Eulerian hydrodynamics simulations, we use the adaptive mesh-refinement (AMR) code RAMSES. RAMSES solves the hydrodynamic equations using a second-order, unsplit Godunov scheme. This method is known to accurately capture shocks. Fluxes are reconstructed from the cell-centred values with the Harten-Lax-van Leer-Contact (HLLC) Riemann solver that uses a first-order MinMod Total Variation Diminishing scheme. RAMSES uses a tree structure, which allows for cell-by-cell refinement, thanks to which computational resources can be focused at high-density regions.

The initial conditions for the density and pressure of the ICM sphere are interpolated from the respective KS01 profiles. The AGN bubble is modelled by raising the temperature of all cells whose centres fall within the bubble radius to 10^9 K. We have used boundary conditions which allow only for outflow. Cells are refined based on the quasi-Lagrangian approach, when gas mass in the cell exceeds $1.94 \times 10^7\,M_\odot$. This leads to a similar number of leaf cells, 59 211 888 at the initial time, compared to the number of particles in GIZMO runs. This also leads to mean mass of $8.6 \times 10^5\,M_\odot$ and median mass $6.6 \times 10^5\,M_\odot$, where the latter is almost identical to the mass resolution in GIZMO. Maximum spatial resolution achieved is 1.64 kpc (11 levels of refinement), while minimum resolution is 52.5 kpc (6 levels of refinement; base grid). We use analytical gravity for the DM halo described in Subsection 5.2.1 and Subsection 5.3.1. Self-gravity of the gas is calculated using the relaxation solver in RAMSES and added to the halo potential.

5.3.4. Spherical 1D validation code

For spherically symmetric initial conditions in general cases where analytic solutions do not exist, we have run a simple spherical 1D MUSCL solver which includes solvers for one-dimensional spherical hydrodynamics and self-gravity. We use this 1D code in order to validate the solutions of the three-dimensional solvers discussed above during those stages when the solution is still close to spherically symmetric. The initial gas density and temperature are set as in RAMSES. The boundary conditions are reflective in the centre and outflow at the outer boundary. Self gravity can be calculated trivially in spherical 1D by summing mass shells up to a given radius and the same analytical potential with that in runs of GIZMO and RAMSES is adopted to compute the gravity of the DM halo.

5.4. Simulations

In what follows, we present the results of our numerical experiments. We summarise all the runs performed in Table 5.1; all spherically symmetric runs were also run with the 1D code. We first verify that our ICM is indeed close to hydrostatic equilibrium and remain so over an extended period of time with all numerical methods. Next, we investigate the evolution of an AGN-inflated hot bubble in such a hydrostatic ICM. We also consider the sophistication of our ICM model by replacing a fraction of its thermal

Table 5.1: Summary of simulation runs used in this study. Parameters varied with respect to the fiducial run are highlighted in bold print. Columns: (1) subsection in which the simulations are discussed; (2) resolution at which simulation was run ('low' means 'levelmax=9' for RAMSES and 8 million particles for GIZMO; 'high' means 'levelmax=11' for RAMSES and 64 million particles for GIZMO); (3) presence and location of bubble: 'no', 'centred', 'off-centre'; (4) presence of turbulence in the initial conditions.

Section (1)	resolution (2)	bubble (3)	turbulence (4)
5.4.1	low	no	no
5.4.2	low+high	centred	no
5.4.3	low+high	off-centre	no
5.4.4	low+high	off-centre	yes

energy with turbulence. Here we emphasize again that the main purpose of this study is to see if any systematic differences between the hydrodynamical solvers, commonly used in cosmological simulations, are observed even in our idealized simulations. Thus, the numerical resolutions employed, and described in Section 5.3, are comparable with those of current state-of-the-art cosmological simulations. We additionally perform simulations with degraded resolution to test the numerical convergence.

5.4.1. Stability of the ambient gas sphere

We first verify how close to hydrostatic equilibrium the clusters remain over an evolution time of 1 Gyr. The results of this stability test are shown as solid lines in Figure 5.2. Despite the differences from the original model of KS01 (self-gravity of the gas and equation of state), the differences between the original model (brown dashed line) and the simulation results are small. The gas profiles for density (first row) and temperature (second row) show a very minor evolution due to the system readjusting to a new hydrostatic equilibrium with an expansion of $\sim$ 30km/s. More remarkably, a similar degree of stability is seen when we replace some thermal energy with turbulent kinetic energy. And, even if we include turbulence at a very high level of $T_{\rm nt} = 0.5T_{\rm vir}$ in the ambient gas sphere, the spherically averaged radial profiles of density and temperature do not significantly deviate from the state shown in Figure 5.2. Here $T_{\rm vir}$ is the virial temperature of the DM halo, $T_{\rm vir} \approx 1.8 \times 10^7$ K and the corresponding velocity dispersion is $\sigma_{\rm vir} \sim 835$ km/s. We can therefore conclude that the gas sphere is reasonably stable and we adopt it as the ambient ICM of the AGN bubble in the following simulations. We note that our decision to neglect radiative cooling throughout this paper is well justified since the cooling timescale is longer than the buoyant timescale ($\sim$ 1 Gyr), that we study here, by a factor of $\sim$ 5, as shown in the fourth row.

In all cases we investigated, the turbulent energy decayed in a much shorter time, $\sim$ 30Myr, than the total time of evolution of 1 Gyr. We also note that the Poisson particle noise puts the gas locally out of hydrostatic equilibrium in all runs using Gizmo . This drives a persistent 'particle jitter' since the system responds by producing velocity dispersion (third row) which carries the difference in internal energy when compared to Ramses and the 1D code.

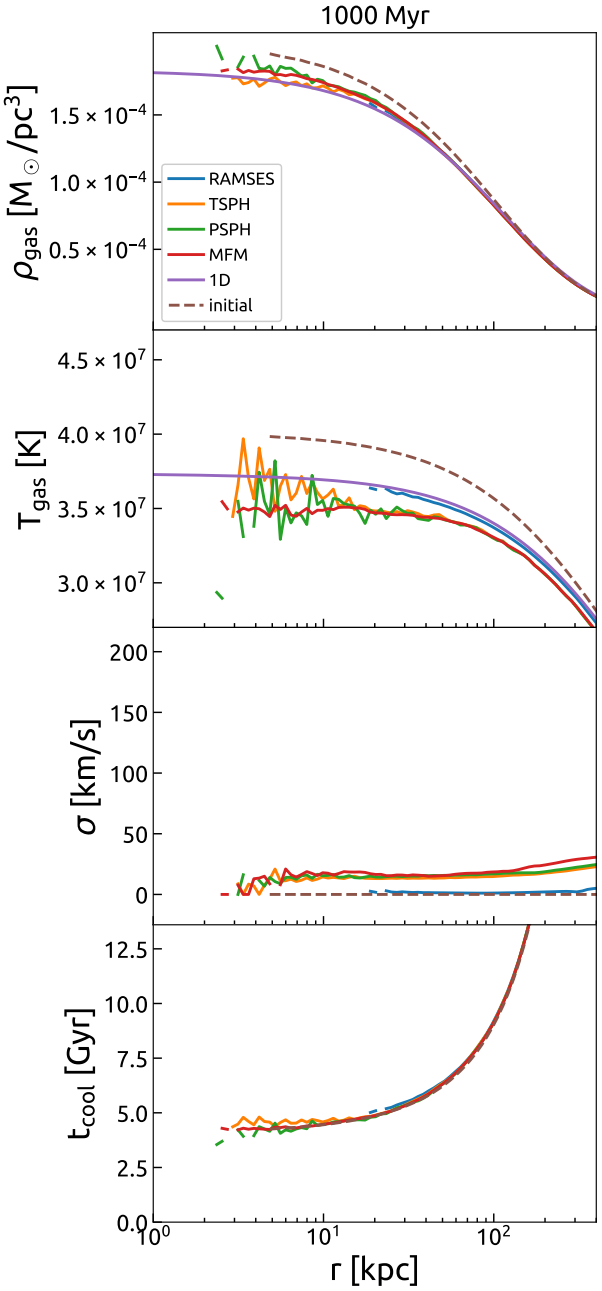

Figure 5.2: Radial profiles of gas density (first panel), temperature (second), velocity dispersion (third) and cooling timescale (fourth) after 1 Gyr of isolated evolution. Solid lines show profiles from numerical simulations using RAMSES(blue), TPSH (yellow), PSPH (green), MFM (red) and the 1D code (purple), and the brown dashed one represents the profiles of the KS01 model. Each simulation is initialised in the same way - density and temperature follow KS01. All runs are performed at a lower resolution than in the runs with an AGN bubble - GIZMO simulations with 8 388 608 particles, RAMSES simulation with `levelmax`=9.

5.4.2. Expansion of a central AGN bubble

In this subsection, we study the expansion of an AGN bubble inflated at the centre of the ICM sphere. We increase the initial temperature of fluid elements, i.e. particles in the Gizmo runs and cells in Ramses and the 1D code, within a central spherical region of 10 kpc to 10^9 K while the density profile follows that of the KS01 model. The initial gas velocity is set to zero, i.e. we do not include turbulent velocities yet. While the central bubble is buoyantly unstable according to the Schwarzschild stability condition for convection, Eq. (5.1), the instability should not arise due to the symmetry of the system. In perfect symmetry it should just expand, but particle noise (Gizmo) and anisotropy due to the Cartesian mesh (Ramses) break this symmetry and let the bubble rise after some time. During the early phase of the simulations the bubble remains however symmetric and we can compare the results of the 3D simulations with that of 1D simulations with a much higher resolution.

Figure 5.3 depicts radial profiles of gas density (upper), temperature (middle) and radial velocity (bottom) after 100 Myr. The expanding bubble creates a strong shock wave which propagates outward. The shock positions in the simulations with different hydrodynamic solvers agree very well with each other (~ 100 kpc). The shock wave leaves a diffuse and hot core at the centre by compressing and accumulating the ambient ICM. While the overall features of the 1D solution are captured by all 3D runs, some differences in the core ($r \lesssim 10$ kpc) are visible due to the lack of resolution in the 3D runs. The profiles obtained in 3D simulations are consistent with each other in the radial range of $r = 10^1 - 10^3$ kpc. Comparing the results of 3D simulations at high (thick lines) and low (thin lines) resolution, the profiles are numerically converged down to $r \sim 20$ kpc, which corresponds to the spatial resolution in the simulations with lower resolution. An additional interesting difference between the 1D and 3D runs is the presence of a pulsating mode in the 1D run interior to the shock and visible as wiggles behind the shock position. It appears that due to lack of resolution such modes are efficiently damped out in the 3D runs.

5.4.3. A rising bubble in non-turbulent ICM

In this subsection, we investigate the rising of buoyantly unstable AGN bubbles and their interaction with the ambient ICM. As in the simulations of the previous section, we change the initial setup by increasing the temperature of fluid elements within the bubble with a radius of 10 kpc to 10^9 K. Now however, the centre of the bubble is shifted to the upper right oblique 45 degree direction in the $x-y$ plane by 10 kpc from the centre, keeping the temperature outside the bubble and density to be those of the KS01 model. Turbulence is not taken into account and the initial velocity is set to be zero. Since the shifted hot bubble breaks both the Schwarzschild stability condition for convection, Eq. (5.1), and the symmetry of the system, it must be buoyantly unstable and rising. The amount of the injected thermal energy is almost the same as that in the simulations with a *central* bubble, $\sim 3 \times 10^{59}$ erg.

Figure 5.4 shows slices of gas density after 1 Gyr in the runs with the shifted bubble. The fate of rising bubbles very clearly depends strongly on the choice of hydrodynamical solvers. The bubble is rising towards the direction of the initial displacement (upper right oblique 45 degree direction in the $x - y$ plane). It survives unharmed and reaches large radii in the TSPH run (upper left). This result is inconsistent with the analytical

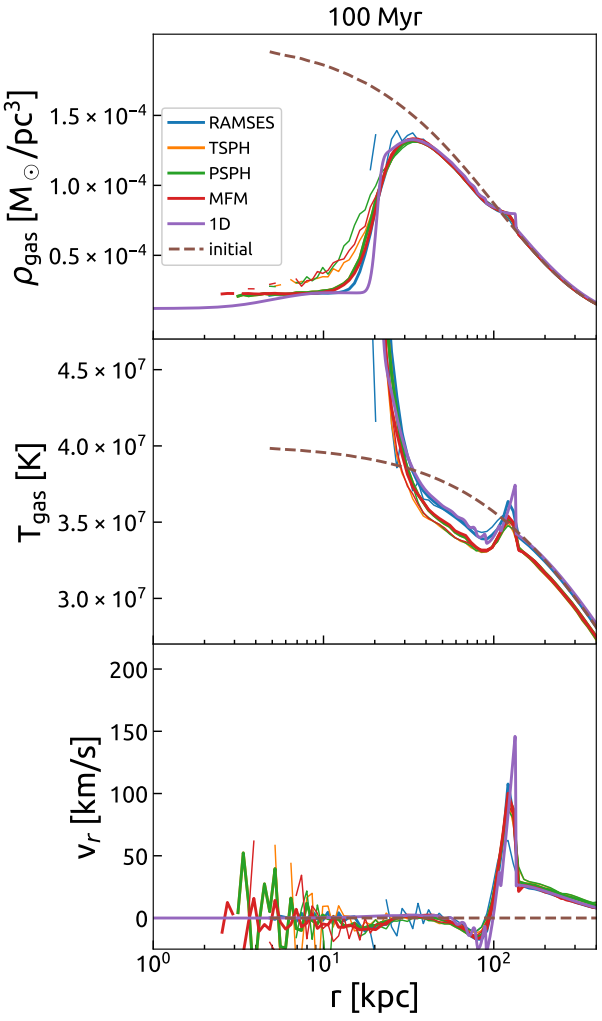

Figure 5.3: Radial profiles of gas density (upper), temperature (middle) and radial velocity (bottom) 100 Myr after an injection of thermal energy by raising the temperature in the central 10 kpc to 10^9 K. Solid lines show profiles from numerical simulations using Ramses(blue), TSPH (yellow), PSPH (green), MFM (red) and the 1D code (purple). Thick and thin lines are the results of simulations with the high- (64 million particles in the Gizmo runs and `levelmax`=11 in the Ramses run) and low resolution (8 million particles in the Gizmo runs and `levelmax`=9 in the Ramses run), respectively. The initial condition is shown as a brown dashed line.

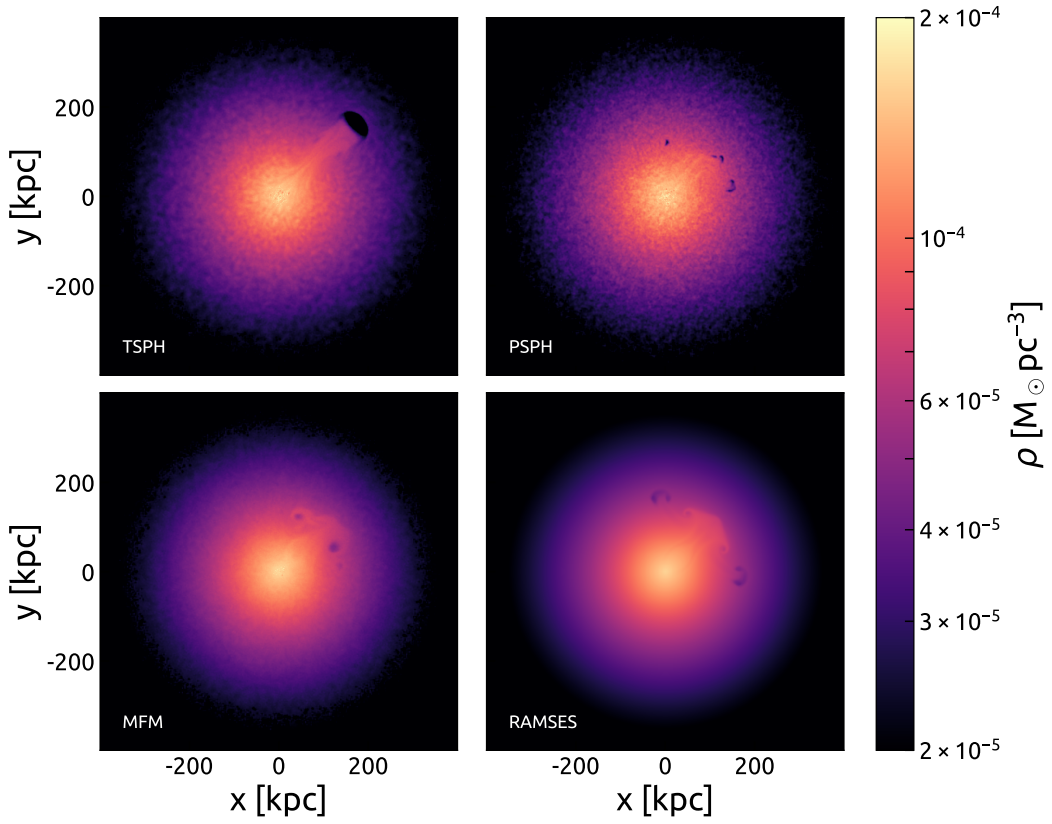

Figure 5.4: Slices through the gas density distribution for TSPH (top left), PSPH (top right), MFM (bottom left) and RAMSES (bottom right) after 1 Gyr of evolution of a bubble initially shifted from the centre. Each simulation is initialised in the same way - density and temperature follow KS01 and we artificially raise the temperature within the bubble whose centre is shifted to the upper right oblique 45 degree direction in the $x - y$ plane by 10 kpc from the centre of the gas sphere to 10^9 K. The radius of the bubble, 10 kpc, is the same as the runs shown in the previous section.

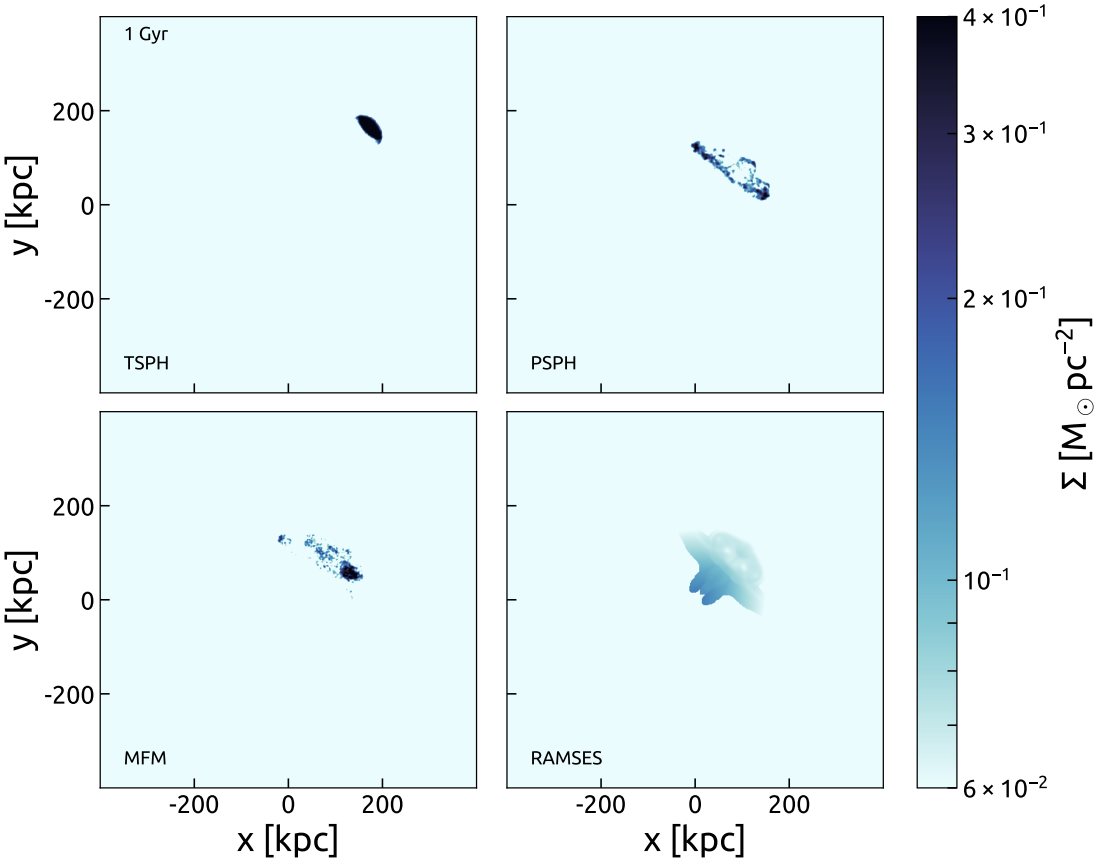

Figure 5.5: Projection of the density distribution of gas initially contained in the heated bubble for TSPH (top left), PSPH (top right), MFM (bottom left) and RAMSES (bottom right) after 1 Gyr of evolution. The same simulations as in Figure 5.4 are shown.

expectation discussed in Figure 5.1 and caused by the well-known suppression of fluid instabilities by the spurious surface tension (e.g. Okamoto et al., 2003; Agertz et al., 2007). In other runs, the bubble is dissolved by the KHI while configurations are different from one another. The bubble is fragmented into smaller ones in the PSPH run (upper right). In contrast, the MFM one (lower left) looks very similar to the Ramses result (lower right), while the symmetry of the structure is broken in the MFM run by Poisson noise contained in the initial particle distribution (see also Figure 5.7 for a discussion of resolution effects). The difference in bubble morphology between hydrodynamical solvers of translates of course directly into differences in the redistribution of mass, including metals, and energy by the rising bubble.

In order to better visualize the fate of the heated fluid elements, we next study how the rising bubble is dissolved in the ICM in more detail by explicitly tracking the fluid elements initially contained in the heated sphere. For the Gizmo runs (TSPH, PSPH and MFM), the Lagrangian nature allows us to follow the heated fluid elements through the ID of particles. If metal mixing is not explicitly performed in SPH, this would also track the evolution of metals contained in the hot bubble. While MFM method computes the

fluxes between particles like Eulerian schemes and thus gas initially contained in the bubble may dissipate, we use the ID of particles to follow the heated fluid elements. In Eulerian schemes, like Ramses, tracking fluid elements is more complicated. We take a simple approach here and follow the gas that was initially within the bubble by injecting a passive tracer variable in the grid, which is advected with the flow of the gas. This is similar in spirit to injecting metals from supernovae explosions, but in our case we inject the tracer only at the beginning of the simulation and its value in no way modifies any other properties of the grid. This method only approximates tracking of the gas flow in the grid and a more advanced method which uses tracer particles in Ramses is currently in development (Cadiou et al., private communication). Having that in mind we caution that direct comparison between grid passive tracer and particle IDs can be only qualitative. On the other hand, both cases in fact correspond rather well to the evolution of metals in the flow in the different methods.

Figure 5.5 shows the projected density, integrated along the line of sight (LoS), of gas initially contained in the heated bubble at 1 Gyr. It is apparent that, in all cases, the bubble is not fully mixed with the ICM yet, while the specific bubble configuration depends on the choice of hydrodynamical solver, just like the density distribution of the ICM. In the TSPH run (upper left), the heated fluid elements are confined to a small region which corresponds to the less-dense cavity in the upper left panel in Figure 5.4. This is another indication that the bubble survives largely unaffected in the TSPH run due to the artificial suppression of the growth of fluid instabilities. In other runs, the bubble is more elongated and less-dense compared with the TSPH run since they handle the instabilities better while the bubble is not completely dissolved and mixed with the ICM even in these runs. In the PSPH (upper right) and MFM (lower left) runs, one can find small density fluctuations on the bubble surface which originate from the Poisson noise in drawing of the initial particle distribution. The bubble has a symmetric structure in the Ramses run thanks to the absence of such noise. Fluctuations in density and velocity fields would of course always exist in the real ICM. We will study the impact of such 'noises' below in Subsection 5.4.4 by introducing, in a controlled way, a turbulent velocity field.

The pressing question is of course whether such morphological differences are also reflected in integral properties of the ICM and thus affect the efficiency of AGN feedback. We thus next investigate how the bubble redistributes mass and energy into the ICM in Figure 5.6. The evolution of the profiles obtained from the quarter of the box in which the bubble rises is drawn from the left-most to right-most columns. As shown in Figure 5.3, the blast wave ignited by the injected thermal energy reaches to $r \gtrsim 100\,\mathrm{kpc}$ at $t = 100\,\mathrm{Myr}$. In those runs the energy was damped at the centre of the gas sphere. Assuming the self-similarity of the Sedov-Taylor solution and that the blast wave expands analogously in the runs in which the bubble is shifted, then it would reach $r = 200 - 300\,\mathrm{kpc}$ at $t = 300\,\mathrm{Myr}$. Indeed, as expected, it appears as peaks in the outskirts ($r \sim 300\,\mathrm{kpc}$) in the profiles of temperature (second row) and velocity dispersion (fourth row) of the left-most column. At later times it passes through the radial range demonstrated in Figure 5.6. Hence the dominating peaks shown in this figure are not originated by the blast wave, but by the rising bubble.

The bubble appears as the bump in the density profile (first row) and as peaks in others. Remarkably, we do not observe significant differences in the density profile. As illustrated in Figure 5.4, the hot bubble robustly survives for a long time in the TSPH run because of the spurious tension and we see rising of the hot bubble in the profiles of

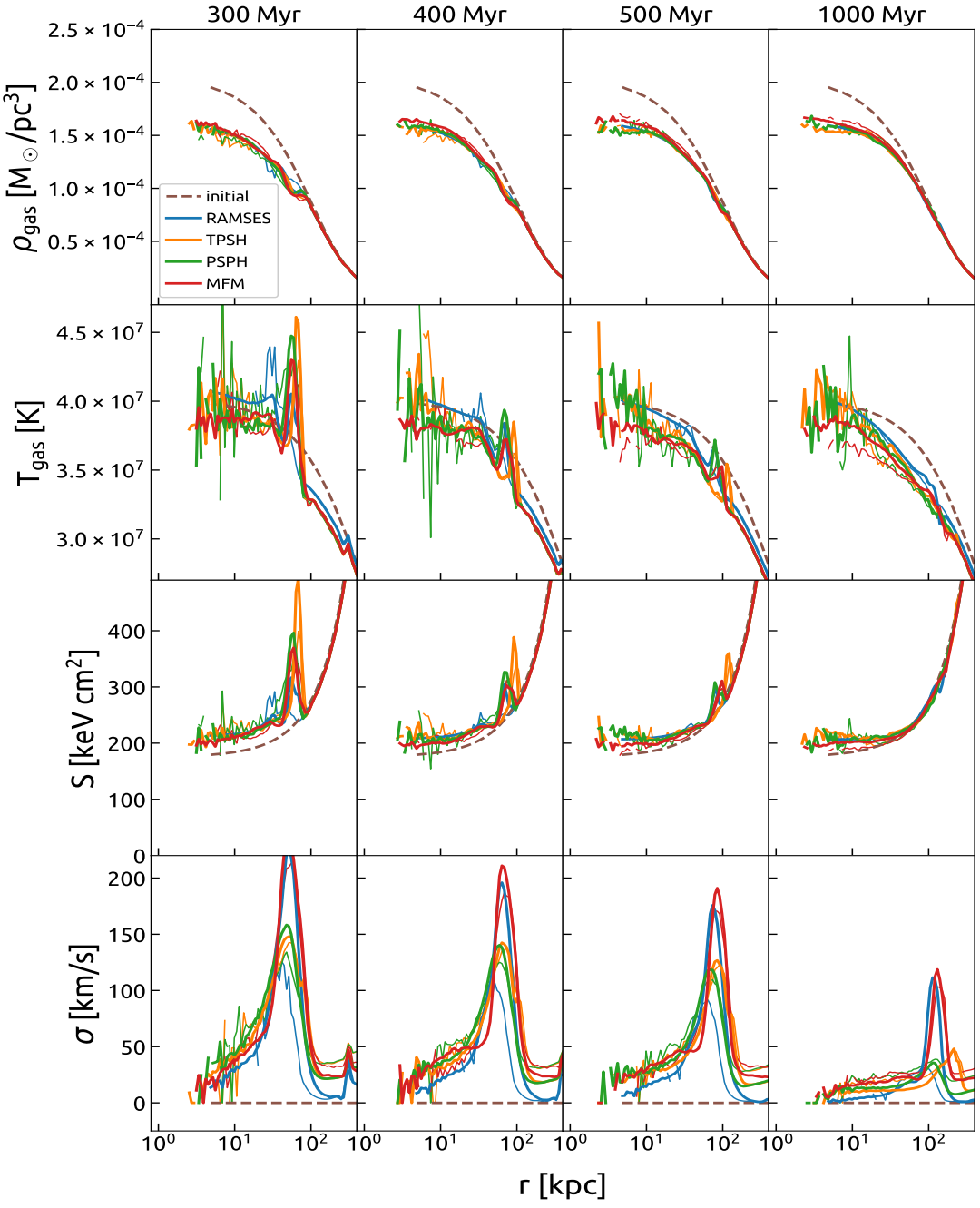

Figure 5.6: Mass-weighted profiles after evolution of 300 Myr (first column), 400 Myr (second), 500 Myr (third) and 1 Gyr (fourth). We focus our analysis only on the quarter of the box in which the bubble evolves. The profiles of gas density (first row), temperature (second), entropy (third) and three-dimensional velocity dispersion (fourth) are shown. Solid lines show profiles from numerical simulations using RAMSES (blue), TPSH (yellow), PSPH (green) and MFM (red). Thick and thin lines are the results of simulations with the high- (64 million particles in the GIZMO runs and `levelmax`=11 in the RAMSES run) and low resolution (8 million particles in the GIZMO runs and `levelmax`=9 in the RAMSES run), respectively. The brown dashed line represents the KS01 model.

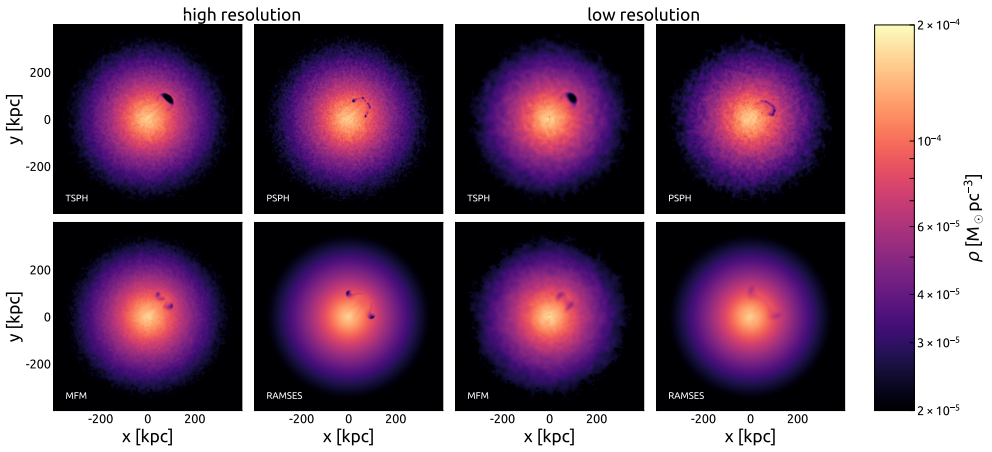

Figure 5.7: Resolution effects in the density slices. The left four panels show the density slices at $t = 500$ Myr obtained from simulations with the high resolution we adopt as the standard level (64 million particles in the Gizmo runs and `levelmax`=11 in the Ramses run) and the right four show those in runs with a degraded resolution (8 million particles in the Gizmo runs and `levelmax`=9 in the Ramses run). A shifted hot bubble is initially set and the turbulent velocity field is *not* introduced in all runs. In each group of panels, the results of simulations using TSPH, PSPH, MFM and RAMSES are illustrated in the upper left, upper right, lower left and lower right panels, respectively.

temperature (second row) and entropy (third row). On the other hand, because the bubble is being dissolved and turbulent motions could arise in MFM and Ramses runs, the thermal energy contained in the bubble is converted into kinetic energy (fourth row) and the peaks are less pronounced in the profiles of temperature and entropy. The behaviour of the PSPH run is intermediate between the two groups, as expected from Figure 5.4 in which the bubble is fragmented into smaller ones in the PSPH run. Note the velocity dispersion, 100-200 km/s, of the turbulent motion driven by the bubble is roughly consistent with the observation of the Perseus cluster (Hitomi Collaboration et al., 2016) and simulation results by Lau et al. (2017, but see also Reynolds et al. 2015).

Regarding the dependence on numerical resolution, the profiles of density and temperature are well converged, while the latter gets noisier in the simulations with the lower resolution (thin lines) compared to the higher resolution simulations (thick lines). By definition, $S \propto \rho T^{-2/3}$, which means that the entropy profile is numerically converged as well. Note that the MFM runs are not perfectly converged with differences at the level of $\sim 10\%$. While the velocity dispersion profiles in the Gizmo (MFM and SPH) runs show relatively good convergence, the Ramses run at lower resolution has a lower maximum velocity dispersion ompared to the higher resolution simulation. This might be due to the diffusive nature of AMR codes at low resolution, but to study this in detail would be beyond the scope of this paper. While we thus observe some dependence of the profiles on the numerical resolution employed, i.e. they are not perfectly converged, it is not significant enough to change our conclusions.

Then we study how the resolution effects affect the structure of the bubbles and their survivability. Figure 5.7 compares the images obtained from the simulations, varying the resolution. The left four panels are the density slices from simulations with the high resolution we adopt as the standard level and the right four are those from the runs

with lower resolution. The RAMSES simulations have similar numbers of leaf cells to the number of particles in the GIZMO simulations of each resolution level. The overall structures, e.g. the direction to which the bubble is rising and position of the bubble, are well captured at the both resolutions. However, there are apparent differences between the two levels of resolution on the small scale, e.g. number of fragmented smaller bubbles and separation between them. In spite of the resolution dependence, our conclusion is not changed because the differences among the hydrodynamical solvers are more significant.

In summary, the choice of hydrodynamical solver does change the fate of the buoyantly unstable hot bubble and the mass and energy redistribution driven by it in simulations. In the TSPH run, the rising bubble survives for a time inconsistent with the analytical expectation and reaches large radii because spurious tension suppresses the growth of fluid instabilities on the surface. As a result, the thermal energy is locked in the bubble and a smaller fraction of energy, compared with those in the runs using the other hydrodynamical solvers, is distributed to the ambient medium. On the other hand, in the simulations using hydrodynamical solvers which can handle fluid instabilities, the bubble is dissolved in a timescale consistent with the analytical expectation (a few 100 Myr, see Figure 5.1) and the thermal energy originally contained in the bubble is converted to non-thermal turbulent energy. In the real ICM, energy would continuously change the form, e.g. transformation from thermal energy to kinetic energy (via bubble rising) and vice versa (via dissipation).

In addition, the different evolution of the bubble can also lead to differences in the metal distribution in the ICM. Supposing that the bubble, which comes from the centre of the cluster, is metal enriched (if metallicity gradients are present), a more diffusive metal distribution, i.e. lower metallicity, would be observed in simulations using the schemes which can handle fluid instabilities (see e.g. Martizzi et al., 2016). This would be further enhanced if the metals are diffused between fluid elements. We study the more complicated and realistic phenomena, rising of an AGN bubble in a turbulent ICM, in the next section.

5.4.4. A rising bubble in a turbulent ICM

This subsection investigates how small fluctuations in the ICM affect the rising bubble and also their back-reaction. In order to study this effect, we introduce a turbulent velocity field following a Kolmogorov power spectrum (see Subsection 5.2.4) with the non-thermal temperature of $T_{\rm nt} = 0.03 T_{\rm vir} \approx 5.4 \times 10^5$K which corresponds to a velocity dispersion of 147km/s, consistent with the X-ray observation of the Perseus cluster (Hitomi Collaboration et al. 2016, see also ZuHone et al. 2018). In the initial conditions of the ICM we subtract the corresponding thermal energy from the ICM. Other parameters such as resolution parameters, bubble temperature and size, are the same as those in Subsection 5.4.3.

Figure 5.8 shows the projected density distribution of gas initially contained in the heated bubble at 1 Gyr in the runs with the turbulent velocity field. Because of the perturbations due to turbulence, the bubble does not rise in the direction of the initial offset (upper right oblique 45 degree direction in the $x-y$ plane). In addition, turbulence introduces perturbations of smaller wavelengths which grow faster (see Eq. (5.4)) and thus enhances instability of the bubble surface. As a result, the bubble is more quickly disrupted and mixed with the ICM compared to the non-turbulent case (Figure 5.5), using hydrodynamical schemes which can handle the instabilities (PSPH, MFM and RAMSES).

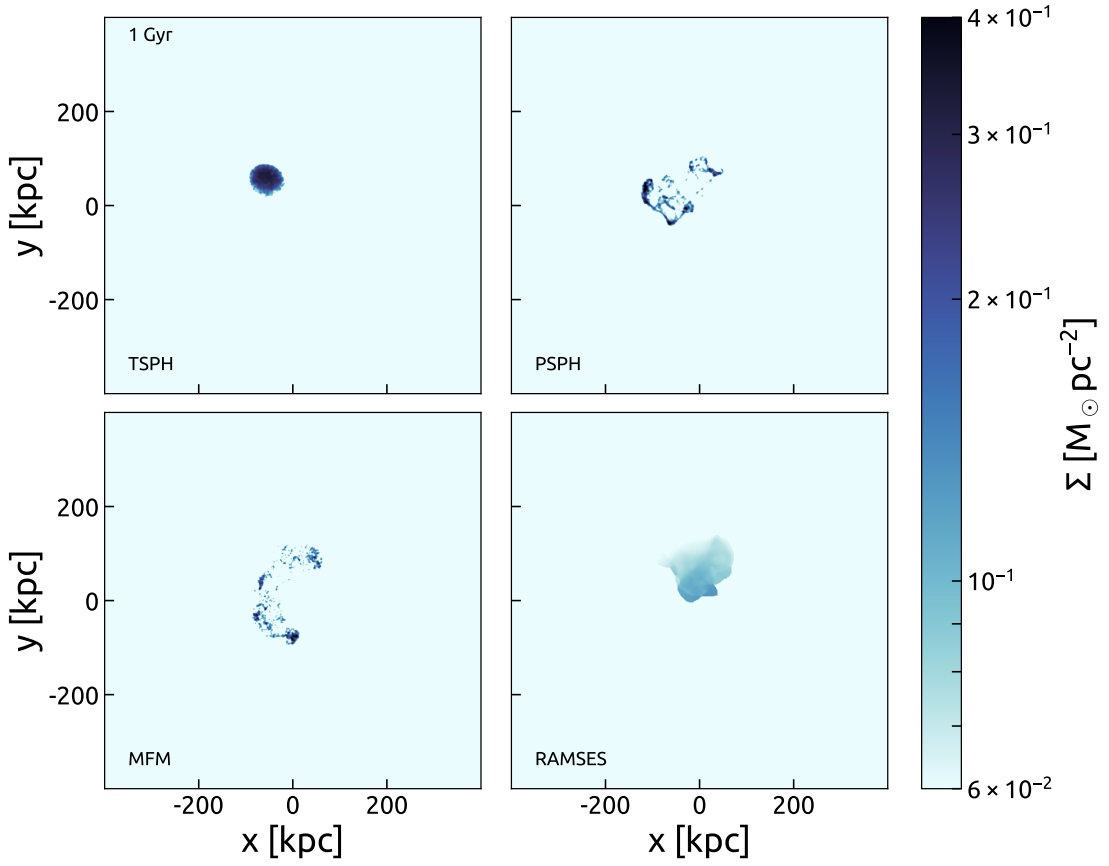

Figure 5.8: Projection of the density distribution of gas initially contained in the heated bubble for TSPH (top left), PSPH (top right), MFM (bottom left) and RAMSES (bottom right) after 1 Gyr of evolution. Here, the results of simulations with a controlled turbulent velocity field of $T_{\mathrm{nt}} = 5.4 \times 10^5$ K are shown.

However, just as in the non-turbulent run, the bubble in the TSPH run robustly survives due to the suppression of the growth of fluid instabilities by artificial surface tension (upper left). Note that the distance from the centre of the cluster to the (remnants of) bubbles in the turbulent runs is smaller than those in the non-turbulent ones. This and enhanced mixing imply that redistribution of mass, including metals, and energy may be also enhanced around the centre in this case.

We study this point using Figure 5.9 which presents the profiles of gas density (first row), temperature (second), entropy (third) and velocity dispersion (fourth). The evolution is shown from the left-most to right-most columns. Unlike before, we now use the whole simulation box to measure the profiles since the direction of rising of the bubble is no longer the same in all runs, as shown in Figure 5.8. We note that this dilutes the signature of bubbles in the profiles since the part of the simulation box that is not significantly affected by the bubble is included in the analysis. We see no significant differences between hydrodynamical solvers in the first three profiles from the top and they are numerically well converged (thick lines vs. thin ones), except for the temperature profile in the MFM runs. However, peaks in the velocity dispersion profiles are more evident in the MFM and Ramses runs compared with the SPH runs at the higher resolution level, comparable to those in the cosmological simulations (thick). Again, we interpret this as differences in the efficiency of conversion of thermal energy to turbulent (kinetic) energy when the bubble rises.

It is also worth mentioning that the turbulence decays in all runs, especially in the centre of the cluster where the crossing time is shorter than that measured at the outskirts. Interestingly, the decay of the turbulent velocity field is more significant in the SPH runs compared with the MFM and Ramses ones in the runs of the higher resolution (thick), while the degree of the turbulent decay in the Ramses run of the lower resolution (blue thin) is comparable to those in the SPH runs. Since perturbations with shorter wavelength, which are introduced by turbulence and grow faster, enhance dissolving of the bubble and mixing with the ICM, these mechanisms would be non-linearly degraded in SPH simulations, while a stronger turbulent velocity field is kept in the MFM and Ramses runs. We expect that the sub-grid physics models in cosmological simulations which trigger sequential and/or multiple AGN bubbles in the ICM can enhance such contrasts between hydrodynamical solvers. To test this hypothesis, more systematic comparison studies varying not only hydrodynamical solvers but also resolution and sub-grid physics would be needed, which is however beyond the scope of this brief study. Note that while some profiles are not numerically converged, the degree of significance is not large enough to change the conclusions.

5.5. Summary and discussion

AGN feedback is believed to be an important heating source to keep the ICM in the cluster centre hot and diffuse, and a key to avoid the central cooling flow problem. A number of studies have used numerical simulations to investigate the effect of AGN feedback on the properties of the ICM. However, despite progress in hydrodynamical solvers and modelling of AGN feedback in numerical simulations, a full consensus among cosmological hydrodynamical simulations has not been reached yet and simulations for cluster cosmology are not yet predictive. This situation motivated us to investigate one of the possible reasons for the inconsistency: the difference in the hydrodynamical schemes

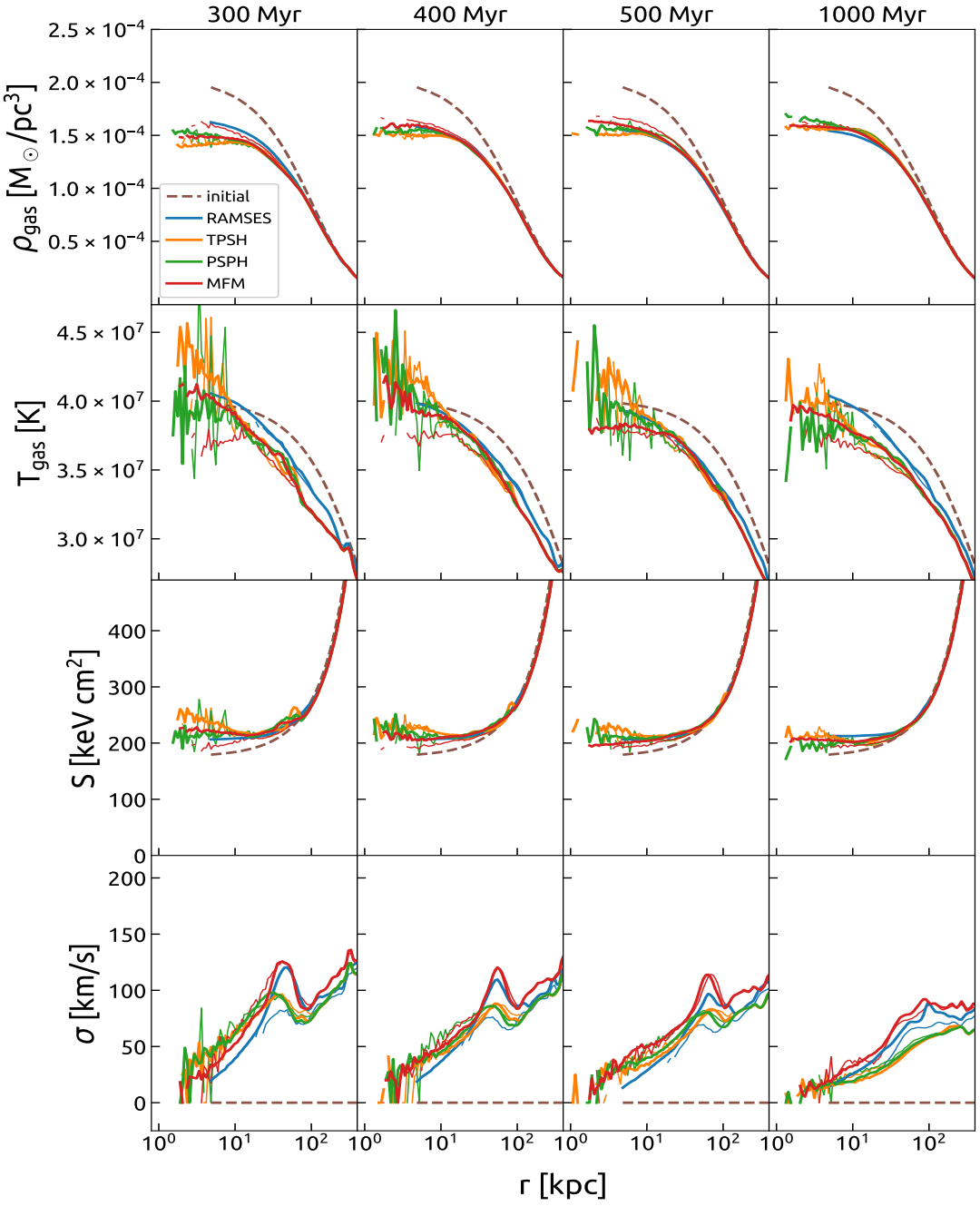

Figure 5.9: Mass-weighted profiles after 300 Myr (first column), 400 Myr (second), 500 Myr (third) and 1 Gyr (fourth) with turbulent initial conditions. Here, we analyse the whole box in each simulation. The profiles of gas density (first row), temperature (second), entropy (third) and three-dimensional velocity dispersion (fourth) are shown. Solid lines show profiles from numerical simulations using Ramses (blue), TPSH (yellow), PSPH (green) and MFM (red). Thick and thin lines are the results of simulations with the high- (64 million particles in the Gizmo runs and `levelmax`=11 in the Ramses run) and low resolution (8 million particles in the Gizmo runs and `levelmax`=9 in the Ramses run), respectively. The brown dashed line represents the KS01 model.

employed in various simulations. For this purpose, we studied the evolution of rising bubbles inflated by AGN feedback in ideal self-gravitating hydrodynamics. According to observations, the bubbles may be pockets of a significant amount of thermal energy (and cosmic rays, which are however not yet routinely included in cosmological simulations) and hence studying the interaction between the bubble and the ICM is important to make progress.

Using a simplified model, we first showed that a hot bubble will rise buoyantly in the ICM and is prone to surface instabilities that act to disrupt and mix it over time scales of 1 Gyr for a typical cluster of a few $10^{14}\,M_{\odot}$. If the hydrodynamical solver captures fluid instabilities (i.e. the KHI here) well (such as MFM and Ramses that we studied here), the bubble is disrupted as expected. However, the bubble survives for a longer time than the analytical expectation in simulations using traditional SPH due to spurious surface tension suppressing the growth of instabilities. In the simulation employing the PSPH scheme, we observed that the bubble instead fragments into smaller ones. In addition, we found that if the bubble is metal enriched compared to the ICM at larger radii, a more diffusive metal distribution, i.e. lower metallicity, may be observed in simulated galaxy clusters using hydrodynamical solvers which can model well fluid instabilities (see also e.g. Martizzi et al., 2016), and particularly so in when comparing with Lagrangian schemes that in addition neglect metal diffusion at the fluid element scale.

Because of the difference in bubble mixing, the energy redistribution in the ICM driven by the rising bubble depends somewhat, but less than initially expected, on the choice of hydrodynamical solvers in simulations. Using the hydrodynamical solvers that can capture fluid instabilities, the thermal energy contained in the bubble is transformed more readily into kinetic energy because dissolving of the bubble drives turbulent motion in the ICM. In contrast, the thermal energy is captured in the surviving bubble and transported to large radii in the TSPH simulation. The energy redistribution observed in the PSPH simulation is similar to that in the TSPH run.

In a second step, we investigated whether the various methods agree better in a turbulent ICM, where random motion act to increase bubble disruption and mixing. When the numerical method resolves well fluid instabilities (here MFM and Ramses), the thermal energy initially contained in the hot bubble is again efficiently converted to kinetic energy of the turbulent motion. More surprisingly, even if we include the turbulent velocity field, the bubble robustly survived in the TSPH simulation while it is more significantly dissolved and mixed with the ICM in all other hydrodynamical solvers. We also found that in general the SPH schemes used in this study damp the turbulent velocity field more strongly than both Ramses and MFM. And, they also lead to less efficient conversion of the hot bubble to turbulent motion.

In summary, we have observed significant differences in the spatial distribution of the hot bubble after it mixes with the ICM when employing different hydrodynamical solvers. Somewhat surprisingly however, the differences in the gas profiles are not very significant. We also observe that some profiles may not be perfectly converged even with the resolution level of the current state-of-the-art cosmological simulations, although the degree of significance is not large to change the conclusion of this paper. While these results might imply that the choice of the hydrodynamical solvers is not the primary factor to explain differences in results obtained in different cosmological hydrodynamical simulations, we can only speculate here whether the differences we observed may be amplified if AGN feedback energy is injected repeatedly as the halo grows in mass. The

amount of injected energy into the AGN bubble in our simulations, $\sim 10^{59}$ erg, was only $\sim 0.1\%$ of the total thermal energy of the ICM. Assuming that the central super massive black hole, which is the engine of the AGN, has a mass of 10^9 $M_\odot$, the feedback energy over the timescale of our simulations, 1 Gyr, can be of order of $\sim 10^{62-63}$ erg if the AGN continues to be active (see e.g. Woo & Urry, 2002). While this naïve estimation provides of course just an upper limit, the budget of feedback energy could be much greater than what we assumed and recursive injections of AGN bubbles are expected in a duty cycle behaviour of central fuel gas consumption and replenishment.

Even if the feedback energy is the same as assumed in this work, the impact of the bubbles may be greater if the ICM has a low-temperature core in the centre, i.e. in a cool-core cluster, so that the central gas is close to a runaway cooling instability. We will revisit this aspect in future work.

Last but not least, additional physical processes that this study does not take into account may alter the evolution of the AGN bubble and the thermodynamics of galaxy clusters. For example, Scannapieco & Brüggen (2008) used idealized simulations of a similar setup to ours (including physical scales) and demonstrated that the buoyantly rising AGN bubbles can survive longer when unresolved turbulence is taken into account as an effective viscosity. The simulations with the turbulent viscosity observed bubbles of mushroom-like structures while the bubbles are more dissolved than those in our simulations when they did not include it. Our simulations have lower resolutions compared to theirs because of the larger size of the simulation box and thus have a larger numerical viscosity, aided further by the nature of hydrodynamical solvers we use. This can thus explain why at the resolutions we investigate we observe very similar mushroom-like structures (cf. e.g. Figure 5.4). Clearly, as cosmological simulations will probe smaller scales also in clusters, the inclusion of subgrid turbulence will become important.

One would further expect that magnetic tension also acts to suppress the disruption and mixing of buoyantly rising bubbles. We will investigate the interactions between the AGN bubble and ICM using idealised MHD simulations of several kinds of hydrodynamical solvers in a subsequent paper (Biernacki et al., in prep.).

6

Prospects

And so it goes...

– Kurt Vonnegut

Recent years brought understanding that modelling of SMBH dynamics and feedback is crucial for galaxy formation models. It is important to realise, however, that there are still many questions that require addressing. In this Thesis I have attempted answering some of them in the context of idealised simulations of massive, gas-rich galaxies. How are supermassive black holes perturbed by their environment? Can nuclear star clusters prevent supernovae feedback and massive clumps from ejecting the SMBH? How is the self-regulation of supermassive black hole growth achieved? How is the feedback from an active galactic nucleus interacting with the galactic fountain and wider halo gas? Do numerical recipes have an impact on the feedback energy deposition?

The answers I have presented here open up many new possible avenues for future research, some of which I will discuss briefly in this chapter. They reflect the ongoing work I am undertaking, thus the results should be seen mostly as preliminary.

6.1. Nuclear star cluster feeding SMBH

A galactic nucleus can be a violent place. A recent star formation event due to accretion of a giant molecular cloud can lead to formation of young massive stars that explode as supernovae within 20 Myr. As an outcome the nuclear region becomes depleted of gas, that could serve as a fuel for the SMBH accretion. Older stars, with masses $1 - 10\ M_{\odot}$, will eventually enter the asymptotic giant branch (AGB) phase and provide strong stellar winds that could feed the SMBH over a longer time scale. Is this scenario feasible and can the accretion be sustained by stellar winds from NSC? Does the AGN feedback matter for the SMBH growth?

Two extremes can be explored for the formation history of the NSC. Assuming that the entire NSC has formed within the aforementioned star formation event is the optimistic one, with only 10% of the cluster stars formed in the most recent event is more realistic.

In order to explore how these two setups influence the evolution of a SMBH, I simulate a NSC, which is modelled with a Plummer sphere with one million stellar particles of equal masses. Assuming that all the gas present in galactic centre was removed by a recent supernova explosion, the computational volume is populated only by the NSC and the SMBH. In practice I set the ambient density of the grid to 10^{-6} H cm^{-3}. In the 'young' NSC setup in which all stars produce wind. The 'old' NSC setup is identical to the previous one, but the wind injection is limited to the additional component - a stellar disc of 10^5 M$_\odot$ (following the Myamoto-Nagai profile). In all simulations the stellar wind is injected with a random direction with fixed velocity and mass rates ($\dot{M}_{\rm inj} = 6 \times 10^{-9}$ M$_\odot$/yr/M$_\odot$, Marigo et al. (2013)). This produces an isotropic wind when averaged over a period of time.

The mass of the NSC is chosen to be 5×10^7 M$_\odot$ with half-mass radius of ~ 8 pc. The SMBH is initialised static with $M_{\rm seed} = 10^6$ M$_\odot$. All initial conditions are generated using the DICE code[1]. The highest spatial resolution is 0.025 pc, thus the SMBH accretion region has radius of 0.1 pc. This allows me to resolve both the Bondi radius ($r_{\rm Bondi} \approx 1 - 5$ pc) and the SMBH radius of influence ($r_{\rm infl} \equiv GM_{\rm SMBH}/\sigma_*^2 \approx 0.5 - 1$ pc). I vary the AGN feedback between the thermal dump, the momentum kick and the direct radiation injection. These are compared to the baseline simulation without AGN feedback, but with Bondi accretion. All simulations are evolved for 1 Myr, which allows the gas disk to reach steady state.

To study the radiative AGN feedback, I use Ramses-RT, (Rosdahl et al., 2013; Rosdahl & Teyssier, 2015b). In this extension to Ramses radiative transport is performed on-the-fly with a moment method with M1 closure for the Eddington tensor. Thanks to this radiation is interacting with gas via photoionisation, photoheating and radiation pressure. A photon group with a chosen frequency interval is defined in each grid cell with the energy density E and the bulk radiation flux $\mathbf{F}$. As in Rosdahl et al. (2015) I group the photons into five bins, with the same energies, which are listed in Table 6.1. In order to keep the simulation runtime manageable, I use the reduced speed of light approximation (Gnedin & Abel, 2001), with $\tilde{c} = c/200$ (the impact of this choice is going to be assessed with a subset of simulations). The energy fraction per photon group follows the average spectrum of the quasar as discussed in Sazonov et al. (2004). Bieri et al. (2017) have used a similar setup for the AGN radiation to study outflows in the ISM. However, their simulations were highly idealised: the photon injection rate was constant, the self-gravity of the gas and cooling. More realistic study has been recently presented by Costa et al. (2018) where the authors have studied the impact of radiation from a high-redshift ($z > 6$) quasar on the star formation quenching in realistic cosmological zoom-in simulations, thus with a limited spatial resolution. Therefore, the setup I have presented here examines previously unexplored scales and environments of the SMBH accretion and AGN feedback.

In Figure 6.1 I show the accretion rate on the SMBH in units of the Eddington rate for the 'old' NSC (left-hand side) and the 'young' NSC (right-hand side). In the 'old' NSC setup (Figure 6.1a) the gas injection rate from stellar winds is sub-Eddington. On the other hand the SMBH is still able to grow at a over 1% of the Eddington rate, if the feedback is not included. Inclusion of the thermal feedback reduces the accretion rate noticeably. The outflow propagates spherically around the SMBH. In effect the gas is heated up, which in turns reduces gas accretion. Simulations with different AGN feedback implementations are currently running.

In the 'young' cluster (Figure 6.1b) the injection rate is higher than the SMBH Ed-

[1] `https://bitbucket.org/vperret/dice`

Table 6.1: Properties of the photon groups used in the radiative transfer simulations.

group	ϵ_0 [eV]	ϵ_1 [eV]	$\sigma_{\mathrm{H_I}}$ [cm^2]	$\sigma_{\mathrm{He_I}}$ [cm^2]	$\sigma_{\mathrm{He_{II}}}$ [cm^2]	$\tilde{\kappa}$ [cm^2 g^{-1}]	$f_{\gamma,\mathrm{i}}$
IR	0.10	1.00	0	0	0	10	0.2289
Opt	1.00	13.60	0	0	0	1000	0.3759
$\mathrm{UV_{H_I}}$	13.60	24.59	3.3×10^{-18}	0	0	1000	0.0829
$\mathrm{UV_{He_I}}$	24.59	54.42	6.3×10^{-19}	4.8×10^{-18}	0	1000	0.0695
$\mathrm{UV_{He_{II}}}$	54.42	∞	9.9×10^{-20}	1.4×10^{-19}	1.3×10^{-18}	1000	0.1243

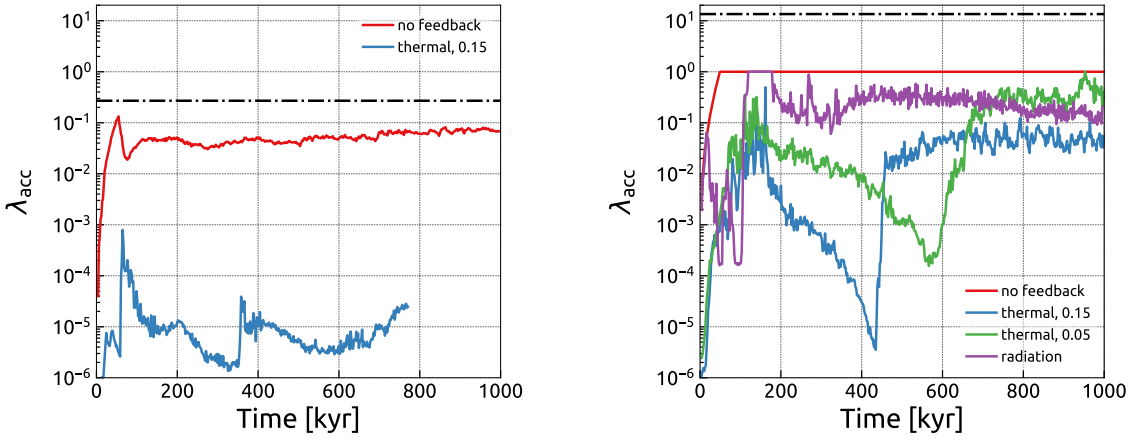

(a) the 'old' NSC

(b) the 'young' NSC

Figure 6.1: The accretion rate on the SMBH in units of the Eddington rate for the 'old' NSC (left panel) and the 'young' NSC (right panel) with different AGN feedback implementations. The black dash-dotted line marks the injection rate.

dington rate (~ 0.02 $M_\odot$/yr). Initially, the radiative feedback seems to have less impact on the accretion rate than the classical thermal dump. At later times, when the system reaches quasi-steady state, the radiation falls between the two runs with thermal feedback, suggesting that the numerical coupling efficiency $\epsilon_c \sim 0.1$ (see the definition in Chapter 3). Most importantly, however, the SMBH can grow fairly quickly, as $\lambda_{acc} \sim 0.1$.

In Figure 6.2 I plot the phase diagrams of radial velocity (top row) and temperature (bottom row) as a function of density for three different AGN feedback prescriptions in the 'young' NSC setup. In the simulation without AGN feedback gas collapses, forming a disc and feeds the SMBH. A very strong outflow develops in the other two setups. However, there is a significant difference between the run with thermal dump and the one with radiation injection - in the latter all gas with densities below $\sim 10^4$ cm^{-3} is heated up to above 10^4 K due to the photoionisation heating. This effect is naturally not captured in the thermal dump model. The dense gas which resides in the circumnuclear disc is largely unaffected by the AGN feedback, as the energy escapes along the path of the least resistance.

A full and careful analysis of the SMBH feeding with the NSC winds and impact of the AGN feedback is currently in progress.

6.2. Circumgalactic medium of massive galaxies: impact of AGN and environment

Galaxies used to be called 'island universes', however today we know that they intimately connected with the large scale environment in which they live. The intergalactic and circumgalactic media (IGM and CGM, respectively) impact the evolution of galaxies by providing fuel that sustains the star formation, while themselves being impacted by large-scale outflows originating from galactic discs. This can be compared to a system of interconnected vessels (known also as a 'bathtub' model, e.g. Dekel & Mandelker, 2014). The morphology of IGM and CGM together with stellar content of galaxies provide us with a unique way of studying both the past and present of galactic halos. Connecting these two environments will lead to the improvement in understanding how various feedback processes work and interact with each other.

There has been a lot of work recently that focused on simulating the spatial distribution and morphology of HI around massive high-redshift galaxies (Faucher-Giguère & Kereš, 2011; Shen et al., 2013; Fumagalli et al., 2014; Faucher-Giguère et al., 2015). All these simulations have problems in reproducing the large amounts of HI seen in observations (e.g. Prochaska et al., 2013). Some of the authors attributed these shortcomings to insufficient resolution of simulations, while it has been also argued that efficient stellar and AGN feedback are required.

In the light of these, as well as some of the results on observations of giant molecular outflows (see also Section 6.3), it seems timely to explore effects of AGN feedback on CGM with cosmological simulations. This is then a natural continuation of the project described in Chapter 4, especially thanks to recently implemented enhancements to sink particle model in Ramses (see Subsection 2.8.3). In order to achieve high-resolution I apply the zoom-in technique[2] to a sample of $M_{halo} \sim 10^{13}$ $M_\odot$ and vary the AGN feedback prescrip-

[2]The zoom-in technique focuses the computational resources on a single halo of interest, while keeping the regions outside of the zoom at low resolution. Consequently high dynamic range and resolution can be achieved without losing the information about surrounding structures.

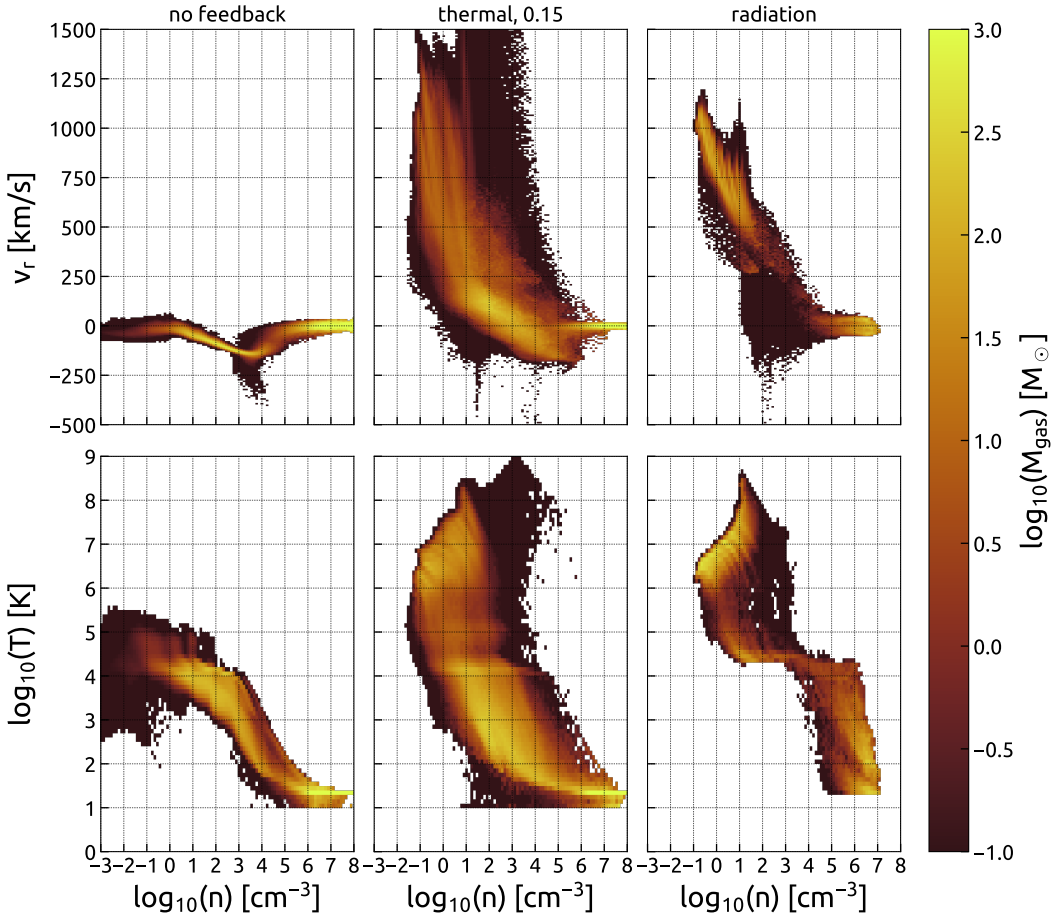

Figure 6.2: The phase diagrams of radial velocity (top row) and temperature (bottom row) as a function of density for three different AGN feedback prescriptions in the 'young' NSC setup - no feedback (left column), thermal feedback (middle) and radiation injection (right).

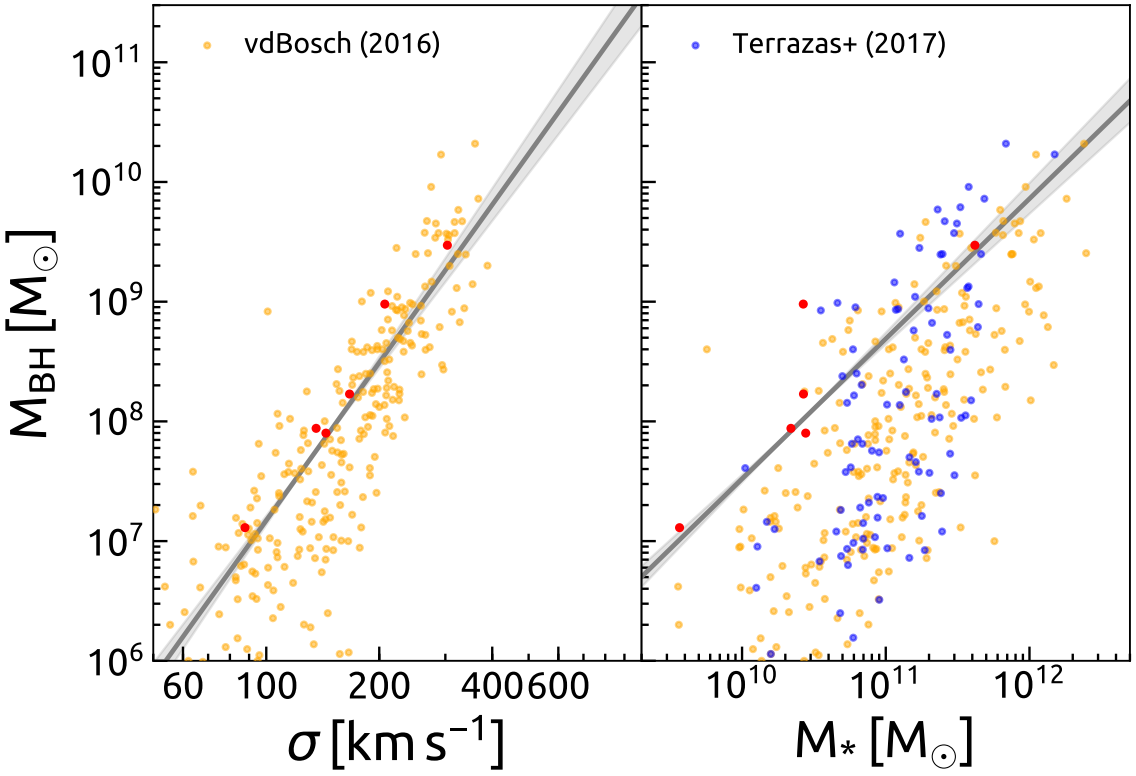

Figure 6.3: Black hole mass as a function of stellar velocity dispersion and stellar mass from cosmological zoom-in simulations ($M_{\rm halo} = 1.4 \times 10^{13}$ M$_\odot$ at $z = 2$). Values measured in simulations (red points) are compared to a sample of SMBH from van den Bosch (2016, orange points) and Terrazas et al. (2017, blue points).

tion. I use the NSC-SMBH model introduced in Chapter 3, and switch between thermal dump and newly implemented momentum kick based on the accretion rate (when the accretion rate is above or below $0.01\dot{M}_{\rm Edd}$, respectively). My box has a size of 150 cMpc/h and the maximum spatial resolution achieved is $\sim$ 130 pc (a cell is refined if the mass contained in it exceeds $\sim 10^8$ M$_\odot$).

In Figure 6.3 I show the comparison of SMBH mass scaling relations between simulations and observations. While there is a good match between simulations and theory, it must be noted that observed relations are dominated by local SMBH measurements, while I stop my simulations at $z = 2$. Furthermore, the combination of SN feedback and AGN feedback modulated by measured Eddington ratio produces realistic stellar mass of the central galaxy. Figure 6.4 compares a run without AGN feedback (left-hand side) to a run that includes full NSC-SMBH modelling. When AGN feedback is modelled, then the stellar mass measured matches the abundance matching relations.

In order to find the cause of the difference in the stellar mass content I turn my attention to temperature-density diagrams (Figure 6.5). They reveal that within $0.1R_{\rm vir}$ in the AGN run (right-hand side) the gas is hotter and has larger density dispersion than in the run without it (left-hand side). A full and careful analysis of the differences seen in the gas morphology of CGM is now underway.

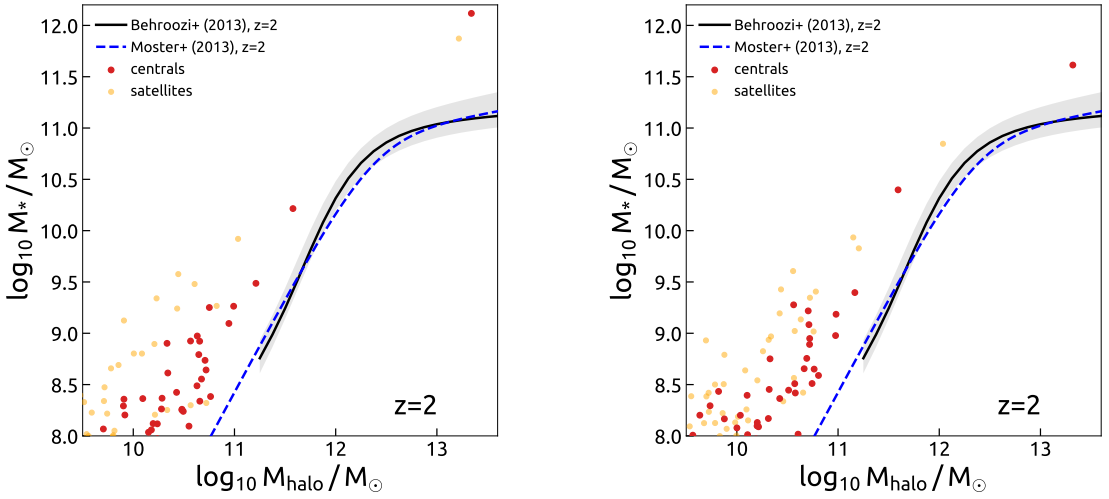

(a) without AGN (b) with AGN

Figure 6.4: Stellar mass vs. halo mass in cosmological zoom-in simulations without AGN feedback (left) and with AGN feedback (right) at $z = 2$. Red and green points mark central galaxies and their satellites, respectively. Black line with grey band and blue dashed lines mark relations found with the abundance matching techniques of Behroozi et al. (2013); Moster et al. (2013), respectively.

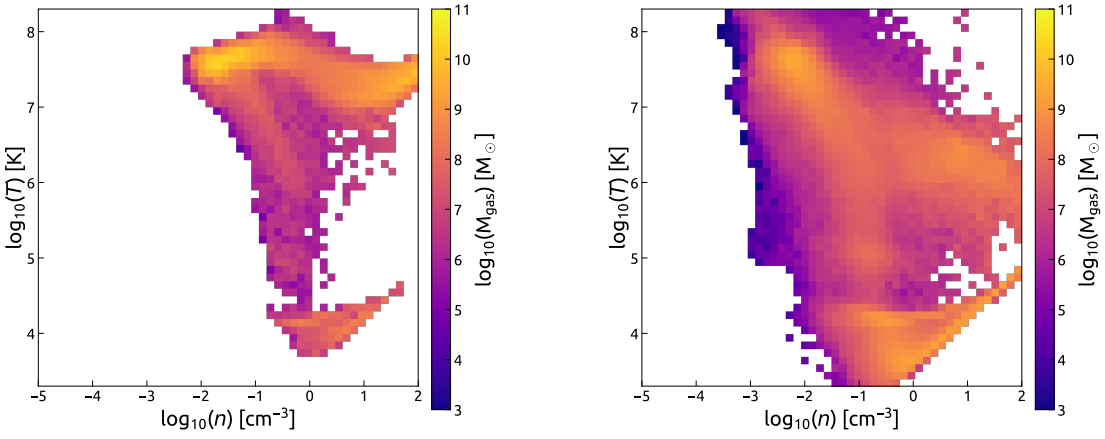

(a) without AGN (b) with AGN

Figure 6.5: Temperature-density diagrams in cosmological zoom-in simulations without AGN feedback (left) and with AGN feedback (right) at $z = 2$.

6.3. Molecular outflow from a medium-redshift quasar

All successful models of galaxy evolution seem to require regulation of star formation via gas outflows. The quenching of star formation can proceed very rapidly, suggesting that the dense, molecular gas acting as fuel for star formation is affected by these outflows as well as the diffuse ISM. There is growing observational evidence of outflows occurring universally at a wide range of redshifts and galaxy masses, however these molecular outflows only rarely carry significant amounts of molecular gas.

It has been argued that in the case of strong SN feedback, SMBH growth is halted and AGN feedback is not relevant for driving the outflow (e.g. Dubois et al., 2015). However, I have shown a scenario in which both SN and AGN are in action (see Chapter 4). This opens up an additional avenue for the debate about the efficiency of AGN and SN feedback.

In a recent observational campaign we have discovered a hyper-luminous starburst galaxy HS1549+19 hosting a quasar at $z \approx 3$ with observed line-of-sight velocities of the molecular gas exceeding $\approx 1300\,\mathrm{km\,s^{-1}}$. Part of the extended emission can be related to large-scale star formation, however the CO emission extends beyond the extent of the infrared continuum. If our interpretation of the outflow is correct, then it would provide direct evidence for predictions provided by galaxy formation models, particularly presented in Chapter 4. I also argue that the starburst driven winds are not energetic enough to account for the starburst-driven gas moving with such high velocities at the observed distances. It seems that the quasar's low coupling efficiency, when compared to low-redshift galaxies, might be due to the more extended distribution of gas. This picture is in agreement with simulations I have presented in Chapter 4, where I have shown that collaboration between AGN and SN feedback can drive dense gas out of galaxies, while only marginally affecting the extended star-forming galactic disc. Stellar feedback generates a massive galactic fountain, where dense gas is swept up by hot, but powerful AGN feedback, accelerating it to high velocities. Our observation seem to find a rare, extreme object, however we predict that many more molecular outflows will be detected at high redshifts with a whole range of outflow rates.

A complete manuscript that describes our findings is currently in preparation.

6.4. Future perspectives

There are multiple ways that the ongoing work presented in this chapter can be extended. I will mention them only very briefly, but all of them seem to be worth looking at in detail.

It can be argued that the NSC setup presented in Section 6.1 is not the most realistic one. Indeed, future studies should focus on more realistic modelling of the IMF, stellar evolution and winds, perhaps via coupling with an external code or a library. Furthermore, I have omitted effects of star formation in the circumnuclear disc, as well as the impact of stellar radiation. While the radiation feedback is a viable way of replacing phenomenological thermal dump, the radio mode could be modelled by a non-thermal pressure from cosmic rays.

None of the simulations presented here include the treatment of magnetohydrodynamics, which is expected to be important for the jet feedback. Furthermore, it is anticipated that massive, dense outflows can be stabilised and prevented from disruption by magnetic fields. Both of these effects could influence the structure of CGM, which in turn

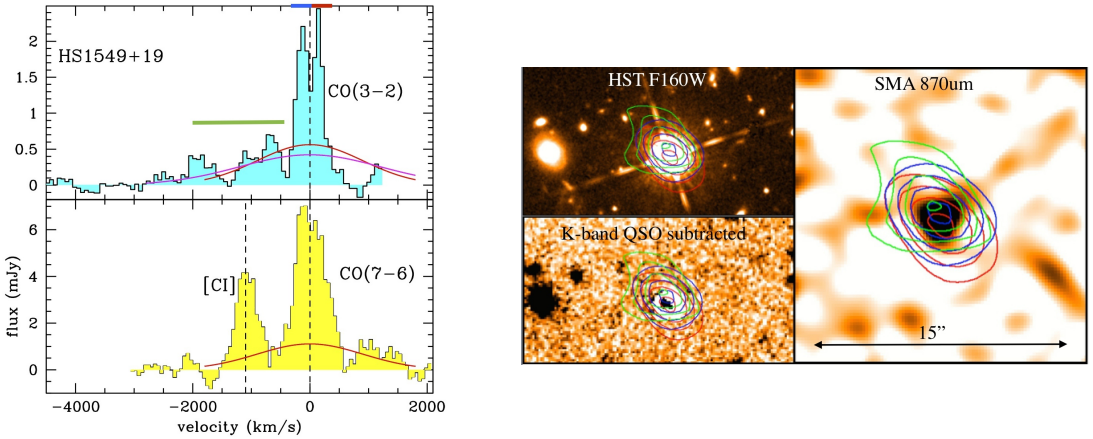

Figure 6.6: **LEFT panel:** The integrated one-dimensional, CO(3–2), CO(7–6) and $[CI]_{2-1}$ spectra of our starburst galaxy hosting a quasar. The outflowing gas is detected at $> 5\sigma$, spatially offset from the quasar host, out to about $-2000\,\mathrm{km\,s^{-1}}$. The green, red and blue bars show the velocity range of the spectrum used to create the contoured map on the right. **RIGHT panel:** Channel maps of the CO(3–2) gas are contoured (colour coded as above in the one-dimensional CO(3–2) spectrum). **Left upper:** The Hubble Space Telescope (*HST*) F160W image: the saturated quasar image completely dominates the bulk of the CO host galaxy and outflowing regions. **Left lower:** The *K*-band and Infrared Array Camera on the Spitzer Space Telescope (IRAC) images: the quasar is not saturated, and we can model and subtract it. **Right:** The deep Sub-Millimeter Array (SMA) 870μm image, detecting the QSO host as a 9 mJy source, which is unresolved in the ∼2.3″ SMA synthesised beam.

impacts star formation and subsequent SN-induced outflows. In order to improve the understanding of the role of feedback on the galaxy formation, the subgrid models used for stellar winds, SN explosions and AGN feedback need to become less phenomenological and more physical. This is especially complicated task in the cosmological simulations, where the resolution is poor.

Last, but not least, an improvement in the comparison between simulations and observations is necessary. With the deluge of the data from the future observatories (e.g. James Webb Space Telescope, Euclid and Athena, to name just a few), better modelling of observable and instrumental effects will be crucial to fully benefit from the new observations.

Bibliography

Aalto S., Garcia-Burillo S., Muller S., Winters J. M., van der Werf P., Henkel C., Costagliola F., Neri R., 2012, A&A, 537, A44

Aarseth S. J., 1963, MNRAS, 126, 223

Abbott B. P., et al., 2016, Phys. Rev. Lett., 116, 061102

Abel T., 2011, MNRAS, 413, 271

Abel T., Bryan G. L., Norman M. L., 2000, ApJ, 540, 39

Agertz O., et al., 2007, MNRAS, 380, 963

Alexander D. M., et al., 2011, ApJ, 738, 44

Andersen D. R., Walcher C. J., Böker T., Ho L. C., van der Marel R. P., Rix H.-W., Shields J. C., 2008, ApJ, 688, 990

Anglés-Alcázar D., Özel F., Davé R., 2013, ApJ, 770, 5

Anglés-Alcázar D., Davé R., Özel F., Oppenheimer B. D., 2014, ApJ, 782, 84

Antonini F., 2013, ApJ, 763, 62

Antonini F., Barausse E., Silk J., 2015, ApJ, 812, 72

Ashman K. M., Zepf S. E., 1992, ApJ, 384, 50

Aubert D., Teyssier R., 2010, ApJ, 724, 244

Bahcall J. N., Kozlovsky B.-Z., Salpeter E. E., 1972, ApJ, 171, 467

Barnes J., Hut P., 1986, Nature, 324, 446

Barnes D. J., et al., 2017a, preprint, p. arXiv:1710.08420

Barnes D. J., et al., 2017b, MNRAS, 471, 1088

Barth A. J., Ho L. C., Rutledge R. E., Sargent W. L. W., 2004, ApJ, 607, 90

Bate M. R., Bonnell I. A., Price N. M., 1995, MNRAS, 277, 362

Battaglia N., Bond J. R., Pfrommer C., Sievers J. L., 2013, ApJ, 777, 123

Begelman M. C., 2010, MNRAS, 402, 673

Begelman M. C., Rees M. J., 1978, MNRAS, 185, 847

Begelman M. C., Volonteri M., Rees M. J., 2006, MNRAS, 370, 289

Begelman M. C., Rossi E. M., Armitage P. J., 2008, MNRAS, 387, 1649

Behroozi P. S., Wechsler R. H., Conroy C., 2013, ApJ, 770

Bellovary J. M., Governato F., Quinn T. R., Wadsley J., Shen S., Volonteri M., 2010, ApJ, 721, L148

Berukoff S. J., Hansen B. M. S., 2006, ApJ, 650, 901

Bieri R., Dubois Y., Rosdahl J., Wagner A., Silk J., Mamon G. A., 2017, MNRAS, 464, 1854

Biernacki P., Teyssier R., Bleuler A., 2017, MNRAS, 469, 295

Binney J., Tremaine S., 2008, Galactic Dynamics: Second Edition. Princeton University Press

Bîrzan L., Rafferty D. A., McNamara B. R., Wise M. W., Nulsen P. E. J., 2004, ApJ, 607, 800

Blandford R. D., McKee C. F., 1982, ApJ, 255, 419

Bleuler A., Teyssier R., 2014, MNRAS, 445, 4015

Bleuler A., Teyssier R., Carassou S., Martizzi D., 2015, Computational Astrophysics and Cosmology, 2, 5

Blitz L., Fukui Y., Kawamura A., Leroy A., Mizuno N., Rosolowsky E., 2007, Protostars and Planets V, pp 81–96

Böker T., Laine S., van der Marel R. P., Sarzi M., Rix H.-W., Ho L. C., Shields J. C., 2002, AJ, 123, 1389

Böker T., Sarzi M., McLaughlin D. E., van der Marel R. P., Rix H.-W., Ho L. C., Shields J. C., 2004, AJ, 127, 105

Bond J. R., Arnett W. D., Carr B. J., 1984, ApJ, 280, 825

Bondi H., 1952, MNRAS, 112, 195

Bondi H., Hoyle F., 1944, MNRAS, 104, 273

Bonnell I. A., Rice W. K. M., 2008, Science, 321, 1060

Booth C. M., Schaye J., 2009, MNRAS, 398, 53

Bournaud F., Dekel A., Teyssier R., Cacciato M., Daddi E., Juneau S., Shankar F., 2011, ApJ, 741, L33

Bournaud F., et al., 2012, ApJ, 757, 81

Bournaud F., et al., 2014, ApJ, 780, 57

Bower R. G., Benson A. J., Malbon R., Helly J. C., Frenk C. S., Baugh C. M., Cole S., Lacey C. G., 2006, MNRAS, 370, 645

Bower R. G., Schaye J., Frenk C. S., Theuns T., Schaller M., Crain R. A., McAlpine S., 2017, MNRAS, 465, 32

Bromm V., Loeb A., 2003, ApJ, 596, 34

Bromm V., Coppi P. S., Larson R. B., 1999, ApJ, 527, L5

Brook C. B., Stinson G., Gibson B. K., Roškar R., Wadsley J., Quinn T., 2012, MNRAS, 419, 771

Brooks A., Christensen C., 2016, in Galactic Bulges. p. 317, doi:https://doi.org/10.1007/978-3-319-19378-6_12

Brüggen M., Kaiser C. R., 2002, Nature, 418, 301

Bryan G. L., et al., 2014, ApJS, 211, 19

Bullock J. S., Dekel A., Kolatt T. S., Kravtsov A. V., Klypin A. A., Porciani C., Primack J. R., 2001, ApJ, 555, 240

Capuzzo-Dolcetta R., Miocchi P., 2008, ApJ, 681, 1136

Cattaneo A., et al., 2009, Nature, 460, 213

Cavagnolo K. W., McNamara B. R., Nulsen P. E. J., Carilli C. L., Jones C., Bîrzan L., 2010, ApJ, 720, 1066

Chandrasekhar S., 1943, ApJ, 97, 255

Chapon D., Mayer L., Teyssier R., 2013, MNRAS, 429, 3114

Cheung E., et al., 2016, Nature, 533, 504

Choi E., Ostriker J. P., Naab T., Johansson P. H., 2012, ApJ, 754, 125

Choi E., Naab T., Ostriker J. P., Johansson P. H., Moster B. P., 2014, MNRAS, 442, 440

Choi E., Ostriker J. P., Naab T., Oser L., Moster B. P., 2015, MNRAS, 449, 4105

Churazov E., Forman W., Jones C., Böhringer H., 2000, A&A, 356, 788

Churazov E., Brüggen M., Kaiser C. R., Böhringer H., Forman W., 2001, ApJ, 554, 261

Cicone C., et al., 2014, A&A, 562, A21

Cicone C., et al., 2015, A&A, 574, A14

Ciotti L., Ostriker J. P., Proga D., 2010, ApJ, 717, 708

Clark P. C., Glover S. C. O., Klessen R. S., 2008, ApJ, 672, 757

Close J. L., Pittard J. M., Hartquist T. W., Falle S. A. E. G., 2013, MNRAS, 436, 3021

Costa T., Sijacki D., Trenti M., Haehnelt M. G., 2014, MNRAS, 439, 2146

Costa T., Sijacki D., Haehnelt M. G., 2015, MNRAS, 448, L30

Costa T., Rosdahl J., Sijacki D., Haehnelt M. G., 2018, MNRAS, p. 1438

Côté P., et al., 2006, ApJS, 165, 57

Cowie L. L., Binney J., 1977, ApJ, 215, 723

Croton D. J., et al., 2006, MNRAS, 365, 11

Curtis H. D., 1917, PASP, 29, 206

Damjanov I., et al., 2009, ApJ, 695, 101

Davé R., Oppenheimer B. D., Finlator K., 2011, MNRAS, 415, 11

Davies M. B., Miller M. C., Bellovary J. M., 2011, ApJ, 740, L42

Debuhr J., Quataert E., Ma C.-P., 2011, MNRAS, 412, 1341

Dekel A., Burkert A., 2014, MNRAS, 438, 1870

Dekel A., Mandelker N., 2014, MNRAS, 444, 2071

Dekel A., Silk J., 1986, ApJ, 303, 39

Dekel A., Sari R., Ceverino D., 2009, ApJ, 703, 785

Dennis T. J., Chandran B. D. G., 2005, ApJ, 622, 205

Devecchi B., Volonteri M., 2009, ApJ, 694, 302

Di Matteo T., Springel V., Hernquist L., 2005, Nature, 433, 604

Di Matteo T., Khandai N., DeGraf C., Feng Y., Croft R. A. C., Lopez J., Springel V., 2012, ApJ, 745, L29

Dijkstra M., Haiman Z., Mesinger A., Wyithe J. S. B., 2008, MNRAS, 391, 1961

Dolag K., Komatsu E., Sunyaev R., 2016, MNRAS, 463, 1797

Dong R., Stone J. M., 2009, ApJ, 704, 1309

Dong R., Rasmussen J., Mulchaey J. S., 2010, ApJ, 712, 883

Dotan C., Rossi E. M., Shaviv N. J., 2011, MNRAS, 417, 3035

Dubois Y., Devriendt J., Slyz A., Teyssier R., 2010, MNRAS, 409, 985

Dubois Y., Devriendt J., Teyssier R., Slyz A., 2011, MNRAS, 417, 1853

Dubois Y., Devriendt J., Slyz A., Teyssier R., 2012, MNRAS, 420, 2662

Dubois Y., Pichon C., Devriendt J., Silk J., Haehnelt M., Kimm T., Slyz A., 2013, MNRAS, 428, 2885

Dubois Y., et al., 2014, MNRAS, 444, 1453

Dubois Y., Volonteri M., Silk J., Devriendt J., Slyz A., Teyssier R., 2015, MNRAS, 452, 1502

Dubois Y., Peirani S., Pichon C., Devriendt J., Gavazzi R., Welker C., Volonteri M., 2016, MNRAS, 463, 3948

Duffell P. C., MacFadyen A. I., 2011, ApJS, 197, 15

Dunn R. J. H., Fabian A. C., Taylor G. B., 2005, MNRAS, 364, 1343

Dursi L. J., Pfrommer C., 2008, ApJ, 677, 993

Ebisuzaki T., et al., 2001, ApJ, 562, L19

Eckert D., Gaspari M., Vazza F., Gastaldello F., Tramacere A., Zimmer S., Ettori S., Paltani S., 2017, ApJ, 843, L29

Eisenstein D. J., Loeb A., 1995, ApJ, 443, 11

Elmegreen B. G., Efremov Y. N., 1997, ApJ, 480, 235

Elmegreen B. G., Bournaud F., Elmegreen D. M., 2008a, ApJ, 684, 829

Elmegreen B. G., Bournaud F., Elmegreen D. M., 2008b, ApJ, 688, 67

Emsellem E., van de Ven G., 2008, ApJ, 674, 653

Evrard A. E., 1997, MNRAS, 292, 289

Fabian A. C., 1994, ARA&A, 32, 277

Fabian A. C., 1999, MNRAS, 308, L39

Fabian A. C., 2012, ARA&A, 50, 455

Fabian A. C., Nulsen P. E. J., 1977, MNRAS, 180, 479

Fabian A. C., et al., 2000, MNRAS, 318, L65

Fan X., et al., 2003, AJ, 125, 1649

Faucher-Giguère C.-A., Kereš D., 2011, MNRAS, 412, L118

Faucher-Giguère C.-A., Hopkins P. F., Kereš D., Muratov A. L., Quataert E., Murray N., 2015, MNRAS, 449, 987

Feldmann R., Hopkins P. F., Quataert E., Faucher-Giguère C.-A., Kereš D., 2016, MNRAS, 458, L14

Ferrarese L., Merritt D., 2000, ApJ, 539, L9

Feruglio C., et al., 2017, A&A, 608, A30

Fiacconi D., Rossi E. M., 2016, MNRAS, 455, 2

Fiacconi D., Mayer L., Roškar R., Colpi M., 2013, ApJ, 777, L14

Fiacconi D., Sijacki D., Pringle J. E., 2018, MNRAS, 477, 3807

Forman W., et al., 2007, ApJ, 665, 1057

Förster Schreiber N. M., et al., 2014, ApJ, 787, 38

Frenk C. S., et al., 1999, ApJ, 525, 554

Fryer C. L., Woosley S. E., Heger A., 2001, ApJ, 550, 372

Fryxell B., et al., 2000, ApJS, 131, 273

Fujii M., Iwasawa M., Funato Y., Makino J., 2010, ApJ, 716, L80

Fumagalli M., Hennawi J. F., Prochaska J. X., Kasen D., Dekel A., Ceverino D., Primack J., 2014, ApJ, 780, 74

Gabor J. M., Bournaud F., 2013, MNRAS, 434, 606

Gabor J. M., Bournaud F., 2014, MNRAS, 441, 1615

Gabor J. M., Capelo P. R., Volonteri M., Bournaud F., Bellovary J., Governato F., Quinn T., 2016, A&A, 592, A62

Gaburov E., Lombardi Jr. J. C., Portegies Zwart S., 2010, MNRAS, 402, 105

Gaburov E., Johansen A., Levin Y., 2012, ApJ, 758, 103

Gao L., Yoshida N., Abel T., Frenk C. S., Jenkins A., Springel V., 2007, MNRAS, 378, 449

Gaspari M., Melioli C., Brighenti F., D'Ercole A., 2011, MNRAS, 411, 349

Gaspari M., Ruszkowski M., Oh S. P., 2013, MNRAS, 432, 3401

Gebhardt K., Thomas J., 2009, ApJ, 700, 1690

Gebhardt K., et al., 2000, ApJ, 539, L13

Genzel R., et al., 2008, ApJ, 687, 59

Genzel R., Eisenhauer F., Gillessen S., 2010, Rev. Mod. Phys. , 82, 3121

Genzel R., et al., 2011, ApJ, 733, 101

Genzel R., et al., 2014, ApJ, 796, 7

George R. D., et al., 2014, MNRAS, 442, 1877

Georgiev I. Y., Böker T., 2014, MNRAS, 441, 3570

Georgiev I. Y., Hilker M., Puzia T. H., Goudfrooij P., Baumgardt H., 2009, MNRAS, 396, 1075

Ghez A. M., et al., 2008, ApJ, 689, 1044

Gillessen S., Eisenhauer F., Trippe S., Alexander T., Genzel R., Martins F., Ott T., 2009, ApJ, 692, 1075

Gingold R. A., Monaghan J. J., 1977, MNRAS, 181, 375

Gitti M., Feretti L., Schindler S., 2006, A&A, 448, 853

Gnedin N. Y., Abel T., 2001, New A, 6, 437

Gnedin O. Y., Ostriker J. P., Tremaine S., 2014, ApJ, 785, 71

Godfrey L. E. H., Shabala S. S., 2013, ApJ, 767, 12

Godunov S. K., 1959, Matematicheskii Sbornik, 89, 271

Graham A. W., Spitler L. R., 2009, MNRAS, 397, 2148

Greene J. E., et al., 2010, ApJ, 721, 26

Greene J. E., Zakamska N. L., Ho L. C., Barth A. J., 2011, ApJ, 732, 9

Greene J. E., Zakamska N. L., Smith P. S., 2012, ApJ, 746, 86

Greif T. H., Springel V., White S. D. M., Glover S. C. O., Clark P. C., Smith R. J., Klessen R. S., Bromm V., 2011, ApJ, 737, 75

Gualandris A., Merritt D., 2009, ApJ, 705, 361

Guillard N., Emsellem E., Renaud F., 2016, MNRAS, 461, 3620

Guillet T., Teyssier R., 2011, Journal of Computational Physics, 230, 4756

Gültekin K., et al., 2009, ApJ, 698, 198

Guo F., Mathews W. G., 2011, ApJ, 728, 121

Guo Y., Giavalisco M., Ferguson H. C., Cassata P., Koekemoer A. M., 2012, ApJ, 757, 120

Gürkan M. A., Fregeau J. M., Rasio F. A., 2006, ApJ, 640, L39

Habouzit M., Volonteri M., Dubois Y., 2017, MNRAS, 468, 3935

Haehnelt M. G., Rees M. J., 1993, MNRAS, 263, 168

Hahn O., Martizzi D., Wu H.-Y., Evrard A. E., Teyssier R., Wechsler R. H., 2017, MNRAS, 470, 166

Häring N., Rix H.-W., 2004, ApJ, 604, L89

Harrison C. M., Alexander D. M., Mullaney J. R., Swinbank A. M., 2014, MNRAS, 441, 3306

Hartmann M., Debattista V. P., Seth A., Cappellari M., Quinn T. R., 2011, MNRAS, 418, 2697

Heckman T. M., Best P. N., 2014, ARA&A, 52, 589

Heckman T. M., Lehnert M. D., Strickland D. K., Armus L., 2000, ApJS, 129, 493

Heger A., Fryer C. L., Woosley S. E., Langer N., Hartmann D. H., 2003, ApJ, 591, 288

Hitomi Collaboration et al., 2016, Nature, 535, 117

Hockney R. W., Eastwood J. W., 1981, Computer Simulation Using Particles. McGraw-Hill

Hopkins P. F., 2013, MNRAS, 428, 2840

Hopkins P. F., 2015, MNRAS, 450, 53

Hopkins P. F., Hernquist L., 2006, ApJS, 166, 1

Hopkins P. F., Quataert E., 2011, MNRAS, 415, 1027

Hopkins P. F., Kereš D., Oñorbe J., Faucher-Giguère C.-A., Quataert E., Murray N., Bullock J. S., 2014, MNRAS, 445, 581

Hopkins P. F., Torrey P., Faucher-Giguère C.-A., Quataert E., Murray N., 2016, MNRAS, 458, 816

Hosokawa T., Yorke H. W., Inayoshi K., Omukai K., Yoshida N., 2013, ApJ, 778, 178

Hoyle F., Fowler W. A., 1963, Nature, 197, 533

Hoyle F., Lyttleton R. A., 1939, Proceedings of the Cambridge Philosophical Society, 35, 405

Hubble E. P., 1927, The Observatory, 50, 276

Hubble E. P., 1929, ApJ, 69

Hurier G., Angulo R. E., 2018, A&A, 610, L4

Iapichino L., Federrath C., Klessen R. S., 2017, MNRAS, 469, 3641

Inutsuka S.-I., 2002, Journal of Computational Physics, 179, 238

Jahnke K., Macciò A. V., 2011, ApJ, 734, 92

Johnson J. L., Whalen D. J., Li H., Holz D. E., 2013, ApJ, 771, 116

Kawata D., Gibson B. K., 2005, MNRAS, 358, L16

Khokhlov A., 1998, Journal of Computational Physics, 143, 519

Kim J.-h., Wise J. H., Alvarez M. a., Abel T., 2011, ApJ, 738, 54

King A., 2003, ApJ, 596, L27

King A. R., Pringle J. E., 2006, MNRAS, 373, L90

Kochanek C. S., Shapiro S. L., Teukolsky S. A., 1987, ApJ, 320, 73

Kollmeier J. A., et al., 2006, ApJ, 648, 128

Komatsu E., Seljak U., 2001, MNRAS, 327, 1353

Komatsu E., et al., 2011, ApJS, 192, 18

Kormendy J., Ho L. C., 2013, ARA&A, 51, 511

Kormendy J., Drory N., Bender R., Cornell M. E., 2010, ApJ, 723, 54

Koushiappas S. M., Bullock J. S., Dekel A., 2004, MNRAS, 354, 292

Kravtsov A. V., Borgani S., 2012, ARA&A, 50, 353

Krumholz M. R., Tan J. C., 2007, ApJ, 654, 304

Krumholz M. R., McKee C. F., Klein R. I., 2004, ApJ, 611, 399

Kudritzki R.-P., Puls J., 2000, ARA&A, 38, 613

Kuo C. Y., et al., 2011, ApJ, 727, 20

Landau L. D., Lifshitz E. M., 1959, Fluid mechanics. Oxford: Pergamon Press

Lanz L., Ogle P. M., Evans D., Appleton P. N., Guillard P., Emonts B., 2015, ApJ, 801, 17

Laor A., 2001, ApJ, 553, 677

Lau E. T., Kravtsov A. V., Nagai D., 2009, ApJ, 705, 1129

Lau E. T., Gaspari M., Nagai D., Coppi P., 2017, ApJ, 849, 54

Le Brun A. M. C., McCarthy I. G., Schaye J., Ponman T. J., 2014, MNRAS, 441, 1270

Lea S. M., Silk J., Kellogg E., Murray S., 1973, ApJ, 184, L105

Levin Y., 2007, MNRAS, 374, 515

Li H., Gnedin O. Y., 2014, ApJ, 796, 10

Li Y., Bryan G. L., Ruszkowski M., Voit G. M., O'Shea B. W., Donahue M., 2015, ApJ, 811, 73

Liang L., Durier F., Babul A., Davé R., Oppenheimer B. D., Katz N., Fardal M., Quinn T., 2016, MNRAS, 456, 4266

Lodato G., Natarajan P., 2006, MNRAS, 371, 1813

Loeb A., Rasio F. A., 1994, ApJ, 432, 52

Lucy L. B., 1977, AJ, 82, 1013

Lynden-Bell D., 1969, Nature, 223, 690

Lynden-Bell D., Rees M. J., 1971, MNRAS, 152, 461

Lyutikov M., 2006, MNRAS, 373, 73

Lyutyi V. M., Cherepashchuk A. M., 1972, Astronomicheskij Tsirkulyar, 688

Madau P., Dickinson M., 2014, ARA&A, 52, 415

Madau P., Rees M. J., 2001, ApJ, 551, L27

Magorrian J., et al., 1998, AJ, 115, 2285

Maiolino R., Krabbe A., Thatte N., Genzel R., 1998, ApJ, 493, 650

Maiolino R., et al., 2012, MNRAS, 425, L66

Mantz A. B., Allen S. W., Morris R. G., Rapetti D. A., Applegate D. E., Kelly P. L., von der Linden A., Schmidt R. W., 2014, MNRAS, 440, 2077

Marconi A., Hunt L. K., 2003, ApJ, 589, L21

Marigo P., Bressan A., Nanni A., Girardi L., Pumo M. L., 2013, MNRAS, 434, 488

Martizzi D., Teyssier R., Moore B., 2013, MNRAS, 432, 1947

Martizzi D., Hahn O., Wu H.-Y., Evrard A. E., Teyssier R., Wechsler R. H., 2016, MNRAS, 459, 4408

Mathews W. G., Bregman J. N., 1978, ApJ, 224, 308

McCarthy I. G., et al., 2010, MNRAS, 406, 822

McConnell N. J., Ma C.-P., 2013, ApJ, 764, 184

McElroy R., Croom S. M., Pracy M., Sharp R., Ho I.-T., Medling A. M., 2015, MNRAS, 446, 2186

McLure R. J., Dunlop J. S., 2002, MNRAS, 331, 795

McNamara B. R., Nulsen P. E. J., 2007, ARA&A, 45, 117

McNamara B. R., Wise M. W., David L. P., Nulsen P. E. J., Sarazin C. L., 2000, in AAS/High Energy Astrophysics Division 5. p. 13.21

McNamara B. R., et al., 2001, ApJ, 562, L149

Meece G. R., Voit G. M., O'Shea B. W., 2017, ApJ, 841, 133

Merritt D., 2009, ApJ, 694, 959

Meyer L., et al., 2012, Science, 338, 84

Milosavljević M., 2004, ApJ, 605, L13

Mingo B., Hardcastle M. J., Croston J. H., Evans D. A., Kharb P., Kraft R. P., Lenc E., 2012, ApJ, 758, 95

Miniati F., 2014, ApJ, 782, 21

Mitchell N. L., McCarthy I. G., Bower R. G., Theuns T., Crain R. A., 2009, MNRAS, 395, 180

Mo H., van den Bosch F. C., White S., 2010, Galaxy Formation and Evolution. Cambridge University Press

Monaghan J. J., 1992, ARA&A, 30, 543

Monaghan J., 2012, Annual Review of Fluid Mechanics, 44, 323

Montero-Castano M., Herrnstein R. M., Ho P. T. P., 2009, ApJ, 695, 1477

Moster B. P., Naab T., White S. D. M., 2013, MNRAS, 428, 3121

Nagai D., Kravtsov A. V., Vikhlinin A., 2007, ApJ, 668, 1

Nandra K., et al., 2007, ApJ, 660, L11

Navarro J. F., Frenk C. S., White S. D. M., 1996, ApJ, 462, 563

Navarro J. F., Frenk C. S., White S. D. M., 1997, ApJ, 490, 493

Nayakshin S., 2014, MNRAS, 437, 2404

Negri A., Volonteri M., 2017, MNRAS, 467, 3475

Nelson K., Lau E. T., Nagai D., Rudd D. H., Yu L., 2014, ApJ, 782, 107

Nemmen R. S., Georganopoulos M., Guiriec S., Meyer E. T., Gehrels N., Sambruna R. M., 2012, Science, 338, 1445

Nesvadba N. P. H., Polletta M., Lehnert M. D., Bergeron J., De Breuck C., Lagache G., Omont A., 2011, MNRAS, 415, 2359

Ohto A., Kawano N., Fukazawa Y., 2003, PASJ, 55, 819

Okamoto T., Jenkins A., Eke V. R., Quilis V., Frenk C. S., 2003, MNRAS, 345, 429

Okamoto T., Nemmen R. S., Bower R. G., 2008a, MNRAS, 385, 161

Okamoto T., Gao L., Theuns T., 2008b, MNRAS, 390, 920

Ostriker E. C., 1999, ApJ, 513, 252

Ostriker J. P., Choi E., Ciotti L., Novak G. S., Proga D., 2010, ApJ, 722, 642

Panagoulia E. K., Fabian A. C., Sanders J. S., Hlavacek-Larrondo J., 2014, MNRAS, 444, 1236

Pedlar A., Ghataure H. S., Davies R. D., Harrison B. A., Perley R., Crane P. C., Unger S. W., 1990, MNRAS, 246, 477

Penzias A. A., Wilson R. W., 1965, ApJ, 142, 419

Perucho M., Martí J.-M., Quilis V., Ricciardelli E., 2014, MNRAS, 445, 1462

Peterson J. R., Fabian A. C., 2006, Phys. Rep., 427, 1

Pizzolato F., Soker N., 2005, ApJ, 632, 821

Planck Collaboration et al., 2016, A&A, 594, A13

Planelles S., Borgani S., Fabjan D., Killedar M., Murante G., Granato G. L., Ragone-Figueroa C., Dolag K., 2014, MNRAS, 438, 195

Pontzen A., Tremmel M., Roth N., Peiris H. V., Saintonge A., Volonteri M., Quinn T., Governato F., 2017, MNRAS, 465, 547

Portegies Zwart S. F., Makino J., McMillan S. L. W., Hut P., 1999, A&A, 348, 117

Portegies Zwart S. F., Baumgardt H., Hut P., Makino J., McMillan S. L. W., 2004, Nature, 428, 724

Power C., Read J. I., Hobbs A., 2014, MNRAS, 440, 3243

Pratt G. W., et al., 2010, A&A, 511, A85

Price D. J., 2012, Journal of Computational Physics, 231, 759

Prieto J., Escala A., Volonteri M., Dubois Y., 2017, ApJ, 836, 216

Prochaska J. X., Hennawi J. F., Simcoe R. A., 2013, ApJ, 762, L19

Puchwein E., Sijacki D., Springel V., 2008, ApJ, 687, L53

Quinlan G. D., Shapiro S. L., 1990, ApJ, 356, 483

Rahmati A., Pawlik A. H., Raičevic M., Schaye J., 2013, MNRAS, 430, 2427

Rasera Y., Teyssier R., 2006, A&A, 445, 1

Rasia E., et al., 2015, ApJ, 813, L17

Read J. I., Hayfield T., Agertz O., 2010, MNRAS, 405, 1513

Regan J. A., Haehnelt M. G., 2009, MNRAS, 396, 343

Reines A. E., Greene J. E., Geha M., 2013, ApJ, 775, 116

Reynolds C. S., McKernan B., Fabian A. C., Stone J. M., Vernaleo J. C., 2005, MNRAS, 357, 242

Reynolds C. S., Balbus S. A., Schekochihin A. A., 2015, ApJ, 815, 41

Richstone D., et al., 1998, Nature, 395, A14

Ritchie B. W., Thomas P. A., 2001, MNRAS, 323, 743

Robinson K., et al., 2004, ApJ, 601, 621

Roediger E., Brüggen M., Rebusco P., Böhringer H., Churazov E., 2007, MNRAS, 375, 15

Roos O., Juneau S., Bournaud F., Gabor J. M., 2015, ApJ, 800, 19

Rosas-Guevara Y. M., et al., 2015, MNRAS, 454, 1038

Rosdahl J., Teyssier R., 2015a, MNRAS, 449, 4380

Rosdahl J., Teyssier R., 2015b, MNRAS, 449, 4380

Rosdahl J., Blaizot J., Aubert D., Stranex T., Teyssier R., 2013, MNRAS, 436, 2188

Rosdahl J., Schaye J., Teyssier R., Agertz O., 2015, MNRAS, 451, 34

Rosen A., Bregman J. N., 1995, ApJ, 440, 634

Rosolowsky E., 2007, ApJ, 654, 240

Rosswog S., 2009, New A Rev., 53, 78

Roškar R., Fiacconi D., Mayer L., Kazantzidis S., Quinn T. R., Wadsley J., 2015, MNRAS, 449, 494

Rupke D. S. N., Veilleux S., 2011, ApJ, 729, L27

Ryden B., 2016, Introduction to Cosmology. Cambridge University Press

Saitoh T. R., Makino J., 2013, ApJ, 768, 44

Salpeter E. E., 1964, ApJ, 140, 796

Sanders J. S., Fabian A. C., Taylor G. B., 2009, MNRAS, 393, 71

Sanderson A. J. R., Finoguenov A., Mohr J. J., 2005, ApJ, 630, 191

Sazonov S. Y., Ostriker J. P., Sunyaev R. A., 2004, MNRAS, 347, 144

Scannapieco E., Brüggen M., 2008, ApJ, 686, 927

Schaller M., Dalla Vecchia C., Schaye J., Bower R. G., Theuns T., Crain R. A., Furlong M., McCarthy I. G., 2015, MNRAS, 454, 2277

Schawinski K., Thomas D., Sarzi M., Maraston C., Kaviraj S., Joo S.-J., Yi S. K., Silk J., 2007, MNRAS, 382, 1415

Schawinski K., Urry M., Treister E., Simmons B., Natarajan P., Glikman E., 2011, ApJ, 743, L37

Schaye J., 2004, ApJ, 609, 667

Schaye J., et al., 2015, MNRAS, 446, 521

Schmidt M., 1963, Nature, 197, 1040

Schmidt W., et al., 2014, MNRAS, 440, 3051

Schneider R., Omukai K., Inoue A. K., Ferrara A., 2006, MNRAS, 369, 1437

Schödel R., et al., 2002, Nature, 419, 694

Schuecker P., Finoguenov A., Miniati F., Böhringer H., Briel U. G., 2004, A&A, 426, 387

Schwarzschild K., 1906, Nachrichten von der Gesellschaft der Wissenschaften zu Göttingen, Mathematisch-Physikalische Klasse, 1906, 41

Scoville N., Norman C., 1995, ApJ, 451, 510

Sembolini F., et al., 2016, MNRAS, 459, 2973

Seth A. C., Dalcanton J. J., Hodge P. W., Debattista V. P., 2006, AJ, 132, 2539

Seth A., Agüeros M., Lee D., Basu-Zych A., 2008, ApJ, 678, 116

Shakura N., Sunyaev R., 1973, A&A, 24, 337

Shankar F., Lapi A., Salucci P., De Zotti G., Danese L., 2006, ApJ, 643, 14

Shen S., Wadsley J., Stinson G., 2010, MNRAS, 407, 1581

Shen S., Madau P., Guedes J., Mayer L., Prochaska J. X., Wadsley J., 2013, ApJ, 765, 89

Shu F. H., 1992, The physics of astrophysics. Volume II: Gas dynamics.. University Science Books

Shurkin K., Dunn R. J. H., Gentile G., Taylor G. B., Allen S. W., 2008, MNRAS, 383, 923

Siegel M. H., et al., 2007, ApJ, 667, L57

Sijacki D., Springel V., 2006, MNRAS, 366, 397

Sijacki D., Springel V., Di Matteo T., Hernquist L., 2007, MNRAS, 380, 877

Sijacki D., Springel V., Haehnelt M. G., 2009, mnras, 400, 100

Sijacki D., Vogelsberger M., Genel S., Springel V., Torrey P., Snyder G. F., Nelson D., Hernquist L., 2015, MNRAS, 452, 575

Silk J., Rees M. J., 1998, A&A, 331, L1

Smith N., 2014, ARA&A, 52, 487

Sokołowska A., Mayer L., Babul A., Madau P., Shen S., 2016, ApJ, 819, 21

Sołtan A., 1982, MNRAS, 200, 115

Somerville R. S., Hopkins P. F., Cox T. J., Robertson B. E., Hernquist L., 2008, MNRAS, 391, 481

Souza Lima R., Mayer L., Capelo P. R., Bellovary J. M., 2017, ApJ, 838, 13

Spoon H. W. W., et al., 2013, ApJ, 775, 127

Springel V., 2010a, ARA&A, 48, 391

Springel V., 2010b, MNRAS, 401, 791

Springel V., Di Matteo T., Hernquist L., 2005, MNRAS, 361, 776

Steinborn L. K., Dolag K., Hirschmann M., Prieto M. A., Remus R.-S., 2015, MNRAS, 448, 1504

Steinhardt C. L., Elvis M., 2010, MNRAS, 402, 2637

Stone N. C., Küpper A. H. W., Ostriker J. P., 2017, MNRAS, 467, 4180

Strickland D. K., Heckman T. M., 2009, ApJ, 697, 2030

Sturm E., et al., 2011, ApJ, 733, L16

Sutherland R. S., Bicknell G. V., 2007, ApJS, 173, 37

Sutherland R. S., Dopita M., 1993, ApJS, 88, 253

Tabor G., Binney J., 1993, MNRAS, 263, 323

Tacconi L. J., et al., 2013, ApJ, 768, 74

Tamburello V., Mayer L., Shen S., Wadsley J., 2015, MNRAS, 453, 2491

Tegmark M., Silk J., Rees M. J., Blanchard A., Abel T., Palla F., 1997, ApJ, 474, 1

Terrazas B. A., Bell E. F., Woo J., Henriques B. M. B., 2017, ApJ, 844, 170

Teyssier R., 2002, A&A, 385, 337

Teyssier R., 2015, ARA&A, 53, 325

Teyssier R., Moore B., Martizzi D., Dubois Y., Mayer L., 2011, MNRAS, 414, 195

Teyssier R., Pontzen A., Dubois Y., Read J. I., 2013, MNRAS, 429, 3068

Thacker R. J., MacMackin C., Wurster J., Hobbs A., 2014, MNRAS, 443, 1125

Thompson T. A., Fabian A. C., Quataert E., Murray N., 2015, MNRAS, 449, 147

Thornton C. E., Barth A. J., Ho L. C., Rutledge R. E., Greene J. E., 2008, ApJ, 686, 892

Toomre A., 1964, ApJ, 139, 1217

Toro E., 2009, Riemann Solvers and Numerical Methods for Fluid Dynamics: A Practical Introduction. Springer Berlin Heidelberg, doi:https://books.google.ch/books?id=SqEjX0um8o0C

Tremaine S. D., Ostriker J. P., Spitzer Jr. L., 1975, ApJ, 196, 407

Tremaine S., et al., 2002, ApJ, 574, 740

Tremmel M., Governato F., Volonteri M., Quinn T. R., 2015, MNRAS, 451, 1868

Truelove J. K., Klein R. I., McKee C. F., Holliman II J. H., Howell L. H., Greenough J. A., 1997, ApJ, 489, L179

Umemura M., Loeb A., Turner E. L., 1993, ApJ, 419, 459

Vazza F., Gheller C., Brunetti G., 2010, A&A, 513, A32

Veilleux S., Cecil G., Bland-Hawthorn J., 2005, ARA&A, 43, 769

Veilleux S., et al., 2013, ApJ, 776, 27

Vernaleo J. C., Reynolds C. S., 2006, ApJ, 645, 83

Vogelsberger M., Genel S., Sijacki D., Torrey P., Springel V., Hernquist L., 2013, MNRAS, 436, 3031

Vogelsberger M., et al., 2014, MNRAS, 444, 1518

Voit G. M., Meece G., Li Y., O'Shea B. W., Bryan G. L., Donahue M., 2017, ApJ, 845, 80

Volonteri M., 2010, A&A Rev., 18, 279

Wadsley J. W., Veeravalli G., Couchman H. M. P., 2008, MNRAS, 387, 427

Wagner A. Y., Bicknell G. V., Umemura M., 2012, ApJ, 757, 136

Weiner B. J., et al., 2009, ApJ, 692, 187

Werner N., et al., 2014, MNRAS, 439, 2291

Wiersma R. P. C., Schaye J., Theuns T., 2011, MNRAS, 415, 353

Wise J. H., Turk M. J., Abel T., 2008, ApJ, 682, 745

Woo J.-H., Urry C. M., 2002, ApJ, 579, 530

Woosley S. E., Weaver T. A., 1986, ARA&A, 24, 205

Wurster J., Thacker R. J., 2013, MNRAS, 431, 539

Yesuf H. M., Faber S. M., Trump J. R., Koo D. C., Fang J. J., Liu F. S., Wild V., Hayward C. C., 2014, ApJ, 792, 84

Zel'dovich Y. B., 1964, Soviet Physics Doklady, 9, 195

Zhang D., Thompson T. A., 2012, MNRAS, 424, 1170

Zhang W., Woosley S. E., Heger A., 2008, ApJ, 679, 639

Zhuravleva I., et al., 2014, Nature, 515, 85

ZuHone J. A., Miller E. D., Bulbul E., Zhuravleva I., 2018, ApJ, 853, 180

den Brok M., et al., 2014, MNRAS, 445, 2385

den Brok M., et al., 2015, ApJ, 809, 101

van Leer B., 1979, Journal of Computational Physics, 32, 101

van de Voort F., Schaye J., Booth C. M., Haas M. R., Dalla Vecchia C., 2011, MNRAS, 414, 2458

van den Bosch R. C. E., 2016, ApJ, 831, 134

van den Bosch R. C. E., van de Ven G., Verolme E. K., Cappellari M., de Zeeuw P. T., 2008, MNRAS, 385, 647

Acknowledgements

Last words are for fools who haven't said enough.

– Karl Marx

Perhaps Karl Marx was right, but let me have these last words to thank all the people who made these last four years such a great experience.

First of all, I would like to thank Prof. Dr. Romain Teyssier for four years of excellent supervision and patience, especially when I have lost all the patience to myself. I will not forget the writing advices ("be like Stephen King!") and his absolute professionalism and devotion at all times. Merci!

Big thanks to Dr. Andreas Bleuler, who was like an older brother and tutor to me, who introduced me to RAMSES and who showed me what it means to be Swiss. Another person who stood the fire of my questions and naivety is Dr. Valentin Perret - thanks for that French cool you took it with!

I would also like to thank my collaborators: Prof. Dr. Oliver Hahn and Dr. Go Ogiya for exploding clusters together, Prof. Dr. Arif Babul and Prof. Dr. Scott Chapman who taught me a lot about observations and the academic life. Honest thanks to Prof. Dr. Davide Martizzi, my predecessor in Zurich, who was a great companion whenever I met him. Also, big thanks to all others whom I worked with or met during conferences - particularly Prof. Dr. Joki Rosdahl, Dr. Alireza Rahmati, Dr. Pedro Capelo and Dr. Tiago Costa, as well as the whole SMAUG collaboration team! I have learned a lot from you, not only about science!

My life in Zurich would be so much more miserable without the people I shared the academic life with at the Institute for Computational Science. Some of you helped me start this journey, while some other joined during it. Sincere and deep thanks to The TEAM - Dr. Elena Gavagnin and Dr. Michael Rieder, Dr. Davide Fiacconi who convinced me that Zurich is the place to be, Dr. Valentina Tamburello and Dr. Niccolo Moretti - for the gym and lunch meetings. Dr. Irshad Mohammed for all the long hours of conversations (on three continents) and for always pushing me to think harder! I would not end up in Zurich if not for Dr. Aleksandra Sokołowska, who pulled me from the Flatlands to the Highlands - Dziękuję! Some others are soon-to-be doctors: Christian Reinhardt, Maria Veiga, Tine Colman, Fulvio Scaccabarozzi, Tomas Tamfal, Rafael Souza, Phillipp Denzel and Mischa Knabenhans - you made my life at ICS interesting and fun! Keep up the great work you are doing! Last, but not least, I would like to give my words of grateful thanks and appreciation to some people without whom ICS would not run: Suzanne Wilde, Regina Schmid and Dr. Douglas Potter - you are the heart of this institute!

Special thanks go to my proofreaders, Dr. Kanta Dihal, and soon-to-be doctors from the Down Under: Fiona Panther and Shourya Khana.

None of this would be possible without constant and unconditional support and faith of my family, my mother Barbara, my father Leszek and my sister Monika. Nie ma słów, które mogłyby wyrazić moją wdzięczność! ¡El año pasado hubiera sido tan diferente sin ti, Ale! ¡Gracias, mi sunshine!